

# Experimental and theoretical study of structural defects and impact on electrochemical performance on Li-rich oxides



Universidad del País Vasco    Euskal Herriko  
Unibertsitatea

**Jon Serrano Sevillano**

Supervisors: Dr. Montse Casas-Cabanas  
Dr. Amaia Saracibar

Euskal Herriko Unibertsitatea (UPV/EHU)

This dissertation is submitted for the degree of  
*Doctor*

Euskal Herriko Unibertsitatea

October 2019

TESI ZUZENDARIAREN BAIMENA TESIA AURKEZTEKO

AUTORIZACIÓN DEL/LA DIRECTORA/A DE TESIS PARA SU PRESENTACIÓN

Zuzendariaren izen-abizenak /Nombre y apellidos del/la director/a: Montserrat Casas Cabanas

IFZ /NIF: 77115350F

Tesiaren izenburua / Título de la tesis:

Experimental and theoretical study of structural defects and impact on electrochemical performance of Li-rich oxides

Doktorego programa / Programa de doctorado: Ciencia y Tecnología de Materiales

Doktoregaiaren izen-abizenak / Nombre y apellidos del/la doctorando/a: Jon Serrano Sevillano

Unibertsitateak horretarako jartzen duen tresnak emandako ANTZEKOTASUN TXOSTENA ikusita, baimena ematen dut goian aipatzen den tesia aurkez dadin, horretarako baldintza guztiak betetzen baititu.

Visto el INFORME DE SIMILITUD obtenido de la herramienta que a tal efecto pone a disposición la universidad, autorizo la presentación de la tesis doctoral arriba indicada, dado que reúne las condiciones necesarias para su defensa.

Tokia eta data / Lugar y fecha: Vitoria 26 de Septiembre de 2019



Sin. / Fdo.: Tesiaren zuzendaria / El/La director/a de la tesis



<b>TESI ZUZENDARIAREN BAIMENA TESI AURKEZTEKO</b>	<b>AUTORIZACIÓN DEL/LA DIRECTORA/A DE TESIS PARA SU PRESENTACIÓN</b>
-------------------------------------------------------	--------------------------------------------------------------------------

Zuzendariaren izen-abizenak /Nombre y apellidos del/la director/a: Amaia Saracibar Ruiz de Ocenda

IFZ /NIF: 44680477x

Tesiaren izenburua / Título de la tesis:

EXPERIMENTAL AND THEORETICAL STUDY OF STRUCTURAL DEFECTS AND IMPACT  
ON ELECTROCHEMICAL PERFORMANCE OF LI-RICH OXIDES

Doktorego programa / Programa de doctorado: Ciencia y Tecnología de Materiales

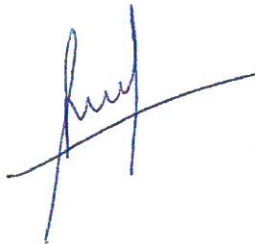
Doktoregaiaren izen-abizenak / Nombre y apellidos del/la doctorando/a: Jon Serrano Sevillano

Unibertsitateak horretarako jartzen duen tresnak emandako ANTZEKOTASUN TXOSTENA ikusita, baimena ematen dut goian aipatzen den tesia aurkez dadin, horretarako baldintza guztiak betetzen baititu.

Visto el INFORME DE SIMILITUD obtenido de la herramienta que a tal efecto pone a disposición la universidad, autorizo la presentación de la tesis doctoral arriba indicada, dado que reúne las condiciones necesarias para su defensa.

Tokia eta data / Lugar y fecha:

VITORIA 11 OCTUBRE 2019



Sin. / Fdo.: Tesiaren zuzendaria / El/La director/a de la tesis



**AUTORIZACION DEL TUTOR/A DE TESIS  
PARA SU PRESENTACION**

Dr/a. Teófilo Rojo Aparicio \_\_\_\_\_

como Tutor/a de la Tesis Doctoral: Experimental and theoretical study of structural defects and impact on electrochemical performance of Li-rich oxides

realizada en el Programa de Doctorado Ciencia y Tecnología de materiales

por el Doctorando Don/ña. Jon Serrano Sevillano ,  
y dirigida por el Dr./a Amaia Saracibar y Montserrat Casas Cabanas

autorizo la presentación de la citada Tesis Doctoral, dado que reúne las condiciones necesarias para su defensa.

En Vitoria \_\_\_\_\_ a 30de Septiembre \_\_\_\_\_ de 2019 \_\_\_\_\_

EL/LA TUTOR/A DE LA TESIS



Fdo.: Teófilo Rojo



**AUTORIZACIÓN DE LA COMISIÓN ACADÉMICA DEL PROGRAMA DE DOCTORADO**

La Comisión Académica del Programa de Doctorado en \_\_\_\_**Ciencia y Tecnología de Materiales**\_\_\_\_\_

en reunión celebrada el día 9 de Octubre de 2019, ha acordado dar la conformidad a la presentación de la Tesis Doctoral titulada:

EXPERIMENTAL AND THEORETICAL STUDY OF STRUCTURAL DEFECTS AND IMPACT ON ELECTROCHEMICAL PERFORMANCE OF LI-RICH OXIDES\_

dirigida por el/la Dr/a. \_\_\_\_\_

**AMAIA SARACIBAR Y MONTSE CASAS CABANAS**

y presentada por Don/Dña. JON SERRANO SEVILLANO

adscrito o adscrita al Departamento \_\_\_\_\_QUIMICA FISICA

En Leioa a 14 de Octubre de 2019

EL/LA RESPONSABLE DEL PROGRAMA DE DOCTORADO

Fdo.: \_\_\_\_\_Luis Mª Lezama Diago\_\_\_\_\_





**AUTORIZACIÓN DEL DEPARTAMENTO**

El Consejo del Departamento de \_\_\_\_\_ QUIMICA FISICA

en reunión celebrada el día \_\_\_ de \_\_\_\_\_ de \_\_\_\_\_ ha acordado dar la conformidad a la admisión a trámite de presentación de la Tesis Doctoral titulada \_\_\_\_\_ EXPERIMENTAL AND THEORETICAL STUDY OF STRUCTURAL DEFECTS AND IMPACT ON ELECTROCHEMICAL PERFORMANCE OF LI-RICH OXIDES

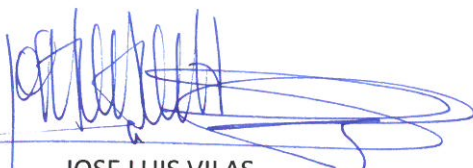
dirigida por el/la Dr/a. AMAIA SARACIBAR Y MONTSE CASAS CABANAS

y presentada por Don/ña. \_\_\_\_\_ JON SERRANO SEVILLANO \_\_\_\_\_

ante este Departamento.

En \_\_\_\_\_ LEIOA \_\_\_\_\_ a 21 de Octubre de 2019

VºBº DIRECTOR/A DEL DEPARTAMENTO

  
Fdo.: \_\_\_\_\_ JOSE LUIS VILAS \_\_\_\_\_

SECRETARIO/A DEL DEPARTAMENTO

  
Fdo.: \_\_\_\_\_ LEYRE PEREZ \_\_\_\_\_



**ACTA DE GRADO DE DOCTOR O DOCTORA**  
**ACTA DE DEFENSA DE TESIS DOCTORAL**

DOCTORANDO/A DON/DÑA. \_\_\_\_\_

TITULO DE LA TESIS: \_\_\_\_\_

\_\_\_\_\_

\_\_\_\_\_

El Tribunal designado por la Comisión de Postgrado de la UPV/EHU para calificar la Tesis Doctoral arriba indicada y reunido en el día de la fecha, una vez efectuada la defensa por el/la doctorando/a y contestadas las objeciones y/o sugerencias que se le han formulado, ha otorgado por \_\_\_\_\_ la calificación de:  
*unanimidad ó mayoría*

*SOBRESALIENTE / NOTABLE / APROBADO / NO APTO*

Idioma/s de defensa (en caso de más de un idioma, especificar porcentaje defendido en cada idioma):

Castellano \_\_\_\_\_

Euskera \_\_\_\_\_

Otros Idiomas (especificar cuál/cuales y porcentaje) \_\_\_\_\_

En \_\_\_\_\_ a \_\_\_\_\_ de \_\_\_\_\_ de \_\_\_\_\_

EL/LA PRESIDENTE/A,

EL/LA SECRETARIO/A,

Fdo.: \_\_\_\_\_  
Dr/a: \_\_\_\_\_

Fdo.: \_\_\_\_\_  
Dr/a: \_\_\_\_\_

VOCAL 1º,

VOCAL 2º,

VOCAL 3º,

Fdo.: \_\_\_\_\_  
Dr/a: \_\_\_\_\_

Fdo.: \_\_\_\_\_  
Dr/a: \_\_\_\_\_

Fdo.: \_\_\_\_\_  
Dr/a: \_\_\_\_\_

EL/LA DOCTORANDO/A,

Fdo.: \_\_\_\_\_





Para Julio, Juani y Noe.





## Acknowledgements

Y por fin parece que el momento ha llegado. Desde que entre al CICE allá por Junio de 2014 han pasado muchas personas importantes por mi vida (a parte de las que ya estaban) a las que me gustaría agradecer el haber estado a mi lado durante estos 5 años, ya que de alguna forma han ayudado a sacar este trabajo adelante.

Antes de nada, me gustaría agradecer al CICE la beca que me han otorgado, así como a la UPV/EHU por la posibilidad que me han dado para realizar la tesis. Por supuesto, me gustaría agradecer tanto a **Montse Casas** como a **Amaia Saracibar** el haber sido unas excelentes directoras de tesis que no solo me han ayudado en la parte científica pero que además me han ayudado a crecer como persona y han estado ahí siempre que lo he necesitado. No me quiero olvidar de **Montse Galceran**, ya que ella fue la primera persona con la que trabajé y que confió en mi. Con ella aprendí las bases de cristalografía y de electroquímica y gracias a ella (o por su culpa) le cogí el gusto; tanto como para haber acabado haciendo una tesis en dicha temática.

Me gustaría también agradecer a **Jordi Cabana** la gran acogida que tuve durante mi estancia en Chicago y a todos los compañeros que me hicieron la estancia más fácil, como **Brian, Gene, Mike, Chao, Haifeng, Sam, Mark** o **Jake**. Por supuesto una mención especial para **Maria, Mari Jose, Raquel, Andrés** y los margaritas, con los que pasé grandes momentos en USA.

También me gustaría agradecer a todo aquel que me ha ayudado en la elaboración de la tesis como **MJ, Fran, Juan Miguel** o **Dany** entre otros. Especial mención para **Marine**, que siempre que he tenido cualquier problema se ha mostrado dispuesta a ayudar, especialmente durante los primeros años que es cuando más ayuda se necesita.

Los grandes momentos que he vivido en el CIC y lo feliz que he sido mientras trabajaba en él ha sido sin ninguna duda gracias al gran ambiente de trabajo que hay. En primer lugar, me gustaría mencionar a tres personas especiales con las que he compartido más tiempo. En primer lugar, a **Oier** agradecerle que me haya tenido al día con todas las novedades de la OMS, así como su preocupación por mi colesterol. Oier ha cambiado mucho durante estos años; cuando entré era un chico comprometido que vestía con camisetas de Malala y pulseras de ACNUR y míralo ahora. Por otra parte, me gustaría agradecer a **Itziar** los

grandes momentos que hemos vivido en las idas y venidas al CIC y toda las cosas que he aprendido con ella. Como Itziar dijo una vez: *me he sentido mal, porque nunca soy borde*. Finalmente, agradecer a **Ane** que entré tan rápido a las provocaciones, lo que nos ha hecho pasar grandes ratos, especialmente el día que nos explicó detalladamente su trabajo con EL HERRAMIENTO. He pasado grandes momentos con los tres, muchas gracias.

A parte de ellos, me gustaría también mencionar a los doctorando que entramos a la vez y hemos compartido batallas como **Edu, Xabi, Iñaki Maria, Begoña** y **Jaione**, así como a **Añas** y **Uxue**.

A los de la mesa de la 1 (**Giorgio, Guillermo, Jon, Oier Lakuntza**) haber amenizado mis momento favorito de relax. Gracias por esos temas de conversación tan variopintos; desde conjeturas morales y sociales hasta el robot de cocina de Jon.

Además, me gustar'ia agradecer a todos con los que he compartido buenos momentos en el CICE como **Gelines, Kristel, Mikel, Silvia, Carlos, Jon Rey, Emanuele, Marco, Aran, Leticia, Yasmina, Jokin, Serio, JuanLu, Iciar, Jose, Leire, Antonio, Ander** o **Alex** entre otros.

Fuera del CICE, en primer lugar me gustaría agradecer a mi familia el apoyo recibido. Empezando por mis **padres Julio** y **Juani** que me han apoyado en todo momento y seguramente sean los que más han aguantado mis cambios de humor. Sin olvidar que en momentos de mucho trabajo me han ayudado via tupper's :). Por supuesto, agradecer también a **Noe**, una de las personas más importantes de mi vida y que más me ha ayudado, aunque algunas veces nos hayamos enfadado. También agradecer a **Aitor** los buenos momentos que hemos vivido. A ver cuando me puedo llevar a **Oihan** a casa, pero no os olvidéis de sus juguetes favoritos (ya sabéis, la fregona y la escoba)! También agradecer a **Unai** que me haya acogido y los buenos ratos que hemos pasado, aunque sea un poco paquete al pro. Tenemos un chuletón pendiente! También agradecer a mis tios, en especial a **Luisi** y **Félix**, todos los buenos momentos que me han dado, aunque me obligasen a ir a vendimiar. Tampoco me puedo olvidar de **Nai, Isra** y **Aimar**, aunque siempre se quieran escaquear de la vendimia. Por otra parte, me quiero acordar de mi prima **Zuri** y de **Andrés, Xabi** y **Julen**, los grades momentos que hemos pasado en la terraza. También a **Tere** y **Ignacio** y esas comidas en Villodas.

Me gustaría también agradecer a **Dr. Mikel Cañizo Zubizarreta, Ugar, Txiki** y **Txapu**, así como a los titulares en el exilio **Z** y **Greño** todo el tiempo que hemos pasado por la Sede y el Txolarre. Asimismo, a los **Tolos**, en especial con los que más tiempo he pasado: a mi entrenador personal **Lizaga, Puro, Flavio** y **Bosuc**. Tampoco me quiero olvidar de **Marti**, un hijo del Alavés. A **Ania** por esas vueltas en bici y esas historias interminables. A mis

amigos de CR, que dudan sobre el estado del fuego: **Angel**, que descubrió el secreto de Euskadi y **Rubén**.

Finalmente, me gustaría agradecer esta tesis al horóscopo, a **Manolo** y a su carro nuevo, así como a la gasolina, que nunca se agota. Espero que el cartero no se haya vuelto a perder...

Muchas gracias!



## Abstract

La creciente preocupación por reducir la contaminación atmosférica en las ciudades está haciendo crecer el interés por el vehículo eléctrico, ya que éste no emite gases ni partículas nocivas *in situ*. Fundamentalmente, los vehículos eléctricos almacenan su energía en baterías de ion litio. Desgraciadamente, el precio de estas baterías es elevado y su autonomía es todavía insuficiente, por lo que es necesario una mejora tanto en el precio como en el rendimiento para la implantación generalizada del vehículo eléctrico. El componente más caro de dichas baterías es el cátodo, que representa cerca del 40% de su precio total, por lo que un abaratamiento de éste acarrearía un importante ahorro en los costes de las baterías. En este sentido, los óxidos laminares ricos en litio formulados como  $\text{Li}_{1+x}\text{M}_{1-x}\text{O}_2$  o  $x\text{Li}_2\text{MnO}_3 \cdot (1-x)\text{LiMO}_2$  están siendo los más estudiados como la próxima generación de materiales de cátodos para baterías de litio debido a que son capaces de almacenar una mayor cantidad de energía por masa y que además son más baratos y menos dañinos con el medio ambiente, ya que no tienen cobalto, o si lo tienen, es en una cantidad considerablemente menor en comparación con los óxidos laminares clásicos. La mayor densidad energética de los óxidos ricos en litio frente a los clásicos reside en que, como su propio nombre indica, los primeros tienen una mayor cantidad de litio por fórmula unidad que los segundos, por lo que en caso de extraer todo el litio de la estructura se consigue mayor energía. Al tener una mayor cantidad de litio, los metales de transición (que en los óxidos laminares clásicos son los que son activos electroquímicamente) no son capaces de compensar toda la carga en la extracción de litio, por lo que el elemento que se convierte electroquímicamente activo se cree que es el oxígeno. Sin embargo, estos compuestos sufren de un rápido agotamiento, consecuencia de los cambios estructurales durante el ciclado. Desafortunadamente, el estudio de estas modificaciones no es trivial, ya que suelen cristalizar con una gran cantidad de defectos de apilamiento, cuyo efecto en la electroquímica es generalmente ignorado. Por si fuera poco, incluso su estructura inicial es un tema de debate ya que la comunidad científica no se pone de acuerdo en si es un intercrecimiento de dos fases o una solución sólida (y de ahí su dualidad nominal).

En esta tesis se ha llevado a cabo un detallado estudio combinando diferentes técnicas experimentales tales como difracción de rayos X y de neutrones, microscopía de electrones y

resonancia magnética nuclear (RMN) en estado sólido con cálculos por primeros principios basados en la teoría del funcional de la densidad (DFT) para analizar el efecto de los defectos de apilamiento y la microestructura en la electroquímica. Para ello, en primer lugar se ha utilizado  $\text{Li}_2\text{MnO}_3$  como modelo, y en un segundo paso se ha estudiado  $\text{Li}_{1.2}\text{Mn}_{0.6}\text{Ni}_{0.2}\text{O}_2$ , que tiene un gran potencial porque presenta un buen comportamiento electroquímico (si se es capaz de evitar su rápido agotamiento) y no contiene cobalto.

En primer lugar se han preparado una serie de muestras de  $\text{Li}_2\text{MnO}_3$  con variada microestructura (diferente grado de defectos de apilamiento, tamaño y forma de cristalito) utilizando diferentes precursores de manganeso y diferentes temperaturas. Un exhaustivo análisis de rayos X con el programa FAULTS, que permite contabilizar el grado de defectos de apilamiento, combinado con microscopía de electrones, ha hecho posible aislar el efecto individual de cada uno de estos parámetros en la electroquímica. El mayor peso para un buen funcionamiento ha resultado estar en el tamaño de cristalito. Si es demasiado pequeño el material se activará rápido, pero su agotamiento también lo será. Por el contrario, si el tamaño es demasiado grande, la activación total del material nunca se llegará a producir. Por lo tanto, un tamaño intermedio de cristalito es lo más recomendable (en este caso de alrededor de 200 nm). La forma de las partículas también ha resultado tener un gran peso específico en el redimiento electroquímico del material. Las partículas planas tienen peor funcionamiento que las isotrópicas. Finalmente, el grado de defectos de apilamiento no tiene un gran peso en la capacidad que el compuesto es capaz de ofrecer. Sin embargo, se ha observado que las muestras con un bajo grado de defectos de apilamiento sufren una transformación de fase laminar a espinela (causa principal del agotamiento de este material) con mayor rapidez que las muestras con alto grado de defectos de apilamiento. Esta diferencia de comportamiento se atribuye a los diferentes entornos locales que los defectos de apilamiento generan, y se ha hipotetizado que estos podrían evitar la migración de manganeso a la capa de litios y, por tanto, la transformación a espinela. En cualquier caso, hemos visto como la elección selectiva y cautelosa de las condiciones de síntesis tiene un gran efecto en la microestructura de las muestras y, por ende, en su funcionamiento electroquímico.

En segundo lugar, se han usado tres muestras detalladamente caracterizadas mediante rayos X para estudiar el efecto de los defectos de apilamiento en los espectros de RMN en estado sólido. Para ello, se ha elegido una muestra sin defectos de apilamiento, una con bajo grado de defectos y otra con un alto grado y se han medido sus respectivos espectros de RMN. Los resultados muestran que, a mayor grado de defectos de apilamiento, mayor es la intensidad de ciertos picos, por lo que se ha podido atribuir el crecimiento de ciertos picos a los nuevos entornos locales de litio formados debido a los defectos de apilamiento. Además, se han utilizado cálculos computacionales para simular los efectos de los defectos en los

espectros de RMN. La buena concordancia entre los espectros experimentales y simulados permite atribuir de forma más precisa los diferentes entornos químicos a las señales de RMN. Gracias a estas atribuciones se ha valorado esta técnica como posible alternativa a los rayos X para determinar el grado de defectos, previsiblemente generados debido a las altas temperaturas utilizadas en la síntesis para suprimir los defectos de apilamiento. Sin embargo, la diversidad de los defectos de apilamiento produce incertidumbre en su determinación por lo que esta técnica solo permite valorar los defectos de una forma cualitativa. Por otra parte, se ha visto que la muestra sin defectos de apilamiento mostraba más resonancias de las esperadas, las cuales han sido atribuidas a otro tipo de defectos. Haciendo uso de los cálculos computacionales se han simulado los espectros que generarían los diferentes tipos de defectos que se han encontrado en este material y ha resultado que esta muestra específica puede contener vacantes de  $\text{Li}_2\text{O}$ .

En tercer lugar, se ha estudiado, haciendo uso de cálculos computacionales, en particular de DFT, las diferencias en términos de estabilidad energética de estructuras delitadas de  $\text{Li}_2\text{MnO}_3$  ideal y defectuosas y se ha encontrado que, mientras que en el rango  $2 \geq x \geq 1$  para  $\text{Li}_x\text{MnO}_3$  tanto la estructura ideal como la defectuosa se comportan de manera similar, a alto grado de delitación la estructura ideal tiende a transformarse a la fase  $O1$ , mientras que los entornos locales generados por los defectos de apilamiento impiden esta transformación. Por otra parte, se ha evaluado el uso de diferentes dopantes para la mejora de la estabilidad estructural de  $\text{Li}_2\text{MnO}_3$  en ciclado. En particular, se han testeado sodio, potasio, berilio y magnesio con una proporción de  $\text{Li}_{1.5}\text{M}_{0.5}\text{MnO}_3$ . El berilio ha sido descartado por su preferencia a ocupar huecos tetrahédricos (en  $\text{Li}_2\text{MnO}_3$  todos los metales ocupan posiciones octaédricas). Por otra parte, el gran tamaño del potasio genera tanto grandes cambios volumétricos entre la fase litiada y la delitada como un voltaje de intercalación de litio demasiado bajo para las baterías de ion litio, por lo que también ha sido descartado. Tanto el sodio como el magnesio han sido seleccionados como posibles dopantes potenciales y se ha estudiado su estabilidad al eliminar el litio de la estructura inicial. Se ha visto que el compuesto dopado con sodio tiende a cambiar de fase mediante un proceso de deslizamiento de capas (en particular, de  $O3$  a  $P3$  y finalmente a  $O1$ ), que es sabido que causa agotamiento de los materiales. En contraste, el uso del magnesio como dopante ha resultado tener dos ventajas. Por una parte, al contrario que la estructura dopada con sodio, el sistema no cambia de fase en ninguno de sus estados de delitación y por la otra parte, el magnesio reduce parcialmente el manganés, por lo que lo hace activo electroquímicamente y por lo tanto, el grado de oxidación del oxígeno es menor.

Finalmente, se ha estudiado la compleja microestructura de  $\text{Li}_{1.2}\text{Mn}_{0.6}\text{Ni}_{0.2}\text{O}_2$  así como su evolución durante el ciclado (en especial durante el primer ciclo, que es donde ocurre la

mayor modificación estructural). Para ello, en primer lugar, se han realizado simulaciones de rayos X y de neutrones con el software FAULTS para encontrar posibles diferencias entre los diferentes modelos microestructurales propuestos para este material (intercrecimiento de dos fases con diferentes celdas unidad:  $\text{Li}_2\text{MnO}_3$  y  $\text{LiMn}_{0.5}\text{Ni}_{0.5}\text{O}_2$ , intercrecimiento nanométrico de dos fases con una única celda unidad y solución sólida). El modelo de intercrecimiento de dos fases con diferentes celdas unidad ha sido descartado ya que incluso si ambas fases tienen un gran parecido estructural, las mínimas diferencias en cuanto al tamaño de la celda unidad son suficientes para que los patrones de difracción de rayos X salgan duplicados (especialmente altos ángulos donde estas diferencias son más notables). Dentro del modelo de intercrecimiento de una fase se han tenido en cuenta dos disposiciones estructurales diferentes. En la primera se ha supuesto que las capas que se forman son bien de  $\text{Li}_2\text{MnO}_3$  puro o bien de  $\text{LiMn}_{0.5}\text{Ni}_{0.5}\text{O}_2$  puro, mientras que en la segunda se han simulado intercrecimientos en tres dimensiones (3D). Los resultados han mostrado que el intercrecimiento de dos fases con una misma celda unidad solo sería posible en caso de que este intercrecimiento fuese en 3D, ya que el crecimiento por capas genera picos en el patrón de difracción no observados experimentalmente. Finalmente, los rayos X simulados para el modelo de solución sólida muestran total similitud con los experimentales, por lo que esta opción también sería posible. Por tanto, aunque por rayos X hemos sido capaces de descartar algún modelo, todavía no es posible discernir entre el intercrecimiento de  $\text{Li}_2\text{MnO}_3$  y  $\text{LiMn}_{0.5}\text{Ni}_{0.5}\text{O}_2$  en 3D y la solución sólida. Así pues, se han simulado patrones de difracción de neutrones de estos dos modelos para ver si existen diferencias y se ha encontrado que mientras que en la solución sólida aparecen reflexiones en una región específica del patrón relativa al orden en la capa de metales de transición, en el modelo de intercrecimiento en 3D no. Sin embargo esta señal es muy débil y en los patrones experimentales podrían estar cubiertas por el alto ruido de la señal, por lo que, a efectos prácticos no es posible diferenciar entre estos dos modelos.

Por otra parte se han estudiado los cambios estructurales que ocurren durante el primer ciclo en  $\text{Li}_{1.2}\text{Mn}_{0.6}\text{Ni}_{0.2}\text{O}_2$  mediante un experimento de sincrotrón de rayos X *operando*. El análisis muestra que, tal y como se describe en trabajos previos, la primera carga del material muestra dos procesos diferentes. En el primer proceso el material se comporta como los óxidos laminares clásicos donde la celda unidad se reduce debido a la oxidación de los metales de transición. En el segundo proceso, todos los metales de transición están totalmente oxidados por lo que el elemento que es electroquímicamente activo es el oxígeno. Durante este proceso, el material sufre una severa transformación estructural, con una importante migración de metales a los huecos tetrahédricos, que se relaciona como un mecanismo para estabilizar el oxígeno oxidado. Este trabajo muestra como, a alto grado de delitiación



ciertos oxígenos tienden a acercarse como mecanismo adicional para estabilizar el oxígeno oxidado. Finalmente, se han estudiado las microtensiones que estos compuestos sufren durante el ciclado y se ha visto que mientras que en la dirección de apilamiento de las capas las microtensiones aumentan en la carga y disminuyen en la descarga debido a que la extracción de litio genera distancias interplanares diferentes y que al reinsertar litio estas distancias se equiparan, los cambios estructurales que ocurren en el primer ciclo aumentan las microtensiones en el plano de los metales de transición irreversiblemente. Este aumento irreversible se ha relacionado con la migración de metales de transición tanto a la capa de litios como a los huecos tetrahédricos.



## Abstract

Li-rich oxides of formula  $\text{Li}_{1+x}\text{M}_{1-x}\text{O}_2$  or  $x\text{Li}_2\text{MnO}_3 \cdot (1-x)\text{LiMO}_2$  are being thoroughly studied as next-generation Li-ion cathode materials because they exhibit much larger capacities compared to other cathode materials. In addition, these materials represent a more environmentally friendly and cheaper alternative because they can be formulated free of cobalt. However, these compounds suffer from a fast voltage and capacity fading as a result of several structural transformations upon cycling. Unfortunately, the study of these modifications is not straightforward, as these compounds often crystallize with large amounts of stacking faults, whose impact in the electrochemical properties has been generally overlooked and not studied in detail.

In this thesis, X-ray diffraction, neutron diffraction, electron microscopy and solid state nuclear magnetic resonance experimental techniques have been combined with first principles calculations to thoroughly analyze the defect structure and microstructure as well as the impact in the electrochemical properties of this family of materials, using  $\text{Li}_2\text{MnO}_3$  as worst case scenario model material. In a second step, the origin of the structural degradation upon cycling of two lithium rich layered oxides has been theoretically and experimentally explored in  $\text{Li}_2\text{MnO}_3$  and  $\text{Li}_{1.2}\text{Mn}_{0.6}\text{Ni}_{0.2}\text{O}_2$ .

FAULTS analyses, combined with electron microscopy measurements, have allowed identifying the main parameters related to electrochemical performance of  $\text{Li}_2\text{MnO}_3$ . Crystallite size has shown to have the major impact in the obtained capacity and cyclability, with the best performance obtained with materials exhibiting an intermediate size. On the other hand, isotropic particle shape has shown to have higher capacities with lower voltage fading in comparison with platelet particles. Finally, stacking faults do not have strong impact in the delivered capacity. In contrast, they have shown to delay the undesired structural transformation to spinel phase. Therefore, by carefully selecting synthesis parameters like nature of Mn precursor or annealing temperature, the electrochemical performances of  $\text{Li}_2\text{MnO}_3$  can be improved by independent control of morphology, size and defects.

Once the microstructure is fully characterized, the  $^6\text{Li}$  ssNMR spectra of three different  $\text{Li}_2\text{MnO}_3$  samples have been studied; one without stacking faults, a second one with a low degree of stacking faults and a highly faulted sample. With the help of DFT calculations,

the effect of stacking faults in the NMR spectra has been rationalized. The quantification of stacking faults using NMR data has been attempted, using the new lithium environments stacking faults generate, although was proven to be challenging as depends on the distribution of defects. On the other hand, ssNMR has allowed to identify additional defects in the sample without stacking faults.

First principles calculations have been used to understand the differences in terms of structural stability of both ideal and defective  $\text{Li}_2\text{MnO}_3$  as well as their behavior upon delithiation. In the fully lithiated  $\text{Li}_2\text{MnO}_3$ , ideal and faulted structures have shown to be equally likely to occur. Upon delithiation, ideal and defective  $\text{Li}_x\text{MnO}_3$  have shown similar behavior in the  $2 \geq x \geq 1$  range and in both, lithium migration to tetrahedral position has been found to stabilize the oxidized oxygen atoms, in agreement with what it is experimentally found. At lower lithium contents, on the contrary, stacking faults seem to prevent  $O3 \rightarrow O1$  structural transformation, which is expected to be highly beneficial for the cyclability of this material. The impact of different cationic substitution (Na, K, Be, Mg) in the structural stability upon material delithiation has also been studied from a theoretical point of view, and the magnesium substituted compound has emerged as a promising candidate.

Finally, the complex microstructure and structural modifications occurring upon the first cycle of  $\text{Li}_{1.2}\text{Mn}_{0.6}\text{Ni}_{0.2}\text{O}_2$  have been studied. Firstly, the XRD and NPD patterns of different microstructural arrangements (two phases, intergrowth of  $\text{Li}_2\text{MnO}_3$  and  $\text{LiMn}_{0.5}\text{Ni}_{0.5}\text{O}_2$  and solid solution) have been simulated and compared with experimental patterns to find the model which better represents the structure. Secondly, an *operando* high resolution XRD experiment has been analyzed to understand the electrochemically driven structural modifications occurring upon the first cycle. In addition to the metal migration to tetrahedral positions in order to stabilize the oxidized oxygen, peroxo-like formation has been detected. Moreover, a thorough analysis of the microstrains has been performed and the differences along the *c* direction and the *ab* plane have been rationalized.

# Table of contents

<b>List of figures</b>	<b>xxxiii</b>
<b>List of tables</b>	<b>xli</b>
<b>1 Introduction</b>	<b>1</b>
1.1 Why electric vehicles? . . . . .	2
1.2 Li-ion batteries . . . . .	3
1.2.1 Composition and operation of Li-ion batteries . . . . .	3
1.2.2 Classification and evolution of the commercially available cathode materials for Li-ion batteries . . . . .	5
1.2.3 Li-rich layered oxides . . . . .	9
1.3 Objectives . . . . .	13
<b>2 Synthesis and characterization techniques</b>	<b>15</b>
2.1 Synthesis methods . . . . .	16
2.1.1 Ceramic synthesis . . . . .	16
2.1.2 Self combustion synthesis . . . . .	16
2.2 Powder diffraction . . . . .	18
2.2.1 Historical context . . . . .	19
2.2.2 Information contained in powder patterns . . . . .	19
2.2.3 Methods for extracting information . . . . .	23
2.2.4 Large facilities . . . . .	25
2.2.5 Measurement conditions . . . . .	26
2.3 Electron microscopy . . . . .	27
2.3.1 Measurement conditions . . . . .	29
2.4 Magnetic measurements . . . . .	29
2.4.1 Solid state nuclear magnetic resonance . . . . .	29
2.4.2 Measurement conditions . . . . .	32

2.5	Computational methods . . . . .	32
2.5.1	Density functional theory . . . . .	32
2.5.2	Ewald's summation . . . . .	36
2.6	Galvanostatic cycling . . . . .	36
<b>3</b>	<b>Microstructural impact study in electrochemistry of <math>\text{Li}_2\text{MnO}_3</math> through synthetic control</b>	<b>39</b>
3.1	Introduction . . . . .	40
3.2	Synthesis and structural characterization . . . . .	41
3.3	Electron Microscopy analysis of $\text{Li}_2\text{MnO}_3$ . . . . .	44
3.4	FAULTS refinements of XRD data . . . . .	48
3.5	Electrochemical characterization . . . . .	54
3.6	Conclusions . . . . .	58
<b>4</b>	<b>DFT-assisted ssNMR characterization of defects in <math>\text{Li}_2\text{MnO}_3</math></b>	<b>61</b>
4.1	Introduction . . . . .	62
4.2	Experimental XRD patterns and ssNMR spectra . . . . .	63
4.2.1	Stacking faults quantification using ssNMR . . . . .	67
4.3	DFT-based ssNMR shift calculation of the effects of defects in $\text{Li}_2\text{MnO}_3$ . . . . .	69
4.3.1	Choice of Hubbard corrective potential value and unit cell size . . . . .	69
4.3.2	Simulated effect of stacking faults in the $^6\text{Li}$ ssNMR spectra . . . . .	70
4.3.3	Simulated effect of vacancies and substitutions in the $^6\text{Li}$ NMR spectra . . . . .	72
4.4	Conclusions . . . . .	77
<b>5</b>	<b>Theoretical assessment of the stacking faults impact in <math>\text{Li}_2\text{MnO}_3</math> and analysis of substitution strategy</b>	<b>79</b>
5.1	Introduction . . . . .	80
5.2	Investigation of stacking defects in $\text{Li}_2\text{MnO}_3$ . . . . .	81
5.3	Computational study of stacking faults in the delithiation mechanism of $\text{Li}_2\text{MnO}_3$ . . . . .	83
5.3.1	Ground states of ideal $\text{Li}_2\text{MnO}_3$ . . . . .	85
5.3.2	Ground states of defective $\text{Li}_2\text{MnO}_3$ . . . . .	86
5.3.3	Study of oxidation state of the oxygen atoms . . . . .	87
5.3.4	Discussion . . . . .	88
5.4	Atomic-scale analysis of substitution strategies to mitigate the manganese migration . . . . .	91
5.4.1	Convex Hull and oxygen oxidation in $\text{Li}_{1.5}\text{Na}_{0.5}\text{MnO}_3$ . . . . .	92

---

5.4.2	Convex Hull and oxygen oxidation in $\text{Li}_{1.5}\text{Mg}_{0.5}\text{MnO}_3$ . . . . .	95
5.5	Conclusions . . . . .	97
<b>6</b>	<b>Structural analysis and study of activation mechanism in <math>\text{Li}_{1.2}\text{Mn}_{0.6}\text{Ni}_{0.2}\text{O}_2</math></b>	<b>99</b>
6.1	Introduction . . . . .	100
6.2	FAULTS XRD and NPD simulations of different microstructural models corresponding to $\text{Li}_{1.2}\text{Mn}_{0.6}\text{Ni}_{0.2}\text{O}_2$ . . . . .	102
6.2.1	Two phase model . . . . .	104
6.2.2	Intergrowth models . . . . .	107
6.2.3	$\text{Li}_{1.2}\text{Mn}_{0.6}\text{Ni}_{0.2}\text{O}_2$ solid solution . . . . .	110
6.3	NPD simulations of $\text{Li}_{1.2}\text{Mn}_{0.6}\text{Ni}_{0.2}\text{O}_2$ . . . . .	113
6.3.1	Effect of stacking faults in the NPD pattern of $\text{Li}[\text{Li}_{1/3}\text{Mn}_{2/3}]\text{O}_2$ . .	113
6.3.2	NPD simulations for 3D intergrowth versus solid solution models .	113
6.3.3	Analysis of the NPD experimental pattern of $\text{Li}_{1.2}\text{Mn}_{0.6}\text{Ni}_{0.2}\text{O}_2$ . .	115
6.4	$\text{Li}_{1.2}\text{Mn}_{0.6}\text{Ni}_{0.2}\text{O}_2$ structural and electrochemical characterization . . . . .	116
6.5	Operando XRD measurement of $\text{Li}_{1.2}\text{Mn}_{0.6}\text{Ni}_{0.2}\text{O}_2$ . . . . .	118
6.5.1	Qualitative HR XRD analysis . . . . .	118
6.5.2	Rietveld refinement . . . . .	121
6.6	Conclusions . . . . .	128
<b>7</b>	<b>General conclusions</b>	<b>129</b>
	<b>References</b>	<b>133</b>
	<b>Appendix A</b>	<b>157</b>
A.1	Chapter 2 . . . . .	157
A.2	Chapter 3 . . . . .	158
A.3	Chapter 4 . . . . .	161
A.3.1	Magnetic measurement . . . . .	161
A.4	Chapter 5 . . . . .	162
A.4.1	Linear regression of the oxidation state of the oxygen atoms in $\text{Li}_2\text{MnO}_3$ . . . . .	162
A.4.2	Bader charges of $\text{Li}_x\text{MnO}_3$ . . . . .	162
A.5	Chapter 6 . . . . .	165
A.5.1	Atomic positions for the unified FAULTS cell . . . . .	165
A.5.2	Rietveld refinement of $\text{Li}_{1.2}\text{Mn}_{0.6}\text{Ni}_{0.2}\text{O}_2$ . . . . .	165
A.5.3	Stacking probability of $\text{LiMn}_{0.5}\text{Ni}_{0.5}\text{O}_2$ and $\text{Li}[\text{Li}_{1/3}\text{Mn}_{2/3}]\text{O}_2$ . . .	165

A.5.4	<i>Operando</i> XRD patterns refinement results . . . . .	167
-------	-----------------------------------------------------------	-----



# List of figures

1.1	(a) Properties taken into account for the choice of materials of a battery cell. (b) Schematic illustration of a Li-ion battery cell. . . . .	3
1.2	Crystal structure of (a) LFP triphylite, (b) LMO <sub>sp</sub> spinel and (c) LCO layered oxide. Green spheres represent lithium, red spheres oxygen, blue octahedra CoO <sub>6</sub> , purple octahedra MnO <sub>6</sub> , orange octahedra FeO <sub>6</sub> and gray tetrahedra PO <sub>4</sub> . . . . .	6
1.3	Relationship between discharge capacity (black), thermal stability (blue) and capacity retention (red) of Li[Ni <sub>x</sub> Co <sub>y</sub> Mn <sub>z</sub> ]O <sub>2</sub> compounds with number in brackets corresponding to the composition (Ni Mn Co). Reproduced with permission from J. Electrochem. Soc., 162, 14, A2490-A2499 (2015). Copyright 2015, The Electrochemical Society. [1] . . . . .	8
1.4	(a) Ideal monoclinic <i>C2/m</i> structure of Li <sub>2</sub> MnO <sub>3</sub> . (b) <i>ab</i> plane of the mixed LiMn <sub>2</sub> layers. The honeycomb arrangement is highlighted with a red hexagon. (c) Model structure containing stacking faults. . . . .	11
1.5	Comparison of the XRD patterns of an ideal Li-rich layered oxide and a strongly faulted and material with the same composition. . . . .	12
2.1	Different steps of the self combustion method. In (a) the dissolution of the metal salts and the chelator is shown, (b) shows the gel phase after the addition of the diol, (c) is the resultant powder after the self combustion and (d) is the resultant powder after the heat treatment at high temperatures. . .	18
2.2	Schematic recreation of Bragg's law. . . . .	21
2.3	Elements needed for the description of the structure using the FAULTS program. . . . .	24
2.4	(a) An exploded representation of the AMPIX cell, (b) the assembled AMPIX cell and (c) a typical battery stack. Photographs of (d) an assembled AMPIX cell and (e) a six-cell multisample holder. Reproduced with permission of the International Union of Crystallography. [2] . . . . .	27

2.5	Representation of the main interactions between the main electron beam of the electron microscopy at atomic level. . . . .	28
2.6	Spin states splitting as a consequence of an external magnetic field. . . . .	30
2.7	A hypothetical Convex hull diagram for $\text{Li}_2\text{MnO}_3$ . . . . .	35
2.8	Schematic configuration of a coin cell. . . . .	37
2.9	(a) Variation of the voltage with respect to the capacity of $\text{Li}_{1.2}\text{Mn}_{0.6}\text{Ni}_{0.2}\text{O}_2$ . Cycles 1 (in black), 5 and 20 are shown. (b) Evolution of the charge and discharge capacity in function of the number of cycles, as well as their Coulombic efficiency. (c) $dQ/dV$ voltage profile of the cycles 5 and 20 in (a). . . . .	37
3.1	Structural deviations arising from stacking faults in $\text{Li}_2\text{MnO}_3$ , according to Abraham's notation. [3, 4] . . . . .	41
3.2	XRD patterns of first calcination step at 500 °C of the sample synthesized with (a) $\text{MnCO}_3$ , (b) $\text{Mn}_2\text{O}_3$ and (c) $\text{MnO}$ . . . . .	42
3.3	XRD patterns of $\text{Li}_2\text{MnO}_3$ synthesized in a temperature range of 700-1000 °C for 5 or 20 hours. The samples have been synthesized with (a-c) $\text{MnCO}_3$ , (d-f) $\text{Mn}_2\text{O}_3$ and (g-i) $\text{MnO}$ precursors. The first column shows the whole XRD pattern, the second one shows a zoom of the $2\theta$ range 20-35°, where the superstructure peaks appear and the third shows a zoom of the $(001)_m$ peak. . . . .	43
3.4	SEM images of samples synthesized at 700, 800 and 900 °C with (a-c) $\text{MnCO}_3$ , (d-f) $\text{Mn}_2\text{O}_3$ and (g-i) $\text{MnO}$ precursors. . . . .	45
3.5	Representative SAED patterns from crystals of sample (a-c) LMO_MnO_900_5 ( $[100]_m$ or $\langle 110 \rangle_m$ zone axes), (d) LMO_MnCO3_900_5 ( $[100]_m$ or $\langle 110 \rangle_m$ zone axes), (e,f) LMO_MnO_900_5 ( $[103]_m$ and $[102]_m$ zone axes). Purple circles are reflections resulting from the interception of diffuse scattering lines, while yellow ones result from double diffraction. . . . .	46
3.6	HR-STEM images of (a) LMO_MnO_900_5 and (b) LMO_MnCO3_900_5 samples. HAADF-STEM images of LMO_MnO_900_5 (c) $[001]_m$ and (d,e) $[100]_m$ or $\langle 110 \rangle_m$ zone axes. The insets represent the atomic positions of lithium, manganese and oxygen atoms. The red lines are guides to follow the stacking direction, which are labeled with R, P and P' according to Abraham's notation. [3, 4] . . . . .	48
3.7	Comparison of (a) the $C2/m$ unit cell used in conventional Rietveld refinements to describe the non-defective structure of $\text{Li}_2\text{MnO}_3$ , (b) the smaller equivalent $P\bar{1}$ unit cell, and (c) the FAULTS cell used to define the layers to be stacked for the FAULTS refinements. . . . .	49

3.8	Example of a possible stacking sequence for $\text{Li}_2\text{MnO}_3$ used in FAULTS structural model. . . . .	51
3.9	FAULTS refinement for all the selected samples made with $\text{MnCO}_3$ , $\text{Mn}_2\text{O}_3$ and $\text{MnO}$ at 700, 800 and 900 °C. . . . .	52
3.10	Comparison of (a) degree of stacking faults and (b) average crystallite size of the selected samples as a function of temperature. . . . .	53
3.11	SAED simulations for samples with (a) 0%, (b) 15% and (c) 40% of stacking faults. Simulation performed with FAULTS software. . . . .	53
3.12	Comparison of the capacity retention obtained for samples synthesized in a 700-900 °C with (a) $\text{MnCO}_3$ , (b) $\text{Mn}_2\text{O}_3$ and (c) $\text{MnO}$ precursors. Results for cycles 1, 5, 10, 20, 50, 100, 150 and 200 are included. The average crystallite size is shown for each sample. . . . .	55
3.13	Derivative curves $dQ/dV$ of the 10 <sup>th</sup> , 50 <sup>th</sup> and 100 <sup>th</sup> galvanostatic cycles (blue, black and red lines, respectively) obtained for the samples synthesized at 800 °C from (a) $\text{MnCO}_3$ , (b) $\text{Mn}_2\text{O}_3$ and (c) $\text{MnO}$ precursors. The positions of the different oxidation and reduction peaks are indicated in green in (c). The voltage difference of P7 between cycles 10 and 100 is highlighted with the red dashed line and the voltage difference is indicated. . . . .	56
3.14	Derivative curves $dQ/dV$ of the 10 <sup>th</sup> , 50 <sup>th</sup> and 100 <sup>th</sup> galvanostatic cycles (blue, black and red lines, respectively) obtained for the samples synthesized at 700 and 900 °C from $\text{MnO}$ , $\text{Mn}_2\text{O}_3$ and $\text{MnCO}_3$ . The voltage difference of P7 between cycles 10 and 100 is highlighted with the red dashed line and the voltage difference is indicated. . . . .	58
4.1	(a) XRD pattern of selected samples. (b) Zoom of the superstructure peaks zone ( $2\theta$ range of 20-35°). (c) ssNMR spectra of the samples from 4000 to -2000 ppm. Spinning sidebands are labeled with * while + corresponds to a small impurity of a paramagnetic lithium compound. (d) Zoom of the spectra of the region of interest. ssNMR Spectra are normalized with the area of the set of peaks at 750 ppm. The dashed red line shows the position for the experimental peaks from LMO_MnO_1000_72. . . . .	64
4.2	Local environment of Li2 <i>b</i> , Li2 <i>c</i> and Li4 <i>h</i> in $\text{Li}_2\text{MnO}_3$ . . . . .	65
4.3	<sup>6</sup> Li MAS-ssNMR spectra deconvolution of the samples. In blue the experimental spectra and in red the convoluted spectra are shown. . . . .	66
4.4	Model of a structure containing stacking faults, where green layers represent ideal stacking, red layers stacking faults and orange layers second coordination sphere of stacking faults. . . . .	68

4.5	Experimental and simulated values for ${}^6\text{Li}$ ssNMR shifts for $\text{Li}_2\text{MnO}_3$ with varying U values and unit cell sizes. . . . .	70
4.6	${}^6\text{Li}$ ssNMR simulated spectra of (a) an ideal structure, (b) a structure with isolated stacking fault and (c) a structure with consecutive stacking faults. The dashed red lines show the position for the simulated ideal peaks for $\text{Li}2b$ , $\text{Li}2c$ and $\text{Li}4h$ . The insets show a reconstruction of the structures simulated with augmented ab plane to better see the stacking faults. . . . .	71
4.7	${}^6\text{Li}$ ssNMR simulated spectra of $\text{Li}_{1.96}\text{H}_{0.04}\text{MnO}_3$ with $\text{Li}^1/\text{H}^1$ exchange in (a) $\text{Li}2b$ , (b) $\text{Li}2c$ and (c) $\text{Li}4h$ positions. The dashed red lines show the calculated position for the ideal peaks. The insets show the proton marked with a black sphere, not the whole computed structure. . . . .	73
4.8	${}^6\text{Li}$ ssNMR simulated spectra of $\text{Li}_{1.96}\text{MnO}_3$ with lithium vacancies on positions (a) $\text{Li}4h$ , (b) $\text{Li}2c$ and (c) $\text{Li}2b$ . The dashed red lines show the calculated positions for the ideal peaks. The insets show the lithium vacancy marked with a gray sphere, not the whole computed structure. . . . .	74
4.9	${}^6\text{Li}$ ssNMR simulated spectra of $\text{Li}_2\text{MnO}_{2.96}$ with oxygen vacancies on positions (a) $4i$ and (b) $8j$ . The dashed red lines show the calculated positions for the ideal peaks. The insets show the oxygen vacancy marked with a gray sphere, not the whole computed structure. . . . .	75
4.10	Computed energy for $\text{Li}_2\text{MnO}_3$ structure with (a) an $\text{O}8j$ vacancy and one lithium vacancy (b) a second lithium vacancy after the removal of one $\text{O}8j$ and the most labile lithium atom ( $\text{Li}4h$ ). Lithium, manganese and oxygen atoms are represented in green, purple and red respectively. The oxygen vacancy is represented in gray and the lithium atoms directly linked to the vacancy in red, brown and orange. . . . .	75
4.11	${}^6\text{Li}$ ssNMR simulated spectra of $\text{Li}_{1.92}\text{MnO}_{2.96}$ with $\text{Li}4h$ , $\text{Li}2b$ and $\text{O}8j$ vacancies. The dashed red line shows the calculated position for the ideal peaks. The inset shows the $\text{Li}_2\text{O}$ vacancy marked with a gray sphere, not the whole computed structure. . . . .	76
5.1	Displacement of the layers involved in the formation of (a) cationic stacking faults and (b) $\text{O}1$ type stacking faults. . . . .	82
5.2	Relaxed structures analyzed by DFT calculations with a different number of stacking faults. (a) Ideal stacking and structures with one (b), two (c) three (d,e) and five (f) stacking faults. (g) Structure with an $\text{O}1$ type defect. . . . .	83
5.3	Ground states of $\text{Li}_x\text{MnO}_3$ proposed by Xiao <i>et al.</i> and Lee <i>et al.</i> , with a x value of 1.25 and 1. [5, 6] . . . . .	84

5.4	Formation energies of $\text{Li}_x\text{MnO}_3$ ( $2 \geq x \geq 0$ ). (a) Relaxed $\text{Li}_2\text{MnO}_3$ structure. Ground states for $\text{Li}_{1.25}\text{MnO}_3$ and $\text{LiMnO}_3$ are shown in (b) and (c) respectively. The lithium atoms in tetrahedral positions are marked with a green tetrahedron. . . . .	85
5.5	Initial and DFT relaxed structures of $\text{Li}_{0.5}\text{MnO}_3$ when the lithium atoms in the $O3$ configuration are (a) in the $2c$ site, (b) some in the $2c$ site and others in the $4h$ site and (c) in the $4h$ site. . . . .	86
5.6	Formation energies in $\text{Li}_x\text{MnO}_3$ ( $2 \geq x \geq 0$ ) for a stacking faults containing structure. (a) Relaxed $\text{Li}_2\text{MnO}_3$ structure. Ground states for $\text{Li}_{1.25}\text{MnO}_3$ and $\text{LiMnO}_3$ are shown in (b) and (c) respectively. The lithium atoms in tetrahedral positions are marked with a green tetrahedron. . . . .	87
5.7	Average Bader oxidation states for the oxygen depending on the number of atoms coordinated to the oxygen and to the number of lithium atoms which are in tetrahedral position. . . . .	89
5.8	$\text{Li}2c$ local environment differences between $O3$ and $O1$ ideal and defective stacking sequences. . . . .	90
5.9	Comparison between ideal and defective $O1$ structure for $\text{Li}_{0.5}\text{MnO}_3$ . . . .	90
5.10	Relaxed structures of $\text{Li}_{1.5}\text{M}_{0.5}\text{MnO}_3$ when $M =$ (a) Na, (b) K, (c) Be and (d) Mg. . . . .	92
5.11	(a) Formation energies in $\text{Li}_x\text{Na}_{0.5}\text{MnO}_3$ ( $1.5 \geq x \geq 0$ ). (b-d). The green area indicate the thermal energy at room temperature. . . . .	93
5.12	Oxygen and manganese average oxidation states according to Bader charge calculation in $\text{Li}_x\text{Na}_{0.5}\text{MnO}_3$ . . . . .	94
5.13	Formation energies in $\text{Li}_x\text{Mg}_{0.5}\text{MnO}_3$ ( $1.5 \geq x \geq 0$ ). In green the ground states which could be accessible by temperature are shown. . . . .	95
5.14	Oxygen and manganese average oxidation states according to Bader charge calculation in $\text{Li}_x\text{Mg}_{0.5}\text{MnO}_3$ . . . . .	96

6.1	TEM images for $\text{Li}_{1+x}\text{M}_{1-x}\text{O}_2$ , showing two phase model. (a) HAADF images of $\text{Li}_{1.2}\text{Co}_{0.4}\text{Mn}_{0.4}\text{O}_2$ revealing the coexistence of $\text{Li}[\text{Li}_{1/3}\text{Mn}_{2/3}]\text{O}_2$ -like (dot contrast) and $\text{LiCoO}_2$ -like (continuous contrast) areas. [7] (b) Left HAADF and right ABF-STEM images for $\text{Li}_{1.2}\text{Mn}_{0.567}\text{Ni}_{0.166}\text{Co}_{0.067}\text{O}_2$ . In top the $\text{LiMO}_2$ -like structure and in bottom the $\text{Li}[\text{Li}_{1/3}\text{Mn}_{2/3}]\text{O}_2$ -like structure are shown. Insets in right images are the crystal-structure image of the $\text{LiMO}_2$ and the $\text{Li}[\text{Li}_{1/3}\text{Mn}_{2/3}]\text{O}_2$ -like structures. [8] (c) HAADF-STEM image of $\text{Li}_{1.2}\text{Mn}_{0.6}\text{Ni}_{0.2}\text{O}_2$ containing $\text{Li}[\text{Li}_{1/3}\text{Mn}_{2/3}]\text{O}_2$ domains (blue) and $\text{LiMO}_2$ domains (green). Reflections characteristic of the ordered slabs are circled in blue and those related to the disordered ones are pointed with green arrows on the Fourier transform in the inset. [9] . . . . .	101
6.2	Steps followed to transform $C2/m$ and $R\bar{3}m$ unit cell to a common one suitable for the FAULTS program. Top shows the transformation of $\text{LiMn}_{0.5}\text{Ni}_{0.5}\text{O}_2$ and bottom the transformation of $\text{Li}[\text{Li}_{1/3}\text{Mn}_{2/3}]\text{O}_2$ . . . . .	103
6.3	Rietveld refined pattern of $\text{L}_{1+x}\text{NMO\_SC\_900\_5}$ sample. . . . .	104
6.4	(a) Simulated XRD patterns of $\text{Li}[\text{Li}_{1/3}\text{Mn}_{2/3}]\text{O}_2$ and $\text{LiMn}_{0.5}\text{Ni}_{0.5}\text{O}_2$ mixture. The Bragg positions for each phase are found below; $\text{Li}[\text{Li}_{1/3}\text{Mn}_{2/3}]\text{O}_2$ in red and $\text{LiMn}_{0.5}\text{Ni}_{0.5}\text{O}_2$ in blue. (b) Experimental XRD pattern of the mixture of $\text{Li}[\text{Li}_{1/3}\text{Mn}_{2/3}]\text{O}_2$ and $\text{LiMn}_{0.5}\text{Ni}_{0.5}\text{O}_2$ compared to $\text{Li}_{1.2}\text{Mn}_{0.6}\text{Ni}_{0.2}\text{O}_2$ . . . . .	105
6.5	Rietveld refinements of (a) $\text{LMO\_MnCO}_3\_900\_5$ and (b) $\text{LNMO\_SC\_900\_5}$ samples. . . . .	106
6.6	(a) Schematic representation of the structures built where red layers represent $\text{Li}[\text{Li}_{1/3}\text{Mn}_{2/3}]\text{O}_2$ and blue layers $\text{LiMn}_{0.5}\text{Ni}_{0.5}\text{O}_2$ . Note that the average block thickness varies from one representation to the other. (b) Simulated XRD patterns corresponding to the four studied samples. The inset shows a zoom to the $2\theta$ range $30\text{-}40^\circ$ . . . . .	108
6.7	(a) Representation of the layers formed by clusters of $\text{Li}[\text{Li}_{1/3}\text{Mn}_{2/3}]\text{O}_2$ (in red) and $\text{LiMn}_{0.5}\text{Ni}_{0.5}\text{O}_2$ (in blue) along the same $ab$ plane used in the simulation of the XRD patterns. (b) simulated XRD patterns using the layers represented in (a). The inset shows a zoom to the $2\theta$ range $30\text{-}40^\circ$ . . . . .	109
6.8	Ewald summation energy of different $\text{Li}_{1.2}\text{Mn}_{0.6}\text{Ni}_{0.2}\text{O}_2$ configurations (a) maintaining the superstructure ordering and (b) with all the metals randomly distributed in the transition metal layer. . . . .	111
6.9	(a) XRD patterns for different solid solution simulations. (b) Zoom of the suprestructure zone. . . . .	112

6.10	NPD simulations for ideal and defective $\text{Li}[\text{Li}_{1/3}\text{Mn}_{2/3}]\text{O}_2$ (maximum degree of stacking faults). The inset shows a zoom of the superstructure zone. . . .	114
6.11	(a) NPD simulations for the intergrowth of two phases and for the solid solution models. The inset of the figure shows a zoom of the superstructure zone. (b,c) Composition of the transition metal layer in the intergrowth of two phases and the solid solution structural models. . . . .	115
6.12	Experimental NPD pattern of $\text{L}_{1+x}\text{NMO\_SC\_900\_5}$ with a $\lambda = 1.623400 \text{ \AA}$ . The inset of the figure shows a zoom of the superstructure zone. . . . .	116
6.13	High resolution XRD patterns of $\text{Li}_{1.2}\text{Mn}_{0.6}\text{Ni}_{0.2}\text{O}_2$ synthesized at 700 and 900°C. . . . .	117
6.14	Rietveld refinement pattern of $\text{L}_{1+x}\text{NMO\_SC\_700\_5}$ sample. . . . .	118
6.15	Voltage versus capacity curve of the first two galvanostatic cycles of the <i>operando</i> measurement of $\text{L}_{1+x}\text{NMO\_SC\_700\_5}$ . Points at selected voltages are marked with green circles. . . . .	119
6.16	(a) Waterfall plot of XRD patterns resulting from the <i>operando</i> measurement of $\text{L}_{1+x}\text{NMO\_SC\_700\_5}$ .(b) <i>operando</i> XRD peaks evolution upon cycling together with the time versus voltage curve shown as contour plot. (c-e) XRD patterns at selected voltages in (c) the charge region 1, (d) in the charge region 2 and (e) in the discharge. . . . .	120
6.17	XRD pattern of (a) discharged state of first three cycles and (b) charged states of the first two cycles. . . . .	121
6.18	Refined HR XRD patterns of selected voltages of the <i>operando</i> experiment of $\text{Li}_{1.2}\text{Mn}_{0.6}\text{Ni}_{0.2}\text{O}_2$ . . . . .	123
6.19	Electronic scattering density difference ( $F_{diff}$ ) between the calculated and the observed experimental pattern at (a) OCV (b) at 4.5 V, (c) 4.8 V. The positive scattering factor is shown in yellow while the negative is shown in blue. The black circles indicate tetrahedral positions. . . . .	124
6.20	Refined parameters upon charge and discharge. Green dashed lines mark the end of the charge region 1 and charge region 2. . . . .	125
6.21	$\text{O}4i\text{-O}4i$ distance of the initial structure and the fully charged structure. . . .	126
6.22	Schematic representation of the origin of strains. . . . .	128
A.1	Visualization of Gaussian and Lorentzian profile functions. . . . .	157
A.2	The inverse of the molar susceptibility in function of the temperature of $\text{LMO\_MnCO}_3\text{\_900\_5}$ . . . . .	161
A.3	Relationship between the calculated Bader charge and the expected oxidation state. . . . .	162

- A.4 Refined unit cell parameters ( $a$ ,  $b$ ,  $c$  and  $\beta$ ) upon charge and discharge. Green dashed lines mark the end of the charge region 1 and the end of charge region 2. 167



# List of tables

1.1	Electrochemical properties of various cathode materials used in commercial Li-ion batteries and their main advantages and disadvantages. The non-commercial $L_{1+x}MO$ is also included for comparative purposes. . . . .	10
2.1	Synthesis conditions for different $Li_2MnO_3$ samples synthesized by ceramic method. . . . .	17
3.1	Average aspect ratio (height/width) of measured samples. . . . .	46
3.2	Initial structural parameters used for the FAULTS refinements. . . . .	50
3.3	General summary of the microstructural properties for the selected samples.	54
4.1	Shift positions and relative populations for the deconvoluted ssNMR peak signals of the samples. . . . .	67
4.2	Degree of stacking faults (SF) obtained with FAULTS program from XRD data and number of modified lithium environments obtained from the ssNMR peak fitting. . . . .	69
4.3	Computed and experimental average $^6Li$ NMR shifts. The latter correspond to the deconvolution using one peak per signal. The values in parenthesis correspond to the difference with respect to the ideal signal (for the case of the simulated shifts) or to LMO_MnO_1000_72 (for LMO_MnO_900_5 and LMO_MnCO3_900_5). . . . .	71
5.1	Relationship between the calculated Bader charge and the expected oxidation state. . . . .	88
5.2	Cationic size of the dopant, interlayer distance and <i>ab</i> plane of $Li_{1.5}M_{0.5}MnO_3$ .	92
5.3	Calculated volume change and intercalation voltage for $Li_{1.5}M_{0.5}MnO_3$ with $M = Na, K$ and $Mg$ . . . . .	93
6.1	Unit cell parameters of $LiMn_{0.5}Ni_{0.5}O_2$ and $Li[Li_{1/3}Mn_{2/3}]O_2$ according to the different descriptions used in this chapter. . . . .	103

---

6.2	Rietveld refined parameters for LNMO_SC_900_5. . . . .	106
6.3	Rietveld refined parameters for LMO_MnCO3_900. . . . .	107
6.4	Calculated DFT energies for structures with different layer transition metal distribution corresponding to the points indicated in Figure 6.8. . . . .	111
6.5	Main structural parameters obtained from the Rietveld refinement for samples $L_{1+x}$ NMO_SC_700_5 and $L_{1+x}$ NMO_SC_900_5. All the refined parameters are shown in Table A.9 in Appendix A. . . . .	118
A.1	FAULTS unit cell values for the refined samples. . . . .	158
A.2	Refined atomic positions in the TM layers (L2=L3=L4) obtained from the FAULTS refinements of the XRD patterns of the 9 samples. . . . .	159
A.3	Bader charges of $Li_{1.25}MnO_3$ ideal structures. . . . .	163
A.4	Bader charges of $Li_{1.25}MnO_3$ defective structures. . . . .	163
A.5	Bader charges of $LiMnO_3$ ideal structures. . . . .	164
A.6	Bader charges of $LiMnO_3$ defective structures. . . . .	164
A.7	Atomic positions for the averaged $Li_{1.2}Mn_{0.6}Ni_{0.2}O_2$ structure in the FAULTS unit cell. . . . .	165
A.8	Transition percentages used in FAULTS program to form blocks with desired the average number of layers and size. . . . .	165
A.9	Comparison of the Rietveld refined parameters of synchrotron data for $L_{1+x}$ NMO_SC_900 and $L_{1+x}$ NMO_SC_700. The refinement has been done using $C2/m$ space group. . . . .	166

# Chapter 1

## Introduction

*An expert is a person who has made all the mistakes that can be made in a very narrow field.*

**Niels Bohr**

The exponential growth of population and the increasing energy demand is bringing serious consequences in environmental contamination, especially in big cities, where the combustion engine vehicle is the main source of air pollution. The use of contaminant vehicles has started to be limited and their use is expected to be progressively banned in midterm future. Electric vehicles can help to reduce pollution in cities, but the high price of the lithium-ion (Li-ion) battery packs (most viable energy storage system for electric vehicles), in addition to their low autonomy, are delaying their widespread utilization. The cathode is the most expensive component of Li-ion batteries, which usually consists on a cobalt-based layered oxide. Replacing cobalt for alternative cheaper transition metals could thus considerably decrease the price of the batteries and increase the energy they can store.

In this thesis cobalt-free lithium-rich layered oxides are studied, which can provide higher energy than classic layered oxides due to their higher amount of lithium atoms per formula unit. However, their commercialization is still not possible, as a consequence of the fast voltage and capacity fading these materials suffer from, as a result of an initial structural rearrangement in the first cycle and subsequent structural evolution. The mitigation of these phenomena requires a full understanding of their complex structure and controversial microstructural arrangement, which includes a high degree of stacking faults.

## 1.1 Why electric vehicles?

In a world with an exponential growth of population and increasing demand of resources, the challenges related to water supply and energy management have become a societal priority. [10–13] In both cases, a more adequate use of resources and alternative methods to obtain them are urgently required. With respect to energy, the world's economy still relies on the use of non renewable energies, primarily petroleum-derived products, which represent the main reason of the global warming coming from human activity. In addition, the principal sources of non renewable energy (gas and oil reservoirs) are running out and therefore the full deployment of renewable energy sources is urgent. According to the European Environment Agency (EEA), around 33% of the total energy consumed in the European Union in 2016 was dedicated to transportation, most of it coming from gasoline and diesel burning. [14] Combustion engines generate air pollution, which is estimated to cause more than 100,000 deaths per year; most of them concentrated in China, India and the United States of America. [15] In order to reduce pollution, many cities have now traffic restrictions. For instance, London has implemented "Congestion Charges" for driving through the city center, and Paris, Madrid and Barcelona, among others, have circulation restrictions in days with high levels of pollution. These restrictions are usually related to the contamination level of the vehicle and electric vehicles are normally exempt.

Within this scenario, the electric vehicle seems to be a good alternative: pollution in urban areas can be greatly diminished with the replacement of old contaminating vehicles for electric ones, and the reduction of greenhouse emissions responsible for the global warming effect can as well be diminished, but only if the electricity used to feed the vehicles comes from renewable energies. Lithium-ion (Li-ion) batteries are the preferred energy storage system for electric vehicles due to their good cycling stability, higher energy density and lighter weight in comparison with other technologies, [16, 17] so scientists and car companies are making great efforts to carry out the fuel-to-electric transition. [18, 19] The Li-ion technology is of great importance. In fact, the Nobel prize in chemistry in 2019 has been awarded to John Goodenough, M. Stanley Whittingham and Akira Yoshino *for the development of lithium-ion batteries*, which have helped to the development of the wireless technology such as the laptops or the mobile phones. Nevertheless, Li-ion batteries still need to be improved in some aspects for the wide commercialization of the electric vehicle, including their low autonomy and their high price.

## 1.2 Li-ion batteries

### 1.2.1 Composition and operation of Li-ion batteries

The most important parameters to consider for the choice of battery cell materials are shown in Figure 1.1a. The energy of a cell is given by its capacity and its operation voltage (commonly measured in mAh/g and V respectively), which should be as high as possible. On the one hand, the capacity of the compound is the current a battery can deliver in discharge and it is given by the amount of lithium atoms that can be reversibly exchanged between the cathode and the anode. On the other hand, the voltage is the potential difference between the cathode and the anode. The total energy the cell can provide with respect to its mass or its volume is defined as gravimetric or volumetric energy density respectively (in Wh/kg and Wh/L). Another important parameter regarding its performance is the power, i.e. the amount of energy the battery can provide per time unit. The power is thus dependent of the rate capability (the ability of the compound to deliver as much energy as possible at high charge and discharge speeds). In this case, not only the total energy of the cell but also the mobility of the electrons and the ions play an important role. The degradation of the battery is generally due to the structural and chemical changes of the components so structural and thermal stability is key to extend the cycle life of batteries. In addition, structural instabilities can cause safety hazards, which could be extremely dangerous for users. Last but not least, the cost, broadly speaking, depends on the natural abundance of the compounds present in the cells and in their processability.

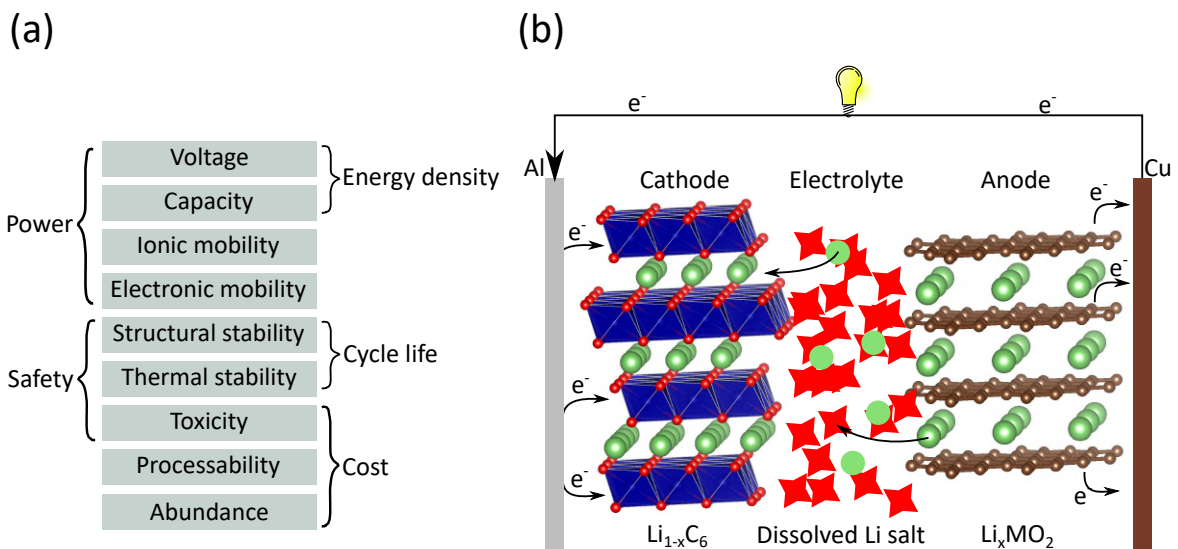


Fig. 1.1 (a) Properties taken into account for the choice of materials of a battery cell. (b) Schematic illustration of a Li-ion battery cell.

Figure 1.1b shows a scheme of a typical Li-ion battery cell which is composed of three components: the anode, the electrolyte and the cathode. The chemistry of a battery is generally based on the insertion mechanism, where the lithium atoms are intercalated and deintercalated in the cathode and anode structures. When a cell is discharging, the lithium atoms move from the anode to the cathode passing through an electrolyte. The migration of a lithium atom charges negatively the anode and positively the cathode so, in order to maintain the electronic neutrality, one electron goes from the anode to the cathode. Provided that the electrolyte is ionic conductor but electronic insulating, the electron travels through an external circuit and this generates an electronic current, which is used to provide energy to a system. In the charging process both the Li-ions and the electrons are forced to move back to the anode following the opposite path. In the next paragraphs the most used materials for each component are shortly summarized.

Graphite is the most used **anode** material nowadays, being its low price and low voltage its main attractive. [20] The high safety standards required by the electric vehicle have however attracted the attention of  $\text{Li}_4\text{Ti}_5\text{O}_{12}$  spinel (LTO), which has higher cycling stability, rate capability and safety than graphite as a consequence of its null volumetric change upon cycling and its higher operation voltage (well above lithium plating voltage). [21] Its theoretical capacity (175 mAh/g) is however smaller compared to graphite (375 mAh/g). In contrast, the capacity of the lithium metal anode, whose electrochemical potential is the lowest (and thus the voltage difference with the cathode the highest), is one order of magnitude larger (3862 mAh/g). Its stabilization during cycling is today an important research topic because lithium generates dendrites upon cycling which can cause important volume changes, shortcuts and undesired side reactions, especially at high rates. [22, 23] The use of additives in liquid electrolytes or the use of solid electrolytes with stable solid-electrolyte interfaces (SEI) are possible solutions to this problem. Silicon, whose natural abundance in Earth crust is high and whose theoretical capacity is  $\sim 4200$  mAh/g, has also attracted high research interest. Its reactivity with the lithium, however is different from those aforementioned as it does not follow an insertion mechanism but an alloying mechanism instead (see Reference [24] for more details). The alloying mechanism implies large volumetric changes upon lithiation/delithiation, which crack the particles, severely diminishing their cycle life. [24, 25]

An ideal **electrolyte** should be able to work at high rates and high voltages without decomposing. The most widely used electrolyte comprise a lithium salt (e.g.  $\text{LiPF}_6$ ) dissolved in an organic solvent or a mixture of them (e.g. ethylene carbonate (EC), propylene carbonate (PC) or dimethyl carbonate (DMC)). Despite their superior ionic conductivity, liquid electrolytes are flammable, corrosive, and thermally unstable, which can cause a

variety of problems. These issues are assumable for small electronic devices, because they work at room temperature and the amount of electrolyte is small, but electric vehicles require higher safety. Therefore, electrolyte research is mostly focused in finding solid state electrolytes, which can be ceramic or polymeric ionic conductors. [26–30] Ceramic electrolytes exhibit a wider voltage window, allowing a higher energy density. Among the most studied materials perovskites such as  $\text{Li}_{0.5}\text{La}_{0.5}\text{TiO}_3$  (LLTO), sulfides (e.g.  $\text{Li}_7\text{P}_3\text{S}_{11}$ ), lithium phosphorus oxynitrides (LiPON), NASICON (e.g.  $\text{Na}_{1+x}\text{Zr}_2\text{Si}_x\text{P}_{3-x}\text{O}_{12}$ ) or garnet (e.g.  $\text{Li}_3\text{Y}_3\text{Te}_2\text{O}_{12}$ ) type structures can be found. The  $\text{Li}^+$  conductivity in these structures is generally good and, in some cases, as high as liquid electrolytes. However, mechanical properties are poor, which can cause breakages, generating shortcuts. Polymeric electrolytes, on the other hand, generally exhibit better mechanical properties (which simplifies their processability), lower prices and lighter weights. These comprise lithium salts (e.g. lithium bis(trifluoromethanesulfonyl)imide (TFSI), lithium bis(fluorosulfonyl)imide (FSI),  $\text{LiClO}_4$  or  $\text{LiPF}_6$ ) solvated in polymer a matrix such as polyethylene oxides (PEO), polycarbonates (PC), polyacrylonitrile (PAN) or polymethyl methacrylate (PMMA). [26] Nevertheless, their conductivity is generally lower and their electrochemical stability is not as good as ceramic electrolytes. In order to merge the best properties of both electrolytes, composite electrolytes combining both polymers and ceramics are also studied.

Finally, most **cathodes** used in electric vehicles are the cobalt based Li-ion layered transition metal oxides, whose price is considerably high. Cobalt is toxic and the largest natural reserves are located in the Democratic Republic of Congo, where its extraction is sometimes marked by human rights abuses. [31, 32] Fortunately, according to the Principles for Responsible Investments (PRI) some cobalt sellers (e.g. Huayou Cobalt) and buyers (Apple, BMW, Samsung...) are committed to ethical principles and ensure that the materials have not been mined in slavery conditions. [32] The amount of cobalt has been reduced in recent years with the combination of alternative transition metals (mainly manganese, nickel and/or aluminum) as a strategy to reduce its price, which represents about the 40% of the total price of a battery. [33] Finding alternative cheaper compounds can considerably reduce the price of the batteries and thus, boost the electric vehicle commercialization.

### 1.2.2 Classification and evolution of the commercially available cathode materials for Li-ion batteries

The commercially available cathode materials can be classified into three different families: phospho-olivine tryphillite, spinel and classic layered oxides.

The first family of compounds here shown are the polyanionic **phospho-olivine triphylite** shown in Figure 1.2a. Pahdi *et al.* were the first ones to report  $\text{LiFePO}_4$  (LFP), the most studied compound within this family, which is commercially available. [34] It crystallizes in the orthorhombic  $Pnma$  space group and consists on corner-shared  $\text{FeO}_6$  octahedra, an edge sharing  $\text{LiO}_6$  octahedra running parallel to the  $b$  axis, which are linked together by  $\text{PO}_4$  tetrahedra. [35]  $\text{Fe}^{\text{II}}$  in the fully lithiated phase oxidizes to  $\text{Fe}^{\text{III}}$  when all the lithium is extracted. Its 3D structure provides a high reversibility, superior thermal stability and an outstanding performance at high rates. Moreover, this material has low cost and low toxicity. Its energy density, however is limited and as it is not a good electronic conductor it requires carbon coating or nanosizing to obtain an excellent performance (with a total capacity of 170 mAh/g at 3.4 V). [36–38]

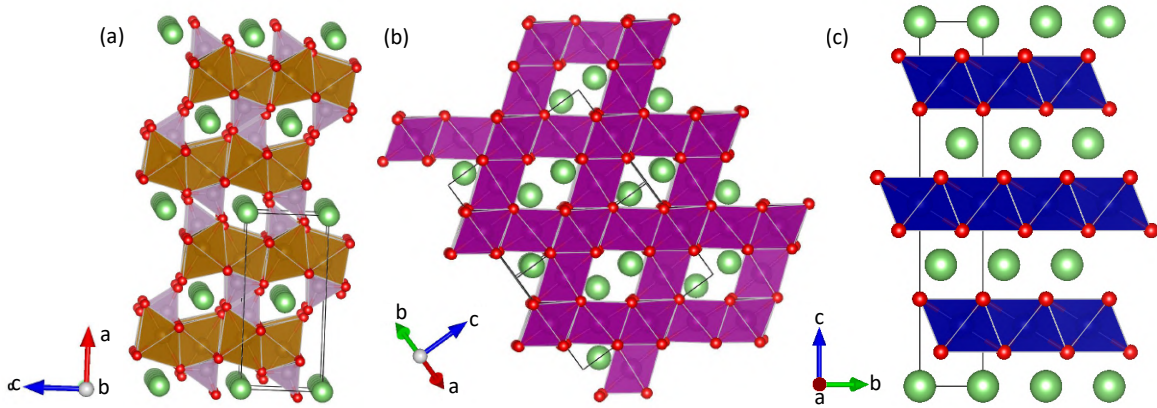


Fig. 1.2 Crystal structure of (a) LFP triphylite, (b)  $\text{LMO}_{sp}$  spinel and (c) LCO layered oxide. Green spheres represent lithium, red spheres oxygen, blue octahedra  $\text{CoO}_6$ , purple octahedra  $\text{MnO}_6$ , orange octahedra  $\text{FeO}_6$  and gray tetrahedra  $\text{PO}_4$ .

The second studied family crystallizes in the **spinel** structure. The extraction/insertion of lithium in the  $\text{LiMn}_2\text{O}_4$  spinel ( $\text{LMO}_{sp}$ ) (Figure 1.2b) was first reported by Thackeray *et al.* [39] Among its main advantages its low price and its high reversibility, even at high rates, can be highlighted. It crystallizes in the cubic  $Fd\bar{3}m$  space group, where manganese forms  $\text{MnO}_6$  octahedra that share corners with  $\text{LiO}_4$  tetrahedra and edges with  $\text{MnO}_6$  octahedra. Lithium occupies  $\text{LiO}_4$  tetrahedra that share corners with  $\text{MnO}_6$  octahedra. [35] In  $\text{LMO}_{sp}$  the manganese is in an average +3.5 oxidation state and can both accommodate and donate lithium. If the material is charged, the lithium abandons the structure oxidizing all the manganese to  $\text{Mn}^{\text{IV}}$  forming  $\text{Mn}_2\text{O}_4$ . On the contrary, if  $\text{LMO}_{sp}$  is discharged, extra lithium is inserted in the structure forming the  $\text{Li}_2\text{Mn}_2\text{O}_4$  phase, with all manganese as  $\text{Mn}^{\text{III}}$ .  $\text{LMO}_{sp}$  therefore shows two main charge/discharge processes, one at 4.1 V related to the  $\text{Mn}_2\text{O}_4/\text{LiMn}_2\text{O}_4$  reaction and a second one at 3 V related to  $\text{LiMn}_2\text{O}_4/\text{Li}_2\text{Mn}_2\text{O}_4$ . [40] This



second step was however found to cause fast capacity fading as a consequence of structural degradation. [41] An average oxidation state lower than +3.5 in manganese induces the Jahn-Teller distortion which generates strains and drastically shortens its cycle life. [1, 42, 43] In addition,  $\text{Mn}^{\text{III}}$  disproportionates into  $\text{Mn}^{\text{II}}$  and  $\text{Mn}^{\text{IV}}$  and the former one is irreversibly dissolved in the electrolyte. This means that, for practical purposes, the redox activity of this spinel is limited to the  $\text{Mn}_2\text{O}_4/\text{LiMn}_2\text{O}_4$  reaction, which limits its energy density.

Replacing some manganese atoms for nickel resulting in  $\text{LiMn}_{1.5}\text{Ni}_{0.5}\text{O}_4$  ( $\text{LMNO}_{sp}$ ) is a strategy to minimize the manganese redox activity and thus avoid the structural degradation related to it. In this case manganese stays as  $\text{Mn}^{\text{IV}}$  in the whole electrochemical process while nickel is as  $\text{Ni}^{\text{II}}$  in the discharged state and it is oxidized to  $\text{Ni}^{\text{IV}}$  during the charge. This material delivers a very similar capacity but at much higher voltage (4.7 V). [44] The stability of current electrolytes is however limited to  $\sim 4.3$  V so these materials cannot be yet commercialized.

Finally, the third family of commercially available compounds are the **classic layered oxides**.  $\text{LiCoO}_2$  (LCO) was first proposed as cathode material for Li-ion rechargeable batteries by Mizushima *et al.* [45] and has been the most widely studied cathode material. This finding resulted in a great success, as only ten years after the first report, the first commercial Li-ion secondary battery was commercialized by Sony, [46] with LCO as the active material in the cathode and graphite in the anode. LCO crystallizes in the trigonal  $R\bar{3}m$  space group. It consists of layers of edges sharing  $\text{CoO}_6$  octahedra that alternate with layers of edges sharing  $\text{LiO}_6$  octahedra. [35] LCO crystallizes in a closed package oxygen array forming an  $O3$  stacking sequence according to Delmas' notation [47], as shown in Figure 1.2c. In the discharged state cobalt is in  $\text{Co}^{\text{III}}$  oxidation state and when charging the material it oxidizes to  $\text{Co}^{\text{IV}}$ . However, at high states of delithiation the  $\text{CoO}_2$  phase suffers severe irreversible structural changes and is chemically unstable, which represents a security hazard. [48–51] Therefore, in practice only half of the lithium atoms can be reversibly extracted.

Isostructural  $\text{LiNiO}_2$  was studied as a cheaper alternative to LCO. Its synthesis is however challenging as the similar cationic size of  $\text{Li}^{\text{I}}$  and  $\text{Ni}^{\text{II}}$  results in a lithium deficient  $\text{Li}_{1-x}\text{Ni}_{1+x}\text{O}_2$  phase with  $\text{Ni}^{\text{II}}$  cations in the lithium layer, which is detrimental for ion diffusion. [1] The use of cobalt with a Co:Ni ratio greater than 3:7 stabilizes the  $\text{Ni}^{\text{III}}$  cation in the transition metal layer and avoids its migration to the lithium layer. [1] Aluminum doping enables to lower the amount of cobalt in the system maintaining all the nickel in the transition metal layers. In addition, it results in a higher thermal stability and lifetime due to the stronger Al-O bonding. The most used composition for the ternary Ni:Co:Al system is  $\text{LiNi}_{0.80}\text{Co}_{0.15}\text{Al}_{0.05}\text{O}_2$ , commonly known as NCA. [52]

In the search of cheaper alternatives to cobalt, manganese was also studied. The direct synthesis of isostructural  $\text{LiMnO}_2$  is not possible due to the strong Jahn-Teller effect of  $\text{Mn}^{\text{III}}$  and results in the  $Pmnm$  space group. [53] Even if  $R\bar{3}m$   $\text{LiMnO}_2$  can be successfully prepared by ion exchange synthesis starting from  $\text{NaMnO}_2$ , it rapidly turns into a more stable spinel phase upon cycling. [54] Mixing manganese with nickel in a 1:1 ratio results in the satisfactory synthesis of the  $R\bar{3}m$   $\text{LiMn}_{0.5}\text{Ni}_{0.5}\text{O}_2$ . However, it crystallizes with certain amount of antisite defects (some nickel occupies in the lithium layer as  $\text{Ni}^{\text{II}}$ ), which is detrimental for electrochemical performance. [55] As for the case of  $\text{LMNO}_{sp}$ , the oxidation states of manganese and nickel in  $\text{LiMn}_{0.5}\text{Ni}_{0.5}\text{O}_2$  are  $\text{Ni}^{\text{II}}$  and  $\text{Mn}^{\text{IV}}$ . Therefore, manganese remains unaltered in the whole electrochemical process while nickel oxidizes to  $\text{Ni}^{\text{IV}}$  in the fully charged state. The non-reactive manganese ions provide a high thermal stability to the system and avoid the Jahn-Teller distortion. [52, 56] As previously mentioned, cobalt inhibits the presence of nickel in the lithium layer so  $\text{LiNi}_{1/3}\text{Mn}_{1/3}\text{Co}_{1/3}\text{O}_2$  (333NMC) can be synthesized free of nickel in the lithium layer. Figure 1.3 shows the effect of the different ratio of transition metals in the electrochemical performance. Overall, manganese provides thermal stability, cobalt improves the rate capability and capacity retention and nickel increases the discharge capacity. [1] Nowadays the proportion of nickel is being increased with new

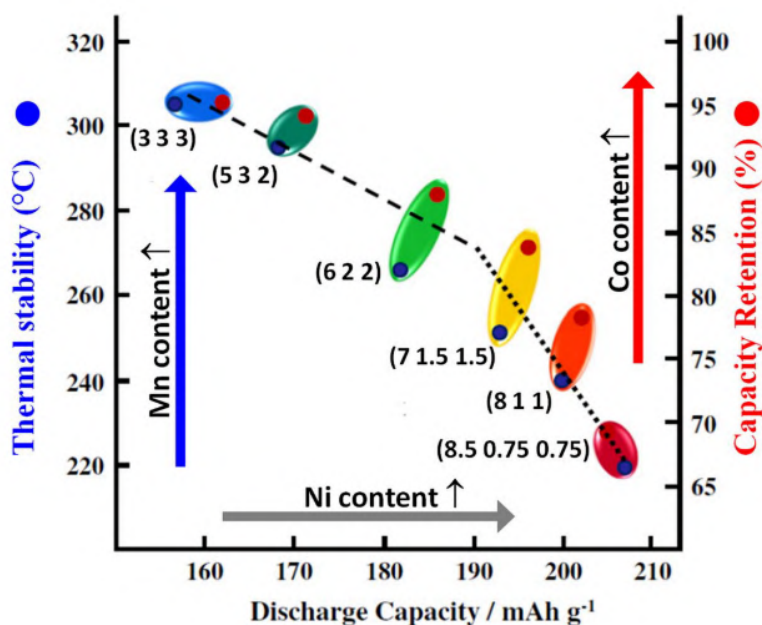


Fig. 1.3 Relationship between discharge capacity (black), thermal stability (blue) and capacity retention (red) of  $\text{Li}[\text{Ni}_x\text{Co}_y\text{Mn}_z]\text{O}_2$  compounds with number in brackets corresponding to the composition (Ni Mn Co). Reproduced with permission from J. Electrochem. Soc., 162, 14, A2490-A2499 (2015). Copyright 2015, The Electrochemical Society. [1]

formulations such as  $\text{LiNi}_{0.5}\text{Mn}_{0.3}\text{Co}_{0.2}\text{O}_2$  (532NMC),  $\text{LiNi}_{0.6}\text{Mn}_{0.2}\text{Co}_{0.2}\text{O}_2$  (622NMC) or  $\text{LiNi}_{0.8}\text{Mn}_{0.1}\text{Co}_{0.1}\text{O}_2$  (811NMC). [57–59] Even if the increase of nickel content in the composition (at the expense of manganese) can improve the electrochemical performance of the battery, it can lead to thermal instabilities, which can be especially dangerous in electric vehicles, where high working temperatures can be achieved. In order to overcome this problem, core shell structures were developed with a nickel rich core and manganese rich shell. This way, thermally stable high capacity compounds were synthesized. [60, 61]

Table 1.1 shows a summary of the cycling properties for the main commercially available cathode materials described above together with their main advantages and disadvantages. With respect to their price they can be divided into two main groups. On the one hand,  $\text{LMO}_{sp}$  and LFP are cheap and non toxic materials, but their energy density does not satisfy the demand for electric vehicles and they are only found in small cars with an autonomy of around 100-140 km such as Chevrolet Spark, Honda Fit EV or Mitsubishi I. [16] On the other hand, NMC and NCA can provide greater autonomy (300-500 km) [16] due to their higher specific energy, but their price is considerably higher. Note that LCO is limited to consumer electronics and does not compete with its homologous NMC and NCA due to its higher cost, lower cycle life and limited safety. The prices of LFP and  $\text{LMO}_{sp}$  ( $\sim 20$  and  $\sim 15$  \$/kg respectively) are approximately half of the prices of NCA and NMC ( $\sim 42$  and  $\sim 45$  \$/kg respectively). [62]

Even if they are not commercially available yet, lithium rich layered oxides (Li-rich or Li-excess) have also been included in Table 1.1 for comparative purposes. While in classic layered oxides the structure is formed of alternate pure layers of lithium and transition metals, in Li-excess layered oxides the transition metal layer also contains lithium atoms, so there is more than one lithium per transition metal atom in its formula and therefore a higher energy density can be achieved if all the lithium atoms are reversibly extracted. In addition, their price is lower as they do not contain cobalt or if they do, it is in reduced amounts. However, these materials are not commercial yet because they suffer from a fast voltage and capacity decay as a consequence of a major structural reorganization occurring upon cycling that is still the object of intense research. [63–69] These materials are the subject of this thesis aiming to their interesting properties.

### 1.2.3 Li-rich layered oxides

Li-rich layered oxides are usually described with the general formula  $\text{Li}_{1+x}\text{M}_{1-x}\text{O}_2$  (where  $1/3 > x > 0$ ) or as a intergrowth between  $\text{Li}_2\text{MnO}_3$  and  $\text{LiMO}_2$ , being M a mixture of manganese and other transition metals, generally cobalt or nickel. Figure 1.4a shows the structure of  $\text{Li}_2\text{MnO}_3$ , the end member of this family of compounds (which can also be

Table 1.1 Electrochemical properties of various cathode materials used in commercial Li-ion batteries and their main advantages and disadvantages. The non-commercial  $L_{1+x}MO$  is also included for comparative purposes.

Material	Average voltage (V)	Capacity (mAh/g)	Specific energy (Wh/kg)	Advantages	Disadvantages
LFP	3.4	170	580	Safe at high temperature Excellent cycling reversibility Cheap and non toxic Thermal and chemical stability	Low electronic conductivity Low energy density
$LMO_{sp}$	4.1	110	450	Cheap and non toxic High power	Low energy density Bad performance at high temperature High price
LCO	3.9	140-160	590	Stable voltage and capacity	Environmental impact Unstable at high voltages
NMC	3.8	140-180	610	Good general performance	Thermal instability (Ni-rich) Large amount of cobalt (Ni-poor)
NCA	3.7	180-200	700	High capacity and voltage High power	Thermal instability
$L_{1+x}MO^a$	3.5	250-280	960	High energy density Reduced price	First cycle irreversible capacity Fast capacity and voltage fading

<sup>a</sup> Non-commercial material.

written as  $\text{Li}[\text{Li}_{1/3}\text{Mn}_{2/3}]\text{O}_2$  to better describe its layered structure, where the term in brackets represent the transition metal layer). Due to the cationic size difference between lithium and manganese, in the  $\text{LiMn}_2$  layer each lithium atom is surrounded by six manganese atoms, forming a honeycomb type scheme as seen in Figure 1.4b. This reduces the cell symmetry from the trigonal  $R\bar{3}m$  space group to the monoclinic  $C2/m$  and three different lithium positions are generated:  $\text{Li}2b$ , which is the lithium in the transition metal layer, and  $\text{Li}2c$  and  $\text{Li}4h$ , which are the lithium atoms in the lithium layer with a stoichiometry of 1:2 respectively. In addition, as seen in Figure 1.4c, depending on how the manganese honeycombs are stacked one with respect to the other along the  $c$  direction, these compounds can contain cationic stacking faults.

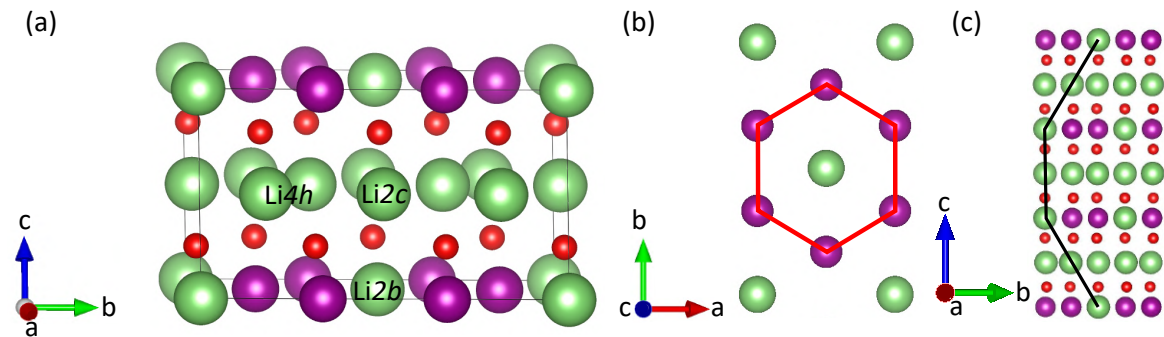


Fig. 1.4 (a) Ideal monoclinic  $C2/m$  structure of  $\text{Li}_2\text{MnO}_3$ . (b)  $ab$  plane of the mixed  $\text{LiMn}_2$  layers. The honeycomb arrangement is highlighted with a red hexagon. (c) Model structure containing stacking faults.

The existence of stacking faults can be assessed using X-ray diffraction (XRD). [70, 71] Figure 1.5 shows an example where the XRD patterns of one  $\text{Li}_2\text{MnO}_3$  sample with ideal stacking and one with a high concentration of stacking faults are compared. The ideal structure contains five well defined reflections in the  $2\theta$  range  $20\text{-}35^\circ$  arising from the superstructure ordering in the transition metal layer. Because stacking faults break the symmetry along the  $c$  direction some reflections are strongly broadened in the highly faulted sample and an asymmetrically broadened peak is found at  $2\theta \simeq 21^\circ$  instead of the 5 well defined peaks. In addition, stacking faults also affect smaller peaks, such as those marked with the blue circles. As these peculiarities are not easily modeled with data treatment softwares, stacking faults have traditionally hindered the complete structural characterization of this family of materials.

Initially,  $\text{Li}_2\text{MnO}_3$  was thought to be electrochemically inactive because, on the one hand, the manganese atom is as  $\text{Mn}^{\text{IV}}$  and it cannot be further oxidized in octahedral environment and, on the other hand, there is no space for additional lithium intercalation. However, if

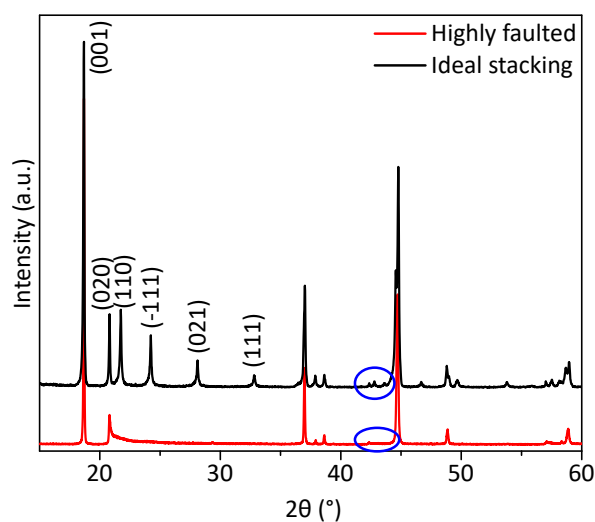


Fig. 1.5 Comparison of the XRD patterns of an ideal Li-rich layered oxide and a strongly faulted and material with the same composition.

$\text{Li}_2\text{MnO}_3$  is charged above 4.6 V it shows redox activity and becomes electrochemically active. Among the explanations for such electrochemical activity the following hypothesis were suggested: i)  $\text{H}^+/\text{Li}^+$  exchange compensated with electrolyte oxidation, [72–74] ii)  $\text{Li}_2\text{O}$  extraction to form  $\text{Li}_x\text{MnO}_2$  like structure, [72, 73, 75, 76] iii) surface densification [77, 78] or iv) irreversible oxygen loss. [79] Nonetheless, the most accepted hypothesis, which has been corroborated both theoretically and experimentally, is the reversible redox participation of the oxygen atoms, i.e. the anionic redox activity. [1, 5, 6, 80–90] In order to better study the oxygen electrochemical redox activity, the group of Tarascon studied isostructural  $\text{Li}_2\text{Ru}_x\text{Sn}_{1-x}\text{O}_3$  and  $\text{Li}_2\text{IrO}_3$  and found that peroxo-like species were formed upon oxidation. [91–96] However, the oxygen evolution is not clear in the commercially interesting manganese, nickel and/or cobalt containing Li-rich oxides. The oxygen redox reactivity in Li-excess layered oxides come from the Li-O-Li  $180^\circ$  configuration, which is a consequence of the presence of lithium atoms in the transition metal layer. While in classic layered oxides all the three 2p orbital of the oxygen atom strongly overlap with the transition metal forming a M-O bond, the weak overlapping of the Li-O-Li configuration generates a non bonding 2p state i.e. an unhybridized orbital, whose electron can be easily extracted. [5, 6, 80, 81, 85–90, 97] However, the oxygen oxidation generates instabilities which lead to irreversible structural transformations. Even if the main structural modification occurs in the first cycle, [98–102] the atomic reorganization continues upon subsequent ones causing continuous fading of the electrochemical properties. [103] Li-excess layered oxides are indeed known to transform to spinel phase as a consequence of manganese migration to the lithium layer. [73, 87, 104–106] The origin of this migration is however controversial

and has been thoroughly studied, as it is additionally linked with several possible structural modifications such as  $O3 \rightarrow O1$  transformation at  $x = 0.5$ , [85, 86] lattice oxygen loss [5, 6, 86, 88, 89, 107, 108] or densification as a consequence of manganese migration within the transition metal layer. [87]

$\text{Li}_2\text{MnO}_3$  exhibits a poor electrochemical performance that results in an important capacity and voltage fading consequence of fast structural degradation. The chemically substituted  $\text{Li}_2\text{MnO}_3$  (mainly with Ni and/or Co, forming compositions such as  $\text{Li}_{1.2}\text{Mn}_{0.6}\text{Ni}_{0.2}\text{O}_2$  or  $\text{Li}_{1.2}\text{Mn}_{0.54}\text{Ni}_{0.13}\text{Co}_{0.13}\text{O}_2$ ) have shown good electrochemistry with capacities over 230 mAh/g. [109–113] However, these materials still suffer from several issues, which are hindering their commercialization: i) low initial Coulombic efficiency (the difference between the capacity delivered in the discharge with respect to the charge) [90, 114] ii) voltage and capacity fading [1, 97, 115] and iii) voltage hysteresis (i.e. the voltage difference between the charge and discharge in certain electrochemical processes). [116–118] Considering the very high potentiality of these cathode materials, significant efforts have been done in recent years to understand and overcome these issues to foster their commercial implementation. These include alternative synthetic methods, [75, 119–121] chemical modifications through the use of dopants [122–134] and surface modifications, [63, 67, 98, 135–137] among others. However, its complex microstructure has hampered a full understanding of the structural modification the material undergoes upon cycling. Indeed, even the exact pristine structure of these compounds is a topic of debate. As we have previously mentioned, some groups describe these materials as an intergrowth of  $\text{Li}_2\text{MnO}_3$  and  $\text{LiMO}_2$  phases, [7, 8, 138–140] while other groups defend a solid solution structural model with general formula  $\text{Li}_{1+x}\text{M}_{1-x}\text{O}_2$  (with  $0 > x > 1/3$ ). [141–145] Stacking faults add even more complexity to the structural study and are generally omitted from the structural analysis, with a consequent loss of information. Such discrepancies have generated intense debate and have even been the object of million dollar patent disputes between relevant material companies. [146]

In summary, Li-rich layered oxides are promising materials which could reduce the price of the cathodes a 20-30%, by increasing their energy density, but several issues still remain to be solved.

### 1.3 Objectives

The main objective of this thesis is to understand the correlations between the structure and microstructure of Li-rich compounds with their electrochemical performance, focusing our research in stacking faults. To do so, advanced characterization techniques such as XRD, neutron powder diffraction (NPD), solid state nuclear magnetic resonance (ssNMR) and

electron microscopy (EM) are employed, which are supported by density functional theory (DFT) calculations and FAULTS refinements. In order to achieve this objective, several specific objectives have been set:

- Uncouple the effect of each initial microstructural parameter (particle morphology, crystallite size, degree of stacking faults) in the electrochemical performance. This objective has been achieved with a careful control of the synthesis method to obtain  $\text{Li}_2\text{MnO}_3$  samples with different microstructure.
- Elucidate the complex ssNMR spectra of  $\text{Li}_2\text{MnO}_3$  samples with different microstructures using DFT calculations to assign the shifts arising from different types of structural defects and evaluate this technique for their quantification.
- Investigate the different structural evolution of ideal and faulted  $\text{Li}_2\text{MnO}_3$  upon delithiation using DFT calculations and explore the effect of cationic substitution in such structural transformations.
- Explore the possibility of discriminating between different microstructural models (solid solution and intergrowth) proposed for Li-rich compounds using XRD and NPD FAULTS structural models.
- Experimentally investigate the structural evolution of faulted  $\text{Li}_{1.2}\text{Mn}_{0.6}\text{Ni}_{0.2}\text{O}_2$  Li-rich compound using *operando* synchrotron XRD experiments.



## Chapter 2

# Synthesis and characterization techniques

*Don't retire too early.*

**John B. Goodenough, the oldest-ever Nobel Prize recipient, at the age of 97.**

In this chapter, the synthetic methods and the different experimental and characterization techniques used in this thesis are described. The two synthesis methods employed are the solid state method, used to synthesize  $\text{Li}_2\text{MnO}_3$ , and the self combustion method, used to synthesize  $\text{Li}_{1.2}\text{Mn}_{0.6}\text{Ni}_{0.2}\text{O}_2$  and  $\text{LiMn}_{0.5}\text{Ni}_{0.5}\text{O}_2$ . The structure, composition and microstructure of the prepared samples have been characterized and studied using XRD, NPD, EM, ssNMR, Physical Property Measurement System (PPMS) and DFT, while their electrochemical behavior has been tested with galvanostatic cycling.

## 2.1 Synthesis methods

In this thesis, three different compounds have been synthesized using two different synthesis routes. While  $\text{Li}_2\text{MnO}_3$  has been synthesized with the classic ceramic or solid state method,  $\text{Li}_{1.2}\text{Mn}_{0.6}\text{Ni}_{0.2}\text{O}_2$  and  $\text{LiMn}_{0.5}\text{Ni}_{0.5}\text{O}_2$  have been synthesized using the self combustion method.

### 2.1.1 Ceramic synthesis

Ceramic or solid state synthesis consists in mixing the reactants in powder form and submitting them to a thermal treatment. The main advantage of this method is that it can be easily used in industry due to its simplicity and scalability, while one of the main drawbacks is the long annealing times and high temperatures needed to complete the reaction. Generally speaking, the smaller the reactant particles are, the faster they will react, as particles with small size have greater contact area. For this reason, the particle size of the precursor powders is sometimes reduced by ball milling, which can additionally be used to uniformly mix the reactants. The pelletizing of the powder mixture can as well improve the contact between the particles, shortening the reaction times.

$\text{Li}_2\text{MnO}_3$  was synthesized using the ceramic method. To do so,  $\text{Li}_2\text{CO}_3$  and a manganese precursor ( $\text{MnO}$ ,  $\text{Mn}_2\text{O}_3$  or  $\text{MnCO}_3$ ) were mixed using a SPEX SamplerPrep 8000 M Mixer/Mill for 5 minutes. This mixture was then pelletized as a 10 mm diameter pellet for 1 min at 5 tons of pressure. Then, a two step calcination process was applied; the first one at 500 °C for 5 hours and a second one at different times and temperatures. The samples are labeled as LMO\_(manganese precursor)\_(temperature)\_(time). A summary of the  $\text{Li}_2\text{MnO}_3$  samples and their synthesis conditions is given in Table 2.1.

### 2.1.2 Self combustion synthesis

The synthesis of multimetallic layered oxides can be challenging when using the solid state method and can result in heterogeneous powder, especially when more than two reactants are used, because the reaction between two reactants can form stable undesired phases which will no further react. Therefore, more sophisticated synthesis techniques such as coprecipitation, Pechini or self combustion methods are sometimes preferred. In this thesis the self combustion method, which is a derivation of Pechini [147] method, has been used to obtain  $\text{Li}_{1.2}\text{Mn}_{0.6}\text{Ni}_{0.2}\text{O}_2$  and  $\text{LiMn}_{0.5}\text{Ni}_{0.5}\text{O}_2$ . The Pechini synthesis consists in forming a chelate (a metal attached to a larger molecule) with a carboxylic acid, such as citric acid (CA) or Ethylenediaminetetraacetic acid (EDTA), to later react it with a polyalcohol (typically

Table 2.1 Synthesis conditions for different  $\text{Li}_2\text{MnO}_3$  samples synthesized by ceramic method.

Precursor	Time	Temperature (°C)	Label
$\text{MnCO}_3$	5	700	LMO_MnCO3_700_5
		800	LMO_MnCO3_800_5
		900	LMO_MnCO3_900_5
		1000	LMO_MnCO3_1000_5
	20	700	LMO_MnCO3_700_20
		800	LMO_MnCO3_800_20
		900	LMO_MnCO3_900_20
		1000	LMO_MnCO3_1000_20
$\text{Mn}_2\text{O}_3$	5	700	LMO_Mn2O3_700_5
		800	LMO_Mn2O3_800_5
		900	LMO_Mn2O3_900_5
		1000	LMO_Mn2O3_1000_5
	20	700	LMO_Mn2O3_700_20
		800	LMO_Mn2O3_800_20
		900	LMO_Mn2O3_900_20
		1000	LMO_Mn2O3_1000_20
$\text{MnO}$	5	700	LMO_MnO_700_5
		800	LMO_MnO_800_5
		900	LMO_MnO_900_5
		1000	LMO_MnO_1000_5
	20	700	LMO_MnO_700_20
		800	LMO_MnO_800_20
		900	LMO_MnO_900_20
		1000	LMO_MnO_1000_20
72	1000	LMO_MnO_1000_72	

ethylene glycol (EG)) to form a polymeric gel as a result of an esterification reaction. In the self combustion synthesis, the polymeric gel formed is heated up until an ash-like powder is formed. Finally, either the polymeric gel in Pechini method or the ash-like powder in the self combustion method are submitted to a heat treatment to get the desired phase. With these methods the synthesis temperatures are usually milder in comparison with classic solid state synthesis, so crystals with lower particle size can be synthesized. In contrast, the scalability of this method and thus, its industrial use, is hindered due to the complexity of the synthesis.

$\text{Li}_{1.2}\text{Mn}_{0.6}\text{Ni}_{0.2}\text{O}_2$  was synthesized by dissolving stoichiometric amounts of  $\text{LiNO}_3$ ,  $\text{Mn}(\text{NO}_3)_2$  and  $\text{Ni}(\text{NO}_3)_2$  in 20 mL of water to obtain a total of  $\sim 5$  g of grams per batch. The dissolved salts were then mixed with CA, which formed a concentrated dissolution as seen in Figure 2.1a. When everything was dissolved, the temperature was raised up to 80

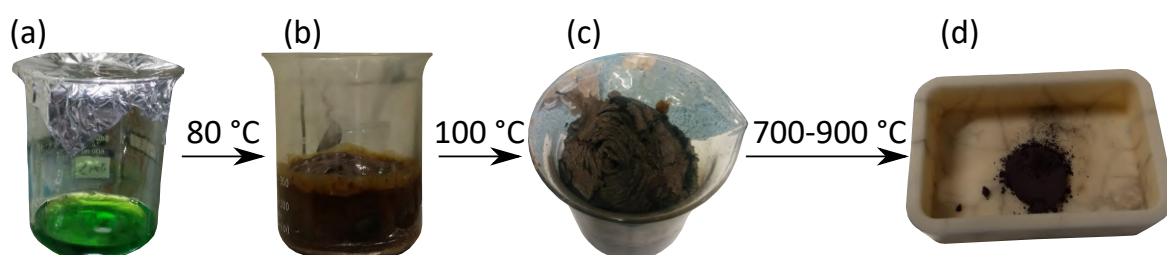


Fig. 2.1 Different steps of the self combustion method. In (a) the dissolution of the metal salts and the chelator is shown, (b) shows the gel phase after the addition of the diol, (c) is the resultant powder after the self combustion and (d) is the resultant powder after the heat treatment at high temperatures.

°C and EG was added. The molar ratio for  $\text{LiNO}_3$ ,  $\text{Mn}(\text{NO}_3)_2$ ,  $\text{Ni}(\text{NO}_3)_2$ , CA and EG is 1.2:0.6:0.2:2:8 respectively. As the water evaporates, the metal-organic complex reacts with EG forming the polymeric ester (Figure 2.1b). Finally, after the self combustion takes place, the ash-like powder obtained (Figure 2.1c) was submitted to a heat treatment (Figure 2.1d). In our case, two different samples were synthesized at 700 °C and at 900 °C for 5 hours, and were labeled as  $\text{L}_{1+x}\text{NMO\_SC\_700\_5}$  and  $\text{L}_{1+x}\text{NMO\_SC\_900\_5}$  respectively (where SC stands for self combustion). On the other hand,  $\text{LiMn}_{0.5}\text{Ni}_{0.5}\text{O}_2$  was synthesized following the same procedure with the required metal stoichiometry. In this case, a single sample was synthesized at 900 °C for 5 hours and was labeled as  $\text{LNMO\_SC\_900\_5}$ .

## 2.2 Powder diffraction

Powder diffraction, in particular using X-ray radiation, is one of the most used characterization techniques in materials science due to its relative low cost, simplicity, short acquisition times and the great amount of information it can provide about the sample, such as crystal structure or microstructural information. Even if it can also be used for obtaining information about amorphous samples (e.g. the radial distribution function, which gives information about the short range ordering of the atoms), its main goal is to decipher the atomic arrangement of a given structure, so mostly crystalline structures are studied with this technique.

X-ray diffraction is based on the scattering of the X-rays when interacting with the electrons of atoms. In the following sections a brief historical context, explaining the basic principles of the technique and how to extract information from the diffractograms is explained. At laboratory level X-rays are produced with copper, cobalt or molybdenum targets. These experiments have usually enough quality to get the desired information. If higher resolution and/or faster acquisition times are required large facilities can be used such

as synchrotrons. Similarly, NPD cannot be acquired at laboratory scale. Both techniques are explained in Section 2.2.4.

### 2.2.1 Historical context

X-rays, which are now the key for systematic phase identification in material science laboratories all over the world, were discovered by Roentgen in 1895. [148] Max Von Laue predicted that if atoms were regularly ordered in a crystal, when the structure was irradiated with X-rays with similar wavelength than atomic bonding distances, some X-rays would diffract. In 1912, Paul Knipping, Walter Friedrich and Max von Laue experimentally demonstrated that crystalline materials diffracted X-rays. [149] Two big discoveries were then made; that atoms were arranged in a regular array in crystals and that the wavelength of X-rays was close to the atomic bonding distance. William Henry Bragg and his son, William Lawrence Bragg studied the crystal diffraction and refraction phenomenon and developed the Bragg's Law, which sets the conditions for diffraction, explained in Section 2.2.2.1.

The first powder diffraction pattern came in 1916. Peter Debye and Paul Scherrer determined the lattice of LiF and Si powders. Almost at the same time, in 1917, Albert Wallace Hull deduced that iron crystallized in a BCC lattice. While Hull used a transmission geometry with the sample in a rotating glass tube and a flat collector, Debye and Scherrer placed the sample in the middle of a photographic collector wrapped forming a circle. [150] This geometry, known as Debye-Scherrer geometry, is still used nowadays. On the early twenties, Johann Christian Michael Brentano created what today is known as Bragg-Brentano geometry, where the distance between the tube and the sample is the same than the distance between the sample and the detector. One of the biggest steps in the resolution of powder diffraction patterns was given by Hugo Rietveld in 1966, when he proposed to refine the crystal structure together with the parameters describing the peak positions and the peak profiles all together, allowing to solve the problem of overlapping peaks in X-ray and neutron patterns. [151, 152] In 1981 Pawley and in 1988 Le Bail developed a method to decompose the pattern, where the unit cell parameters and the space group could be determined without knowing the position nor the nature of the atoms. [153, 154] Nowadays, many different softwares are used to perform Rietveld or Le Bail refinements, such as JANA2006, [155] TOPAS, [156] GSAS [157] or FullProf [158, 159], the latter being the one used in this work.

### 2.2.2 Information contained in powder patterns

A powder diffraction pattern consists in a series of peaks with different intensities and shapes (e.g. Figure 1.5). In order to have a trustworthy results, the data collection must be cautiously

done. For instance, working with non powder samples such as rocks or metallic pieces can be challenging and the equipment needs to be configured to ensure a proper data acquisition. In powder diffraction, issues such as the preferred orientation of the samples should be taken into account. Powder materials could have tendency to be oriented in certain directions due to, for example, a platelet particle shape and this can cause several problems as the pattern will exhibit systematic errors with the peak intensities. There are different ways to overcome this problem; from the most rudimentary but effective ones such as lateral charging to using transmission powder diffraction or two dimensional detectors. In this thesis, lateral charging has been systematically used at laboratory scale to avoid the error coming from the preferential orientation of the crystals. The information contained in a powder diffraction pattern is given by three main characteristics; the peak positions, the peak profile and the peak intensities, described in more detail in the following sections.

### 2.2.2.1 Peak position

When a crystal (whose atoms, by definition, are displaced in a periodic array forming a cell in the space) is irradiated with a beam, those rays interacting with the matter will diffract. The beams diffracted by two atoms will interact and these interactions can be constructive or destructive, giving as a result (or not) a diffraction peak. The rule for the diffraction to be constructive is given by the Bragg's law:

$$n\lambda = 2d\sin\theta \quad (2.1)$$

Figure 2.2 is a schematic representation of the Bragg's law, where an array of atom planes separated by a distance  $d$  (the interplanar distance) is shown. For this example the crystal is considered to be formed by repeating this single atom, forming rows of atoms in 2 dimensions. As beam 2 does a larger distance than beam 1 (extra path shown in red) the two beams will not necessarily be in phase after the reflection. Being  $d$  the distance between the atoms, the red extra path of beam 2 can be described as  $2d\sin\theta$ . According to Bragg's law, there will be a constructive interference (and therefore a diffraction peak) if the extra path is equal to (or an integer of) the wavelength of the incident beam, as it is shown in the Bragg's law in Equation 2.1. The peaks in a diffractogram will thus entail information about **the symmetry and size of the unit cell**, i.e. its space group and cell parameters.

### 2.2.2.2 Peak profile

The peak profile can be defined by a Voigt function, which corresponds to the convolution of a Gaussian and a Lorentzian function (Figure A.1 in Appendix A shows the difference

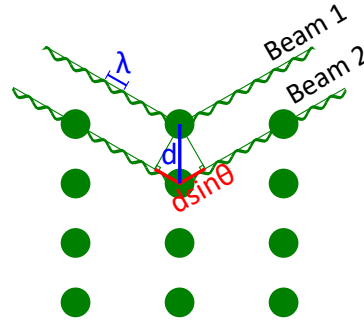


Fig. 2.2 Schematic recreation of Bragg's law.

between a Gaussian and a Lorentzian peak profile). The computational resolution of this function is time consuming so the pseudo-Voigt approximation is normally used, which is a linear combination of a Lorentzian and a Gaussian curve instead of their convolution, described as follows:

$$pV(x; \eta, H) = \eta L^p(x; H) + (1 - \eta) G^p(x; H) \quad (2.2)$$

where  $x$  is  $2\theta - \theta_k$ ,  $\eta$  is the mixture parameter,  $H$  is the full width at half maximum (FWHM) and  $L^p$  and  $G^p$  are the Lorentzian and Gaussian components of the FWHM. The pseudo-Voigt function will be an approximation of the Voigt function when the Thompson-Cox-Hastings formulae is fulfilled: [160]

$$H = (H_G^5 + 2.69269H_G^4H_L + 2.42843H_G^3H_L^2 + 4.47163H_G^2H_L^3 + 0.07842H_GH_L^4 + H_L^5)^{\frac{1}{5}} \quad (2.3)$$

and

$$\eta = 1.36603 \frac{H_L}{H} - 0.47719 \left( \frac{H_L}{H} \right)^2 + 0.11116 \left( \frac{H_L}{H} \right)^3 \quad (2.4)$$

The FWHM of the Gaussian ( $H_G$ ) and Lorentzian ( $H_L$ ) components generally vary with the  $2\theta$  angle and can be calculated in different ways according to the refinement methods used (the refinement methods are later explained in detail). In **Rietveld** refinement, for instance, the first one is modeled with the Caglioti equation [161]

$$H_G^2 = (U_0 + U_\epsilon) \tan^2 \theta + V_0 \tan \theta + W_0 + \frac{P}{\cos^2 \theta} \quad (2.5)$$

while  $H_L$  is described as

$$H_L = (X_0 + X_\varepsilon)\tan\theta + \frac{Y_0 + Y_S}{\cos\theta} \quad (2.6)$$

where  $U_0$ ,  $V_0$ ,  $W_0$ ,  $X_0$  and  $Y_0$  are the profile parameters used to account for the instrumental contribution to peak broadening,  $U_\varepsilon$  and  $X_\varepsilon$  describe the contribution of microstrains (i.e. fluctuations in cell parameter values) and  $Y_S$  and  $P$  is the contribution of the small size of coherent diffraction domains.

In **FAULTS** refinement, [162–164] on the contrary,  $H_G$  and  $H_L$  are given by

$$H_G^2 = U\tan^2\theta + V\tan\theta + W + \frac{4\ln 2\lambda^2}{\pi D_G \cos^2\theta} \left(\frac{180}{\pi}\right)^2 \quad (2.7)$$

and

$$H_L = X\tan\theta + \frac{2\lambda}{\pi D_L \cos\theta} \left(\frac{180}{\pi}\right) \quad (2.8)$$

It should be taken into account that the peak width is the result of instrumental effects and the microstructure of the sample itself. In order to obtain accurate information regarding solely the microstructure of the sample it is necessary to separate the contribution coming from the sample from the contribution coming from the instrument. The contribution of the instrument is usually obtained by refining a measurement of a standard sample such as  $\text{LaB}_6$  or  $\text{Al}_2\text{O}_3$  corundum. In any case, once the FWHM of the sample is calculated ( $H$  in Equation 2.3), the apparent crystallite size can be given by the Scherrer formula, shown in Equation 2.9 as, [165]

$$\varepsilon = \frac{K\lambda}{H\cos\theta} \quad (2.9)$$

where  $K$  is the Scherrer constant, which is usually set to 0.94 if the crystals are cubic and to 0.89 if the crystals are spherical and  $H$  is given by Equation 2.3. [166] On the other hand, the peak widening coming from microstrains can be measured with the Stokes-Wilson equation, [167] defined as

$$\varepsilon' = \frac{\beta_D}{k\tan\theta} \quad (2.10)$$

where  $\beta_D$ , calculated using the De Keijser formula, [168] is the peak width and  $k$  is a constant dependent on the definition of the microstrain (usually 4 or 5). Therefore, the peak profile will give information about the **microstructure** of the sample (i.e. the average crystallite size or the microstrains).



### 2.2.2.3 Peak intensities

The integrated intensity for a given reflection obtained after irradiating the sample with an  $I_p$  primary intensity is given by the following equation: [169]

$$I = I_p K \lambda^3 V^{-2} m P L v F^2 \quad (2.11)$$

where  $K$  depends on the radiation source,  $V$  is the unit cell volume,  $m$  is the multiplicity of the given reflection,  $P$  is the polarization factor of the diffracted beam,  $L$  is the Lorentz factor which takes into account the effects of the geometry,  $v$  is the volume of the sample where the absorption effects are included and  $F$  is the structure factor, which depends on the atomic position on the cell. Therefore, knowing the properties of the radiation source, the peak intensities will provide information about the **atomic nature and their position** in the cell.

## 2.2.3 Methods for extracting information

### 2.2.3.1 Rietveld refinement

The Rietveld refinement consists in minimizing the difference between a simulated and an experimental diffraction pattern using an approximate starting model and iteratively vary the values of some parameters such as the unit cell or the atomic positions until the difference is minimum. The minimization process is done using the least squares fitting method and the final result, is a detailed description of the average unit cell of our compound.

The Rietveld method is a very convenient refinement method for most cases. It allows to refine specific features such as anisotropic strain or size broadening (when for example there are planar crystallites), anisotropic thermal factors, amount of each phase when there is a mixture of them or some kind of defects like point defects. However, it is not able to refine planar defects such as stacking faults. In this case, the FAULTS method, developed by our group, can be used as alternative. [162–164]

### 2.2.3.2 FAULTS refinement

FAULTS [162–164] is a refinement software based on DIFFaX [170] (which is a simulation software) and built using the Fortran 95 crystallographic library CrysFML, [171] which was developed to refine non periodic structures with planar defects, such as those containing twinning or stacking faults. The Rietveld method uses unit cells and atomic positions to describe the structural model to calculate the diffraction pattern. As a result, planar defects such as stacking faults cannot be modeled and therefore, some structural information is

omitted. The FAULTS program enables to extract this information at the same time the structure is refined because the structural model is described in a different way so that any type of planar defect can be included. The elements needed for the structure description in FAULTS are shown in Figure 2.3. In particular, FAULTS describes its structural model with a sequence of layers stacked following a stacking vector. Since more than one vector and/or layer type is provided, a probability for each transition to happen is requested. Therefore, the structure no longer needs to be periodic along the stacking direction.

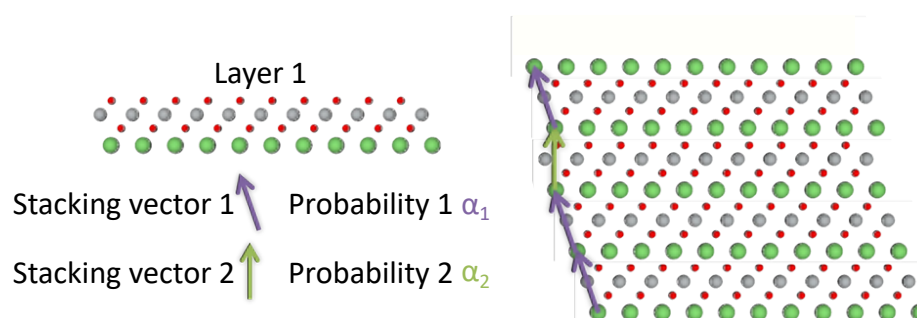


Fig. 2.3 Elements needed for the description of the structure using the FAULTS program.

The atomic positions are described using fractional coordinates along the unit cell edges. However, as no space group is required, the unit cell used in FAULTS can differ from that used to describe the average structure in Rietveld refinement programs. In general, the smallest possible unit cell is searched to minimize computational time. The stacking vectors must be perpendicular to the  $ab$  plane, which means that the unit cell has fixed  $\alpha$  and  $\beta$  angles of  $90^\circ$ . The transformation of the classic unit cell to FAULTS unit cell can be direct, but monoclinic and triclinic unit cells may require modifications to adapt the unit cell to this condition.

The refinable parameters are the  $a$ ,  $b$ ,  $c$  and  $\gamma$  FAULTS cell parameters, the stacking vectors and their stacking probabilities, the peak profile and the atomic positions, occupancies and thermal factors. The crystallite coherent domain size given by the peak profile can be calculated in two different ways; by providing the layer width and the number of stacked layers (as it is done in DIFFaX) or using the values used to determine the profile function, as it is usually done in Rietveld refinements using Equations 2.7 and 2.8. For the later case,  $U$ ,  $V$ ,  $W$ ,  $X$ ,  $D_G$  and  $D_L$  parameters are refinable.

## 2.2.4 Large facilities

### 2.2.4.1 Synchrotron radiation

Synchrotron light is the electromagnetic radiation generated in a particle accelerator when charged particles at relativistic speed (close to the speed of light) are forced to move in a curved trajectory by applying magnetic fields. It is a really intense radiation which covers a wide wavelength range from infrared to hard X-rays and can be used for the acquisition of fast and high quality X-ray absorption and diffraction data. [172]

In 1897 Langmor [173] and 1898 Lienard [174] predicted and formulated the radiated energy an accelerated charged particle would emit. In 1940 the first operational betatron (a cyclic particle accelerator) was constructed in the USA to study fundamental particle behavior. Synchrotron radiation was there considered as a problem, as it was a great energy loss. The first record of synchrotron radiation was in 1947 by General Electrics. [175] Since then, some groups used the synchrotron light to perform some X-ray spectroscopies. [176, 177] At that time, however, beamlines were built in facilities for particle studies and synchrotron radiation was not the main purpose of these facilities. The 2<sup>nd</sup> generation of synchrotron facilities were *ex profeso* built for synchrotron light use. The first 2<sup>nd</sup> generation synchrotron was built in the UK and the experiments began in 1980. Nowadays 3<sup>rd</sup> generation synchrotrons are the most used, where the light source is optimized by adding "insertion devices" such as undulators or wiggler magnets. Undulators increase the intensity and make the coherent light beam narrower, while wiggler magnets create a broad and intense incoherent light. The upcoming 4<sup>th</sup> generation of synchrotrons will use X-ray free electron lasers, which consists on a long undulator with a high energy electron linear acceleration. Sweden's MAX-IV laboratory will host the first two 'fourth-generation' light sources.

### 2.2.4.2 Neutron diffraction

Neutron powder diffraction (NPD) is a complementary diffraction technique which can contribute to the determination of the structure of a crystal. There are two different neutron sources: reactor based and spalation. The first one uses a radioactive source such as <sup>235</sup>U to maintain a constant flux of neutrons while in the second one the neutrons are generated hitting accelerated protons to a heavy metal such as tungsten. [178] Its main advantage towards X-rays comes from the fact that, contrary to X-rays, which are scattered by electrons and therefore the scattering length is proportional to the electronic density of the atoms (and thus their Z atomic number), neutrons are scattered by the atomic nuclei. This means that XRD fails to differentiate between atoms which are close in the periodic table and the detection of light elements is tough, but neutron diffraction can result in very different scattering lengths

for atoms with similar  $Z$  or even for different isotopes of the same atom. As a consequence NPD can help us to:

- Precisely determine the position and occupancy of light atoms in a cell (which is tricky with XRD, especially if they coexist with heavier atoms in the cell).
- Distinguish between atoms with similar  $Z$  (as for example the case of Ni, Co, Fe or Mn in cathode materials) which is especially useful if these exhibit ordered schemes.
- Identify where an atom preferentially locates after a reaction by using isotopes as markers.

Neutrons have additional advantages in comparison with XRD. The scattering power is independent of  $2\theta$  and therefore the scattering intensity does not decrease at high  $2\theta$  values. In addition, neutrons interact with the magnetic moments of the crystals so they can be used to study magnetic properties.

Apart to the need of large facilities to acquire NPD, one of the biggest limitations of neutron scattering is their weaker interaction with atoms in comparison with X-rays. Therefore, higher amounts of samples are usually needed, which hinders the development of some techniques such as the *operando* analysis of battery materials, which is well established for XRD. This weak atomic interaction can also be an advantage as neutrons can penetrate deeper in materials so they can be used to determine the bulk structure of thick samples. Another important drawback is that the sample may absorb the neutrons and become radioactive so depending on its decay half-life the sample will not be recoverable for a defined time.

## 2.2.5 Measurement conditions

In this thesis the laboratory scale XRD patterns were recorded on a Bruker D8 Discover instrument using monochromatic copper radiation ( $\text{Cu K}\alpha_1$   $\lambda = 1.54056 \text{ \AA}$ ). Patterns acquired for analysis were measured in a  $2\theta$  range of  $15\text{-}110^\circ$  with a step size of  $0.01^\circ$  and a time per step of 1.550 s.

The synchrotron measurements were acquired at the 11 ID-B beamline at the Atomic Photon Source (APS) at the U.S. Department of Energy's Argonne National Laboratory with a wavelength of  $0.2113 \text{ \AA}$  and a stepsize of  $0.0119^\circ$ . This synchrotron light was used to perform an *operando* XRD measurement, which was carried out in an AMPIX cell. [2] Figure 2.4a shows a representation of this cell, which is composed of an electrically insulating polymeric body, a conical-shape cap which enables the acquisition of the X-rays with an angle of  $\sim 100^\circ$  (Figure 2.4b), corrosion resistant electrodes, a disc like X-ray transmissive

window made of Sigradur-(G) electrically conductive dense glassy carbon and a gasket to accommodate the materials as seen in Figure 2.4c. The AMPIX cell (Figure 2.4d) can be located in a six cell multisampler holder (Figure 2.4e) which enables multiple measurements at the same time.

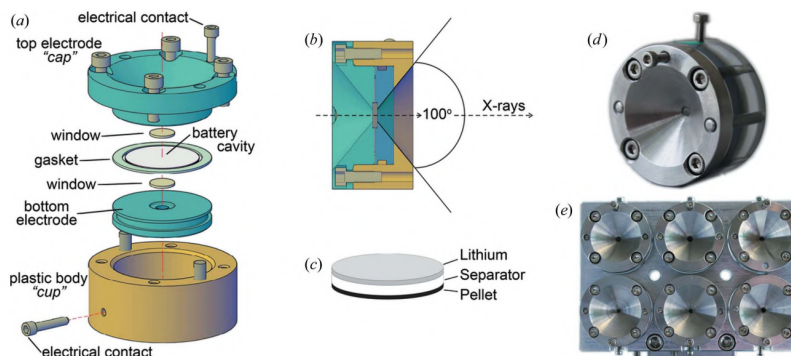


Fig. 2.4 (a) An exploded representation of the AMPIX cell, (b) the assembled AMPIX cell and (c) a typical battery stack. Photographs of (d) an assembled AMPIX cell and (e) a six-cell multisample holder. Reproduced with permission of the International Union of Crystallography. [2]

Finally, the NPD data has been acquired at the ECHIDNA high-resolution powder diffractometer at ANSTO (Australia) with a wavelength of  $1.6237 \text{ \AA}$  and a stepsize of  $0.125^\circ$ .

## 2.3 Electron microscopy

A microscope is an instrument which uses lenses to magnify objects beyond eye resolution (0.1-0.2 mm). The resolution of the microscope is limited by the wavelength of the light used. Visible light, which is used in optical microscopes, has a wavelength of 400-700 nm, and its corresponding resolution is about 200 nm. Accelerated electrons have considerably lower wavelength so they can be used instead of visible light to achieve higher magnifications.

In electron microscopies an electron beam is focused in a sample. Depending on how the electrons interact with the sample, these electrons can be absorbed, reflected or transmitted. Figure 2.5 shows the different interactions of the main beam with the sample. There are two main types of electron microscopies; scanning electron microscopy (SEM), where the images are produced from the reflected electrons, and transmission electron microscopy (TEM), where the images are formed from the transmitted electrons. The absorbed electrons are not used in imaging.

**SEM** uses a thin electron beam to scan a selected area and recovers the electrons which scatter with an angle higher than  $90^\circ$  (backscattered electrons, BSE). The BSE are related to

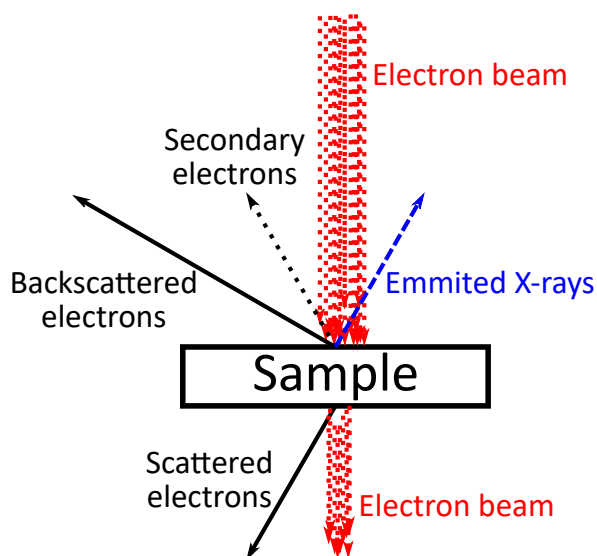


Fig. 2.5 Representation of the main interactions between the main electron beam of the electron microscopy at atomic level.

the atomic number  $Z$ ; the higher  $Z$  is, the higher the signal of those electrons will be. This allows to differentiate zones with light elements from zones with heavy ones. Some electrons can transfer some energy to the atoms in the sample, which can generate phenomena like secondary electrons (SE). Their signal does not depend so much on the  $Z$  atomic number so the elemental contrast is poorer. In contrast, as the energy of the SE is lower the electrons from the atoms in the surface are the main contributors to this signal. This allows to observe the topography of the sample with more detail.

**TEM** uses the transmitted electrons to build the image. Since the electron beam needs to cross all the sample, thin samples are preferred. In addition, TEM uses considerably higher voltage electron beams (around 200-300 keV in comparison with the  $\sim 50$  keV used in SEM) so that they can penetrate the sample. The scattered electrons can be used for low-resolution imaging to obtain information about particles shapes and sizes, but due to its much higher resolution it also allows a deeper analysis. From the several imaging techniques available three different have been used in this thesis: i) high resolution TEM (HRTEM), where atomic resolution can be reached and defects on the sample such as stacking faults or dislocations can be directly observed. ii) high-angle annular dark-field scanning TEM (HAADF-STEM), where the use of a thin electron beam to scan the sample like in SEM with a HAADF detector enables to differentiate elements in a sample according to the  $Z$  atomic number and its thickness. iii) selected area electron diffraction (SAED), where diffraction patterns corresponding to projections of the reciprocal lattice are obtained. This last technique is

widely used to determine crystal structures and obtain approximate lattice parameters. It can also be valid to detect defects such as stacking faults.

As previously mentioned, the electron beam can transfer energy to electrons in the atom which can excite the electrons of atomic inner shells, being ejected from the atom. The outer electrons will then occupy these generated holes, releasing energy as X-rays, which are characteristic for each element. As a consequence, these X-rays are used to obtain compositional information of the sample and can be detected in both techniques, SEM and TEM. They are usually collected with a Energy Dispersive Spectroscopy (EDS) and can semiquantitatively give the elemental composition of the measured sample. This technique has two main limitations that must be considered. On the one hand, light elements are not easily detected, so, in practice, lithium atoms will not give any signal. On the other hand surface atoms will have higher contribution than inner ones. This means that non homogeneous particles or *core shell* structures can lead to erroneous measurement of the elemental composition. In this thesis, the generated X-rays have been acquired to semiquantitatively confirm the composition of the samples under measurement.

### 2.3.1 Measurement conditions

For the SEM measurements, both BSE and SE imaging modes are used to obtain images of the samples, which were prepared by diluting a small amount of powder in ethanol and sonicating for two minutes. Image acquisitions were performed in a FEI Quanta 200 field-emission gun SEM at CIC EnergiGUNE.

All the TEM measurements in this thesis were performed at the Electron Microscopy for Materials Science (EMAT) at the university of Antwerp (Belgium). The samples were crushed in a mortar with acetone and the suspension was sonicated for a couple of minutes. Drops of this suspension were then deposited onto carbon-coated copper grids. SAED patterns and EDS were acquired using a FEI Tecnai Osiris electron microscope, equipped with a ChemiSTEM system, and a FEI Tecnai G2 electron microscope, both operated at 200 kV. HAADF-STEM images were acquired using an aberration corrected cubed FEI Titan electron microscope operated at 120 and 300 kV.

## 2.4 Magnetic measurements

### 2.4.1 Solid state nuclear magnetic resonance

NMR is a characterization technique where structural information of a structure is obtained from the nuclear magnetic moment of the atoms. NMR basis were established by Pauli

in 1924, but it was not until 1946 when the first experiment was carried out by Bloch and Purcell. [179–181]

The NMR is the consequence the electromagnetic radiation absorption as a consequence of the magnetic field induced energy levels' splitting. This splitting is the result of the angular magnetic moment interaction with some nucleus with non zero spin. The nucleus of an atom is formed of protons and neutrons which are defined with  $Z$  atomic number (corresponding to the number of protons) and  $A$  mass number (corresponding to the number of protons and neutrons) and they have a spin angular momentum, which is dependent on the values of  $Z$  and  $A$ . The quantum number for the nuclear spin angular momentum is defined as  $I$ . If  $Z$  and  $A$  are even  $I = 0$ , if  $A$  is even and  $Z$  is odd  $I = n$  (where  $n$  is an integer) and if  $A$  is odd  $I = n/2$ , regardless  $Z$  is odd or even. Therefore, the atoms will be NMR active unless  $Z$  and  $A$  are even.

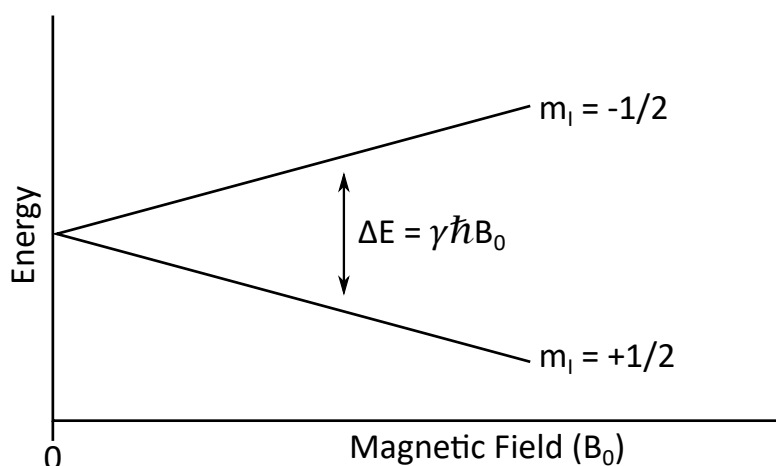


Fig. 2.6 Spin states splitting as a consequence of an external magnetic field.

When  $I \neq 0$  (for instance  $I = 1/2$ ), if the sample is under an external  $B_0$  magnetic field, the spins will align either parallel to  $B_0$  or antiparallel to it. This creates two different energy levels which linearly increase with an increasing magnetic field, called the Zeeman effect. As seen in Figure 2.6, these two configurations have a energy difference which is described as

$$\Delta E = \gamma \hbar B_0 \quad (2.12)$$

where  $\gamma$  is the gyromagnetic ratio, which is an intrinsic property of each atom,  $\hbar$  is the reduced Planck's constant and  $B_0$  is the applied magnetic field. The magnetic nuclear resonance is thus given when a transition between these two levels is introduced. The population of the different energy levels are given by the Boltzmann distribution as



$$\frac{N_{upper}}{N_{Lower}} = e^{-\frac{\Delta E}{k_B T}} \quad (2.13)$$

where  $k_B$  is the Boltzmann constant and  $T$  is the temperature. In atomic nuclei  $\Delta E$  is really small (in the order of  $2 \cdot 10^{-26}$  J in a 1.5 T field at room temperature), so high magnetic fields are needed for a significant contrast.

According to this, the same atoms should have the same NMR signal regardless their local environment. In practice, however, this is not true because the electrons of the atoms can modify the effective  $B_0$  they receive. These electrons will interact with  $B_0$ , generating a magnetic field which is usually opposed to  $B_0$ . Therefore, the effective magnetic field (the magnetic field the atoms receive) is usually smaller than  $B_0$  and can be defined as

$$\omega_L = 2\pi\nu_L = \gamma(1 - \sigma)B_0 \quad (2.14)$$

where  $\sigma$  is the shielding of the atom. Each different atomic local environment will thus exhibit a different chemical shift and the distribution of these resonance frequencies give as a result the NMR spectrum. [182] When a standard is used as calibrant the difference between  $\omega_L$  of the sample and the calibrant is known as the chemical shift and is defined as Equation 2.15. [183]

$$\delta = \frac{(\omega_L - \nu_{ref}) \cdot 10^6}{\nu_{ref}} \quad (2.15)$$

In a crystal the atoms are not isolated, so they can interact. This means that, in addition to the Zeeman effect, additional interactions can affect to the NMR spectra, such as the dipolar and the quadrupolar couplings, the time dependent field, the chemical shift or the hyperfine coupling. In our case, we are dealing with paramagnetic materials (where some atoms have unpaired electrons), so the interaction governing the NMR spectra is the hyperfine coupling.

The **hyperfine coupling** is the interaction between the unpaired electron of the paramagnetic material with the atoms been analyzed, which generates an important shift and a broadening of the NMR signal. The shift is consequence of the dipolar interaction and the Fermi contact interaction. The **dipolar interaction** is the interaction through space between the unpaired electron of the paramagnetic atom with the atom being measured. This interaction can be reduced or even suppressed spinning the sample at the Magic Angle Spinning (MAS);  $\sim 54.7^\circ$  [184–186] with respect to the  $B_0$ . By eliminating this interaction, the Fermi contact shift is the main contributor to the hyperfine coupling. In contrast with the dipolar interaction, the **Fermi contact interaction** is given by the presence of unpaired electrons in the atom in measurement. This generates large shifts which can be expressed as

$$\delta_{iso}^i = \frac{A^i \chi_M}{\hbar \mu_0 \gamma g_e \mu_B} \quad (2.16)$$

where  $A^i$  is the Fermi contact coupling constant,  $\chi_M$  is the molar magnetic susceptibility,  $\hbar$  is the reduced Planck's constant,  $\mu_0$  is the magnetic constant,  $\gamma$  is the gyromagnetic ratio,  $g_e$  is the g factor of the electron and  $\mu_B$  is the Bohr magneton. In this thesis  $A^i$  is calculated using DFT as explained in Section 2.5.1.2 and  $\chi_M$  is calculated experimentally using a physical property measurement system (PPMS).

## 2.4.2 Measurement conditions

$^6\text{Li}$  Magic Angle Spinning solid state-NMR experiments were performed on a Bruker 300 WB at CIC EnergiGUNE spectrometer charged to a field of 4.69 T equipped with a standard 1.3 mm MAS probe. Spinning frequencies were set to 50 kHz in all cases. A rotor synchronized spin-echo pulse sequence ( $90^\circ - \tau - 180^\circ \tau_1$  acquisition) was used with typical  $90^\circ$  and  $180^\circ$  pulses of 1.3 and 2.6  $\mu\text{s}$ , respectively. A recycle delay of 0.5 s was used and around 165000 scans were typically acquired in a  $^6\text{Li}$  NMR experiment. The spectra were referenced to a 1 M solution of LiCl and fitted using the Dmfit software. [187]

Magnetic measurements were carried out using a Quantum Design PPMS, equipped with an AC measurement system (ACMS) option at CIC EnergiGUNE. The zero field cooled (ZFC) susceptibility measurements have been performed while heating from 2.5 K to 300 K in AC magnetic field of 10 Oe at a frequency of 1 kHz, with a step of 2 K/min in the range 2.5-70 K and 12 K/min in the range 70-300 K. The samples have been measured in mildly packed powder form placed inside sample holder, surrounded by a pure He atmosphere.

## 2.5 Computational methods

### 2.5.1 Density functional theory

The fast development of computing resources has allowed an exponential growth of the computing materials science field. Computer science allows to predict the behavior of a given structure, so instead of synthesizing and testing thousands of compounds, their properties can be scanned and the best ones can be chosen, avoiding the waste of time and resources. Furthermore, relating the microscopic behavior with the experimental observations and theoretical studies are usually very helpful. Computational methods are classified by the time and the length scales they can describe. Quantum methods (QM) reach the electron scale, molecular dynamics (MD) the atom scale, coarse grained (CG) methods the microscale and

finite elements methods the macroscale. In this thesis, computational methods are chosen to study the evolution of the considered materials upon cell delithiation in terms of structural stability and its relationship with the oxidation state of the atoms. [188, 189]

Computational methods require a solution to the well known Schrödinger equation, which unfortunately is impossible to solve nowadays for crystals. The use of approximations is, however, a powerful technique to calculate the total energy of a system. One of the most used one is the DFT, which offers a good compromise between accuracy and computational time and it is widely used in the development of new materials for batteries. The Schrodinger equation is shown in Equation 2.17.

$$\left[ -\frac{\hbar^2}{2m_e} \sum_{i=1}^N \nabla_i^2 + \sum_{i=1}^N V(\mathbf{r}_i) + \sum_{i=1}^N \sum_{j<i}^N U(\mathbf{r}_i, \mathbf{r}_j) \right] \psi = E\psi \quad (2.17)$$

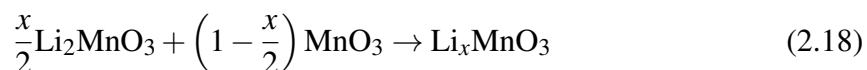
In addition to the two fundamental constants ( $\hbar$  the reduced Plank's constant and  $m_e$  the mass of the electron), the three terms in brackets represent the kinetic energy of each electron, the interaction energy between electrons and nuclei and the exchange correlation (the interaction energy between the electrons) respectively. This equation can be solved using the Kohn and Hohenberg [190] theorems. The first theorem states that the ground state energy from the Schrödinger equation is a unique functional of the electron density. In other words, the ground state electron density determines all the properties. DFT is an approach to convert the unsolvable many body Schrödinger equation into a set of coupled one electron equations [191] where all the many body interactions are taken into account in the exchange correlation functional. [192] Still with this approximation, the exchange-correlation term is unknown and further approximations need to be used. The second Kohn and Hohenberg theorem says that the electron density that minimizes the energy of the functional is the true electron density corresponding to the solution of the Schrödinger equation. By knowing the functional, the electron density could be varied to obtain the minimum energy of the system (the ground state).

The simplest approximation to determine the exchange correlation term is the local density approximation (LDA), where the energy density is a uniform electron gas of the same density. [192] This system works well for metallic systems but fails when there are localized electrons in the structure. The generalized gradient approximation (GGA) is more suitable for systems with localized electronic states. GGA introduces a dependence of the exchange correlation energy on the local gradient of the electron density. [192] This method is not enough to properly describe compounds whose electrons tend to be localized and interacting (e.g. transition metals) so the GGA + U method was developed to add a correction term to d or f orbitals.

The wave function can be described either as local basis set or as plane waves basis set. Even if the former one is computationally less time consuming the results are less trustworthy, so plane wave calculations are preferred. In plane wave calculations the interactions between the core electrons and the ions are described with **pseudopotentials** instead of using a whole electron system. All the electrons which do not participate in the bondings (the core electrons) are joined in a single effective potential which saves computational time. However, in order to avoid problems derived from the interactions between the core and the valence electrons, the projector augmented wave (PAW) method is used. [193]

### 2.5.1.1 Energy and convex Hull

The analysis of energies can predict if reactions are likely or able to occur. All computational chemistry techniques define energy such as the system with the lowest energy is the most stable. In this thesis, the total energy is used to compute the formation energy of a given process. In Chapter 5, in particular, the stability of intermediate phases in the delithiation of  $\text{Li}_2\text{MnO}_3$  and other isostructural compounds is studied by convex hull diagrams. In these, the formation energies of the different phases are plotted with respect to the lithium composition. For instance, for the the reaction below,



the formation energies are calculated as:

$$E_f(x) = E(\text{Li}_x\text{MnO}_3) - \left(1 - \frac{x}{2}\right)E(\text{MnO}_3) - \frac{x}{2}E(\text{Li}_2\text{MnO}_3) \quad (2.19)$$

where  $E(\text{Li}_x\text{MnO}_3)$  is the total energy of the studied structure and  $E(\text{MnO}_3)$  and  $E(\text{Li}_2\text{MnO}_3)$  are the total energy of the end members of the Hull. Figure 2.7 shows a hypothetical convex Hull diagram for  $\text{Li}_x\text{MnO}_3$ . The energies of the two end members of the compositions are taken as reference and the compounds whose energy is lower are plotted. In this case,  $\text{LiMnO}_3$  and  $\text{Li}_{0.5}\text{MnO}_3$  are more stable than the two end members, meaning that at that  $x$  value, those compositions are preferably formed rather than the two adjacent ones. At  $x = 1.5$ , even if there are structures with negative formation energies, there are no points in the Hull line or below, meaning that  $\text{Li}_{1.5}\text{MnO}_3$  would decompose into the more stable  $\text{Li}_2\text{MnO}_3$  and  $\text{LiMnO}_3$ .

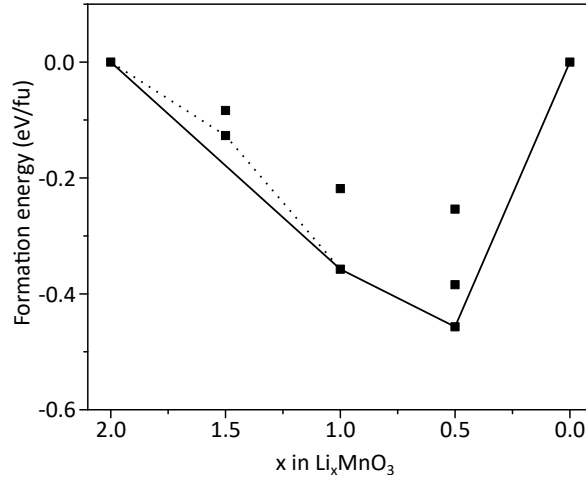


Fig. 2.7 A hypothetical Convex hull diagram for  $\text{Li}_2\text{MnO}_3$ .

### 2.5.1.2 NMR shift calculation

One of the properties analyzed with DFT calculations is the hyperfine coupling constant, in particular to predict the NMR shifts of the compounds being studied. According to VASP manual [194] the hyperfine coupling constant is obtained as

$$(A_{iso}^I)_{ij} = \frac{2\mu_0\gamma_e\gamma_I}{3\langle S_z \rangle} \delta_{ij} \int \delta_T(r) \rho_s(r + R_I) dr \quad (2.20)$$

where  $\mu_0$  is the magnetic susceptibility of free space,  $\gamma_e$  is the electron gyromagnetic ratio,  $\gamma_I$  the nuclear gyromagnetic ratio at  $R_I$ ,  $\langle S_z \rangle$  the expectation value of the  $z$ -component of the total electronic spin,  $\delta_T(r)$  is a smeared out of  $\delta$  function as described by Blöchl, [195] and  $\rho_s$  is the spin density. The gyromagnetic ratios for  ${}^6\text{Li}$ ,  ${}^{55}\text{Mn}$  and  ${}^{16}\text{O}$  are 6.266, 10.576 and  $-5.774 \text{ MHz}\cdot\text{T}^{-1}$  respectively. The hyperfine coupling constant is then used in Equation 2.16 to obtain the Fermi contact shift.

### 2.5.1.3 Computational details

In this thesis, the calculations were carried out in three different supercomputing centers: the Spanish i2Basque center, Altamira Supercomputer at the Institute of Physics of Cantabria (IFCA- CSIC) and Barcelona Supercomputer center. The software used is the Vienna *Ab-initio* Simulation Package (VASP). [196, 193] Spin-polarized DFT calculations were performed. PAW potentials [193] were used to replace core electrons whereas Li (2s), Mn (3p, 3d, 4s) and O (2s, 2p) valence electrons were expanded in plane waves with a cut off energy of 600 eV. The Perdew-Burke-Ernzerhof (PBE) [197] exchange-correlation function was used together with a Monkhorst-Pack grid with using a representative amount of  $k$ -points.

Unless the opposite is specified, structures were fully relaxed (cell parameters, volume cells and atomic positions) with a residual force threshold of  $0.02 \text{ eV \AA}^{-1}$ . The generalized gradient approximation with the Hubbard parameter correction (GGA+U) of Dudarev *et al.* [198] was employed (with a U of 3.9 eV for Mn and 6.2 for Ni). [199] A convergence of the total energy close to 0.5 meV/fu (fu=formula unit) was achieved with these parameters.

### 2.5.2 Ewald's summation

Ewald summation is an alternative computational method developed by Ewald in 1921 to determine the electrostatic energy of ionic crystals. [200] The method consist on the summation of the  $\varphi_{sr}(\mathbf{r})$  short range electrostatic interactions term, which is converged in the direct space, with the  $\varphi_{lr}(\mathbf{r})$  long range electrostatic interactions term, converged in the reciprocal space, as shown in Equation 2.21.

$$\varphi(\mathbf{r}) \stackrel{\text{def}}{=} \varphi_{sr}(\mathbf{r}) + \varphi_{lr}(\mathbf{r}) \quad (2.21)$$

This method only takes into account the electrostatic interactions between the atoms, so in comparison with DFT the calculation times are considerably reduced from hours to few seconds. However, the method is not as accurate because, among other limitations, the atoms in the crystal are static and do not move to find the energetically most favored position. Therefore, this method can be used as a first screening to discard electrostatically unstable compounds and choose possible structures for a DFT analysis.

## 2.6 Galvanostatic cycling

In the galvanostatic cycling a constant current is applied to the battery cell and the voltage variation is registered versus the capacity, until a limit voltage, defined as **cutoff voltage**. The **theoretical specific capacity**, i.e. the maximum capacity the material is able to provide, is calculated using Faraday's law:

$$c = \frac{nF}{W} \quad (2.22)$$

where n is the number of electrons exchanged per ion, F is the Faraday constant with a value of  $26.801 \text{ A}\cdot\text{h}\cdot\text{mol}^{-1}$  and W is the molecular weight of the active material. Once this value is known, the desired current applied to the system is calculated. Usually, the applied current (calculated with respect to the mass or the area of the active material) is given in terms of **C-rate**, which is the time a battery needs to be discharged. For instance, a C/20 rate

means that the battery will need 20 hours to completely discharge and with a 4C rate the battery will discharge in 15 minutes. The testing of the material is usually carried out in a coin cell type configuration, shown in Figure 2.8.

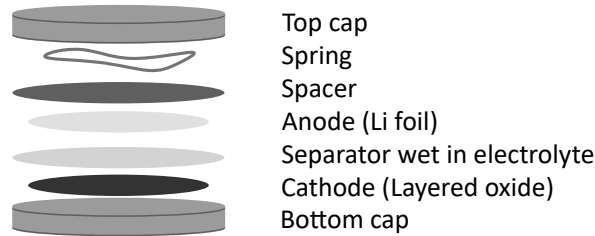


Fig. 2.8 Schematic configuration of a coin cell.

An example of a charge-discharge voltage profile of a typical cycle (in this case corresponding to  $\text{Li}_{1.2}\text{Mn}_{0.6}\text{Ni}_{0.2}\text{O}_2$ ) is shown in Figure 2.9a. In this plot the variation of the capacity versus the voltage is observed and the electrochemical processes occurring upon the cycling can be identified. Broadly speaking, a plateau indicates a two phase reaction in the lithium removal/insertion process, while a constant capacity delivery is related with a solid solution reaction. Figure 2.9b shows the evolution of the capacity versus the number of cycles, as well as the Coulombic efficiency, which is the ratio between the capacity in the charge/discharge process. This type of plot is good to follow the capacity fading of the material upon cycling, but the voltage fading or hysteresis cannot be identified. Finally, Figure 2.9c shows the differential capacity plot, which follows the evolution of the capacity increase as a function of the voltage. Even if this plot contains similar information to that in Figure 2.9a, the processes are more easily identified in these plots and the possible hysteresis or voltage fading are more accurately found. In contrast, this plot does not allow to follow the total capacity delivered by the material.

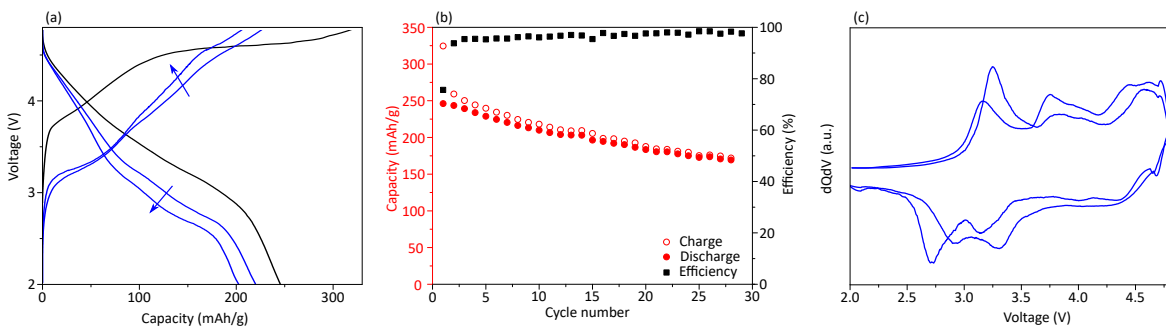


Fig. 2.9 (a) Variation of the voltage with respect to the capacity of  $\text{Li}_{1.2}\text{Mn}_{0.6}\text{Ni}_{0.2}\text{O}_2$ . Cycles 1 (in black), 5 and 20 are shown. (b) Evolution of the charge and discharge capacity in function of the number of cycles, as well as their Coulombic efficiency. (c)  $dQ/dV$  voltage profile of the cycles 5 and 20 in (a).

Unless the contrary is specified, the cathode material has been laminated in an aluminum foil with a 80:10:10 active material:Kejten carbon:polyvinylidene fluoride (PVDF) mass ratio. The electrochemical measurements were carried out in half-cell configuration using CR2032-type coin cells assembled in an argon-filled glovebox. A glass fiber separator was soaked with the electrolyte consisting in a solution of 1.2 M  $\text{LiPF}_6$  in ethylene carbonate (EC) and ethyl methyl carbonate (EMC) (3:7 in volume) with 5 wt% of 1-fluoroethylene carbonate (FEC) and 0.5 wt% of lithium bis(ethanedioato)borate (LiBOB) as additives. This formulation was developed and optimized in a former work dealing with lithium rich oxides. [201] Lithium foil was used as reference and counter electrode. The cycling window was of 2-4.8 V, unless the contrary is specified. The charging rate of the battery was C/10. All the electrochemical tests were carried out at room temperature and at least two cells were built for each sample to ensure reproducibility. On the other hand, *operando* X-ray electrochemical experiments were performed at 11 ID-B at APS in a AMPIX cell configuration. [2] The active material was a pellet composed of 60:20:10:10 of active material:polytetrafluoroethylene (PTFE):acetylene black:graphite. The electrolyte used was 1 M  $\text{LiPF}_6$  in EC:DMC (1:1 in volume). The anode was composed of a 100  $\mu\text{m}$  thick lithium foil and the cycling window was 2.5-4.8 V. The experiment was carried out in a C/10 rate.



## Chapter 3

# Microstructural impact study in electrochemistry of $\text{Li}_2\text{MnO}_3$ through synthetic control

*Crystals are like people: it is the defects in them which tend to make them interesting!*

**Collin Humphreys** [202]

The microstructural complexity of Li-rich cathode materials has so far hampered understanding the critical link between size, morphology and structural defects with both capacity and voltage fading that this family of materials exhibits.  $\text{Li}_2\text{MnO}_3$  is used here as a model material to extract reliable structure-electrochemical performance relationships that can be further exploited for the development of high-performing and long-lasting Li-rich oxides. A series of samples with microstructural variability have been prepared and thoroughly characterized using the FAULTS software, which, together with TEM results, has allowed rationalizing the synthesis conditions and identifying the individual impact of concurrent microstructural features on both voltage and capacity fading.

### 3.1 Introduction

As mentioned in Section 1.2.3, lithium rich materials suffer from a fast voltage and capacity fading due to the transition metal migration to the lithium layer and oxygen evolution.  $\text{Li}_2\text{MnO}_3$ , the end member of the lithium rich family, is known to exhibit poor electrochemistry in comparison with other family members. However, it can be used as a model for better understanding the complex structure of these materials, that often contains an important amount of stacking faults. The presence of stacking faults in  $\text{Li}_2\text{MnO}_3$  is highly dependent on the synthesis temperature. Low synthesis temperatures generally form phases with a large amount of stacking faults. [71] Particle size is as well temperature dependent and small particles are obtained at low synthesis temperature. [78, 105] Regarding that the performance of  $\text{Li}_2\text{MnO}_3$  is highly size-dependent and nanosizing is required to achieve high capacities, samples with small crystallite size and thus, high degree of stacking faults have been selected as best for electrochemistry. [78] Nevertheless, the individual effect of the size and the degree of stacking faults has not been uncoupled yet.

Stacking faults result from a  $\pm 1/3$  displacement of the mixed Li/Mn layer along  $b$  axis in the  $C2/m$  unit cell, which causes a misalignment of the cationic ordering. Figure 3.1 shows the three possible stacking arrangements the material can have, which are labeled following the previous works of Abraham's group. [3, 4] The rectangular (R) stacking refers to manganese dumbbells stacked on top of each other (ideal structure), whereas the parallelogram terms P and P' indicate layer displacements. Stacking faults have been detected with different techniques such as HRTEM, [3, 4, 7, 71, 203, 204] XRD [70, 205, 206] or ssNMR. [70] As we have seen in Section 2.2.3.2, the anisotropic peak broadening (mainly in the  $2\theta_{Cu} \leq 20\text{-}35^\circ$  range) in the XRD pattern coming from the effect of the stacking faults is not properly described when using the Rietveld method and alternative methods are required to extract the whole information the diffractogram can provide. Thanks to FAULTS program, developed in our group, [162–164] the degree of stacking faults can be now quantified from XRD patterns. [93, 205, 207] Shunmugasundaram *et al.* [207] used this program to study the effect of nickel in the stacking disorder of  $\text{Li}[\text{Li}_{1/3-2x/3}\text{Ni}_x\text{Mn}_{2/3-x/3}]\text{O}_2$  compounds and demonstrated that there is an increment in the number of stacking faults when the Ni content is increased. In a different study, Matsunaga *et al.* [208] showed that Li-rich compounds mostly exhibit stacking faults related to the honeycomb cationic ordering (i.e. the stacking faults denoted with R, P and P'), with less than 1% of the defects related to the oxygen sublattice. However, neither the correlations between synthesis parameters and amount of defects, nor the individual impact of stacking faults on the capacity and cycling performance decoupled from size and morphology effects were studied for this system in previous works.

In this chapter the effect of the different microstructural parameters in the electrochemical performance is studied.

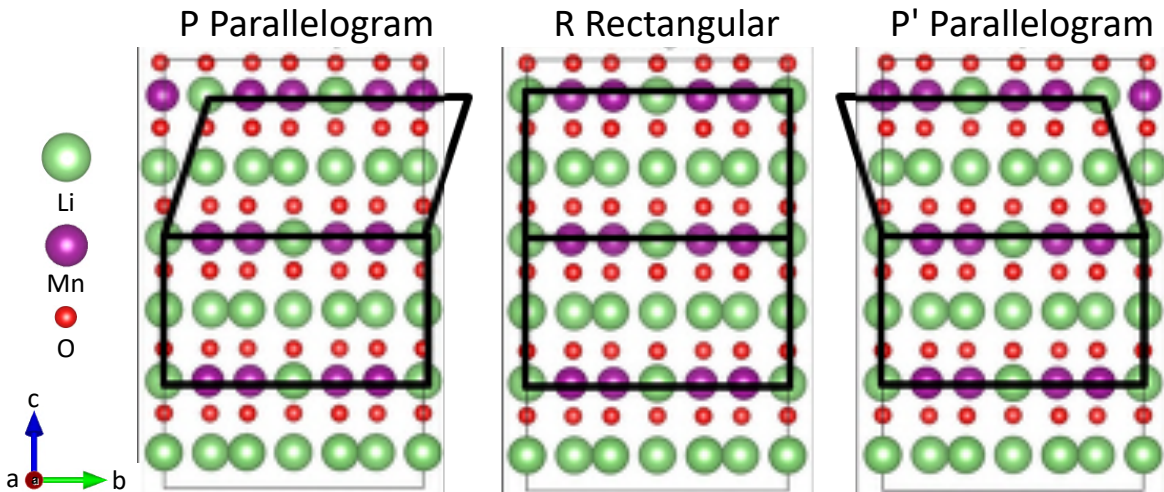


Fig. 3.1 Structural deviations arising from stacking faults in  $\text{Li}_2\text{MnO}_3$ , according to Abraham's notation. [3, 4]

## 3.2 Synthesis and structural characterization

A series of  $\text{Li}_2\text{MnO}_3$  samples have been synthesized by solid state reaction as described in Section 2.1, varying time, temperature and initial manganese precursor. Previous works analyzed the effect of lithium precursor on the degree of stacking faults and no variations were noticed from using  $\text{LiOH}$  or  $\text{Li}_2\text{CO}_3$ . [71] In view of these results and in order to avoid the complications derived from the hygroscopic nature of  $\text{LiOH}$  (which can lead to stoichiometrical variability),  $\text{Li}_2\text{CO}_3$  has been used in this work.

The XRD pattern of the product obtained after the first calcination step (5 hours at  $500\text{ }^\circ\text{C}$ ) for each precursor is shown in Figure 3.2. When using  $\text{MnCO}_3$ ,  $\text{Li}_2\text{MnO}_3$  is already obtained as main product, although there are some impurities whose main peaks are marked with an asterisk (Figure 3.2a).  $\text{MnCO}_3$  decomposes before melting at around  $200\text{ }^\circ\text{C}$  [209, 210] and this decomposition decreases its crystallite size, increasing contact between crystallites and thus, the reaction rate. [211] As a consequence, even at low temperatures,  $\text{Li}_2\text{MnO}_3$  is obtained as main product. When  $\text{Mn}_2\text{O}_3$  is used as manganese precursor (Figure 3.2b), the main product obtained is also  $\text{Li}_2\text{MnO}_3$  with small impurities. Contrary to the previous case,  $\text{Mn}_2\text{O}_3$  does not decompose so the crystallite size of the reactants is not reduced. As a consequence, the crystallite size of the products is larger, as it can be deduced from the thinner

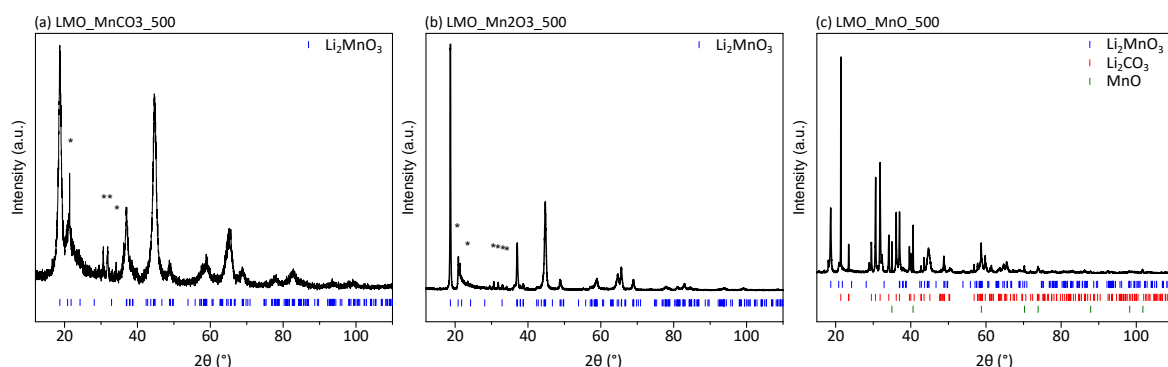


Fig. 3.2 XRD patterns of first calcination step at 500 °C of the sample synthesized with (a)  $\text{MnCO}_3$ , (b)  $\text{Mn}_2\text{O}_3$  and (c)  $\text{MnO}$ .

peaks in the XRD pattern. Finally, when  $\text{MnO}$  is used as manganese source the behavior is different (Figure 3.2c). After the first calcination step  $\text{Li}_2\text{MnO}_3$  has barely formed, and the precursors still appear in significant amount. Note that according to Tamman's rule, for a solid state reaction to take place the temperature should be at least  $2/3$  of the melting point of the reactants. [209]  $\text{Li}_2\text{CO}_3$  barely exceeds this point (1080 °C, 87%) and  $\text{MnO}$  is far from this ratio (1945 °C, 33%). Therefore, the high melting point of both precursors slows down the reaction rate.

Figure 3.3 gathers the XRD patterns for all the synthesized samples after the second calcination step classified by manganese precursor (a-c for  $\text{MnCO}_3$ , d-f for  $\text{Mn}_2\text{O}_3$  and g-i for  $\text{MnO}$ ). The full XRD pattern is shown in the left part, a zoom of the superstructure peaks is shown in the middle part and the right side shows only the  $(001)_m$  peak, whose width can be qualitatively used to evaluate the size of the crystallites as this reflection is not affected by stacking faults. Note that for an easier visualization, only the samples calcined 20 hours are shown in the latter case. From this figure, the following observations can be made:

- All the synthesized samples were pure, except sample LMO\_MnO\_700\_5. In this case, as reaction kinetics are slow, longer reaction times are needed.
- Higher synthesis temperatures form samples with larger crystallite size due to the coalescence of the crystallites (Figure 3.3c,f,i). The largest crystallite size variation is obtained when  $\text{MnCO}_3$  is used as precursor.
- When  $\text{MnO}$  is used as precursor, all the pure samples present well defined superstructure peaks which indicate that these samples exhibit a low amount of stacking faults (Figure 3.3h). These superstructure peaks become more intense when increasing the synthesis temperature and time.

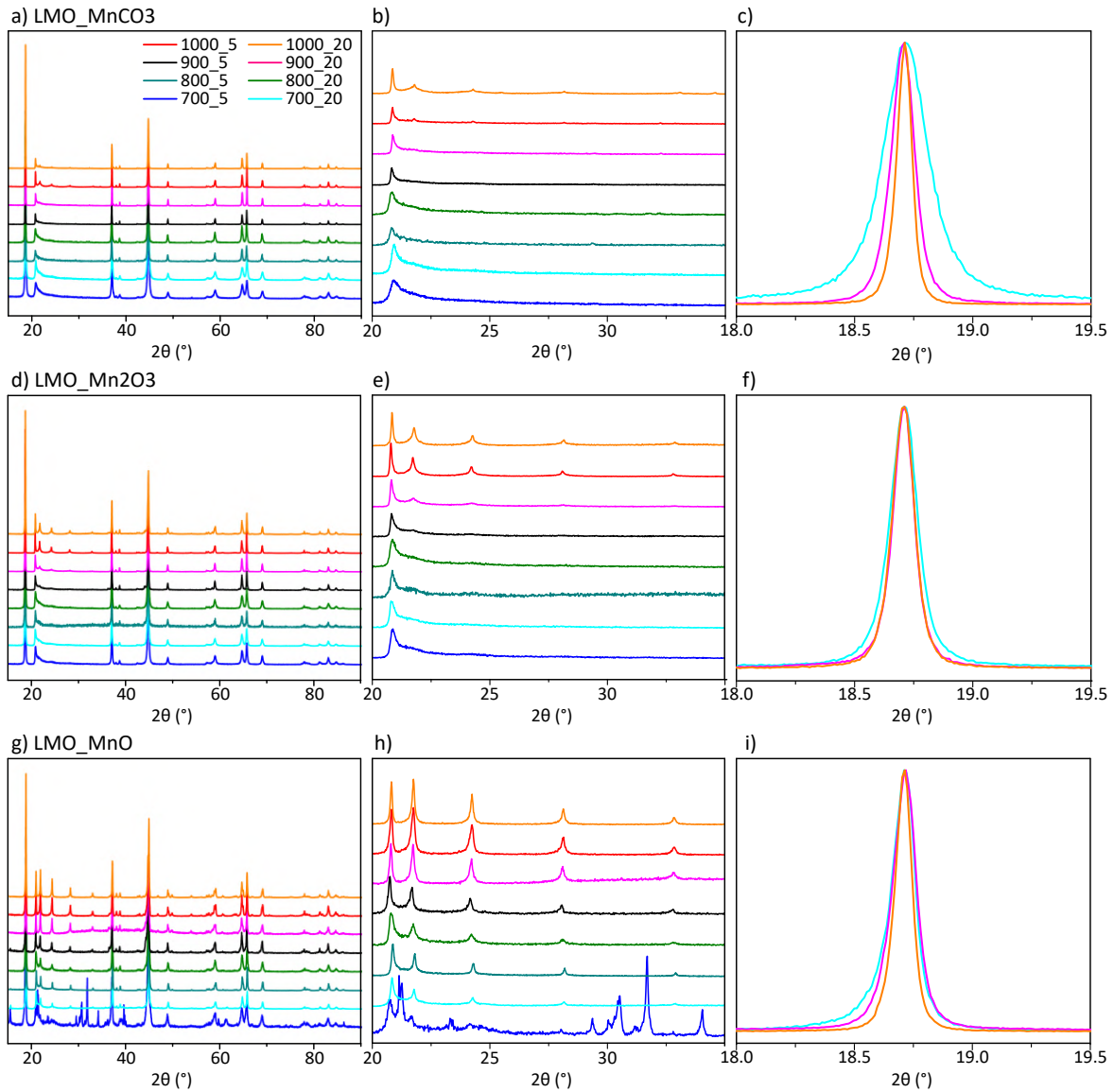


Fig. 3.3 XRD patterns of  $\text{Li}_2\text{MnO}_3$  synthesized in a temperature range of 700-1000 °C for 5 or 20 hours. The samples have been synthesized with (a-c)  $\text{MnCO}_3$ , (d-f)  $\text{Mn}_2\text{O}_3$  and (g-i)  $\text{MnO}$  precursors. The first column shows the whole XRD pattern, the second one shows a zoom of the  $2\theta$  range 20-35°, where the superstructure peaks appear and the third shows a zoom of the  $(001)_m$  peak.

- When  $\text{Mn}_2\text{O}_3$  or  $\text{MnCO}_3$  are used as precursor, the synthesis at low temperature results in samples with a high concentration of stacking faults as no superstructure peaks are visible (Figure 3.3b,e). For the first case, superstructure peaks begin to appear at 900 °C for 20 hours or higher temperatures, while for the second 1000 °C are needed. Longer annealing times are not sufficient to reduce the amount of defects when the

temperature is not high enough. Once a threshold temperature is reached, annealing time leads to the growth of defect-free domains.

The notable difference in the degree of stacking faults obtained when using MnO as precursor can be rationalized looking at the structures of each precursor. MnO crystallizes in a NaCl-type  $Fm\bar{3}m$  space group so it shares the oxygen skeleton with  $\text{Li}_2\text{MnO}_3$ . As a consequence, we propose a topotactic reaction (chemical solid-state reaction such that the orientations of the product crystals are determined by the orientation of the initial crystal) [212] where lithium replaces manganese, maintaining the NaCl-type array. On the contrary, the structure of  $\text{Mn}_2\text{O}_3$  and  $\text{MnCO}_3$  are not NaCl-like so the reaction involves a major structural modification.

### 3.3 Electron Microscopy analysis of $\text{Li}_2\text{MnO}_3$

SEM was used to investigate the effect of both Mn precursor and the annealing temperature on the particle size and shape. To do that, the samples synthesized for 5 hours were selected, with the exception of LMO\_MnO\_700\_20, as after for 5 hours the sample still had a great amount of impurities. Figure 3.4a-c shows SEM images of the samples synthesized from the  $\text{MnCO}_3$  precursor. In all cases, isotropic particles are observed, with increasing size as a function of temperature. When using  $\text{Mn}_2\text{O}_3$  and MnO precursors (Figure 3.4d-i) platelets are obtained which grow as a function of temperature. For all cases, higher synthesis temperatures induce a larger particle size. Therefore, the synthesis temperature has a major impact on the particle size, while the nature of the manganese precursor affects the particle shape.

Table 3.1 shows the average aspect ratio (height/width) of the samples analyzed, which have been measured from SEM images using a representative amount of random particles (between 20-40 particles). The aspect ratio is a value that ranges between 0 (planar limit) and 1 (isotropic limit). The particles obtained using  $\text{MnCO}_3$  as precursor have an aspect ratio around 0.7, which corresponds to rather isotropic particles, and does not vary regardless of the synthesis temperature.  $\text{Mn}_2\text{O}_3$  and MnO form particles with low aspect ratio and therefore, platelet shape. In both cases, high temperatures result in increasing aspect ratio and this is considerably more noticeable for MnO.

Two samples prepared at same temperature with equal annealing time were selected to explore the local distribution of stacking faults within the particles by TEM, one with a high concentration of stacking faults (LMO\_MnCO3\_900\_5) and a second one with a low (LMO\_MnO\_900\_5) concentration. The Mn:O ratio of both samples was investigated by EDS and their nominal composition was confirmed.

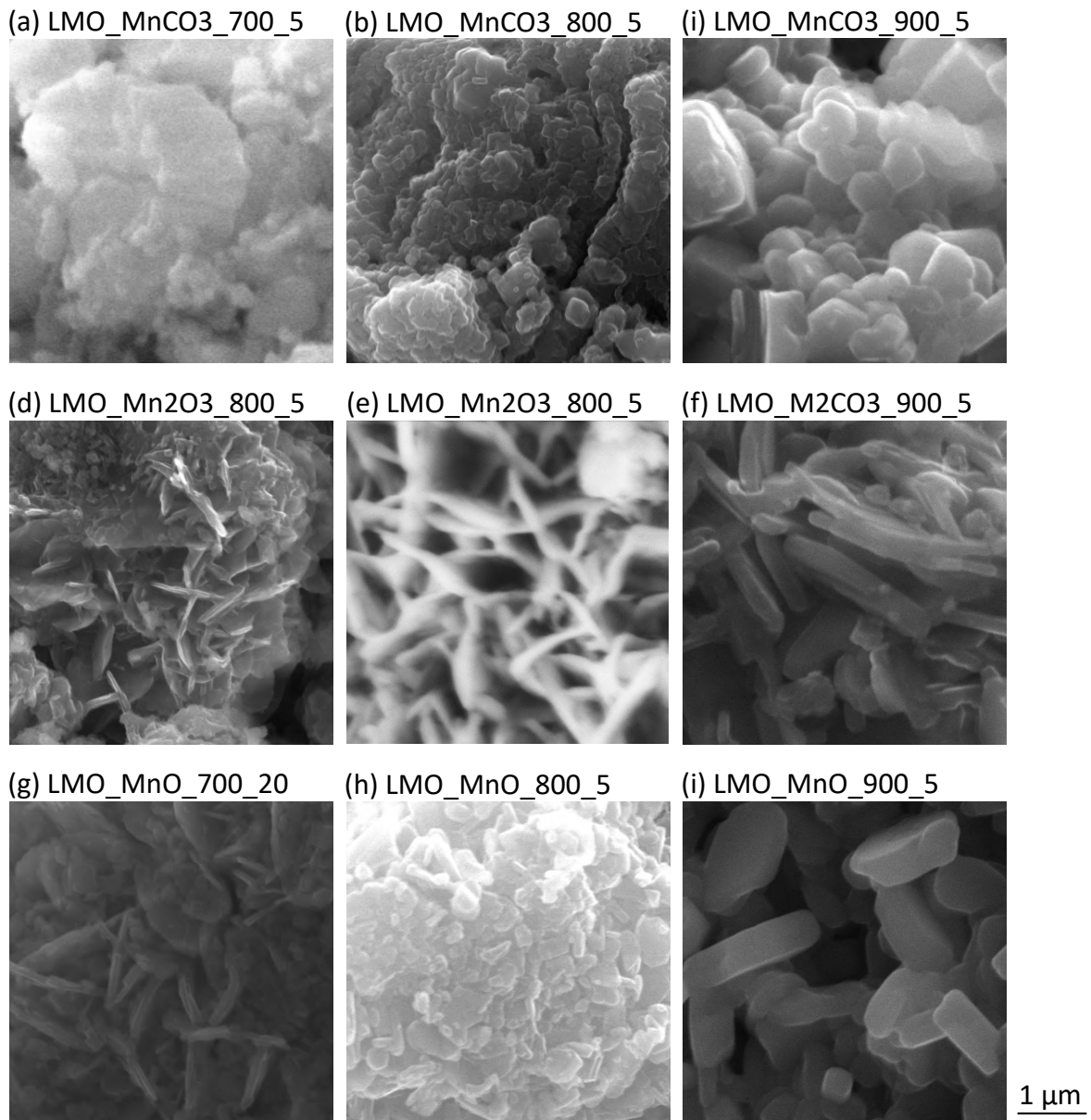


Fig. 3.4 SEM images of samples synthesized at 700, 800 and 900 °C with (a-c)  $\text{MnCO}_3$ , (d-f)  $\text{Mn}_2\text{O}_3$  and (g-i)  $\text{MnO}$  precursors.

For both samples, SAED patterns were acquired along the  $[001]$  zone axis and were indexed with the  $C2/m$  monoclinic cell, which is typically used to describe  $\text{Li}_2\text{MnO}_3$ . As we can see in Figure 3.5, all particles characterized by SAED showed evidence of Li/Mn ordering in the TM slabs through the presence of weak superstructure reflections and/or diffuse scattering lines parallel to the  $[001]^*$  direction marked with white arrows, in agreement with literature. [3, 71, 204, 206] Figure 3.5a-c presents the SAED patterns for LMO\_MnO\_900\_5 along the  $\langle 110 \rangle_m$  zone axis. All of them present diffuse lines that evidence the existence of

Table 3.1 Average aspect ratio (height/width) of measured samples.

Precursor	700 °C	800 °C	900 °C
$\text{MnCO}_3$	0.70	0.73	0.65
$\text{Mn}_2\text{O}_3$	0.10	0.20	0.33
$\text{MnO}$	0.01	0.22	0.43

a considerable amount of stacking faults in the material along the  $c$ -axis (i.e. the stacking direction). However, different kind of SAED patterns have been observed: i) some SAED patterns show sharp weak superstructure reflections, which can be unambiguously indexed either as the  $\langle 110 \rangle$  zone axis (Figure 3.5a) or as the  $[100]$  zone axis (not shown) and correspond to the least defective zones; ii) other SAED patterns corresponding to regions with an intermediate degree of defects (Figure 3.5b) show that both sharp weak reflections

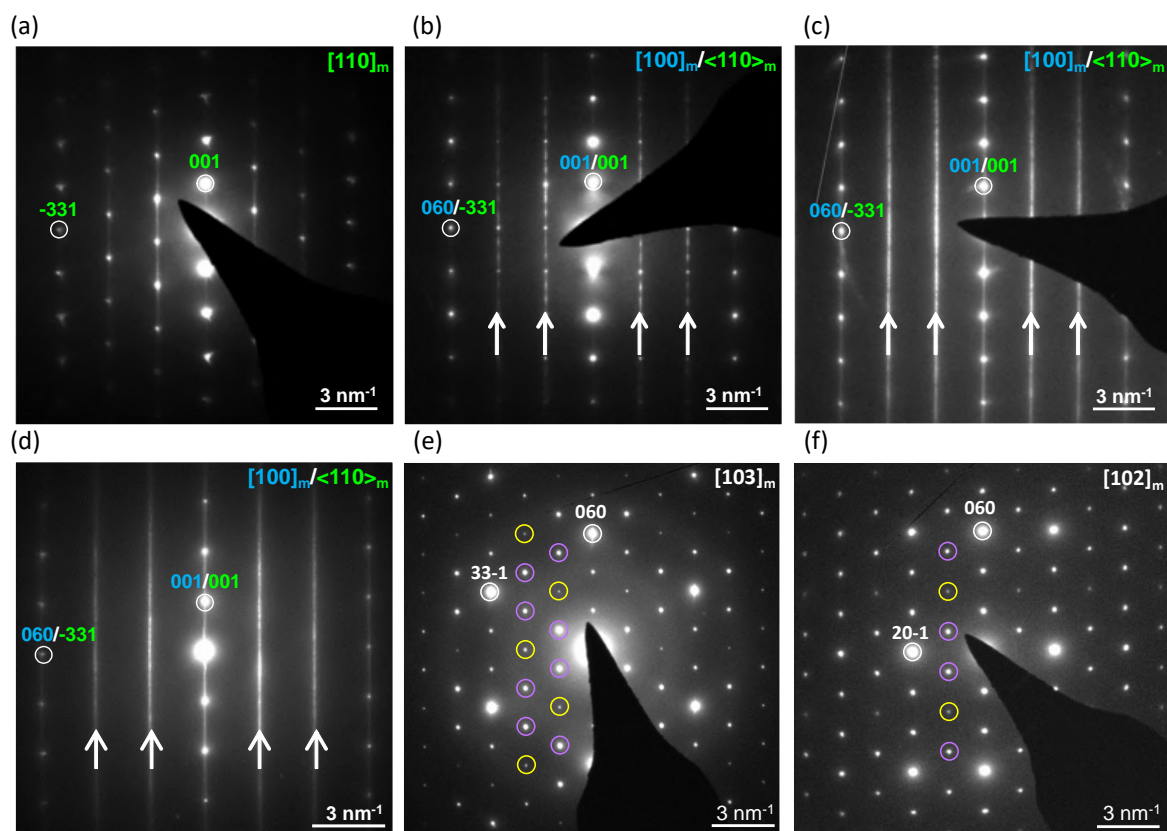


Fig. 3.5 Representative SAED patterns from crystals of sample (a-c) LMO\_MnO\_900\_5 ( $[100]_m$  or  $\langle 110 \rangle_m$  zone axes), (d) LMO\_MnCO3\_900\_5 ( $[100]_m$  or  $\langle 110 \rangle_m$  zone axes), (e,f) LMO\_MnO\_900\_5 ( $[103]_m$  and  $[102]_m$  zone axes). Purple circles are reflections resulting from the interception of diffuse scattering lines, while yellow ones result from double diffraction.



and more diffuse reflections, which can be indexed in the [100] and  $\langle 110 \rangle$  zone axis; iii) finally other SAED patterns corresponding to highly defective regions (Figure 3.5c) show that continuous diffuse scattering lines instead of weak superstructure reflections, hampering a straightforward distinction between the [100] and the  $\langle 110 \rangle$  zone axes. These three kind of patterns can be observed within a single crystal by moving to different regions, indicating that the amount of stacking faults varies significantly within the same particle. For the LMO\_MnCO<sub>3</sub>\_900\_5 sample the distribution of defects is more homogeneous (Figure 3.5d), since all the SAED patterns indexed along the [100] or  $\langle 110 \rangle$  zone axes were similar and showed intense diffuse lines comparable to Figure 3.5c, evidencing a high amount of stacking faults thorough all the particle. Besides the presence of these diffuse lines, SAED patterns acquired along the [102] and [103] zone axes shown in Figure 3.5e,f (which are representative for both samples) also show additional weak reflections that are not consistent with the  $C2/m$  monoclinic cell. These extra reflections can be explained as the intersection of diffuse scattering lines with Ewald's sphere, as previously shown by *Boulineau et al.* and *Weill et al.* [204, 213]

In order to get further insight in the distribution of stacking faults within the particles, HR-STEM and HAADF-STEM images from different regions of samples LMO\_MnO\_900\_5 and LMO\_MnCO<sub>3</sub>\_900\_5 were acquired. In accordance with SEM observations, the LMO\_MnO\_900\_5 particles analyzed had platelet shape as shown in Figure 3.6a, while the LMO\_MnCO<sub>3</sub>\_900\_5 particles, shown in Figure 3.6b, had a more isotropic size. Figure 3.6c shows a HAADF-STEM image of the  $[001]_m$  zone axis, representative for both analyzed samples. As described in Section 2.3, in this imaging mode the intensity of the images is proportional to the atomic number  $Z^n$  ( $1.6 < n < 2$ ), [214] meaning that the columns of heavier atoms will look brighter in the projection images compared to those of lighter elements. The  $[001]_m$  zone axis of a hypothetical ideal structure would be composed of diffraction spots forming hexagons with an empty space in the middle (the location of the lithium in the ideal stacking), as seen in the inset of the Figure 3.6c and experimentally observed by *Lei et al.* in a defect free sample. [3] In our case, no empty spaces were found as a consequence of the presence of sacking faults, in accordance with other studies. [215]

Finally, in Figure 3.6d,e HAADF-STEM images oriented along the [100] or  $\langle 110 \rangle$  zone axes are presented. The Mn atomic columns are arranged in a dumbbell geometry along the direction perpendicular to the  $c$ -axis, and each Mn-Mn pair is separated by a column of Li atoms, which cannot be observed here because its atomic number is very low. Large defect-free areas such as those in Figure 3.6d and areas with high stacking fault concentration such as those in Figure 3.6e appear in the same particle for sample LMO\_MnO\_900\_5 (the stacking sequence can be visually followed with the red lines in the figures). For

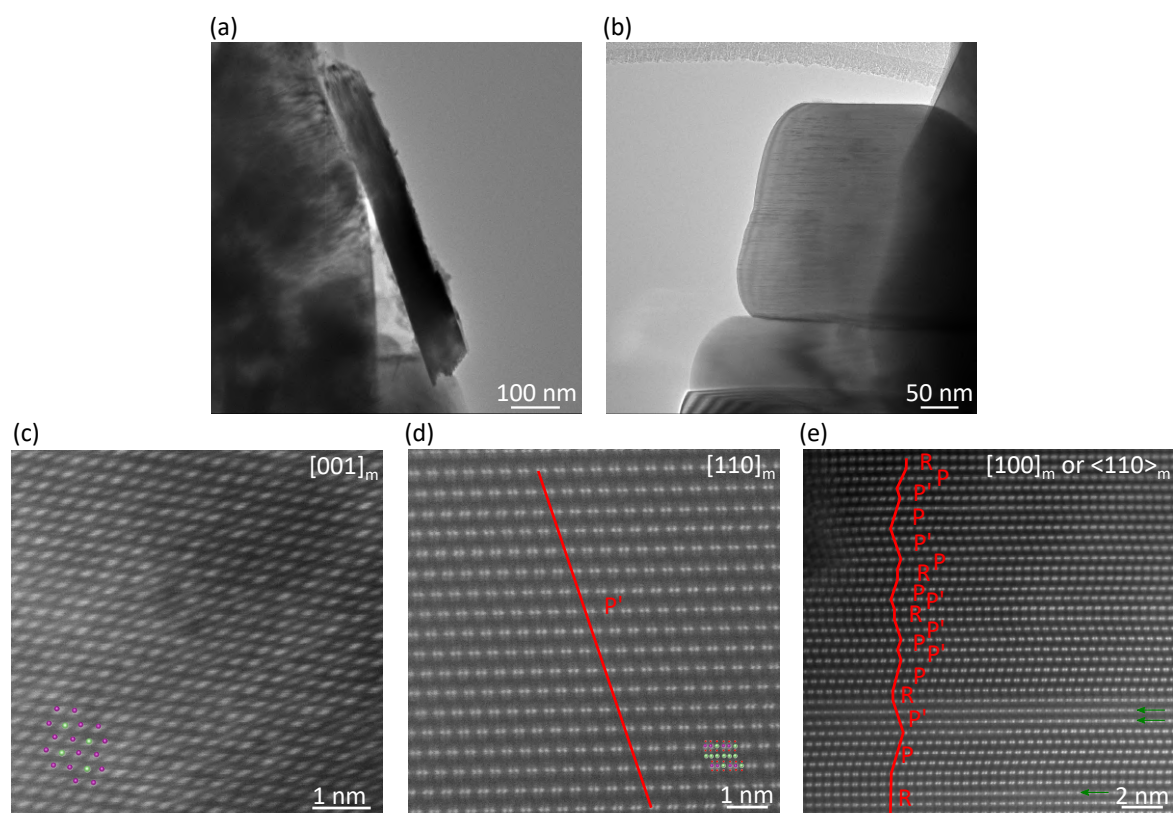


Fig. 3.6 HR-STEM images of (a) LMO\_MnO\_900\_5 and (b) LMO\_MnCO<sub>3</sub>\_900\_5 samples. HAADF-STEM images of LMO\_MnO\_900\_5 (c)  $[001]_m$  and (d,e)  $[100]_m$  or  $\langle 110 \rangle_m$  zone axes. The insets represent the atomic positions of lithium, manganese and oxygen atoms. The red lines are guides to follow the stacking direction, which are labeled with R, P and P' according to Abraham's notation. [3, 4]

LMO\_MnCO<sub>3</sub>\_900\_5, on the contrary, only zones with a high concentration of stacking faults have been found. Besides these features, some isolated rows of Mn defects within some TM slabs could be observed (Figure 3.6e), indicated with green arrows. The sequence Mn dumbbell-blank-Mn dumbbell is lost, and replaced by a sequence of the type 1 Mn column-2 grey columns-1 Mn column. This may be the result of either the loss of the honeycomb ordering within the TM layer (i.e. cation mixing), or twinning and antiphase defects within the TM layers with two different orientations of the honeycomb ordering in the same TM layer. [71, 216]

### 3.4 FAULTS refinements of XRD data

In order to extract quantitative information regarding the amount of stacking faults and average crystallite sizes in the studied samples, the X-ray patterns were refined using the FAULTS

program. The FAULTS model was built using a  $P\bar{1}$  unit cell instead of the conventional  $C2/m$  cell typically used to describe  $\text{Li}_2\text{MnO}_3$ , as in the  $P\bar{1}$  cell a lower number of atoms are required to describe the structure. Starting from the conventional  $C2/m$  unit cell (Figure 3.7a), whose unit cell parameters are taken from bibliography ( $a = 4.9292 \text{ \AA}$ ,  $b = 8.5315 \text{ \AA}$ ,  $c = 5.0251 \text{ \AA}$  and  $\beta = 109.337^\circ$ ), [204] the transformation matrix shown in Matrix 3.1 is applied to form the smaller unit cell shown in Figure 3.7b.

$$\begin{pmatrix} 0.5 & 0.5 & 0 \\ -0.5 & 0.5 & 0 \\ 0 & 0 & 1 \end{pmatrix} \quad (3.1)$$

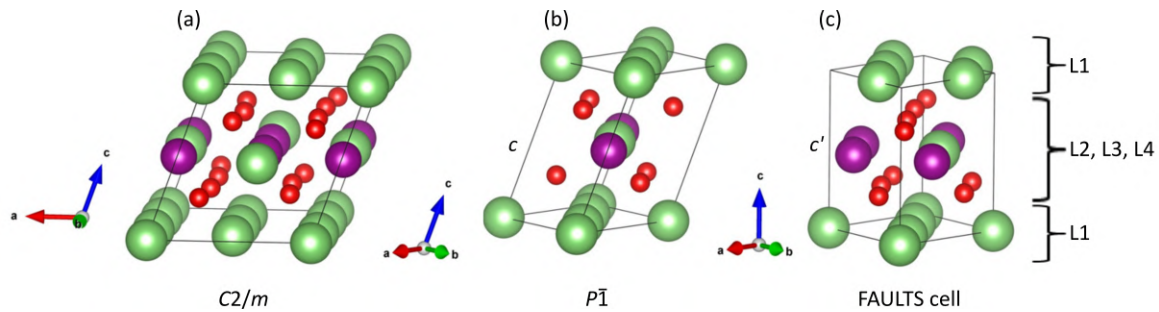


Fig. 3.7 Comparison of (a) the  $C2/m$  unit cell used in conventional Rietveld refinements to describe the non-defective structure of  $\text{Li}_2\text{MnO}_3$ , (b) the smaller equivalent  $P\bar{1}$  unit cell, and (c) the FAULTS cell used to define the layers to be stacked for the FAULTS refinements.

This new  $P\bar{1}$  unit cell (Figure 3.7b) has the following cell parameters:  $a = b = 4.9265 \text{ \AA}$ ,  $c = 5.0251 \text{ \AA}$ ,  $\alpha = 80.465^\circ$ ,  $\beta = 73.099^\circ$  and  $\gamma = 60.036^\circ$ . Nevertheless, as in FAULTS the stacking direction is by definition perpendicular to  $ab$  plane, this new cell needs to be transformed and the  $c$  axis must be redefined. The norm of this new axis vector is set to  $c' = 4.7416 \text{ \AA}$  (Figure 3.7c). From this FAULTS cell, two types of layers were defined: L1 constituted by the lithium atoms of the Li slabs (lithium layer), and L2 containing lithium, manganese and oxygen atoms (TM layer). Stacking faults were generated using two extra layers in the FAULTS model: L3 and L4 that are equivalent to L2 but that are stacked with different stacking vectors in order to introduce stacking faults (P and P' stacking). From L1, solely transitions to L2, L3 and L4 are possible (and *vice versa*) and correspond to R, P and P' stacking possibilities, respectively. The ideal structure is thereby built with a  $L1 \rightarrow L2 \rightarrow L1$  stacking sequence, while P and P' correspond to  $L1 \rightarrow L3 \rightarrow L1$  and  $L1 \rightarrow L4 \rightarrow L1$  sequences.

Table 3.2 shows the initial structural parameters used to describe the structure in the FAULTS refinements of the XRD patterns, as well as the possible transitions vectors. Note that from the transition metal layer to the lithium layer the same transition vector is provided

for all the cases. As the lithium layer is composed of a single type of atom there is no need for additional vectors. Each transition vector is associated to a stacking probability, from which the degree of defects can be calculated. Figure 3.8 shows an example of the resulting defective structure using the transition vectors given in Table 3.2.

Table 3.2 Initial structural parameters used for the FAULTS refinements.

Layer composition						
Layer	Atom	x/a	y/b	z/c	Occ.	$B_{iso}$
L1	$\text{Li}^I$	0	0	0	1	1
	$\text{Li}^I$	1/3	1/3	0	1	1
	$\text{Li}^I$	2/3	2/3	0	1	1
L2, L3, L4	$\text{Li}^I$	0	0	0	1	1
	$\text{Mn}^{IV}$	1/3	1/3	0	1	1
	$\text{Mn}^{IV}$	2/3	2/3	0	1	1
	$\text{O}^{II-}$	0.340	0.000	0.225	1	1
	$\text{O}^{II-}$	0.660	0.000	-0.225	1	1
	$\text{O}^{II-}$	0.000	0.340	-0.225	1	1
	$\text{O}^{II-}$	0.340	0.660	-0.225	1	1
	$\text{O}^{II-}$	0.660	0.340	0.225	1	1
	$\text{O}^{II-}$	0.000	0.660	0.225	1	1
Transition vectors						
Transition	x/ a	y/ b	z/ c	Stacking type		
L1→L2	1/3	-1/3	1/2	R		
L1→L3	2/3	0	1/2	P		
L1→L4	0	-2/3	1/2	P'		
L2→L1	1/3	-1/3	1/2	-		
L3→L1	1/3	-1/3	1/2	-		
L4→L1	1/3	-1/3	1/2	-		

The following parameters were refined with FAULTS: scale factor unit, cell and profile parameters, stacking fault probabilities, atomic positions (except for lithium atoms) and Li/Mn exchange. Background was fitted with a linear interpolation of selected points and was manually refined. Thermal factors and atomic occupations were fixed to 1. Lithium vacancies are not considered in the refinement due to the low scattering factor of lithium in XRD. The XRD patterns of the samples synthesized from MnO were treated as two-phase mixtures to describe the particles as a combination of large defect-free and defective diffraction domains, in agreement with the high resolution HAADF-STEM observations. To do so, the ideal (defect-free) phase was simulated with the FullProf suite [159] and then included in the FAULTS refinement as a secondary phase. The scale of this secondary phase was refined in addition to the other parameters previously mentioned.



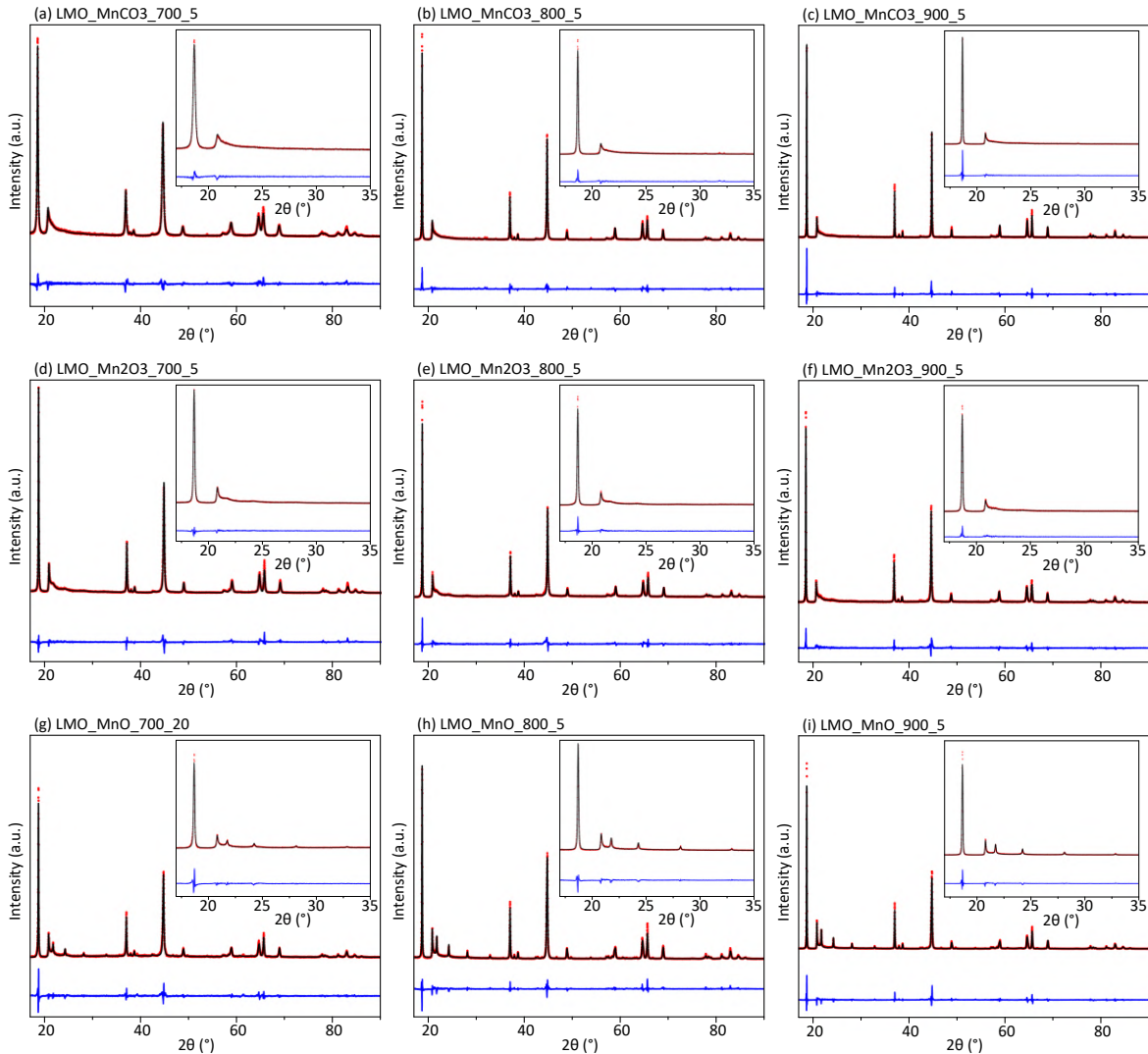


Fig. 3.9 FAULTS refinement for all the selected samples made with  $\text{MnCO}_3$ ,  $\text{Mn}_2\text{O}_3$  and  $\text{MnO}$  at 700, 800 and 900 °C.

$$D_{SF\_2Ph} = D_{SF} \cdot \frac{A_{SF}}{A_{SF} + A_{Id}} \quad (3.3)$$

where  $A_{SF}$  is the area of the subpattern with stacking faults and  $A_{Id}$  is the area of the ideal phase.

The evolution of both the degree of defects and the average crystallite size (calculated using the Scherrer formula) as a function of the synthesis temperature and the precursors used for each sample is represented in Figure 3.10.

From Figure 3.10a, the nature of the precursor has shown to have a stronger impact in stacking faults than the synthesis temperature. Irrespective of the temperature used,

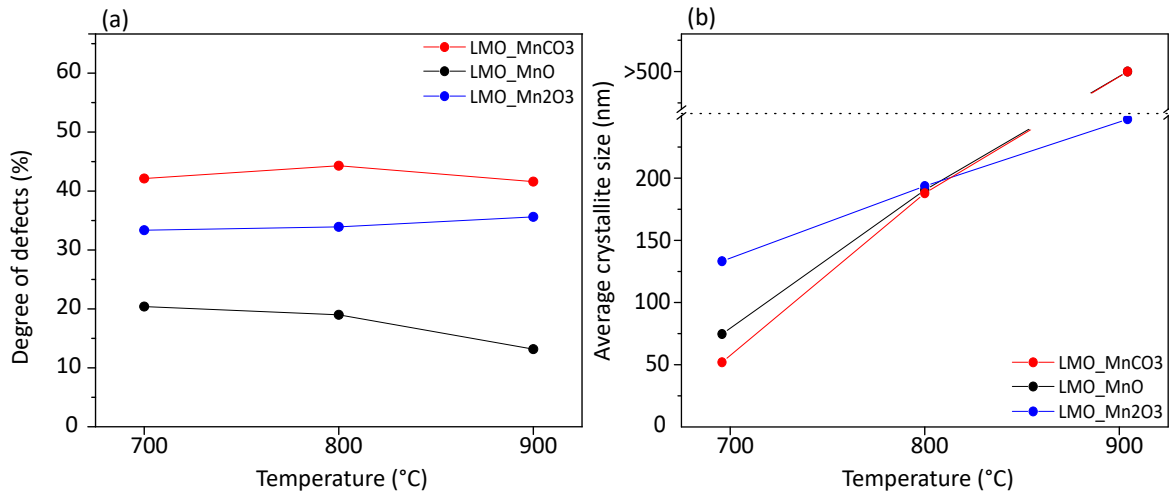


Fig. 3.10 Comparison of (a) degree of stacking faults and (b) average crystallite size of the selected samples as a function of temperature.

MnCO<sub>3</sub> leads to the largest amount of defects (41 to 45%) while MnO to the lowest amount (13 to 20%). Although the amount of defects is maintained with temperature when using MnCO<sub>3</sub> and Mn<sub>2</sub>O<sub>3</sub> as precursors, the amount of defects in samples prepared from MnO slowly decreases with increasing the temperature. FAULTS was also used to simulate the SAED patterns of the refined structures (Figure 3.11), which confirm that the refined amount of stacking faults in these samples is large enough to make the superstructure reflections disappear in favor of diffuse scattering lines as observed in the experimental SAED patterns (Figure 3.5a-d).

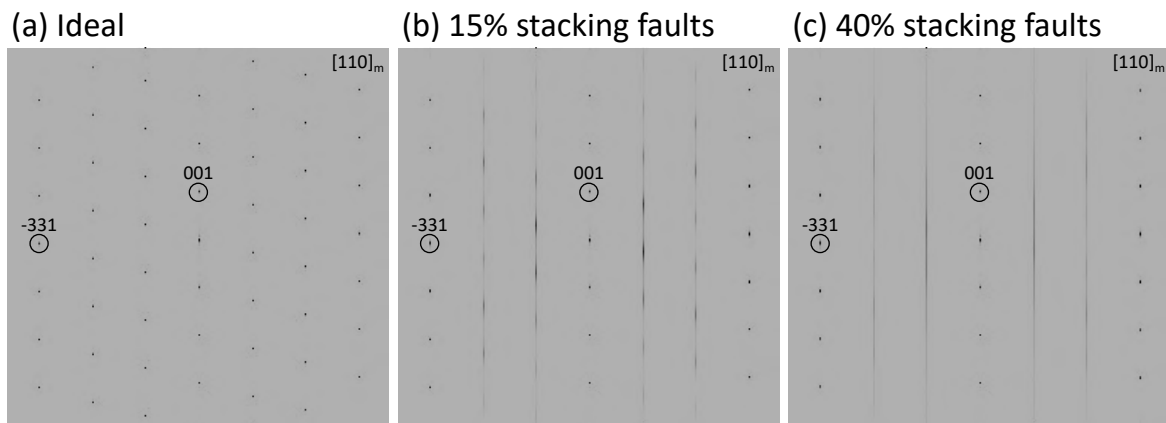


Fig. 3.11 SAED simulations for samples with (a) 0%, (b) 15% and (c) 40% of stacking faults. Simulation performed with FAULTS software.

Independently of the precursor used, the size of the crystallites increases with annealing temperature (Figure 3.10b). The sample synthesized from the MnCO<sub>3</sub> precursor at 700 °C

is the one exhibiting the smallest crystallite size; although the series of samples prepared from  $\text{MnCO}_3$  also shows a more rapid growth when the annealing temperature increases. Interestingly, all samples exhibit a very similar crystallite size at 800 °C, whereas at 900 °C size broadening of the XRD peaks is only appreciated for the sample prepared from  $\text{Mn}_2\text{O}_3$ , with a resulting size of 250 nm. At 900 °C, the size of the crystallites of the samples obtained from  $\text{MnO}$  and  $\text{MnCO}_3$  is indeed too large (>500 nm) to be precisely determined from diffraction data. Note that the average crystallite sizes calculated from FAULTS refinements are in good agreement with the particle sizes estimated from SEM images for all the samples.

The combination of electron microscopy and diffraction techniques allows to conclude that the choice of the Mn precursor has a strong impact on the amount of stacking faults and the morphology of the particles; while temperature dominates the size of the crystallites (although the Mn precursor used also partially contributes). Reaction time has an impact on the formation of the phase when the kinetics are slow (e.g. LMO\_MnO\_700 requires 20 h of annealing), but it is not critical on defect growth at synthesis temperatures below 900 °C. The results obtained in Sections 3.3 and 3.4 are summarized in Table 3.3.

Table 3.3 General summary of the microstructural properties for the selected samples.

Sample name	Degree of SF	Particle size	Particle shape
LMO_MnO_900	Low	High	Platelet
LMO_MnO_800	Low	medium	Platelet
LMO_MnO_700	Low	Medium-low	Platelet
LMO_Mn2O3_900	High	Medium-high	Platelet
LMO_Mn2O3_800	High	Medium	Platelet
LMO_Mn2O3_700	High	Medium-low	Platelet
LMO_MnCO3_900	High	High	Isotropic
LMO_MnCO3_800	High	Medium	Isotropic
LMO_MnCO3_700	High	Low	Isotropic

### 3.5 Electrochemical characterization

Galvanostatic experiments were performed on all the synthesized samples. Preliminary voltage window tests have shown that at 5 V the total capacity achieved is higher but the fading of the material is fast for all cases due to degradation of the electrolyte. As a consequence, the upper voltage cut-off is set to 4.8 V.

Figure 3.12a shows the effect of synthesis temperature on the capacity for samples prepared from  $\text{MnCO}_3$ . Since the degree of stacking faults is almost invariable with synthesis temperature and samples prepared from  $\text{MnCO}_3$  always exhibit a similar aspect ratio it can be



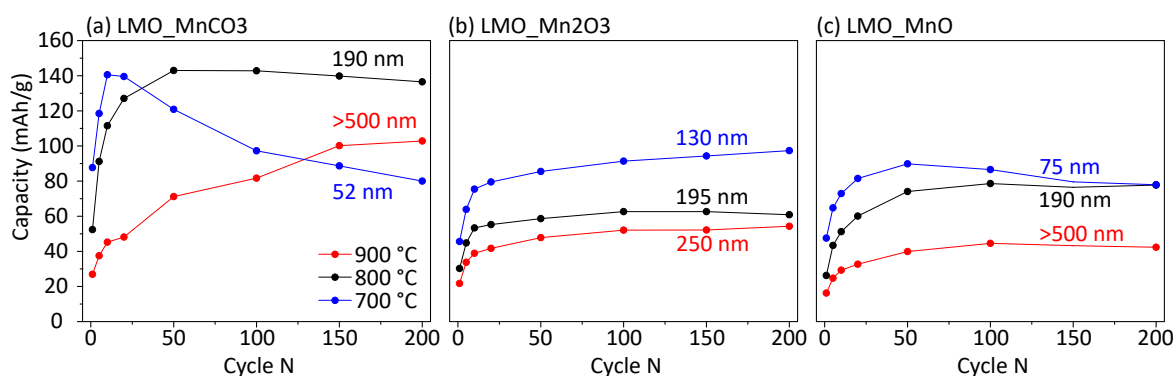


Fig. 3.12 Comparison of the capacity retention obtained for samples synthesized in a 700-900 °C with (a)  $\text{MnCO}_3$ , (b)  $\text{Mn}_2\text{O}_3$  and (c)  $\text{MnO}$  precursors. Results for cycles 1, 5, 10, 20, 50, 100, 150 and 200 are included. The average crystallite size is shown for each sample.

considered that the differences in capacity are a result of the different average crystallite size (indicated in the figure). Crystallites with size around 50 nm as determined from the FAULTS refinement achieve the maximum capacity in the first 10 cycles. However, the capacity drastically drops in subsequent cycles. On the contrary, for the sample exhibiting the largest crystallite size (in red), the activation is extremely slow: the maximum capacity is achieved after 200 cycles and still does not reach the same value as samples with lower crystallite size. However, when the crystallite size is around 200 nm, the compromise between fast activation and cycling stability is the best, reaching a stable capacity as high as that of the sample with the smallest crystallites around cycle 50. Figure 3.12b,c show the effect of the synthesis temperature on the samples synthesized with  $\text{Mn}_2\text{O}_3$  and  $\text{MnO}$  respectively. In general, in this size range (>500-75 nm), the lower the crystallite size, the better the electrochemical performance. Nevertheless, in this case, different aspect ratios and degree of stacking faults (for  $\text{MnO}$ ) are obtained and these can also play a role.

For the correlation of additional microstructural features, a comparison of the capacity of the samples synthesized at 800 °C will be considered, as they exhibit similar crystallite size (around 190 nm) but differ in morphology and degree of defects. By comparing the three samples distributed in Figure 3.12a-c (black lines) it can be seen that  $\text{LMO\_MnCO}_3\text{_{800\_5}}$  shows by far the best performance while  $\text{LMO\_Mn}_2\text{O}_3\text{_{800\_5}}$  and  $\text{LMO\_MnO\_800\_5}$  exhibit a much lower capacity. There is thus a clear correlation between the morphology of the particles and the capacity of the sample. The largest capacity is obtained with the sample with isotropic particles, having more available access points for the extraction/insertion of  $\text{Li}^+$  ions than platelet-shaped particles, and thus allowing to achieve a higher degree of activation. Interestingly, decoupling size and defects reveals that, contrary to previous reports, [71, 105] the degree of defects does not show a clear correlation with the capacity. If one compares

LMO\_Mn2O3\_800\_5 and LMO\_MnO\_800\_5 samples, which exhibit similar shape and size but different degree of stacking faults, the obtained capacity is similar with a slightly better behavior for the defective sample.

In order to assess the individual impact of microstructural features on the voltage fading,  $dQ/dV$  plots at cycles 10, 50 and 100 of the samples synthesized at  $800\text{ }^\circ\text{C}$  (and therefore with the same crystallite size) are compared in Figure 3.13. Several peaks are observed:

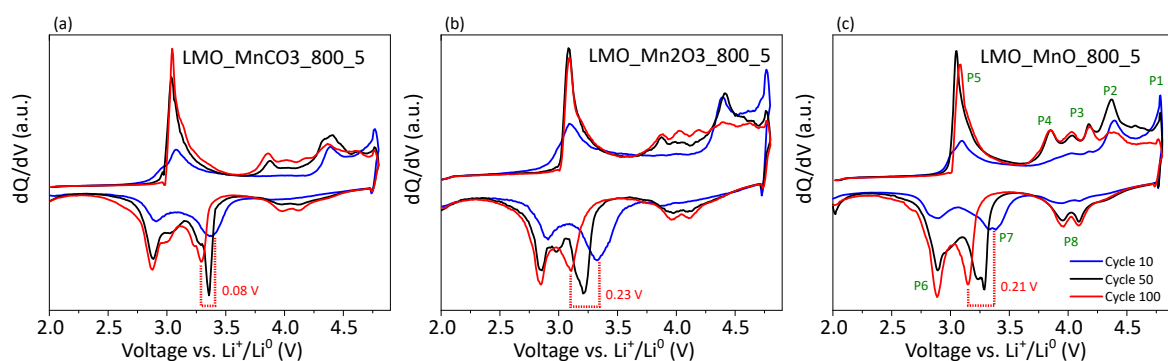


Fig. 3.13 Derivative curves  $dQ/dV$  of the  $10^{\text{th}}$ ,  $50^{\text{th}}$  and  $100^{\text{th}}$  galvanostatic cycles (blue, black and red lines, respectively) obtained for the samples synthesized at  $800\text{ }^\circ\text{C}$  from (a)  $\text{MnCO}_3$ , (b)  $\text{Mn}_2\text{O}_3$  and (c)  $\text{MnO}$  precursors. The positions of the different oxidation and reduction peaks are indicated in green in (c). The voltage difference of P7 between cycles 10 and 100 is highlighted with the red dashed line and the voltage difference is indicated.

- i) The activation peak at  $4.7\text{ V vs. Li}^1/\text{Li}^0$  (P1) that only appears at the early cycles and whose intensity decreases as the activation of the material is completed. This peak is attributed to structural rearrangement and  $\text{O}_2$  release, both at the surface and in the bulk, as well as to electrolyte oxidation. [73, 87, 218]
- ii) A peak at around  $4.3\text{ V vs. Li}^1/\text{Li}^0$  in charge (P2) whose equivalent in discharge appears with a hysteresis of  $\sim 1\text{ V}$  (P7 at  $\sim 3.3\text{ V vs. Li}^1/\text{Li}^0$ ). This peak is associated with oxygen redox activity and its hysteresis is thought to come from consecutive structural rearrangements caused either by transition metal rearrangement due to lithium removal [6, 219] or by oxygen network distortion due to oxygen redox activity. [220, 221]
- iii) A doublet of peaks at  $4.0\text{--}4.2\text{ V vs. Li}^1/\text{Li}^0$  in charge (P3) and  $3.9\text{--}4.1\text{ V vs. Li}^1/\text{Li}^0$  in discharge (P8). These peaks, not present in early cycles but visible in latter ones, are characteristic of  $\text{LiMn}_2\text{O}_4$  spinel. [40] Lithium migration to tetrahedral positions has been previously evidenced from solid-state NMR and *operando* XRD, which would be at the origin of this spinel phase formation. [222, 223]

- iv) A peak at 3.8 V vs.  $\text{Li}^{\text{I}}/\text{Li}^{\text{0}}$  in charge (P4) whose equivalent is found at 3.1 V vs.  $\text{Li}^{\text{I}}/\text{Li}^{\text{0}}$  in discharge, overlapping with P6 and P7. One can indeed see the appearance of a shoulder next to P6 between cycles 10 and 50, which is probably the equivalent of the P4 peak in discharge. This peak is possibly related to manganese redox activity.
- v) A peak at 3.0 V vs.  $\text{Li}^{\text{I}}/\text{Li}^{\text{0}}$  (P5) in charge and 2.9 V vs.  $\text{Li}^{\text{I}}/\text{Li}^{\text{0}}$  (P6) in discharge. This peak is the signature of lithium insertion in octahedral positions. [219] Even if this peak is characteristic for spinel phase [40, 140] it is already present at early stages, although the characteristic doublet for spinel at 4.0-4.2 V is not yet observed. Therefore, this peak could be the sum of two different peaks, one related with the aforementioned spinel material and the other with the activated  $\text{MnO}_2$ -like material. [218, 224, 225]

From the comparison of our set of samples, one can observe that the growth of the spinel doublet P3 is specially marked for the low-defect-containing sample (LMO\_MnO\_800\_5), while it is delayed for the more defective samples (LMO\_Mn2O3\_800\_5 and LMO\_MnCO3\_800\_5). For the three samples, this peak doublet progressively grows at similar rate, and it remains significantly lower after 50 cycles in the more defective samples (LMO\_Mn2O3\_800\_5 and LMO\_MnCO3\_800\_5). On the other hand, remarkable differences between the three samples are observed in the characteristic voltage fading occurring in  $\text{Li}_2\text{MnO}_3$ , which is primarily seen in the displacement of the discharge peak P7 at  $\sim 3.3$  V upon cycling (while the corresponding charge peak P2 appears at a constant potential of 4.3 V). This voltage fading, appreciated in the difference in P7 from cycle 10 to 100, marked with a red dashed line, is indeed smaller ( $\Delta V = 0.08$  V) for the sample with more defects and isotropic particles (LMO\_MnCO3\_800\_5) than for the others ( $\Delta V = 0.21$  and  $0.23$  V).

Figure 3.14 shows similar trends for samples synthesized at 700 and 900 °C for both the formation rate of spinel and the voltage fading, indicating that the particle size has no effect on those features and confirming the correlations previously described (except for LMO\_MnCO3\_700\_5, whose fast degradation modifies the shape of the plot). Thus, samples with a low degree of stacking faults convert faster to spinel and particles with isotropic shape have lower voltage fading upon cycling, regardless their crystallite size.

In view of these results, it can be concluded that the local environments created by stacking faults stabilize manganese in the TM sites while being less favorable for migration of Mn to lithium slabs, thus delaying the formation of spinel environments. All in all, through microstructural control we have found that  $\text{Li}_2\text{MnO}_3$  has best performance when its crystallite size is around 200 nm, when its particle shape is isotropic and when it contains a high degree of stacking faults.

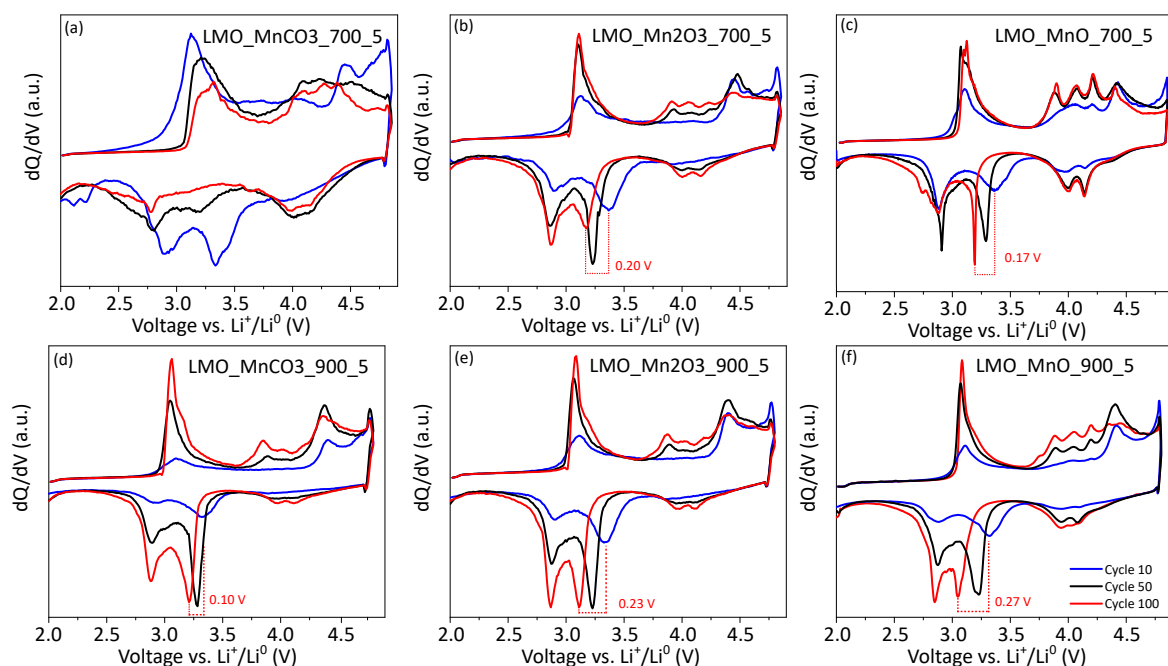


Fig. 3.14 Derivative curves  $dQ/dV$  of the 10<sup>th</sup>, 50<sup>th</sup> and 100<sup>th</sup> galvanostatic cycles (blue, black and red lines, respectively) obtained for the samples synthesized at 700 and 900 °C from  $\text{MnO}$ ,  $\text{Mn}_2\text{O}_3$  and  $\text{MnCO}_3$ . The voltage difference of P7 between cycles 10 and 100 is highlighted with the red dashed line and the voltage difference is indicated.

### 3.6 Conclusions

A set of  $\text{Li}_2\text{MnO}_3$  samples have been synthesized starting from different Mn precursors and using different temperatures. The samples obtained exhibit a large and reproducible microstructural diversity (in terms of size, morphology and amount of defects) which has allowed rationalizing synthesis conditions and decoupling the individual role of each microstructural feature in the electrochemical properties. The use of the FAULTS program has been key to extract quantitative correlations with crystallite size and amount of defects.

It has been found that synthesis temperature has a strong impact on crystallite size, while the Mn precursor allows tuning the particles shape and the amount of defects. HAADF-STEM images reveal that there are no preferential defective sequences and that stacking faults occur randomly. The structure of highly-defective samples (>30%) can indeed no longer be described with stacking faults but rather as a random stacking. While low-defect samples convert faster to the spinel phase, seriously affecting cycling stability, high capacities are achieved with the defective sample exhibiting spherical particles of around 200 nm.

In this study, we have demonstrated that electrochemical performances of  $\text{Li}_2\text{MnO}_3$  can be tuned by independent control of morphology, size and defects. Therefore, systematically

decoupling and quantifying microstructural features in Li-rich materials is essential to reach a complete understanding of these complex systems and govern their electrochemical performance.



## Chapter 4

# DFT-assisted ssNMR characterization of defects in $\text{Li}_2\text{MnO}_3$

*Nothing in life is to be feared, it is only to be understood. Now is the time to understand more, so that we may fear less.*

**Marie Curie**

In this chapter DFT calculations are used to simulate the ssNMR spectra of structures with stacking faults and different kind of point defects;  $\text{Li}^{\text{I}}/\text{H}^{\text{I}}$  exchange, and Li, O and combined  $\text{Li}_2\text{O}$  vacancies. The qualitative comparison of the experimental spectra with the simulated ones allow to confirm that the additional peaks observed in the experimental ssNMR samples synthesized at 900 °C are mainly consequence of stacking faults, but the synthesis at 1000 °C generates  $\text{Li}_2\text{O}$  vacancies, which are undetected by XRD. The combination of XRD, DFT and ssNMR provides a better description of all the microstructural features that otherwise remain undetected.

## 4.1 Introduction

NMR is a very useful technique for the evaluation and quantification of the structural features of a material at a local level and offers a very interesting perspective for the full structural description of a material in combination with the global picture provided by XRD. [226–230] In particular, ssNMR of paramagnetic cathode materials is very sensitive to local discontinuities as the magnetic interactions governing the ssNMR spectra of these materials are strongly affected by even very minor changes in the bond distances and angles linking the atoms. [229–233] Carlier *et al.* and Middlemiss *et al.* simulated the influence of different transition metals in the NMR shifts in layered oxides and olivines. [234, 235]

As seen in Chapter 3, stacking faults can be detected by different characterization techniques such as XRD or TEM. Previous works have reported that the ssNMR spectra of faulted  $\text{Li}_2\text{MnO}_3$  is also strongly modified and therefore ssNMR can as well be used for their detection. [70, 236] However, the quantification of stacking faults from ssNMR was shown to be a challenging task. Bréger *et al.* used DiFFaX [170] simulations to model XRD data to qualitatively analyze stacking faults in  $\text{Li}_2\text{MnO}_3$ , [70] and were first to show that defects strongly modify its ssNMR spectrum, although additional resonances were not assigned. In a more recent work, the assignment of extra  $^{17}\text{O}$  ssNMR resonances has been done by Seymour *et al.* and the percentage of stacking faults has been estimated from the ratio of the areas of the ssNMR peaks corresponding to the ideal and defective environments of  $\text{O}4i$  and  $\text{O}8j$ . [236] The acquisition and analysis of  $^{17}\text{O}$  ssNMR spectra is however challenging due to the low natural abundance of  $^{17}\text{O}$  and due to the fact that the active center is directly bonded to the oxygen, causing signal broadening and large shifts.

The quantitative results in terms of degree of stacking faults obtained in Chapter 3 combining XRD and TEM represents an excellent opportunity to endeavor the analysis and assignment of the  $^6\text{Li}$  ssNMR spectra of defective  $\text{Li}_2\text{MnO}_3$ . Assisted by first-principles calculations, an explanation to how local environments alterations change the Fermi contact shift is provided in this chapter, allowing the assignment of the different signals in the ssNMR spectra, to enable correlating ssNMR shifts to microstructural features. The combination of the results obtained from different techniques has allowed us achieving an accurate description of defects in Li-rich oxides, representing an excellent case study to discuss the suitability of each technique for their study and providing new pathways to understand the correlation between disorder and function.



## 4.2 Experimental XRD patterns and ssNMR spectra

Two of the samples previously described in the Chapter 3 (LMO\_MnO\_900\_5 and LMO\_MnCO<sub>3</sub>\_900\_5) have been characterized using ssNMR. A third sample was prepared in order to compare the ssNMR spectra with that of a sample with negligible amount of stacking faults. This sample was prepared using MnO as precursor, 1000 °C and 72 hours of annealing time and labeled LMO\_MnO\_1000\_72. Figure 4.1 shows the XRD patterns and ssNMR spectra of the three samples. From the XRD patterns shown in Figure 4.1a,b the samples exhibit notable differences owing to their different microstructure as expected from the synthesis conditions. The diffraction peaks of LMO\_MnO\_1000\_72 are sharp and the Warren fall typical of materials with stacking faults is absent, and therefore it can be considered that this sample is free of stacking faults. According to the FAULTS refinement performed in Chapter 3, LMO\_MnO\_900\_5 contains a low degree of stacking faults (around 13%) and LMO\_MnCO<sub>3</sub>\_900\_5 a high degree (42%).

Figure 4.1c shows the full <sup>6</sup>Li ssNMR spectra of the samples, where the rotational sidebands are marked with an asterisk. Samples synthesized at 900 °C have a small paramagnetic impurity (probably Li<sub>2</sub>CO<sub>3</sub>, but its fraction is very small as it is not detected in the XRD patterns). Figure 4.1d shows the region of interest, where the signals of Li<sub>2</sub>MnO<sub>3</sub> are present. The dominant interactions in the ssNMR spectra of paramagnetic Li<sub>2</sub>MnO<sub>3</sub> are the Fermi contact shifts generated by the unpaired electron density transferred from the paramagnetic manganese metals into the <sup>6</sup>Li spins through hybridization of the TM-O-Li bond. The size of this interaction is a function of the unpaired electron spin density transferred to the nucleus and this property is considered to be additive. [234, 237–240] The final Fermi interaction, or paramagnetic shift observed in the ssNMR spectrum, can be therefore theoretically estimated considering all the individual interactions, where the sign of the transfer can be positive or negative. [238] In a fully coordinated MnO<sub>6</sub> octahedron Li-O-Mn bonds at 90° have a positive net spin density transfer of 120-150 ppm, while the bonds at 180° induce a negative spin polarization of 60-125 ppm. [234] As shown in Figure 1.4a, the ideal structure of this compound exhibits three different lithium atomic positions; one corresponding to the lithium in the transition metal layer (Wyckoff position *2b*) and two of them located in the lithium layers (Wyckoff positions *2c* and *4h*). Figure 4.2a,b shows their local environments. Li<sub>2c</sub> and Li<sub>4h</sub> are coordinated by eight manganese atoms in the first coordination sphere; four of them are double bonded via 90° Li-O-Mn angle and the other four single bonded via 180° Li-O-Mn angle. Assuming the additive nature of the Fermi contact interaction, the ssNMR signals of the lithiums in the lithium layer (Li<sub>2c</sub> and Li<sub>4h</sub>) are expected to appear at around 750 ppm. On the other hand, as shown in Figure 4.2c, Li<sub>2b</sub> is surrounded by six manganese atoms, which are linked by a double 90° Li-O-Mn bond. The signal of Li<sub>2b</sub> is therefore expected

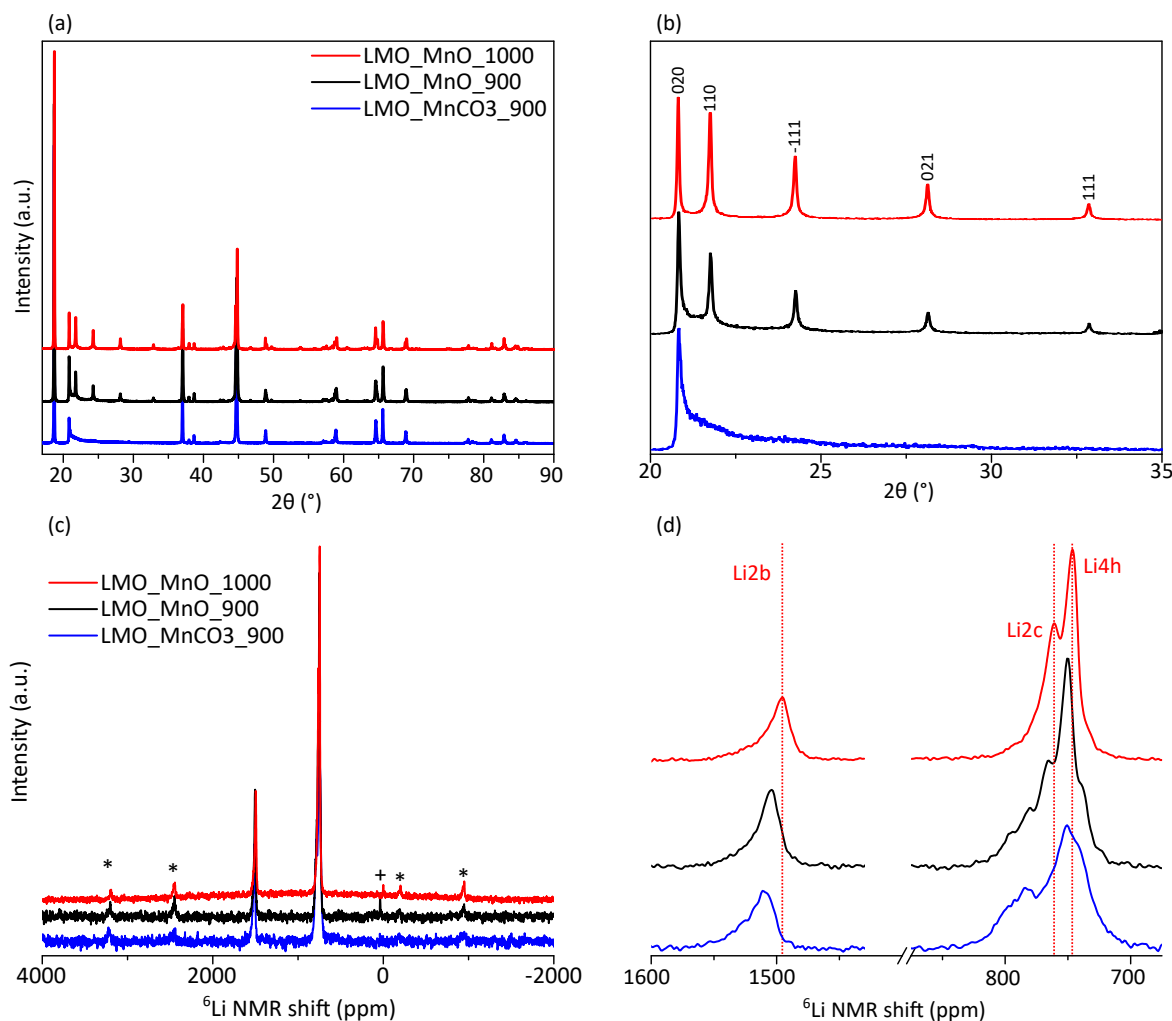


Fig. 4.1 (a) XRD pattern of selected samples. (b) Zoom of the superstructure peaks zone ( $2\theta$  range of  $20\text{--}35^\circ$ ). (c) ssNMR spectra of the samples from 4000 to  $-2000$  ppm. Spinning sidebands are labeled with \* while + corresponds to a small impurity of a paramagnetic lithium compound. (d) Zoom of the spectra of the region of interest. ssNMR Spectra are normalized with the area of the set of peaks at  $750$  ppm. The dashed red line shows the position for the experimental peaks from LMO\_MnO\_1000\_72.

at around  $1500$  ppm in the ssNMR spectrum. In agreement with this, previous  $^6\text{Li}$  and  $^7\text{Li}$  ssNMR studies of  $\text{Li}_2\text{MnO}_3$  assigned the two bands at around  $750$  ppm to Li2c and Li4h and the third one at  $1600\text{--}1800$  ppm to Li2b positions. [70, 231, 238, 241–244]

From the close inspection of the experimental spectra shown in Figure 4.1d, LMO\_MnO\_1000\_72 indeed exhibits two main resonances at around  $750$  ppm related to Li2c and Li4h, while LMO\_MnO\_900\_5 and LMO\_MnCO3\_900\_5 on the contrary, exhibit a higher number of overlapped signals in this region. These additional resonances are ascribed to the new lithium sites generated by stacking faults, as previously reported

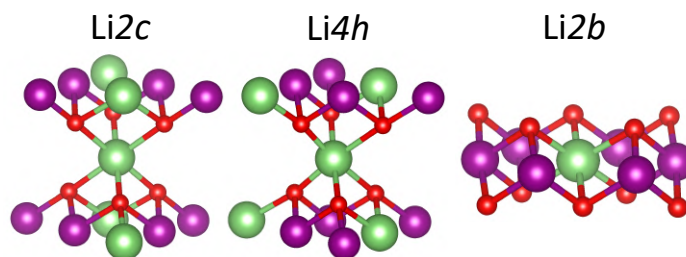


Fig. 4.2 Local environment of Li2b, Li2c and Li4h in Li<sub>2</sub>MnO<sub>3</sub>.

by Bréger *et al.* [70] In turn, while a single resonance is expected at around 1500 ppm for lithium ions in Li2b positions, all three samples exhibit an asymmetric shape of this signal due to the presence of overlapped signals at higher ppm values.

In general, NMR experiments can be regarded as quantitative being the integral intensity under a particular signal directly proportional to its population in the sample. Nevertheless, in certain cases, quantification by solid state NMR might not be straightforward (but still possible). [245] This is for example the case for paramagnetic materials due to their large spectral window and broad resonances where pulse imperfections or distinct magic angle spinning (MAS) rotational sideband patterns should be carefully considered. [246] In addition, the extremely rapid longitudinal and transversal relaxation of the nuclear spins due to paramagnetic interactions could lead to undetectable resonances. However, the evaluation of similar <sup>6</sup>Li NMR signals ascribed to analogous lithium environments is feasible as in these cases the effects previously mentioned are approximately constant. The ratio between the clusters of signals at around 750 ppm and 1500 ppm corresponds to the percentage of lithium in lithium layers vs. lithium in manganese layers, and the ideal value should be 3 (two Li4h and one Li2c against Li2b). The calculated ratios for LMO\_MnO\_900\_5 and LMO\_MnCO3\_900\_5 are similar (3.12 and 3.13 respectively) while for LMO\_MnO\_1000\_72 is larger (3.26), which suggests that LMO\_MnO\_1000\_72 has a lower content of lithium ions in Li2b position with respect to LMO\_MnO\_900\_5 and LMO\_MnCO3\_900\_5. The long reaction time and the higher temperature used in the synthesis of LMO\_MnO\_1000\_72 could entail some lithium evaporation which would not be detected from XRD analysis due to the weak scattering factor of lithium nor using other analytical techniques such as ICP, as minor stoichiometry differences are under the detection limit.

Figure 4.3a-c shows the deconvolution of both groups of signals for LMO\_MnO\_1000\_72, LMO\_MnO\_900\_5 and LMO\_MnCO3\_900\_5 respectively, and the fitting parameters are listed in Table 4.1. The ssNMR signal of LMO\_MnO\_1000\_72 observed at 1500 ppm could not be deconvoluted using a single resonance and at least three bands were required. In turn, the signals observed at 750 ppm can be described using two

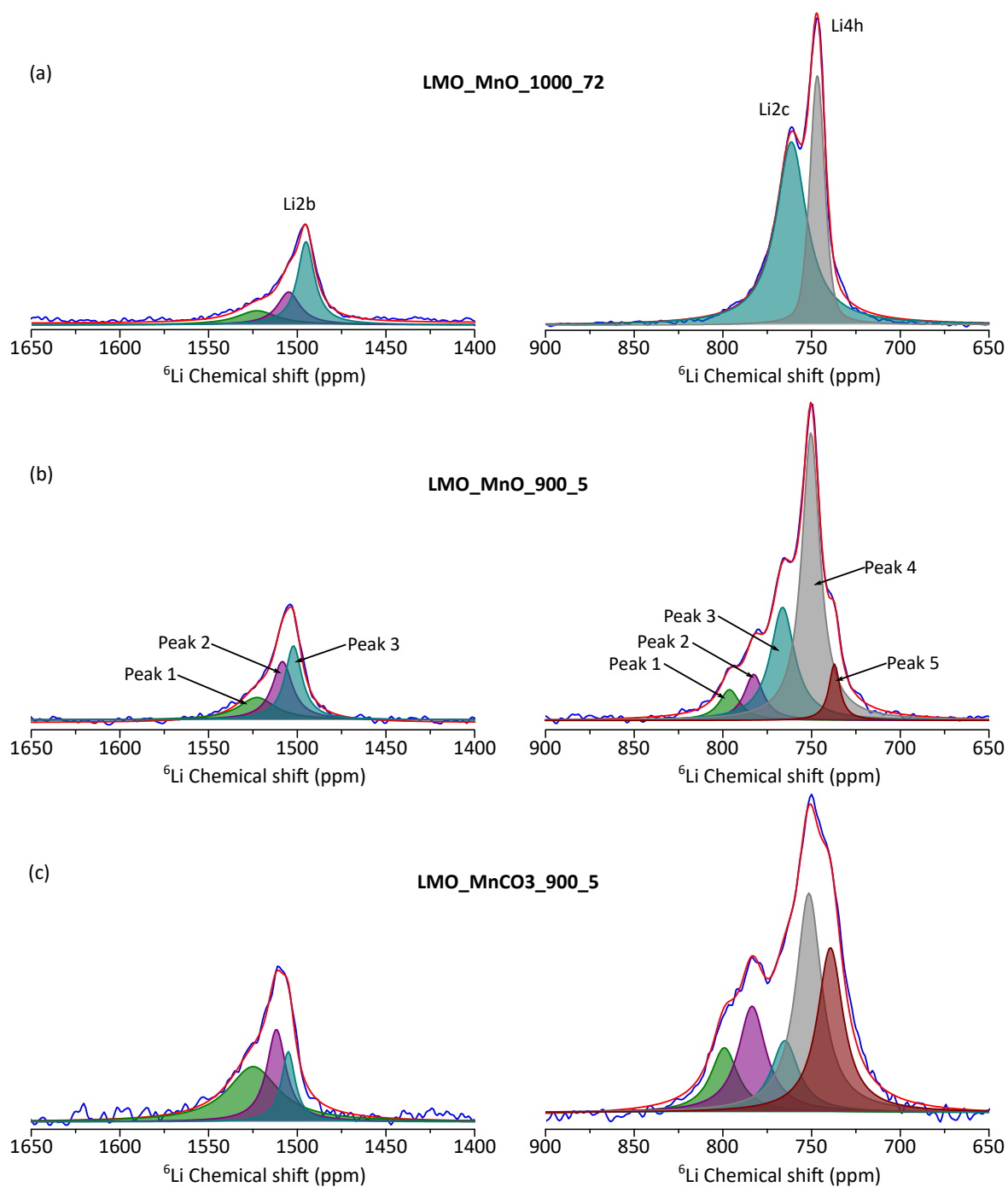


Fig. 4.3  $^6\text{Li}$  MAS-ssNMR spectra deconvolution of the samples. In blue the experimental spectra and in red the convoluted spectra are shown.

peaks. However, the intensity ratio of these two bands is the opposite to what is expected from the theoretical relative population between  $\text{Li}2c$  and  $\text{Li}4h$ . This is indicative that the two bands are in fact an overlap of more signals with similar local environments.

Table 4.1 Shift positions and relative populations for the deconvoluted ssNMR peak signals of the samples.

Peak at 1500 ppm	LMO_MnO_1000_72		LMO_MnO_900_5		LMO_MnCO3_900_5	
	Position (ppm)	%	Position (ppm)	%	Position (ppm)	%
p1	1524	20	1523	25	1525	50
p2	1506	28	1508	36	1512	32
P3	1496	52	1502	39	1505	18
Peak at 750 ppm	LMO_MnO_1000_72		LMO_MnO_900_5		LMO_MnCO3_900_5	
	Position (ppm)	%	Position (ppm)	%	Position (ppm)	%
p1	–	–	796	6	799	10
p2	–	–	783	9	784	17
p3	762	34	766	27	765	12
p4	746	66	750	52	752	33
p5	–	–	737	6	739	28

Similarly, LMO\_MnO\_900\_5 and LMO\_MnCO3\_900\_5 could neither be properly described using the ideal number of resonances, and the bands centered at 1500 ppm were deconvoluted considering three different components. The signals centered at 750 ppm required at least five peaks for a proper deconvolution, as shown in Figure 4.3b,c. Therefore, in this case, the extra peaks can be attributed to stacking faults. This is further confirmed by the fact that the positions of the shifts are similar for both samples. The relative intensities of peaks 3 and 4 become smaller as the degree of stacking faults increases, while signals 1, 2 and 5 grow. As, according to XRD analysis in Chapter 3, LMO\_MnO\_900\_5 has less stacking faults than LMO\_MnCO3\_900\_5, peaks 3 and 4 are assigned to the ideal stacking environments and resonances 1, 2 and 5 to the new Li environments generated by the stacking faults.

### 4.2.1 Stacking faults quantification using ssNMR

The sum of the peaks related to new lithium environments from Figure 4.3 can be used to quantify the degree of stacking faults as previously done by Seymour *et al.* using  $^{17}\text{O}$  ssNMR data. [236] They found that stacking faults affect both the first and second coordination spheres. Therefore, it was calculated that the number of oxygen atoms (and thus lithium) affected by stacking faults was three times the amount of stacking faults. However, this approach is only valid if stacking faults are isolated from one another. If they are consecutive (which is certainly the case of samples with large amounts of stacking faults as has been observed by HRTEM in Section 3.3), the number of modified environments will be lower, as the effects of consecutive defects will overlap. Figure 4.4 shows a schematic representation of

a structure with 20 layers. The red layers correspond to a shifted layer (stacking fault) and the orange ones are the adjacent layers (second coordination sphere). With 10% of faulted layers, different possibilities can be considered. In the first scenario, stacking faults are isolated. As a consequence, the amount of lithium atoms that will be affected is 30%. The second and the third scenarios correspond to two consecutive stacking faults, either with or without a layer between them. Here the second coordination sphere is shared and therefore, the total amount of affected lithium atoms decreases. Hence, while the amount of stacking faults obtained from XRD data will be 10% for the three examples, the relative Li populations that will be experimentally found by  $^6\text{Li}$  ssNMR will be different in each case and will range from 1 (for 100% consecutive stacking faults) to 3 (for 100% isolated stacking faults). Since it is not possible to distinguish between the three scenarios, it will be no longer possible to reliably quantify the amount of stacking faults by ssNMR. However, the comparison of ssNMR and XRD results can provide complementary information about the degree of clustering of stacking faults. Table 4.2 shows the comparison of the degree of stacking faults obtained by XRD using the FAULTS software and the sum of the percentage of new lithium environments measured by ssNMR and their ratio. For both LMO\_MnO\_900\_5 and LMO\_MnCO3\_900\_5 samples the ratio is close to 1.5, which indicates that stacking faults are not isolated, which is in accordance with previous TEM observations in Chapter 3 and therefore the amount of modified lithium environments determined from ssNMR are overestimated.

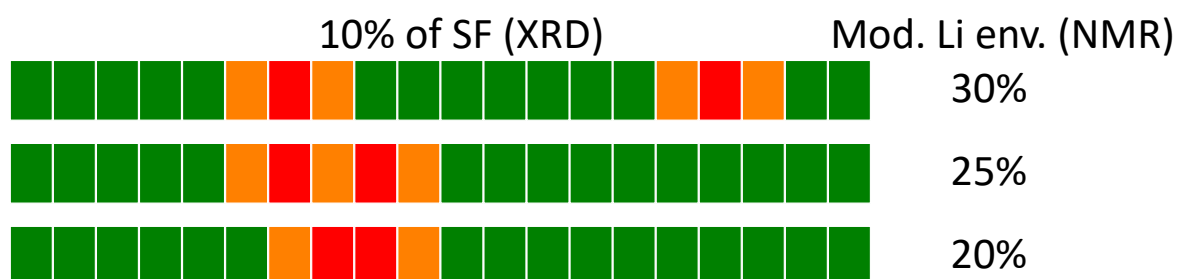


Fig. 4.4 Model of a structure containing stacking faults, where green layers represent ideal stacking, red layers stacking faults and orange layers second coordination sphere of stacking faults.

These results illustrate that the quantification of stacking faults from ssNMR data is only possible in samples where stacking faults appear as isolated defects, which is not the case here. However, the combination of XRD and ssNMR results can be used to estimate the trend of stacking faults to locally concentrate.

Table 4.2 Degree of stacking faults (SF) obtained with FAULTS program from XRD data and number of modified lithium environments obtained from the ssNMR peak fitting.

Sample	SF (XRD) (%)	Modified Li environment (ssNMR) (%)	Ratio
LMO_MnO_1000_72	None	None	None
LMO_MnO_900_5	13	21	1.6
LMO_MnCO3_900_5	42	57	1.4

### 4.3 DFT-based ssNMR shift calculation of the effects of defects in $\text{Li}_2\text{MnO}_3$

The use of DFT calculations is generally crucial for the assignment of subtle local environment changes on ssNMR shifts. Computed Fermi contact shifts can be used to predict the ssNMR shift positions and thus unravel the origin of unknown extra bands. In the following sections the NMR shifts of ideal and defective  $\text{Li}_2\text{MnO}_3$  structures are calculated as shown in Section 2.5.1.2. For this calculation magnetic molar susceptibility is needed, which is calculated as shown in Section A.3.1 in Appendix A.

#### 4.3.1 Choice of Hubbard corrective potential value and unit cell size

The choice of the Hubbard corrective potential ( $U$ ) can be tricky as it is an empirical value which varies for each element and its coordination sphere. Its value is generally set empirically to the parameters in study, e.g. the voltage of a cell. [247, 248] In this case the property in study is the Fermi contact shift so the value which fits best with the experimental one will be chosen.

Four different  $U$  values (0, 3.9, 4.5 and 5 eV) found in bibliography for  $\text{Li}_2\text{MnO}_3$  have been tested. [5, 199, 248, 249] The atomic positions have been relaxed but the unit cell size is fixed to a defined value. Three different unit cell parameters have been tested: one corresponding to experimental refined values of LMO\_MnO\_1000\_72 ( $a = 4.927(3)$  Å,  $b = 8.523(3)$  Å,  $c = 5.024(2)$  Å and  $\beta = 109.39(3)^\circ$ ), and the other two obtained relaxing the unit cell with no  $U$  value ( $U = 0$  eV) and with a  $U$  value of 5 eV. Figure 4.5 shows the experimental and all the calculated positions for the ssNMR shifts. When the  $U$  value is zero the  $^6\text{Li}$  ssNMR shift is too high in comparison with the experimental one. In turn, with increasing  $U$  the electronic charge is more localized and thus, the chemical shift is lower. The increase of the unit cell parameters reduces the  $^6\text{Li}$  ssNMR shift as well. The best agreement with the experimental  $^6\text{Li}$  chemical shifts for  $\text{Li}_2\text{MnO}_3$  is found with the experimental values

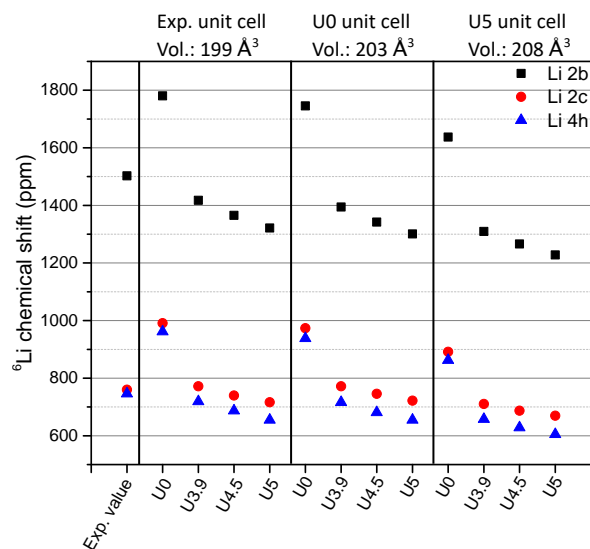


Fig. 4.5 Experimental and simulated values for  $^6\text{Li}$  ssNMR shifts for  $\text{Li}_2\text{MnO}_3$  with varying U values and unit cell sizes.

of the unit cell combined with a U value of 3.9 eV, and therefore these values have been used in our DFT calculations.

### 4.3.2 Simulated effect of stacking faults in the $^6\text{Li}$ ssNMR spectra

With the optimized U and unit cell values, the calculated ssNMR shifts of ideal and structures with stacking faults are examined to get further insight into their nature in the ssNMR spectra of Figure 4.1d. In order to use the same cell size in all cases, a 6-fold along the *c* axis supercell of the primitive unit cell has been generated with pymatgen. [250] These correspond to (a) an ideal structure with no stacking faults, (b) a structure with a single isolated stacking fault corresponding to a consecutive displacement of  $(1/3, -1/3, 0)$  of all the layers above the stacking fault and (c) a highly faulted structure with several alternate layer displacements of  $(1/3, -1/3, 0)$  or  $(-1/3, 1/3, 0)$ . The ideal structure (Figure 4.6a) exhibits, as expected, three signals in agreement with the assignments of Figure 4.3 and previous reports, [70, 231, 238, 241–244] while the presence of stacking faults in  $\text{Li}_2\text{MnO}_3$  splits the three main resonances of the ideal structure into additional signals (Figure 4.6b,c). The average calculated shifts of the simulated structures are shown in Table 4.3, together with average experimental peak positions for comparison. In the simulated spectra, the signals of Li2*b* and Li2*c* of the defective structures are gradually displaced to higher ppm values with increasing amounts of stacking faults. On the contrary, Li4*h* exhibits additional signals at both lower and higher shifts, resulting in an average position that remains almost unmodified. These



results agree well with the experimental patterns shown in Table 4.3 and in Figure 4.3, where the same trend is found.

Table 4.3 Computed and experimental average  $^6\text{Li}$  NMR shifts. The latter correspond to the deconvolution using one peak per signal. The values in parenthesis correspond to the difference with respect to the ideal signal (for the case of the simulated shifts) or to LMO\_MnO\_1000\_72 (for LMO\_MnO\_900\_5 and LMO\_MnCO3\_900\_5).

Computed	Li2 <i>b</i> (ppm)	Li2 <i>c</i> (ppm)	Li4 <i>h</i> (ppm)
Ideal	1342	719	675
Isolated SF	1355 (+13)	738 (+19)	679 (+4)
Consecutive SF	1377 (+35)	760 (+41)	681 (+6)
Experimental	Li2 <i>b</i> (ppm)	Li2 <i>c</i> (ppm)	Li4 <i>h</i> (ppm)
LMO_MnO_1000_72	1499	762	747
LMO_MnO_900_5	1506 (+7)	772 (+10)	750 (+3)
LMO_MnCO3_900_5	1511 (+12)	787 (+25)	747 (+0)

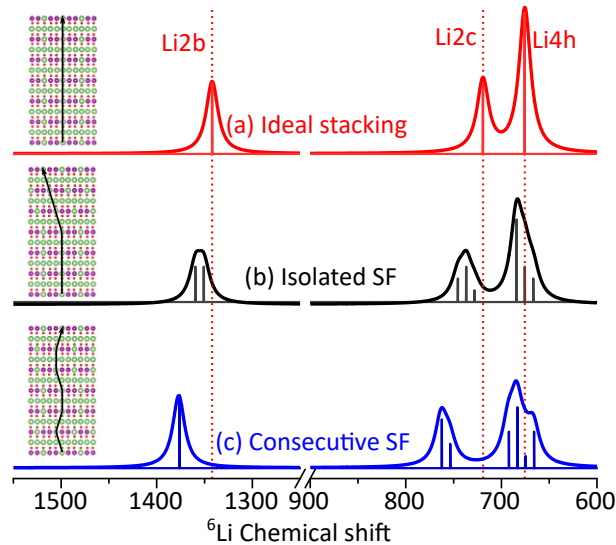


Fig. 4.6  $^6\text{Li}$  ssNMR simulated spectra of (a) an ideal structure, (b) a structure with isolated stacking fault and (c) a structure with consecutive stacking faults. The dashed red lines show the position for the simulated ideal peaks for Li2*b*, Li2*c* and Li4*h*. The insets show a reconstruction of the structures simulated with augmented *ab* plane to better see the stacking faults.

### 4.3.3 Simulated effect of vacancies and substitutions in the $^6\text{Li}$ NMR spectra

The combination of XRD, ssNMR and DFT techniques has led us to relate the extra peaks shown in the spectra of LMO\_MnO\_900\_5 and LMO\_MnCO3\_900\_5 in Figure 4.3 to new environments created by the stacking faults. The peak shapes in LMO\_MnO\_1000\_72, however, cannot be explained with planar defects, as XRD pattern has shown to be free of stacking faults. On one hand, the resonance at 1500 ppm shows at least three different environments. On the other, even if the peak at 750 ppm of LMO\_MnO\_1000\_72 is deconvoluted using two peaks, their intensity ratio is opposite to the ideal one for  $\text{Li}^{1c}:\text{Li}^{4h}$  (2:1 instead of 1:2). These two features suggest that additional overlapped peaks caused by other unknown structural defects should be considered. For this reason, the ssNMR spectra of structures with different microstructural defects are simulated to identify the origin of such extra peaks:  $\text{Li}^{\text{I}}/\text{H}^{\text{I}}$  exchange, lithium vacancies, oxygen vacancies and  $\text{Li}_2\text{O}$  vacancies.

#### 4.3.3.1 $\text{Li}^{\text{I}}/\text{H}^{\text{I}}$ exchange

As previously mentioned LMO\_MnO\_1000\_72 exhibits a lower content of lithium ions in  $\text{Li}^{2b}$  position with respect to LMO\_MnO\_900\_5 and LMO\_MnCO3\_900\_5. A first scenario where the  $\text{Li}^{\text{I}}$  are replaced by  $\text{H}^{\text{I}}$  from moisture has been considered.  $\text{Li}^{\text{I}}/\text{H}^{\text{I}}$  exchange has been reported to occur in acidic medium as well as when electrochemically oxidized in non aqueous electrolyte. [72, 79, 251–253] Figure 4.7 shows the computed ssNMR spectra corresponding to a material with  $\text{Li}_{1.96}\text{H}_{0.04}\text{MnO}_3$  formula. Strikingly, less than 2% of hydrogen severely modifies the local environments which makes the ssNMR signals appear at much higher ppm than the one calculated for ideal  $\text{Li}_2\text{MnO}_3$ . We believe that such difference arises from the fact that in the calculated relaxed structure hydrogen atoms are displaced from the center of the octahedron. As a consequence, the density charge of the oxygen atoms is severely modified and this is spread further away. Although the possibility of having a lower amount of  $\text{Li}^{\text{I}}/\text{H}^{\text{I}}$  defects in the experimental spectrum is plausible, from the comparison of the ssNMR spectra in Figure 4.3 and the simulated one in Figure 4.7 we believe these defects are unlikely to exist in our material.

#### 4.3.3.2 Lithium vacancies

A second scenario to account for lithium deficiencies in LMO\_MnO\_1000\_72 would be that the high synthesis temperatures generate lithium vacancies that are charge compensated via electron hole formation in oxygen atoms, as proposed to occur during the charge process. [80–82, 5] In order to evaluate the impact of how lithium vacancies modify the ssNMR

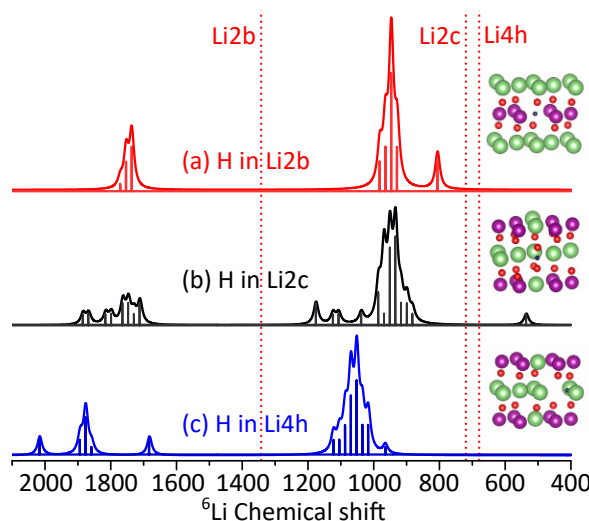


Fig. 4.7  ${}^6\text{Li}$  ssNMR simulated spectra of  $\text{Li}_{1.96}\text{H}_{0.04}\text{MnO}_3$  with  $\text{Li}^{\text{I}}/\text{H}^{\text{I}}$  exchange in (a)  $\text{Li}2b$ , (b)  $\text{Li}2c$  and (c)  $\text{Li}4h$  positions. The dashed red lines show the calculated position for the ideal peaks. The insets show the proton marked with a black sphere, not the whole computed structure.

spectra, a single isolated lithium atom is removed from the structure and its total energy is calculated. Since the calculated energy when removing lithium from its three crystallographic positions ( $2b$ ,  $2c$  and  $4h$ ) is the same we have considered that any of these three lithium defect structures would be equally likely to occur. As seen in Figure 4.8a-c lithium vacancies increase the ssNMR shifts for all the crystallographic lithium positions. Even if the presence of electron holes has only been proposed to occur after electrochemical oxidation, [80, 82] this kind of defect cannot be totally discarded in the pristine sample as they can overlap with the main signal.

#### 4.3.3.3 Oxygen vacancies

Reductive atmospheres have been used by some groups to synthesize oxygen vacant structures. [218, 254] Vacancies have been reported to reduce manganese to  $\text{Mn}^{\text{III}}$ , which improves the conductivity, enhancing charge-transfer ability and the electrochemical performance. [218, 254, 255] The experimental detection and quantification of such vacancies would be very interesting and useful to support these synthetic efforts. Oxygen vacancies in both  $\text{O}4i$  and  $\text{O}8j$  positions were considered and the resultant spectra are shown in Figure 4.9. In both cases the average formula unit of the computed structure is  $\text{Li}_2\text{MnO}_{2.96}$ . Oxygen vacancies are found to modify the local environment changing the spin transfer mechanisms and thus, generating a large set of new peaks. In addition to the resonances close to ideal signals (shown with a dashed red line), some additional peaks appear in the range 1000-1250

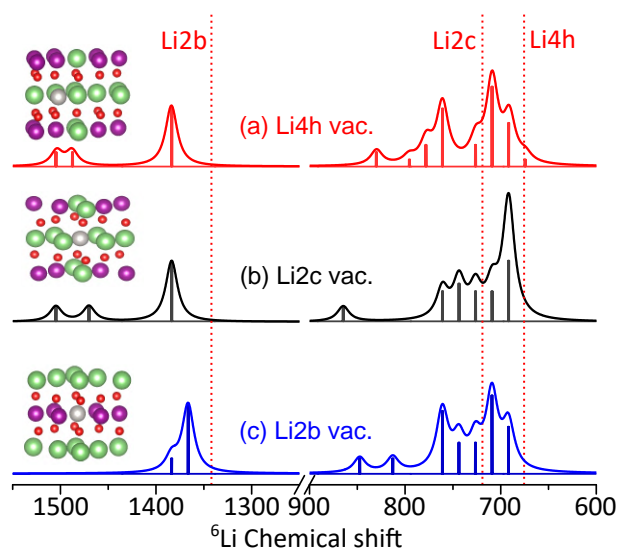


Fig. 4.8  $^6\text{Li}$  ssNMR simulated spectra of  $\text{Li}_{1.96}\text{MnO}_3$  with lithium vacancies on positions (a)  $\text{Li}4h$ , (b)  $\text{Li}2c$  and (c)  $\text{Li}2b$ . The dashed red lines show the calculated positions for the ideal peaks. The insets show the lithium vacancy marked with a gray sphere, not the whole computed structure.

ppm and 0-200 ppm. These peaks are not observed in the experimental ssNMR spectra (Figure 4.1c,d) and again, even if differences between the simulated defect concentration and the experimental one should be considered, the presence of oxygen vacancies in the material can be ruled out because the extra peaks would still be present. The absence of a reducing atmosphere in the synthesis of the material further supports this result.

#### 4.3.3.4 $\text{Li}_2\text{O}$ vacancies

Finally, the combination of lithium and oxygen removal with the loss of  $\text{Li}_2\text{O}$  has also been considered. It is well established that  $\text{Li}_2\text{O}$  removal upon electrochemical oxidation occurs. [66, 72, 73, 75, 76, 138, 252, 256–259] In agreement with previous reports [86, 260, 261] we have found that the structure with an  $\text{O}8j$  vacancy is more energetically favored (-36.67 eV) than the structure with a  $\text{O}4i$  (-36.65 eV) so the  $\text{Li}_2\text{O}$  vacancy has been simulated with a  $\text{O}8j$  vacancy. The  $\text{Li}_2\text{O}$  removal from  $\text{Li}_2\text{MnO}_3$  has been done in two steps. After removing one  $\text{O}8j$  atom, one lithium atom is removed. All the possible lithium atoms have been tested (48 possibilities) and the resulting energy is compared (shown in Figure 4.10a). It has been found that the lithium atoms directly linked to the vacant oxygen, especially the  $\text{Li}4h$  with a  $180^\circ$  angle  $\text{Li}4h\text{-vac.}-\text{Li}2b$ , are more likely to leave. Once the most labile lithium atom is removed, a second lithium atom is extracted. As for previous case, all the possibilities have been tested and the most energetically favored are again those close to the

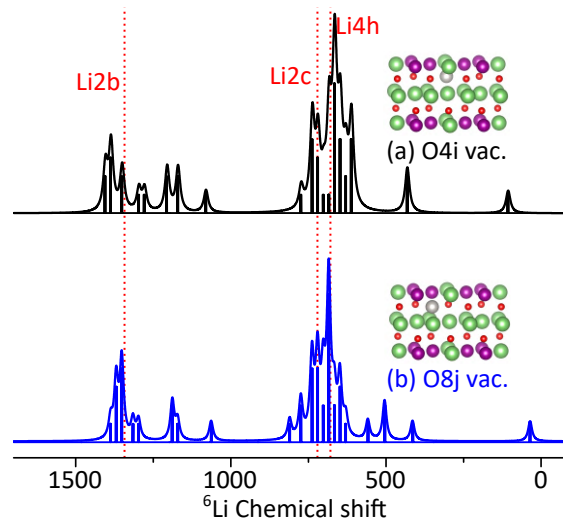


Fig. 4.9  $^6\text{Li}$  ssNMR simulated spectra of  $\text{Li}_2\text{MnO}_{2.96}$  with oxygen vacancies on positions (a) 4i and (b) 8j. The dashed red lines show the calculated positions for the ideal peaks. The insets show the oxygen vacancy marked with a gray sphere, not the whole computed structure.

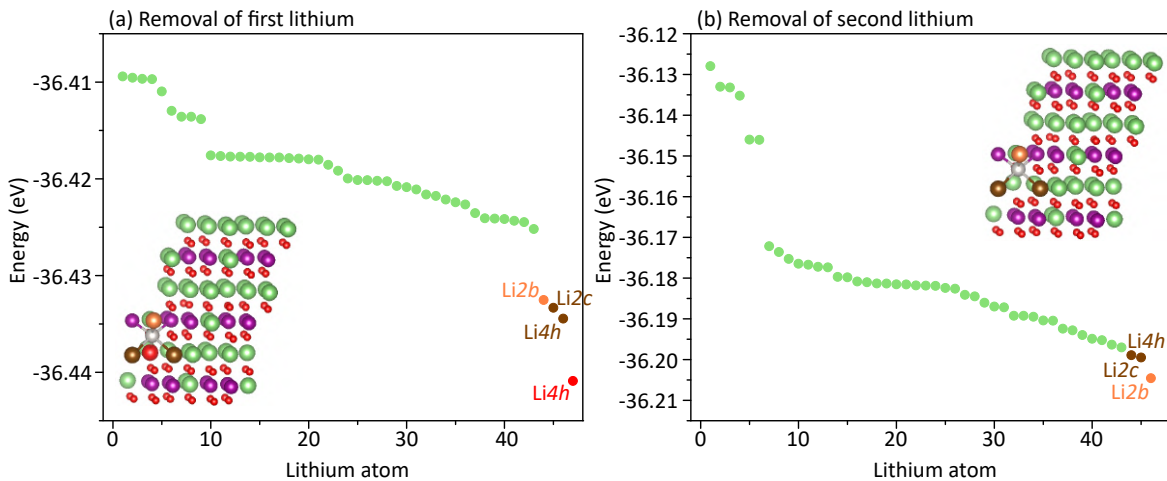


Fig. 4.10 Computed energy for  $\text{Li}_2\text{MnO}_3$  structure with (a) an  $\text{O}8j$  vacancy and one lithium vacancy (b) a second lithium vacancy after the removal of one  $\text{O}8j$  and the most labile lithium atom ( $\text{Li}4h$ ). Lithium, manganese and oxygen atoms are represented in green, purple and red respectively. The oxygen vacancy is represented in gray and the lithium atoms directly linked to the vacancy in red, brown and orange.

vacancy, being  $\text{Li}2b$  the most labile one (Figure 4.10b). The removal of  $\text{Li}4h$ - $\text{O}8j$ - $\text{Li}2b$  with a  $180^\circ$  angle has found to be the most favorable, in agreement with Xiao *et al.* [5] The ssNMR simulated spectrum corresponding to the most stable  $\text{Li}_{1.92}\text{MnO}_{2.96}$  structure is shown in Figure 4.11. The removal of two lithium and one oxygen atoms generate a slight shift of  $\text{Li}2c$  and  $\text{Li}4h$  signals to higher ppm values, and a number of new signals around all ideal

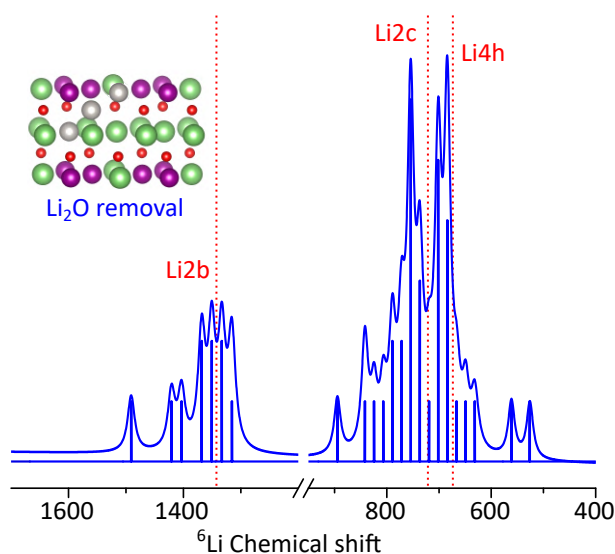


Fig. 4.11  $^6\text{Li}$  ssNMR simulated spectra of  $\text{Li}_{1.92}\text{MnO}_{2.96}$  with  $\text{Li}4h$ ,  $\text{Li}2b$  and  $\text{O}8j$  vacancies. The dashed red line shows the calculated position for the ideal peaks. The inset shows the  $\text{Li}_2\text{O}$  vacancy marked with a gray sphere, not the whole computed structure.

positions. Simulations including the ideal and new  $\text{Li}2b$  environments are able to reproduce the asymmetric lineshape found experimentally, except for the two peaks at 500-600 ppm. These, which are the consequence of 5-coordinated lithium atoms whose transferred spin density is reduced with respect to ideal 6-coordinated lithium atoms, are believed to overlap with the main peak at 750 ppm and thus they are not visible in the experimental pattern. The presence of  $\text{Li}_2\text{O}$  vacancies seems thus reasonable to be present in  $\text{LMO\_MnO\_1000\_72}$ .

#### 4.3.3.5 Point defect evaluation in $\text{LMO\_MnO\_1000\_72}$

Even if the sample without stacking faults can be deconvoluted using two resonances, their intensity distribution does not correspond to the expected one. It has been thus concluded that other types of defects must be present and a deeper study to elucidate the origin of such deviation has been performed. The effect of  $\text{Li}^I/\text{H}^I$  exchange and lithium, oxygen and  $\text{Li}_2\text{O}$  vacancies in the ssNMR shifts have been simulated. On the one hand, DFT calculated spectra show that single oxygen vacancies and  $\text{Li}^I/\text{H}^I$  exchange generate shifts which are clearly not present in our samples. On the other hand, both lithium and  $\text{Li}_2\text{O}$  vacancies result in new environments and shifts to higher ppm that could be in agreement with our experimental data. However, the shifts obtained for lithium vacancies appear more isolated, which is why we believe that overall  $\text{Li}_2\text{O}$  vacancies better reproduce the experimental spectrum of  $\text{LMO\_MnO\_1000\_72}$ . The strong overlapping of the different ssNMR signals coupled to the low amount of these defects (as they were not detected by XRD) hinders their

quantification. The dominant effect of stacking faults in the spectra of LMO\_MnO\_900\_5 and LMO\_MnCO3\_900\_5 neither allows assessing the presence of Li<sub>2</sub>O vacancies in their structure, although a lesser extent is expected (if any) from the different synthesis conditions used to prepare these samples. Therefore, while XRD can give us quantitative information about the degree of stacking faults, ssNMR is highly sensitive to other defects that are undetected by other techniques such as XRD or ICP. The decoupling of different types of defects and their quantification by <sup>6</sup>Li ssNMR however remains a challenge.

## 4.4 Conclusions

In this chapter Li<sub>2</sub>MnO<sub>3</sub> samples with different microstructures have been selected and their ssNMR spectra have been elucidated with the help of DFT and XRD data. Samples prepared at 900 °C were found to mainly exhibit stacking faults resulting in additional peaks in their ssNMR spectra. DFT calculations have accurately reproduced the peak assignment of the ideal structure and structures with stacking faults. Their quantification by <sup>6</sup>Li ssNMR is only possible if these are isolated, however, the comparison of the number of modified environments with XRD results can be used to characterize their trend to locally concentrate. From XRD data it was concluded that the sample prepared at 1000 °C was stacking faults-free, but a close inspection of its ssNMR spectrum suggested other structural defects instead. DFT calculations were used to discriminate between Li<sup>I</sup>/H<sup>I</sup> exchange and lithium, oxygen and Li<sub>2</sub>O vacancies, being the latter the scenario that could best reproduce the additional ssNMR features. While XRD gives accurate information about the degree of stacking faults, ssNMR is shown to be highly sensitive to other microstructural defects which are not easily detected with XRD. Both techniques are thus complementary and combined provide an accurate description of the microstructural complexities Li<sub>2</sub>MnO<sub>3</sub> can exhibit.





## Chapter 5

# Theoretical assessment of the stacking faults impact in $\text{Li}_2\text{MnO}_3$ and analysis of substitution strategy

*Give me six hours to chop down a tree and I will spend the first four sharpening the axe.*

**Abraham Lincoln**

In this chapter, based on DFT calculations, the phase stability of ideal and defective  $\text{Li}_2\text{MnO}_3$  has been analyzed. Firstly, the energy of ideal structure and different stacking sequences have been calculated and compared. Secondly, differences between the delithiation mechanisms of the ideal and the defective structures have been sought by comparing the formation energies of ground states at different delithiation level of ideal and defective structures. Thirdly, the stability of the oxygen atoms in the delithiated structures has been studied with a Bader charge analysis. Finally, the effect of different lithium substituent (Na, K, Be, Mg) in the structural stability upon delithiation is tested.

## 5.1 Introduction

Intensive theoretical work has been done aimed to understand the structural stability of  $\text{Li}_2\text{MnO}_3$  upon delithiation and its relationship with the undesired capacity and voltage fading. The lithium removal from the structure, which was found to happen in both the lithium and the transition metal layer, was calculated to be at approximate 4.6 V and it was accompanied by a oxygen oxidation. [5, 6, 85, 88, 89] Several ground states upon the delithiation of  $\text{Li}_x\text{MnO}_3$  were found in the  $2 \geq x \geq 1$  range using cluster expansion technique. [5, 6] However, due to their proximity to the Hull, a solid solution or weak two-phase behavior was proposed. Even if the stability of ideal and stacking faults containing  $\text{Li}_2\text{MnO}_3$  have been studied and both structures have shown to be energetically degenerated, [70, 85] there are no studies about the structural stability of the defective structure upon delithiation.

At higher delithiation levels the structure was no longer stable and was found to suffer modifications. Preliminary studies found that at  $x = 0.5$  the structure transformed to  $O1$ . [85, 86] Regarding that the degradation of  $\text{Li}_2\text{MnO}_3$  has been experimentally attributed to the layered-to-spinel transformation, consequence of manganese migration to lithium layer, [79, 108, 215] this migration, which most likely happens through a tetrahedral site, was theoretically studied. Lee *et al.* found with a ternary cluster expansion that at  $x \leq 1$  the manganese was thermodynamically favored to migrate the lithium layer, even if it was kinetically sluggish to happen (1.9 eV at  $x = 1$  and 0.7 eV at  $x = 0.5$ ). [6] Other works, on the contrary suggested spontaneous manganese migration to the lithium layer at  $x \leq 0.75$ . [87] In any case, experimental works found transformation to spinel at early stages of delithiation, [73] so a non homogeneous delithiation was suggested, which could generate locally overdelithiated zones where the manganese migrates even if the overall lithium content is  $x > 1$ . [249, 262]

Even if different theories have been suggested to explain the redox activity of  $\text{Li}_2\text{MnO}_3$ , the most accepted and widely studied one is that the oxygen atom is the main redox active atom. The oxidized oxygen atom is thought to eventually form  $\text{O}_2$  molecule and leave the structure, as a result of its instability. Highly undercoordinated oxygen atoms (coordinated to less than three atoms in octahedral environment) have been suggested to be behind the  $\text{O}_2$  formation. [263] However, the point at which the oxygen leaves in  $\text{Li}_x\text{MnO}_3$  is not clear and varies from  $x \leq 1.5$ , to [5]  $x \leq 1$  [6, 86, 88] or to  $x \leq 0.5$ . In any case, the oxidation of the oxygen has been suggested to precipitate the manganese migration. [87–89, 264] Other works have suggested that molecular  $\text{O}_2$  could remain trapped in the structure and reversibly be reduced in the discharge. [5, 89, 264] Radin *et al.* hypothesized that the formation of

in-lattice  $\text{O}_2$  could induce a manganese migration to tetrahedral positions and oxidation to  $\text{Mn}^{\text{VII}}$ , which explains the voltage hysteresis these compounds are known to suffer. [264]

As a strategy to avoid the structural transformation caused by the manganese migration cationic substitution of manganese has been attempted, which in addition improves the capacity. [125, 126, 265–267] Nickel, cobalt and/or aluminum are generally used to considerably enhance the electrochemical properties, as they can act as stabilizers and/or active redox center. Theoretical studies have found that aluminum, iron, molybdenum and ruthenium preferentially occupy the manganese site while magnesium occupies the lithium site. Nickel on the contrary does not have site preference. [265] The doping of the lithium site, which was theoretically found to be plausible at synthesis temperatures, [268] is believed to have detrimental effects on the battery performance, as it can block diffusion pathways. Nevertheless, experimental works have shown that magnesium doping improves the electrochemical performance in layered oxides. [269–275] In addition, lithium has also been successfully substituted with sodium [129, 276] or potassium [131, 277] among others. These substitutions have however only been done in dopant range (low contents of lithium is substituted). Large amount of dopant evenly spread along the structure (partial cationic substitution of the lithium atom) could avoid the formation of undercoordinated oxygen atoms and thus, inhibit the oxygen release and subsequent layered-to-spinel transformation.

In this work, the stability of different stacking sequences in the totally lithiated  $\text{Li}_2\text{MnO}_3$  has been firstly described. Later, the effect of stacking faults upon delithiation have been studied by comparing the formation energies of ground states at different delithiation levels of ideal and stacking faults containing structures. In addition, the stability of the oxidized oxygen atoms in the delithiated structures has been studied. On the other hand, the cationic substitution as manganese migration inhibitor has been proposed. Different cations have been tested and sodium and magnesium have been found as promising candidates. The stability of the delithiated phases in  $\text{Li}_x\text{Na}_{0.5}\text{MnO}_3$  and  $\text{Li}_x\text{Mg}_{0.5}\text{MnO}_3$  have been then studied and the predicted structural evolution upon the delithiation has been described.

## 5.2 Investigation of stacking defects in $\text{Li}_2\text{MnO}_3$

In order to analyze the structure stability of stacking faults in  $\text{Li}_2\text{MnO}_3$  a number of different structures with varying stacking sequences were built and their total energy was calculated and compared with the ideal one. In Figure 5.1 the two types of stacking faults that result from layer gliding considered in this work are shown. Both can coexist in the structure but cannot be visualized from the same direction, only after a rotation of the structure  $30^\circ$  through the  $c$  axis. In the first one (Figure 5.1a) the  $O3$  stacking is maintained as the transition metal

layer together with the oxygen atoms of the monoclinic unit cell  $\pm 1/3b$  are displaced. This induces a cationic disorder denoted by R, P and P' [3, 4] as described in Section 3.1. In order to differentiate these stacking faults from the  $O1$  stacking faults described below, in this chapter we will refer to them as cationic stacking faults. The second type of stacking fault here considered, described in Figure 5.1b, consists on a displacement of  $+1/3a$  of the transition metal layer together with the oxygen atoms, followed by a transition metal layer extra displacement of  $-1/6a$  (maintaining the oxygen atoms in the previous position), which generates a  $O1$  type stacking fault in a  $O3$  matrix.

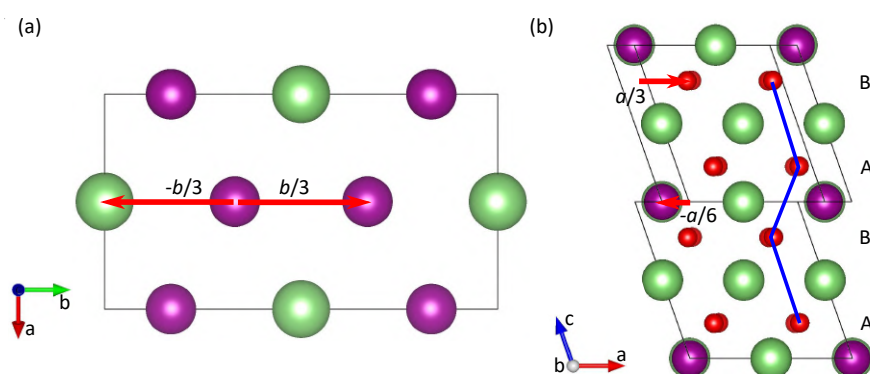


Fig. 5.1 Displacement of the layers involved in the formation of (a) cationic stacking faults and (b)  $O1$  type stacking faults.

In order to analyze the effect of diluted and concentrated cationic stacking faults, a  $1 \times 1 \times 6$  supercell of the primitive unit cell has been built. In addition to the ideal structure (Figure 5.2a) the total energy of a series of hypothetical  $\text{Li}_2\text{MnO}_3$  structures has been calculated. Figure 5.2b shows an structure formed of ideal blocks of three layers linked with an isolated stacking fault, the structure in Figure 5.2c contains a large block of ideal stacking sequence linked with two concatenated stacking faults, the structures in Figure 5.2d,e are formed of an ideal block and a faulted block and finally, the structure shown Figure 5.2f contains a highly faulted stacking sequence. On the other hand, in order to study the effect of  $O1$  type stacking fault, the energy of a structure with this defect is as well calculated (Figure 5.2g). This unit cell is made of 8 layers instead of 12 following the stacking sequence ABCACABC. As the total energy of the structure depends on the number of atoms, the calculated energy values have been normalized to the number of atoms of the formula unit.

The total calculated energy of the studied structures with cationic stacking faults (Figure 5.2a-f) is  $-37.01$  eV, with an energy difference between them of less than  $\pm 0.001$  eV. This energy difference is very small so all the structures are thought to be energetically degenerated and therefore, in principle there is not any preferential stacking sequence and both ideal and stacking faults containing configurations are equally likely to occur. The

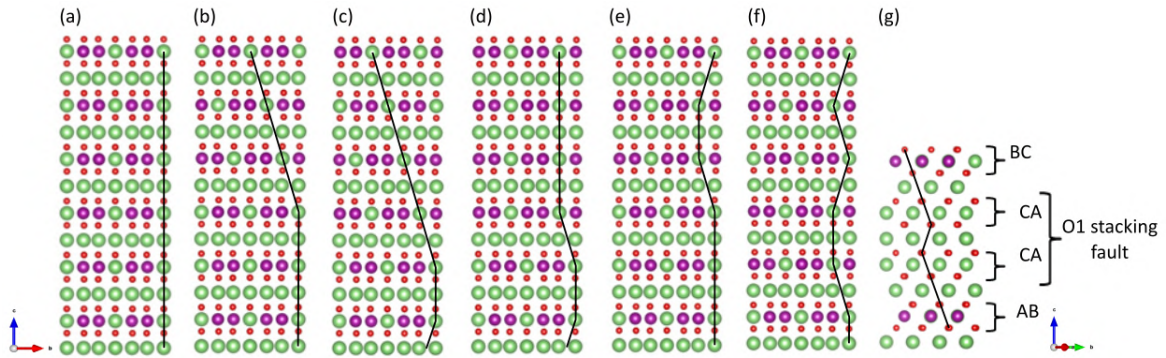


Fig. 5.2 Relaxed structures analyzed by DFT calculations with a different number of stacking faults. (a) Ideal stacking and structures with one (b), two (c) three (d,e) and five (f) stacking faults. (g) Structure with an  $O1$  type defect.

result agrees well with the previously calculated energy difference ( $\pm 0.002$  eV) of the ideal structure with stacking faults containing structures (using  $P3_112$  and  $C2/c$  space groups). [70] In our case, a broader study with many different stacking sequences has been performed and it shows that this small energy difference is maintained regardless the stacking sequence, so the long range ordering does not have a strong impact the total energy of the system. On the other hand, the structure containing  $O1$  stacking faults (Figure 5.2g) have an energy of  $-36.91$  eV,  $0.1$  eV higher than the ideal stacking. This difference is significant, so we believe that the  $O1$  type stacking faults are unlikely to occur in the fully lithiated  $\text{Li}_2\text{MnO}_3$ . This results agrees with the FAULTS analyses in Chapter 3, where a wide range of cationic stacking faults have been experimentally found but there was no evidence for  $O1$  type stacking faults.

### 5.3 Computational study of stacking faults in the delithiation mechanism of $\text{Li}_2\text{MnO}_3$

Even if both, ideal and stacking faults containing structures are equally likely to be formed, the atomic environments created by stacking faults could have an impact in the delithiation mechanism of  $\text{Li}_2\text{MnO}_3$ . In view of the large amount of stacking faults that the best performing sample exhibits (see Chapter 3), in this section, the effect of stacking faults in the delithiation process is considered. To do so, the energies of different configurations at different values of  $x$  in  $\text{Li}_x\text{MnO}_3$  of an ideal and a defective structure are calculated and compared.

The ground states for ideal  $\text{Li}_x\text{MnO}_3$  at different values of  $x$  previously found using cluster expansion method [5, 6] are shown in Figure 5.3. According to Xiao *et al.*, [5] the

ground state for  $\text{Li}_{1.25}\text{MnO}_3$  loses half of the  $\text{Li}4h$  and half of the  $\text{Li}2b$  (Figure 5.3b1) and for  $\text{LiMnO}_3$  is that without the second half of  $\text{Li}2b$  (Figure 5.3c1). On the other hand, according to Lee *et al.*, [6] at  $\text{Li}_{1.25}\text{MnO}_3$  the ground state loses half of the  $\text{Li}2b$  and all the  $\text{Li}2c$  (Figure 5.3b2) and latter at  $\text{LiMnO}_3$  the remainder  $\text{Li}2b$  (Figure 5.3c2). Nevertheless, there are not reported ground states for stacking faults containing structures.

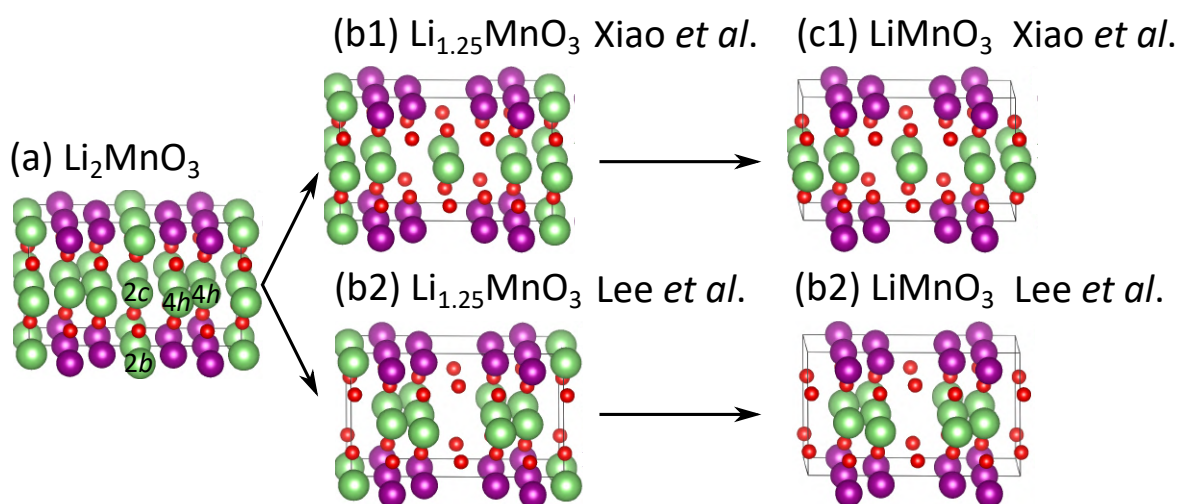


Fig. 5.3 Ground states of  $\text{Li}_x\text{MnO}_3$  proposed by Xiao *et al.* and Lee *et al.*, with a  $x$  value of 1.25 and 1. [5, 6]

Since structures with stacking faults have a lower symmetry, a larger unit cell needs to be used to describe them. The structure used in this calculation consists on a unit cell  $2 \times 2 \times 3$  of the primitive one, involving 144 atoms. This large unit cell can be detrimental when using typical methods to find the ground states such as cluster expansion and makes the calculation time consuming. In this work an alternative procedure is used to find the most stable ground states. Its validity will be first tried with the ideal structure, where stable ground states are reported [5, 6] and then applied to a structure with stacking faults. The method we have used follows the steps here listed:

1. The energy of the fully lithiated and the fully delithiated structures is calculated.
2. For each delithiation step ( $x = 1.25, 1$  and  $0.5$  for  $\text{Li}_x\text{MnO}_3$ ), the structure is randomly delithiated 10,000 times and the Ewald's energy of each structure is calculated using pymatgen module [250] (see Section 2.5.2 for information about the Ewald's energy calculation).
3. The DFT energy of the 10 most stable structures of the step 2 is calculated.

- Using Equation 2.19 in Section 2.5.1.1, the formation energy of each structure is calculated and plotted in a convex Hull.

### 5.3.1 Ground states of ideal $\text{Li}_2\text{MnO}_3$

Figure 5.4 shows the computed formation energies of  $\text{Li}_x\text{MnO}_3$  at different delithiation stages ( $x = 1.25$  and  $x = 1$ ) of the ideal structure. For a comparison with those proposed in bibliography, the structures proposed by Xiao *et al.* and Lee *et al.* are reproduced and the calculated formation energy is plotted with red and blue symbols. We found that, the ground states proposed by Lee *et al.* are energetically more favored than those proposed by Xiao *et al.* With this sampling method we have been able to find structures with similar and even lower energy than those proposed in the bibliography so this procedure can be considered to be effective for finding the most energetically favored structures. In the  $2 \geq x \geq 1$  range, different structures have found to be close to the Hull which means that they could be accessible at room temperature (green area in the plot), so a solid solution like delithiation mechanism is expected, as previously predicted. [6] As seen in Figure 5.4b,c, the ground states calculated in this work have some lithium atoms in tetrahedral position which increase as the number of  $x$  is lower (5% for  $\text{Li}_{1.25}\text{MnO}_3$  and 14% for  $\text{LiMnO}_3$ ). This is indicative that some lithium atoms in the tetrahedral positions somehow stabilize the structure among the delithiation [249] as it will be studied in more detail in Section 5.3.3.

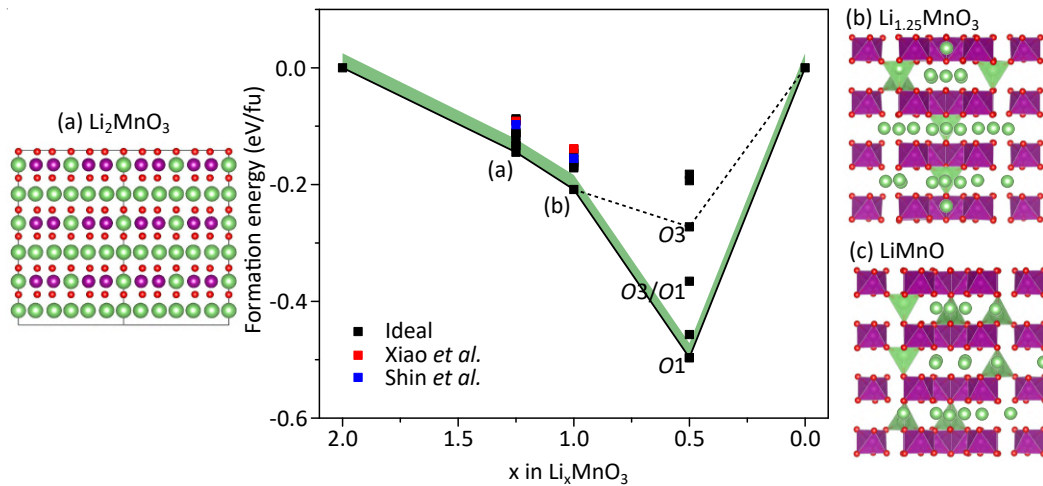


Fig. 5.4 Formation energies of  $\text{Li}_x\text{MnO}_3$  ( $2 \geq x \geq 0$ ). (a) Relaxed  $\text{Li}_2\text{MnO}_3$  structure. Ground states for  $\text{Li}_{1.25}\text{MnO}_3$  and  $\text{LiMnO}_3$  are shown in (b) and (c) respectively. The lithium atoms in tetrahedral positions are marked with a green tetrahedron.

For  $x = 0.5$ , the most stable configuration is that with all the lithium atoms in the  $2c$  position and with  $O1$  stacking sequence, as proposed in bibliography. [85, 86] We have

however found that this transformation is not always achieved and depends on the lithium removal sequence. As it is seen in Figure 5.5a, if in the  $O3$  configuration all the lithium atoms are in the  $2c$  position a saddle point is reached and it does not transform to  $O1$ . On the other hand, if the lithium atoms are in the  $4h$  position (Figure 5.5b,c), the layers will glide so that the lithium goes to the  $2c$  position, inducing  $O3 \rightarrow O1$  transformation and a layer shrinkage from  $\sim 4.7 \text{ \AA}$  to  $\sim 4.1 \text{ \AA}$ . This shrinkage could additionally promote the interlayer formation of peroxo-like bonds.

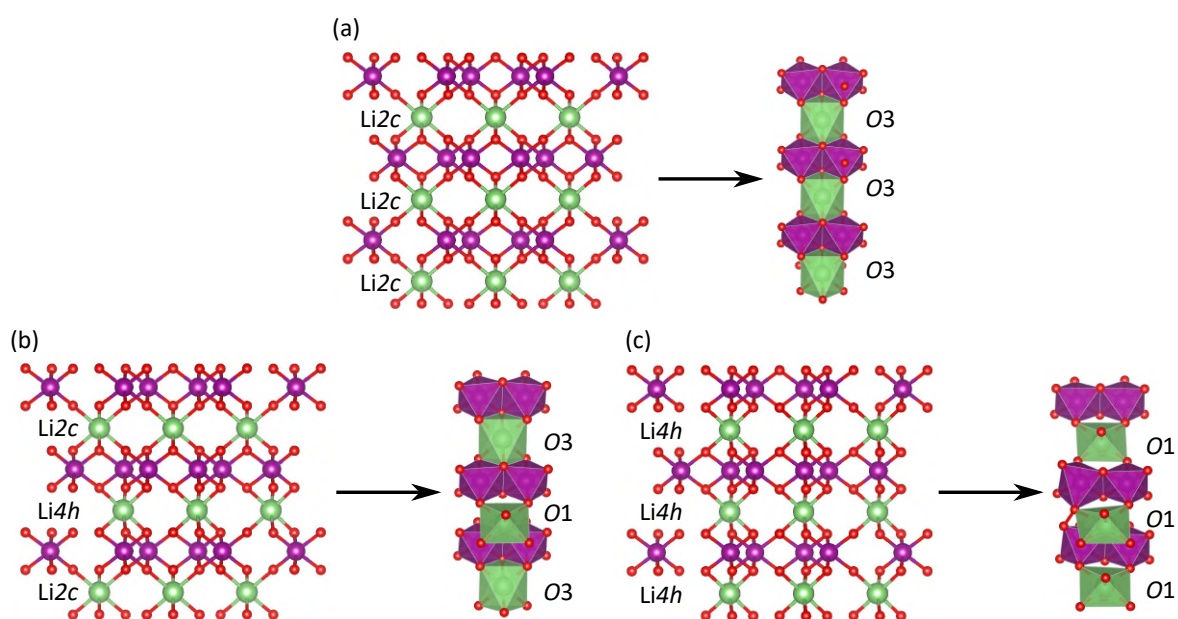


Fig. 5.5 Initial and DFT relaxed structures of  $\text{Li}_{0.5}\text{MnO}_3$  when the lithium atoms in the  $O3$  configuration are (a) in the  $2c$  site, (b) some in the  $2c$  site and others in the  $4h$  site and (c) in the  $4h$  site.

### 5.3.2 Ground states of defective $\text{Li}_2\text{MnO}_3$

As the Ewald's sampling method has been successfully used to find ground states in the ideal structure, the same approach has been followed to sample structures in the stacking faults containing  $\text{Li}_2\text{MnO}_3$  and the results are shown in Figure 5.6. As a starting point, a highly faulted structure has been used as initial structure as shown in Figure 5.6a. In the  $x = 1.25$  and  $x = 1$  range the Hull has similar shape to those of the ideal ones: several configurations energetically degenerated are close to the convex Hull and the ground states contain some lithium atoms in tetrahedral positions (Figure 5.6b,c). The percentage of lithium in tetrahedral positions for  $\text{Li}_{1.25}\text{MnO}_3$  and  $\text{LiMnO}_3$  (5% and 16% respectively) is similar than that in the ideal structure so the lithium migration to tetrahedral position is independent on the stacking



sequence. However, at  $x = 0.5$  the shape of the convex Hull differs from the ideal one. For the stacking faults containing structure the  $O1$  structure is no longer the most stable one.

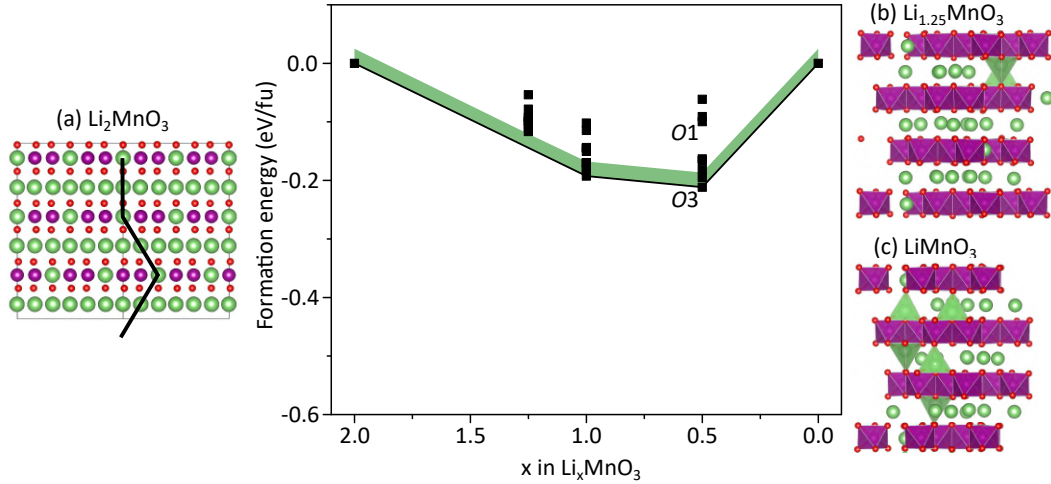


Fig. 5.6 Formation energies in  $\text{Li}_x\text{MnO}_3$  ( $2 \geq x \geq 0$ ) for a stacking faults containing structure. (a) Relaxed  $\text{Li}_2\text{MnO}_3$  structure. Ground states for  $\text{Li}_{1.25}\text{MnO}_3$  and  $\text{LiMnO}_3$  are shown in (b) and (c) respectively. The lithium atoms in tetrahedral positions are marked with a green tetrahedron.

### 5.3.3 Study of oxidation state of the oxygen atoms

In this section the oxidation state of the oxygen atoms is followed with a Bader charge analysis. [278–280] Note that Bader analysis will not give the exact oxidation state of the oxygen atoms but it can be useful to compare oxygen atoms in different oxidation states. Table 5.1 shows the average Bader charge of each studied composition and its comparison with the expected oxygen oxidation state at that lithium content, assuming that the oxidation state for the manganese and lithium are  $\text{Mn}^{\text{IV}}$  and  $\text{Li}^{\text{I}}$ . From these values a linear regression has been carried out, which will be later used to relate the obtained Bader charge to the expected oxidation state of the oxygen atoms (see Figure A.3 in Appendix A). The oxygen charge for the pristine material (-1.18) agrees well with those found in bibliography. [5, 88]

For a more detailed analysis the individual oxidation state of each oxygen has been analyzed in two ideal and two defective  $\text{Li}_{1.25}\text{MnO}_3$  structures and in two ideal and two defective  $\text{LiMnO}_3$  structures (more than 500 different oxygen atoms). Interestingly, the oxidation state of each individual oxygen does not depend on the total oxidation state of the structure. Instead, it depends on the coordination number of each individual oxygen, i.e. the number of lithium and manganese atoms the oxygen is linked to. For instance, a pentacoordinated

Table 5.1 Relationship between the calculated Bader charge and the expected oxidation state.

Structure	Average Bader charge	Expected O oxidation state
$\text{Li}_2\text{MnO}_3$	-1.18	-2
$\text{Li}_{1.25}\text{MnO}_3$	-0.98	-1.75
$\text{LiMnO}_3$	-0.91	-1.67
$\text{Li}_{0.5}\text{MnO}_3$	-0.76	-1.5
$\text{MnO}_3$	-0.62	-1.33

oxygen atom in  $\text{Li}_{1.25}\text{MnO}_3$  has the same oxidation state than a pentacoordinated oxygen atom in  $\text{LiMnO}_3$ .

Figure 5.7 shows the average Bader Charge of the oxygen atoms from Tables A.3-A.6 in Appendix A with respect to their coordination number together with their expected oxidation state, calculated using the lineal regression from Figure A.3 in Appendix A. As expected, the oxidation state of the oxygen atoms increases when lowering their coordination number. Note that the hexacoordinated oxygen is as well partially oxidized when there are lithium vacancies, as their average oxidation state is -1.91, meaning that there is a initial general charge compensation at the first stages of delithiation. As seen in Figure 5.7, when the oxygen atom is linked to lithium atoms in tetrahedral position its oxidation state is lower regardless its coordination number. The shorter tetrahedral Li-O bonds in comparison with the octahedral ones ( $\sim 1.96 \text{ \AA}$  vs.  $\sim 2.15 \text{ \AA}$ ) reduces the degree of oxidation of the oxygen atoms and this reduces the total energy of the system, which could explain why the computed convex Hull shows an evidence of spontaneous migration to tetrahedral sites. However, note that even if the lithium in tetrahedral positions stabilizes the adjacent oxygen atoms when a lithium atom migrates from a octahedral position to a tetrahedral one its coordination number decreases from 6 to 4, so overall, two oxygen atoms loose one lithium in their coordination sphere. Therefore, there is a trade-off between both phenomena. Finally, few stable configurations with oxygen atoms with a coordination number of 2 have been found, meaning that this local configuration is highly unstable. Indeed, these tetravacancies have experimentally been found to induce undesired  $\text{O}_2$  release. [263]

### 5.3.4 Discussion

As proposed in bibliography, in the range  $2 \geq x \geq 1$  several ground states have been found close to the convex Hull for ideal  $\text{Li}_2\text{MnO}_3$ . [5, 6] This behavior has been reproduced for stacking faults containing structure, meaning that the lithium will irregularly leave the structure following a solid solution like reaction regardless the degree of stacking faults. In both cases, some lithium atoms migrate to the tetrahedral position to stabilize the overdelithiated

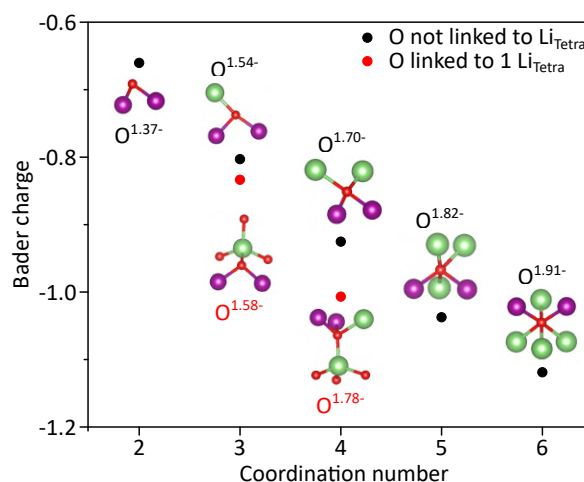


Fig. 5.7 Average Bader oxidation states for the oxygen depending on the number of atoms coordinated to the oxygen and to the number of lithium atoms which are in tetrahedral position.

oxygen atoms. The Bader charge analysis has allowed us to find that the oxidation state of the oxygen atoms depends only on their local coordination environment, and not in the total oxidation state of the structure. The overdelithiated oxygen atoms as a consequence of lithium removal from the structure become highly unstable. The lithium atoms migration to tetrahedral position shortens the Li-O bonds, reducing the oxidation state of the oxygen and thus, this migration stabilizes the implied oxygen.

At  $x = 0.5$ , the ground states of the ideal and the defective structures are different. In the  $O3$  stacking sequence, the lithium in the lithium layer share octahedral edges with lithium and manganese in the transition metal layer, as seen in Figure 5.8a. This means that, regardless the structure has or not stacking faults, the  $\text{Li}2c$  will share edges with two manganese and one  $\text{Li}2b$  atoms. In the  $O1$  stacking sequence, on the contrary, the metal atoms in the lithium layers share octahedral faces with the atoms in the transition metal layers. In the ideal stacking, the two  $\text{Li}2b$  atoms are aligned with the  $\text{Li}2c$  as seen in Figure 5.8b. This means that at highly delithiated states the absence of the  $\text{Li}2b$  permits  $\text{Li}2c$  to accommodate between these vacancies and, as it is the only occupied site in the lithium layer, the interlayer distance is reduced. If stacking faults are present (Figure 5.8c), on the contrary, the  $\text{Li}2b$  atoms are no longer aligned so the  $\text{Li}2c$  shares faces with one  $\text{Li}2b$  and with one manganese. As a result, the layer shrinkage is hindered by the Mn- $\text{Li}2c$  repulsion.

Figure 5.9 shows a comparison of the  $O1$  configurations for both ideal and defective  $\text{Li}_{0.5}\text{MnO}_3$ . In the ideal stacking configuration, the distance between the transition metal layer and the lithium layer shrinks to  $\sim 2.06 \text{ \AA}$ . In contrast, in the defective structure this shrinkage only occurs for one layer (where  $\text{Li}2c$  and the vacant  $\text{Li}2c$  are aligned), while the

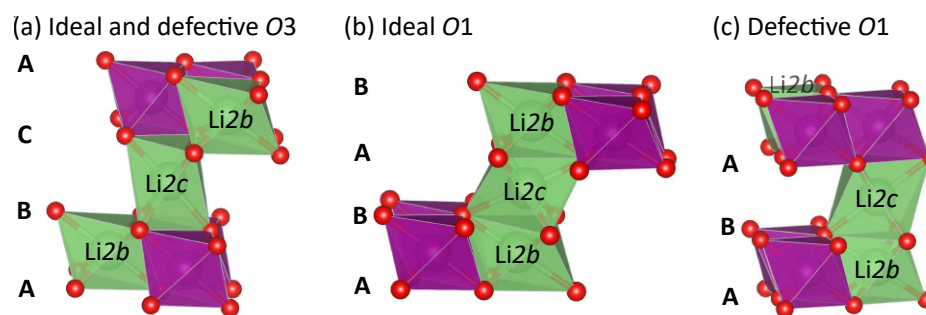


Fig. 5.8  $\text{Li}2c$  local environment differences between  $O3$  and  $O1$  ideal and defective stacking sequences.

face shared with the manganese maintains at the distance relative to the  $O3$  configuration ( $\sim 2.84 \text{ \AA}$ ). This Li-Mn repulsion increases the energy of the system so as a result, the defective  $O1$  configuration is less favored than the  $O3$  configuration, as it can be seen in the Hull of Figure 5.6. Mortemard de Boisse *et al.* found that, in isostructural defective  $\text{Na}_2\text{RuO}_3$ , at  $x = 0.5$  the structure transformed to ideal  $O1$  configuration. [281] This means that, contrary to  $\text{Li}_2\text{MnO}_3$ , the larger Ru-O and Na-O interlayer distances allow the layers to self order.

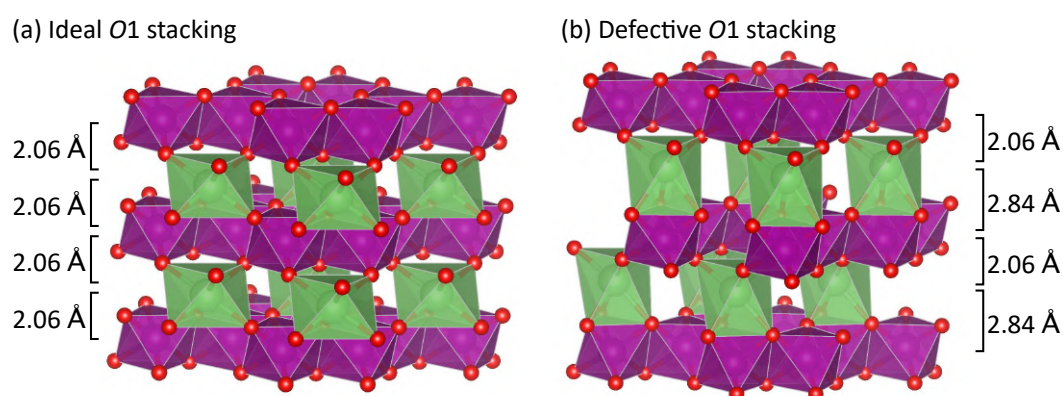


Fig. 5.9 Comparison between ideal and defective  $O1$  structure for  $\text{Li}_{0.5}\text{MnO}_3$ .

In summary, we have found a different delithiation mechanism for ideal and defective  $\text{Li}_2\text{MnO}_3$  at high delithiation states. In Section 3.5 we found that structures with low degree of stacking faults convert faster to spinel than highly faulted structures so it was deduced that the manganese migration is hindered by stacking faults. However, in our electrochemical experiment we did not reach the  $x = 0.5$  value, so, in principle, the transformation to  $O1$  should not be achieved yet. In any case, finding a metal which can be stabilized in the  $2c$  position could thus be an effective strategy to avoid undesired structural transformations.

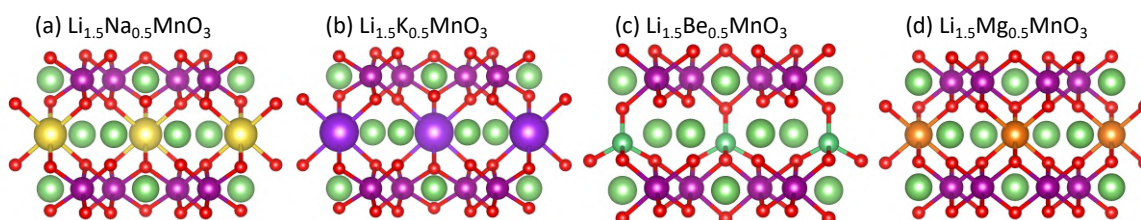
## 5.4 Atomic-scale analysis of substitution strategies to mitigate the manganese migration

Several experimental and theoretical works have reported that the high instability of the oxidized oxygen is thought to be behind the manganese migration and oxygen release. [87–89, 263, 264] The  $2c$  site has shown to be key for the stabilization of the  $O3$  configuration and avoid structural transformations. The presence of a non-mobile atom in  $2c$  position sets the minimum coordination number of all the oxygen atoms to three so it avoids its undercoordination. In this section the substitution of the  $Li_{2c}$  atom for a non mobile atom is tested which could act as a pillar which stabilizes the structure. Regarding that most of the transition metals are reported to preferentially occupy the manganese position [265] in this section alkali and earth-alkali sodium, potassium, beryllium and magnesium metals are used for this purpose. The substitution of the  $2c$  position with M gives a composition of  $Li_{1.5}M_{0.5}MnO_3$ . In the the relaxation of these structures a good energy convergence has been achieved so in principle they can be considered as stable. Even if the replacement of lithium by an inert metal diminishes the total specific capacity, this will still be considerably higher than those commercially available nowadays (shown in Table 1.1 in Chapter 1). For instance, the specific capacity of  $Li_{1.5}Mg_{0.5}MnO_3$  would be 320 mAh/g.

In order to follow the effect of the dopant in the unit cell parameters, the interlayer distance (defined here as the distance between two transition metal layers) and the  $ab$  plane area have been followed, which are shown in Table 5.2. The larger Na and K metals increase the interlayer distance. A higher interlayer distance will presumably lower the intercalation voltage due to weaker Li-O bonds, as calculated to happen for  $Na_2MnO_3$ . [282] Beryllium and magnesium, on the contrary, do not significantly vary the interlayer distance as they have similar or lower cationic size. The  $ab$  plane does not suffer from drastic changes related to the dopant size. For the case of the sodium the  $ab$  plane area remains similar. However, the bigger size of potassium enlarges the plane. For the case of magnesium, its higher oxidation state partially reduces the manganese atoms, increasing its size and thus, the  $ab$  plane. Finally, in the case of beryllium even if it as well reduces the manganese, its smaller cationic size decreases the  $ab$  plane distance. The relaxed structures drawn in Figure 5.10 show that while sodium, potassium and magnesium maintain the same  $Li_2MnO_3$  structure, the beryllium atom will preferably occupy the tetrahedral position. As a consequence, half of the  $O_{8j}$  atoms lose their Be-O bonding and become pentacoordinated and the unit cell symmetry is reduced from  $C2/m$  to  $Cm$ . Its preference for the tetrahedral site makes beryllium not suitable for the purpose of substituting lithium so it will no longer be considered in this work.

Table 5.2 Cationic size of the dopant, interlayer distance and  $ab$  plane of  $\text{Li}_{1.5}\text{M}_{0.5}\text{MnO}_3$ .

M in $\text{Li}_{1.5}\text{M}_{0.5}\text{MnO}_3$	Cationic size	Interlayer distance (Å)	$ab$ plane area (Å <sup>2</sup> )
Li	90	4.78	43.2
Na	116	5.01	43.9
K	152	5.35	46.0
Be	59	4.73	44.9
Mg	86	4.82	45.1


 Fig. 5.10 Relaxed structures of  $\text{Li}_{1.5}\text{M}_{0.5}\text{MnO}_3$  when M = (a) Na, (b) K, (c) Be and (d) Mg.

In addition to the pristine structure stability, the volume changes upon delithiation and the intercalation voltage are key for the suitability of a compound as a cathode material. While the former one is approximated by comparing the fully lithiated and fully delithiated structures, the operational voltage is calculated using the computed total energy calculated by DFT as proposed by Zhou *et al.* [248] as follows:

$$V = -\frac{E_{\text{Li}_{1.5}\text{M}_{0.5}\text{MnO}_3} - E_{\text{M}_{0.5}\text{MnO}_3} + 1.5 \cdot E_{\text{Li}}}{1.5} \quad (5.1)$$

Table 5.3 shows the volume difference and the intercalation voltage for  $\text{Li}_{1.5}\text{M}_{0.5}\text{MnO}_3$ . The volume change for the structure with potassium is 30%, while for  $\text{Li}_{1.5}\text{Na}_{0.5}\text{MnO}_3$  and  $\text{Li}_{1.5}\text{Mg}_{0.5}\text{MnO}_3$  are less than 4% and 5% respectively. Large volumetric changes are known to be detrimental for cathode durability. [52, 283, 284] In addition, the lithium intercalation voltage for the potassium containing material is too low for a lithium ion battery, as a consequence of the large interlayer distance induced by its presence, so potassium would neither be suitable to be used as a substituent. Sodium and magnesium, on the contrary could, in principle, be adequate for a deintercalation process. Therefore, in the following sections, the structural modifications upon delithiation in  $\text{Li}_{1.5}\text{Na}_{0.5}\text{MnO}_3$  and  $\text{Li}_{1.5}\text{Mg}_{0.5}\text{MnO}_3$  are studied by DFT.

#### 5.4.1 Convex Hull and oxygen oxidation in $\text{Li}_{1.5}\text{Na}_{0.5}\text{MnO}_3$

The Ewald's sampling procedure explained in Section 5.3 has been here applied to generate the different structures of the delithiated  $\text{Li}_{1.5}\text{Na}_{0.5}\text{MnO}_3$  and the DFT energy of the ten

Table 5.3 Calculated volume change and intercalation voltage for  $\text{Li}_{1.5}\text{M}_{0.5}\text{MnO}_3$  with  $\text{M} = \text{Na}, \text{K}$  and  $\text{Mg}$ .

M in $\text{Li}_{1.5}\text{M}_{0.5}\text{MnO}_3$	Volume change (%)	Voltage (V)
Na	3.8	4.2
K	30.2	1.6
Mg	4.6	3.9

most electrostatically stable structures have been calculated with DFT. Figure 5.11 shows the formation energies of  $\text{Li}_x\text{Na}_{0.5}\text{MnO}_3$  in a delithiation range of  $1.5 \geq x \geq 0$ , calculated as follows:

$$E_f(x) = E(\text{Li}_x\text{Na}_{0.5}\text{MnO}_3) - \left(\frac{1.5-x}{1.5}\right)E(\text{Na}_{0.5}\text{MnO}_3) - \frac{x}{1.5}E(\text{Li}_{1.5}\text{Na}_{0.5}\text{MnO}_3) \quad (5.2)$$

In contrast with  $\text{Li}_2\text{MnO}_3$ , all the intermediate phases are found to have higher formation energies than the end members so a two phase mechanism would be expected. However, at  $x = 0.5$  and  $x = 0.25$  the energies of some ground states are close to the Hull and could be accessible at room temperature (green area in Figure 5.12) as found to happen in other cathode materials. [285]

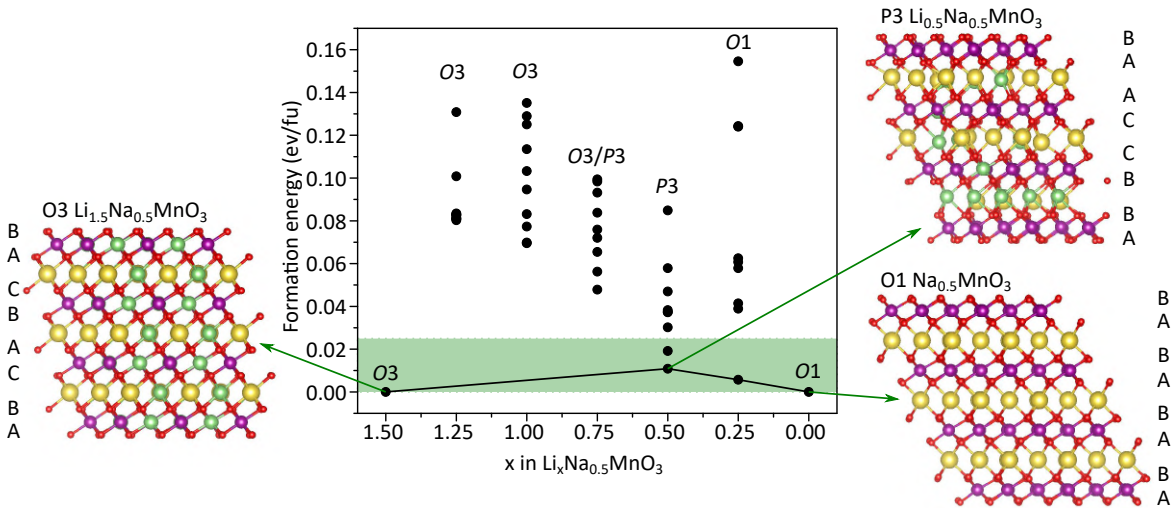


Fig. 5.11 (a) Formation energies in  $\text{Li}_x\text{Na}_{0.5}\text{MnO}_3$  ( $1.5 \geq x \geq 0$ ). (b-d). The green area indicate the thermal energy at room temperature.

Even if the formation energies are positive the path along the ground states could represent a driving force upon delithiation. From the Hull three different mechanisms are proposed, depending if these ground states are formed or not. In the first one, the phase transformation

would be hindered and the structure would maintain the  $O3$  stacking sequence. In the second one, a direct  $O3\text{-Li}_{1.5}\text{Na}_{0.5}\text{MnO}_3 \rightarrow O1\text{-Na}_{0.5}\text{MnO}_3$  reaction would occur. Finally, in the last path a two step mechanism  $O3\text{-Li}_{1.5}\text{Na}_{0.5}\text{MnO}_3 \rightarrow P3\text{-Li}_{0.5}\text{Na}_{0.5}\text{MnO}_3 \rightarrow O1\text{-Na}_{0.5}\text{MnO}_3$  is proposed, as found to happen in sodiated layered materials such as  $\text{NaCoO}_2$ . [286–288]

The calculated average intercalation voltage using the approximation of Zhou *et al.* [248] is 4.2 V, lower than for  $\text{Li}_2\text{MnO}_3$  (4.7 V), but still appropriate for a lithium cell. The larger interlayer distance in comparison with  $\text{Li}_2\text{MnO}_3$  due to the presence of larger sodium atoms in the lithium layer weakens the Li-O bonds and thus, its extraction from the structure happens at lower voltage. [282] This lower voltage of the first charging plateau is interesting because it can be useful to experimentally study the processes involved in it without the inconvenience of the electrolyte decomposition occurring at high voltages.

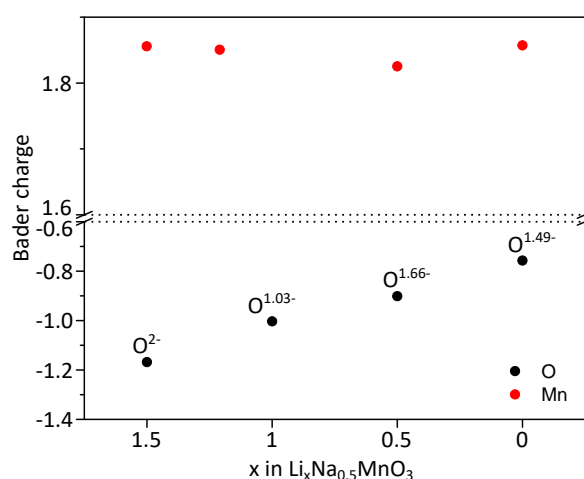


Fig. 5.12 Oxygen and manganese average oxidation states according to Bader charge calculation in  $\text{Li}_x\text{Na}_{0.5}\text{MnO}_3$ .

The Bader analysis of the oxygen and manganese in the three possible ground states of  $\text{Li}_x\text{Na}_{0.5}\text{MnO}_3$  (structures are in Figure 5.11 as insets) shows that oxygen is the main redox active center. According to our calculation, the oxidation states of the oxygen atoms are comparable with those for  $\text{Li}_2\text{MnO}_3$  seen in Table 5.1 at the same delithiation level, so the substitution of some lithium by sodium will not alter the oxygen oxidation, even if there is structural change upon the delithiation. The presence of 0.5 sodium per formula unit sets the maximum oxidation state of the oxygen to -1.5. On the other hand, the manganese remains inactive among all the delithiation process.

The homogeneous sodium distribution along the structure presents several advantages in comparison with the delithiated phases of  $\text{Li}_2\text{MnO}_3$ . On the one hand it avoids oxygen overoxidation as the highest level of vacancies it can have is three. This could minimize the metal migration to the tetrahedral positions which are thought to be behind the transformation



to spinel. [289, 290] On the other hand, the larger size of the sodium in comparison with the lithium inhibits the layer shrinkage in the  $O1$  phase. Nevertheless, for both  $\text{Li}_2\text{MnO}_3$  and  $\text{Li}_{1.5}\text{Na}_{0.5}\text{MnO}_3$  DFT calculations predict that  $O3 \rightarrow P3 \rightarrow O1$  layer gliding could occur, which is known to cause fading in the materials as a result of lattice invariant shear in layered oxides [288, 291] and should therefore be avoided.

#### 5.4.2 Convex Hull and oxygen oxidation in $\text{Li}_{1.5}\text{Mg}_{0.5}\text{MnO}_3$

The stability upon the delithiation of  $\text{Li}_{1.5}\text{Mg}_{0.5}\text{MnO}_3$  with all the Mg in the  $2c$  position has as well been studied using the same Ewald's sampling method used in previous sections and the DFT energy of the ten most electrostatically stable configurations per composition is plotted in Figure 5.13. The substitution of 0.5 lithium for a divalent cation reduces the manganese oxidation state to  $3.5+$ . This lower average oxidation state enables the redox participation of the manganese in the electrochemical activity and thus, could avoid the strong oxygen oxidation. Oxidation states lower than  $\text{Mn}^{3.5+}$  are reported to induce an undesired Jahn-Teller distortion in spinel structures, but at this oxidation state the structure is reported to be stable. [40, 292] Torres-Castro *et al.* synthesized magnesium doped  $\text{Li}_2\text{MnO}_3$  ( $\text{Li}_{1.5}\text{Mg}_{0.25}\text{MnO}_3$ ,  $\text{LiMg}_{0.5}\text{MnO}_3$  and  $\text{Li}_{0.5}\text{Mg}_{0.75}\text{MnO}_3$ ) [274] and showed that the increase in magnesium improved its capacity and the cycling stability, even if the XRD patterns showed important amounts of spinel phase.

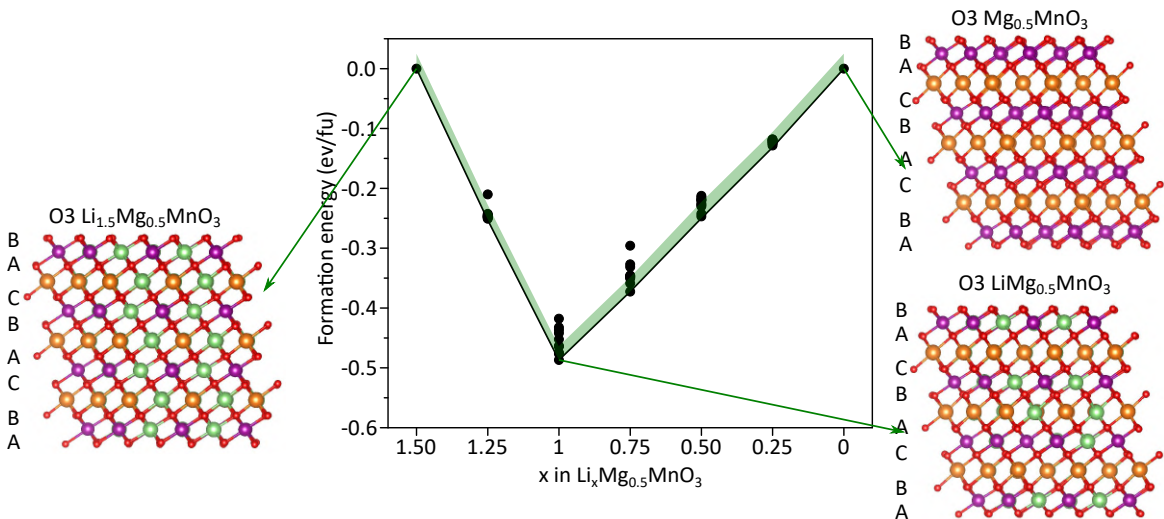


Fig. 5.13 Formation energies in  $\text{Li}_x\text{Mg}_{0.5}\text{MnO}_3$  ( $1.5 \geq x \geq 0$ ). In green the ground states which could be accessible by temperature are shown.

Figure 5.13 shows the convex Hull of  $\text{Li}_x\text{Mg}_{0.5}\text{MnO}_3$  in the  $1.5 \geq x \geq 0$  range calculated from the energies as for  $\text{Li}_x\text{Na}_{0.5}\text{MnO}_3$  in Equation 5.2. Opposite to its sodium homologous,

a deep convex Hull is obtained, and for all compositions ground states with negative formation energies are found, being that with the lowest energy at  $\text{LiMg}_{0.5}\text{MnO}_3$ . In addition, the  $O3$  configuration is maintained along the whole Hull. This represents an advantage against the sodium containing layered oxides because structural changes are known to cause capacity and voltage fading. [288, 291]

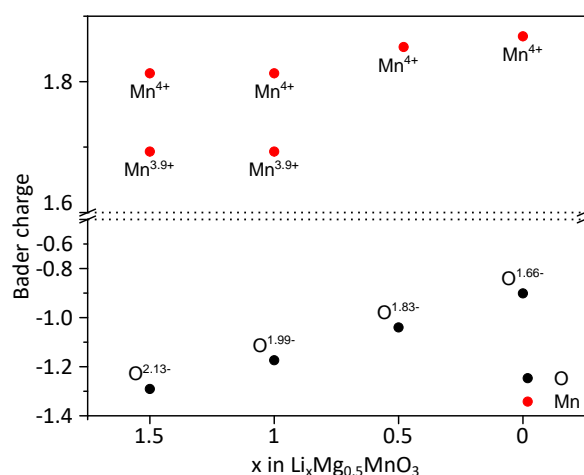


Fig. 5.14 Oxygen and manganese average oxidation states according to Bader charge calculation in  $\text{Li}_x\text{Mg}_{0.5}\text{MnO}_3$ .

The electrochemical activity of the redox pairs has been studied performing a Bader analysis. Figure 5.14 shows the average oxidation states of the manganese and the oxygen. In contrast with  $\text{Li}_2\text{MnO}_3$  and  $\text{Li}_{1.5}\text{Na}_{0.5}\text{MnO}_3$ , the fully lithiated structure contains half of the manganese atoms in  $\text{Mn}^{\text{III}}$  state and half in the  $\text{Mn}^{\text{IV}}$ . The oxidation states show that the charge of the manganese is delocalized in the oxygen atom. Note that the oxidation state of the oxygen atoms is lower than for  $\text{Li}_{1.5}\text{Na}_{0.5}\text{MnO}_3$ . This could be a consequence of charge delocalization from the reduced manganese. The removal of the first 0.5 lithium atoms oxidizes this delocalized charge. Further lithium removal oxidizes the oxygen atoms as in previous cases. As a results of the manganese redox activity, the final  $\text{Mg}_{0.5}\text{MnO}_3$  state contains oxygen atoms at -1.67 oxidation state, less oxidized than its sodium homologous.

The calculated lithium intercalation voltage of this compound is split into two plateaus; the first one at 2.9 V for the first 0.5 Li (where the delocalized charge of the manganese in the oxygen atoms is oxidized) and a second plateau in the x range of  $1 \geq x \geq 0$  at 4.3 V, related to the oxygen activity. The manganese redox activity diminishes the oxygen activity so the formation of peroxo like bonds remains unlikely. So, even if has a penalty in the total capacity in comparison with  $\text{Li}_2\text{MnO}_3$ , this compound would have a suitable operational voltage, absence of phase transformation and small unit cell volume changes, so it could be promising for electrochemical testing.

## 5.5 Conclusions

In this chapter the phase stability of both ideal and faulted  $\text{Li}_2\text{MnO}_3$  is studied by first principle calculations. The DFT energies of fully lithiated  $\text{Li}_2\text{MnO}_3$  structures with cationic stacking faults and  $O1$  type stacking faults have been calculated. The results show that, contrary to  $O1$  type stacking faults which are not likely to be found, cationic stacking faults are thermodynamically favored to happen. Among the delithiation of ideal and defective  $\text{Li}_2\text{MnO}_3$ , no big differences have been found in the  $2 \geq x \geq 1$  range. In both cases, lithium migration to tetrahedral position has found to stabilize the structure and no phase transformation is predicted. At  $\text{Li} = 0.5$ , however, the ideal stacking shows preference for the  $O1$  stacking. Blocking the  $2c$  position with a non mobile atoms (Na, K, Be, Mg) has been tough as a strategy to impede undesired structural modifications. From these, sodium and magnesium have been selected as possible candidates and their stability towards delithiation has been studied.  $\text{Li}_{1.5}\text{Na}_{0.5}\text{MnO}_3$  has shown undesired phase transformation at high delithiation states, whereas its magnesium homologous maintains the  $O3$  stacking sequence upon all the delithiation process. In addition, the lower average oxidation state of the manganese enables it to participate in the redox activity, lowering the total oxidation of the oxygen and thus hindering the peroxo formation.



# Chapter 6

## Structural analysis and study of activation mechanism in $\text{Li}_{1.2}\text{Mn}_{0.6}\text{Ni}_{0.2}\text{O}_2$

*Never memorize something you can look up.*

**Albert Einstein**

This chapter is divided into two parts. In the first one the different microstructural models proposed for Li-rich compounds are explored using diffraction techniques. These materials have been proposed to crystallize as an intergrowth of two phases or as a solid solution. XRD and NPD FAULTS simulations have been carried out considering several different microstructural arrangements for  $\text{Li}_{1.2}\text{Mn}_{0.6}\text{Ni}_{0.2}\text{O}_2$ : i) two phase mixture of  $\text{Li}[\text{Li}_{1/3}\text{Mn}_{2/3}]\text{O}_2$  and  $\text{LiMn}_{0.5}\text{Ni}_{0.5}\text{O}_2$ , ii) layered and 3D two phase intergrowth models and iii) single phase solid solution. The results obtained from the different models are discussed and compared to experimental data. In the second part of the chapter an *operando* synchrotron XRD experiment is performed for  $\text{Li}_{1.2}\text{Mn}_{0.6}\text{Ni}_{0.2}\text{O}_2$ . The patterns have been refined using a solid solution model and the use of the  $C2/m$  space group (instead of the generally used  $R\bar{3}m$  in published *operando* experiments) has resulted in new insights in the structural modification occurring upon cycling.

## 6.1 Introduction

In previous chapters the complex microstructure of the  $\text{Li}_2\text{MnO}_3$  (or  $\text{Li}[\text{Li}_{1/3}\text{Mn}_{2/3}]\text{O}_2$ ) model material has been studied and the impact of size, morphology and stacking faults in the electrochemical performance has been investigated.  $\text{Li}[\text{Li}_{1/3}\text{Mn}_{2/3}]\text{O}_2$ , represents the worst case scenario model material because related compounds where manganese is partially replaced by other transition metals like nickel or cobalt deliver much higher experimental capacities. However, these materials suffer from the same degradation phenomena (voltage and capacity fading). As mentioned in Chapter 1, there is still intense debate regarding the exact structural arrangement of these compounds. Some authors have proposed they crystallize as an intergrowth of two-phase ( $\text{Li}[\text{Li}_{1/3}\text{Mn}_{2/3}]\text{O}_2$  and  $\text{LiMO}_2$ , where  $M = \text{Mn, Ni, Co...}$ ), as first proposed by Thackeray *et al.*, [7, 8, 43, 138–140, 203] while others have proposed a single phase solid solution ( $\text{Li}_{1+x}\text{M}_{1-x}\text{O}_2$ ), according to Dahn's group. [99, 141–145] The origin of this debate is the similar structure of  $\text{Li}[\text{Li}_{1/3}\text{Mn}_{2/3}]\text{O}_2$  and  $\text{LiMO}_2$ . Even if they crystallize in different space groups ( $C2/m$  for the first one and  $R\bar{3}m$  for the latter) they both share the same NaCl-type atomic array, and the only difference resides on the extra cationic ordering of  $\text{Li}[\text{Li}_{1/3}\text{Mn}_{2/3}]\text{O}_2$ .

Local techniques such as TEM, usually combined with long range techniques (XRD, NPD, Raman), have been widely used to discriminate between the two phases and the solid solution models. Cobalt containing Li-rich compounds were found to segregate into two different domains involving  $\text{Li}[\text{Li}_{1/3}\text{Mn}_{2/3}]\text{O}_2$ -like and  $\text{LiCoO}_2$ -like domains. For instance, according to Wen *et al.*, as seen in Figure 6.1a HAADF-STEM images were indicative of a segregation with clusters below 2-3 nm in  $\text{Li}_{1.2}\text{Mn}_{0.4}\text{Co}_{0.4}\text{O}_2$ . [7, 293] Similarly, in Figure 6.1b HAADF and annular bright field (ABF) STEM images showed that  $\text{Li}[\text{Li}_{1/3}\text{Mn}_{2/3}]\text{O}_2$ -like and  $\text{LiCoO}_2$ -like zones could be distinguished in  $\text{Li}_{1.2}\text{Mn}_{0.567}\text{Ni}_{0.166}\text{Co}_{0.067}\text{O}_2$ . [8] Nevertheless, Genevois *et al.* found that  $\text{Li}_{1.20}\text{Mn}_{0.54}\text{Co}_{0.13}\text{Ni}_{0.13}\text{O}_2$  crystallized as solid solution. [294] For the case of cobalt free samples, there is as well controversy. Boulineau *et al.* found a layered stacking comprising  $\text{Li}[\text{Li}_{1/3}\text{Mn}_{2/3}]\text{O}_2$  and  $\text{LiMn}_{0.5}\text{Ni}_{0.5}\text{O}_2$  domains in  $\text{Li}_{1.2}\text{Mn}_{0.6}\text{Ni}_{0.2}\text{O}_2$  as seen in Figure 6.1c, [9] Jarvis *et al.* described the same compound as a solid solution. [295] In addition, Shukla *et al.* showed in different samples that  $\text{Li}_{1.2}\text{Mn}_{0.6}\text{Ni}_{0.2}\text{O}_2$  crystallized as a solid solution and proposed that the existing discrepancies arose from the fact that several different structures can give the same projections, especially in the  $[010]_m$  direction. [145] Different models have been proposed using the same characterization methods and the only reconciling explanation found so far has been the differences in the synthetic method. [137]

XRD and NPD have been as well used to try to distinguish between an intergrowth of two phases [113, 144, 296] or a solid solution generally using the  $R\bar{3}m$  space group

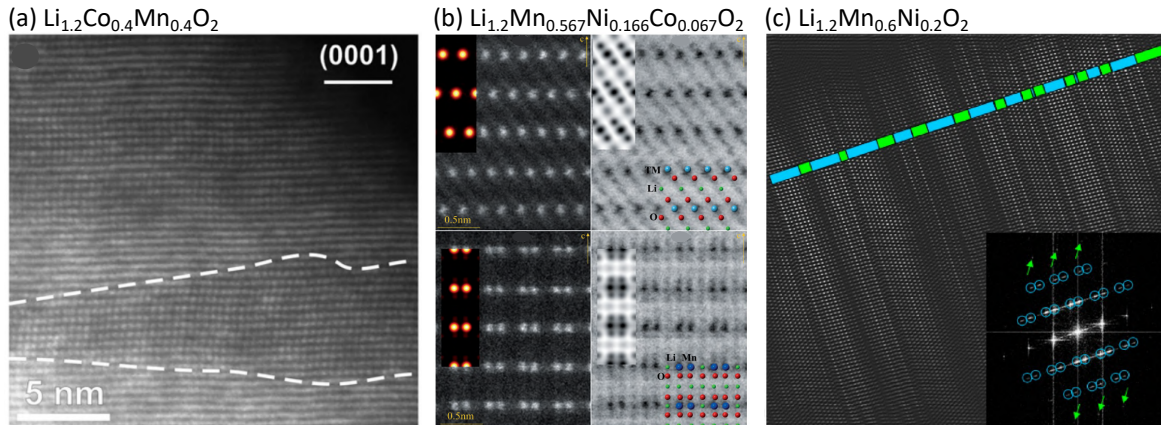


Fig. 6.1 TEM images for  $\text{Li}_{1+x}\text{M}_{1-x}\text{O}_2$ , showing two phase model. (a) HAADF images of  $\text{Li}_{1.2}\text{Co}_{0.4}\text{Mn}_{0.4}\text{O}_2$  revealing the coexistence of  $\text{Li}[\text{Li}_{1/3}\text{Mn}_{2/3}]\text{O}_2$ -like (dot contrast) and  $\text{LiCoO}_2$ -like (continuous contrast) areas. [7] (b) Left HAADF and right ABF-STEM images for  $\text{Li}_{1.2}\text{Mn}_{0.567}\text{Ni}_{0.166}\text{Co}_{0.067}\text{O}_2$ . In top the  $\text{LiMO}_2$ -like structure and in bottom the  $\text{Li}[\text{Li}_{1/3}\text{Mn}_{2/3}]\text{O}_2$ -like structure are shown. Insets in right images are the crystal-structure image of the  $\text{LiMO}_2$  and the  $\text{Li}[\text{Li}_{1/3}\text{Mn}_{2/3}]\text{O}_2$ -like structures. [8] (c) HAADF-STEM image of  $\text{Li}_{1.2}\text{Mn}_{0.6}\text{Ni}_{0.2}\text{O}_2$  containing  $\text{Li}[\text{Li}_{1/3}\text{Mn}_{2/3}]\text{O}_2$  domains (blue) and  $\text{LiMO}_2$  domains (green). Reflections characteristic of the ordered slabs are circled in blue and those related to the disordered ones are pointed with green arrows on the Fourier transform in the inset. [9]

[109, 141] without a concluding result. As mentioned in Chapter 1, the use of  $R\bar{3}m$  space group represents an oversimplification as it excludes the superstructure peaks at  $2\theta = 20\text{-}35^\circ$ .

This unsolved controversy has actually led to a million dollar battle between two battery companies and therefore still deserves attention. BASF licensed the patent of Argonne National Laboratory (ANL) which describes NMC compounds as a composite or a two phase material. Umicore, on the contrary started manufacturing NMC material which, according to their research, was single phase solid solution. On 30 March 2015 BASF and ANL complained on the U.S. International Trade Commission (ITC) alleging the infringement of two patents. On December 16<sup>th</sup> 2016 the ITC notified its decision of the infringement of these two patents. Finally, in 25 April 2017 both companies reached an agreement that allows Umicore to sell their Li-rich NMC product under the patent of BASF and ANL. [146]

The structural complexity of the pristine material is not the only issue to solve in these materials. The structural transformation occurring in the first charge is neither well understood. As discussed in Chapter 3 for  $\text{Li}_2\text{MnO}_3$  the first charge is usually described as two different regions. In the first one, up to  $\sim 4.5$  V, the compound operates as a classic layered oxide and the electrochemical activity is attributed to the oxidation of the transition metals. [99, 100, 222, 297] In the second one, easily identified with a voltage plateau at  $\sim 4.7$  V, an irreversible structural reorganization occurs which includes i) transition metal migration

within the transition metal layer or to the lithium layer, which causes a reduction or a loss of the honeycomb like ordering [103, 222, 290, 298, 299] and ii) oxidation of the oxygen which can be either reversible and described as the loss of the labile electron from the unhybridized 2p orbital, [84, 89, 102, 264, 300–303] or irreversible as a consequence of peroxide species formation and partial lattice oxygen loss. [74, 77, 100, 102, 222, 225, 251, 290, 304]

In this chapter the FAULTS program will be used to build different structural models that take into account the microstructural features described in the bibliography. The use of FAULTS opens the possibility to simulate structural models that combine stacking faults and intergrowth structures and explore the capability of XRD and NPD to discriminate between the two main proposed models. The selected composition for the simulations is  $\text{Li}_{1.2}\text{Mn}_{0.6}\text{Ni}_{0.2}\text{O}_2$ , which is known to exhibit good electrochemistry [67, 98, 112, 140, 201, 305–308] and it is cobalt free. Later, this compound is synthesized and the experimental results of an *operando* XRD experiment are analyzed. The use of  $C2/m$  space group has allowed to identify novel aspects related to the oxygen evolution not reported up to date.

## 6.2 FAULTS XRD and NPD simulations of different microstructural models corresponding to $\text{Li}_{1.2}\text{Mn}_{0.6}\text{Ni}_{0.2}\text{O}_2$

In this section the XRD patterns of the different structural models are simulated. These correspond to: i) a two phase model, ii) intergrowth model and iii) solid solution model. Note that the nomenclature of  $\text{Li}_2\text{MnO}_3$  affect the stoichiometry.  $\text{Li}_{1.2}\text{Mn}_{0.6}\text{Ni}_{0.2}\text{O}_2$  can be described as a 1:1 mixture of  $\text{Li}_2\text{MnO}_3$  and  $\text{LiMn}_{0.5}\text{Ni}_{0.5}\text{O}_2$  or as a 0.6:0.4 for mixture of  $\text{Li}[\text{Li}_{1/3}\text{Mn}_{2/3}]\text{O}_2$  and  $\text{LiMn}_{0.5}\text{Ni}_{0.5}\text{O}_2$ . In this chapter, for an easier comparison, we will refer to  $\text{Li}_2\text{MnO}_3$  as  $\text{Li}[\text{Li}_{1/3}\text{Mn}_{2/3}]\text{O}_2$ . As  $\text{Li}[\text{Li}_{1/3}\text{Mn}_{2/3}]\text{O}_2$  and  $\text{LiMn}_{0.5}\text{Ni}_{0.5}\text{O}_2$  share the same skeleton both can be described with a common unit cell. The steps for the unification of both unit cells are shown in Figure 6.2. Firstly, the primitive unit cell of each structure is found according to certain standards defined in Reference [309] (Figure 6.2b) using pymatgen modules for python [250]. Later, these are transformed using the Matrices 6.1 and 6.2 for  $\text{LiMn}_{0.5}\text{Ni}_{0.5}\text{O}_2$  and  $\text{Li}[\text{Li}_{1/3}\text{Mn}_{2/3}]\text{O}_2$  respectively to a common unit cell that is averaged (same dimensions, but different content) shown in Figure 6.2c. Since the layers described in FAULTS structural models need to be perpendicular to the stacking direction (i.e.  $\alpha$  and  $\beta$  need to be  $90^\circ$ ) a final transformation is performed (see Figure 6.2d).

$$\begin{pmatrix} -1 & -1 & 0 \\ 1 & -2 & 0 \\ 0 & 0 & 1 \end{pmatrix} \quad (6.1)$$



$$\begin{pmatrix} 1 & 1 & 0 \\ 0 & 1 & 0 \\ 0 & 0 & 1 \end{pmatrix} \quad (6.2)$$

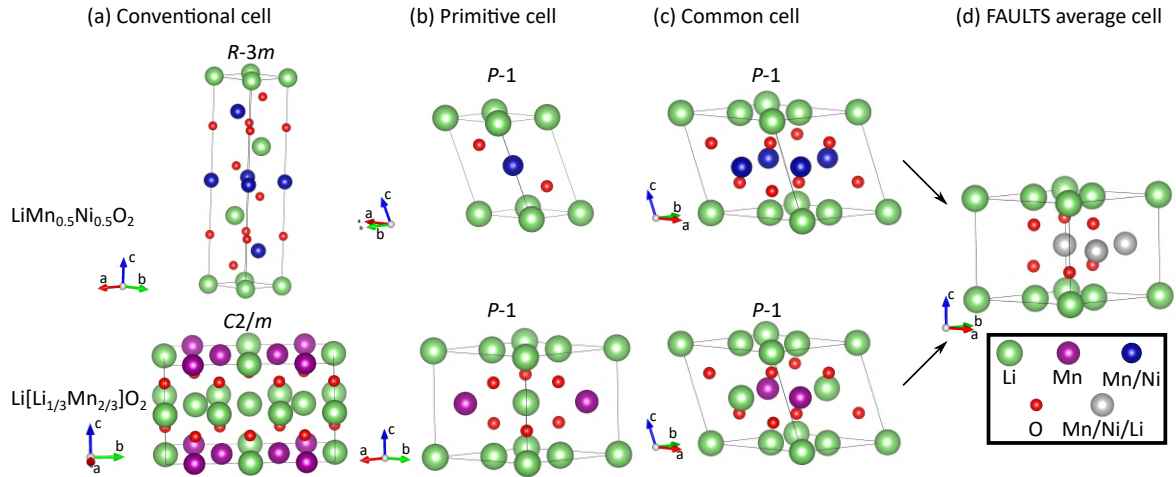


Fig. 6.2 Steps followed to transform  $C2/m$  and  $R\bar{3}m$  unit cell to a common one suitable for the FAULTS program. Top shows the transformation of  $\text{LiMn}_{0.5}\text{Ni}_{0.5}\text{O}_2$  and bottom the transformation of  $\text{Li}[\text{Li}_{1/3}\text{Mn}_{2/3}]\text{O}_2$ .

Table 6.1 Unit cell parameters of  $\text{LiMn}_{0.5}\text{Ni}_{0.5}\text{O}_2$  and  $\text{Li}[\text{Li}_{1/3}\text{Mn}_{2/3}]\text{O}_2$  according to the different descriptions used in this chapter.

Unit cell	Structure	<i>a</i>	<i>b</i>	<i>c</i>	$\alpha$	$\beta$	$\gamma$
Conventional	$\text{LiMn}_{0.5}\text{Ni}_{0.5}\text{O}_2$ ( $R\bar{3}m$ )	2.891	2.891	14.30	90	90	120
	$\text{Li}[\text{Li}_{1/3}\text{Mn}_{2/3}]\text{O}_2$ ( $C2/m$ )	4.929	8.532	5.025	90	109.34	90
Primitive	$\text{LiMn}_{0.5}\text{Ni}_{0.5}\text{O}_2$	2.891	2.891	5.051	73.37	73.37	60
	$\text{Li}[\text{Li}_{1/3}\text{Mn}_{2/3}]\text{O}_2$	4.927	4.927	5.025	99.54	99.54	119.96
Common	$\text{LiMn}_{0.5}\text{Ni}_{0.5}\text{O}_2$	5.008	5.008	5.051	99.51	109.30	60
	$\text{Li}[\text{Li}_{1/3}\text{Mn}_{2/3}]\text{O}_2$	4.927	4.927	5.025	99.54	109.34	59.98
	Average	4.961	4.961	5.041	99.33	109.32	59.99
	FAULTS cell	4.961	4.961	4.742	90	90	59.99

This averaged unit cell represents the smallest possible unit to describe both structures. The atomic positions for the unified unit cell are given in Table A.7 in Appendix A. Depending on the needs for each model, however, supercells have been built using this cell as basic structural unit.

On the other hand, in order to compare the simulated patterns with an experimental one,  $\text{Li}_{1+x}\text{NMO\_SC\_900\_5}$  sample has been synthesized (whose synthesis conditions summarized

in Section 2.1). A relatively high synthesis temperature of 900 °C has been chosen for a better definition of the peaks. Its Rietveld refined pattern is shown in Figure 6.3 and the final refined values are shown in Table A.9 in Appendix A (data acquired at the 11 ID-B beam line at the APS at Chicago). Below, the different models are described and the resulting simulations are compared to the experimental XRD pattern.

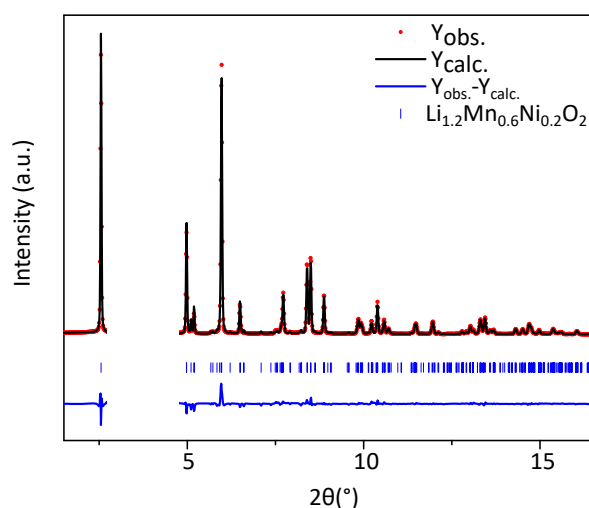


Fig. 6.3 Rietveld refined pattern of  $\text{Li}_{1+x}\text{NMO\_SC\_900\_5}$  sample.

### 6.2.1 Two phase model

In this first model  $\text{Li}[\text{Li}_{1/3}\text{Mn}_{2/3}]\text{O}_2$  and  $\text{LiMn}_{0.5}\text{Ni}_{0.5}\text{O}_2$  are considered to crystallize as micrometric independent particles. Figure 6.4a shows the sum of the two simulated XRD patterns, whose unit cell values are taken from bibliography. [204, 310] As we can appreciate in Table 6.1,  $\text{LiMn}_{0.5}\text{Ni}_{0.5}\text{O}_2$  has larger unit cell parameters than  $\text{Li}[\text{Li}_{1/3}\text{Mn}_{2/3}]\text{O}_2$ , meaning that the diffraction peaks will appear at lower  $2\theta$  values. As it is better appreciated in the inset of Figure 6.4a, at low  $2\theta$  angles the peaks coming from  $\text{Li}[\text{Li}_{1/3}\text{Mn}_{2/3}]\text{O}_2$  and from  $\text{LiMn}_{0.5}\text{Ni}_{0.5}\text{O}_2$  are strongly overlapped and cannot be distinguished. Nonetheless, at higher  $2\theta$  values the peaks of the two phases are better resolved. For instance, the peak at  $45^\circ$  is displaced to lower  $2\theta$  values for  $\text{LiMn}_{0.5}\text{Ni}_{0.5}\text{O}_2$  and it is easily distinguished from its  $\text{Li}[\text{Li}_{1/3}\text{Mn}_{2/3}]\text{O}_2$  homologous peak. Therefore, even if the atomic array of  $\text{Li}[\text{Li}_{1/3}\text{Mn}_{2/3}]\text{O}_2$  and  $\text{LiMn}_{0.5}\text{Ni}_{0.5}\text{O}_2$  is similar their XRD can be easily differentiated.

This result has been experimentally validated with the experimental pattern of a mixture of two samples prepared in our laboratory (samples  $\text{LMO\_MnCO}_3\text{\_900\_5}$  and  $\text{LNMO\_SC\_900\_5}$ ; synthesis conditions summarized in Section 2.1) whose Rietveld refined patterns are shown in Figure 6.5 and the refined parameters in Tables 6.2 and 6.3. These

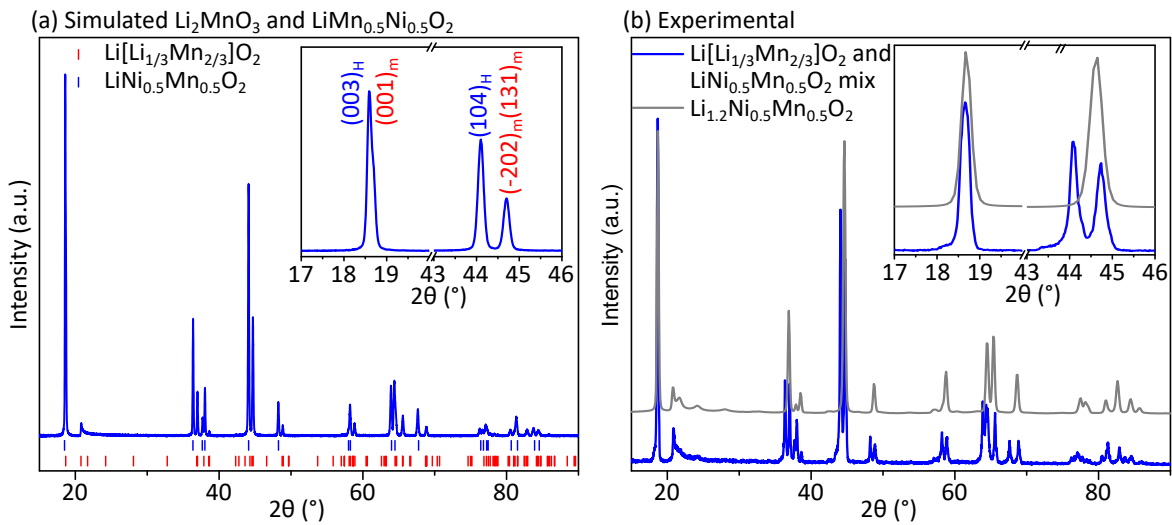


Fig. 6.4 (a) Simulated XRD patterns of  $\text{Li}[\text{Li}_{1/3}\text{Mn}_{2/3}]\text{O}_2$  and  $\text{LiMn}_{0.5}\text{Ni}_{0.5}\text{O}_2$  mixture. The Bragg positions for each phase are found below;  $\text{Li}[\text{Li}_{1/3}\text{Mn}_{2/3}]\text{O}_2$  in red and  $\text{LiMn}_{0.5}\text{Ni}_{0.5}\text{O}_2$  in blue. (b) Experimental XRD pattern of the mixture of  $\text{Li}[\text{Li}_{1/3}\text{Mn}_{2/3}]\text{O}_2$  and  $\text{LiMn}_{0.5}\text{Ni}_{0.5}\text{O}_2$  compared to  $\text{Li}_{1.2}\text{Mn}_{0.6}\text{Ni}_{0.2}\text{O}_2$ .

samples were mixed in a 0.6:0.4 ratio for  $\text{Li}_2\text{MnO}_3:\text{LiMn}_{0.5}\text{Ni}_{0.5}\text{O}_2$  and the resulting XRD is shown in Figure 6.4. Note that the intensity differences in some peaks between the simulated mixture in Figure 6.4a and the experimental one in Figure 6.4b (such as that at  $\sim 45^\circ$ ) can be the consequence of differences between the simulated and experimental atomic positions and occupancies, as well as the Li/Ni mixing the experimental patterns shows. However, as seen in the simulations, two diffraction peaks appear at  $45^\circ$  in the mixture, while the  $\text{Li}_{1.2}\text{Mn}_{0.6}\text{Ni}_{0.2}\text{O}_2$  patterns exhibits a single reflection in this region. Therefore, it can be unambiguously concluded that  $\text{Li}_{1.2}\text{Mn}_{0.6}\text{Ni}_{0.2}\text{O}_2$  does not crystallize as a two phase mixture of micrometric particles and this model can thus be discarded.

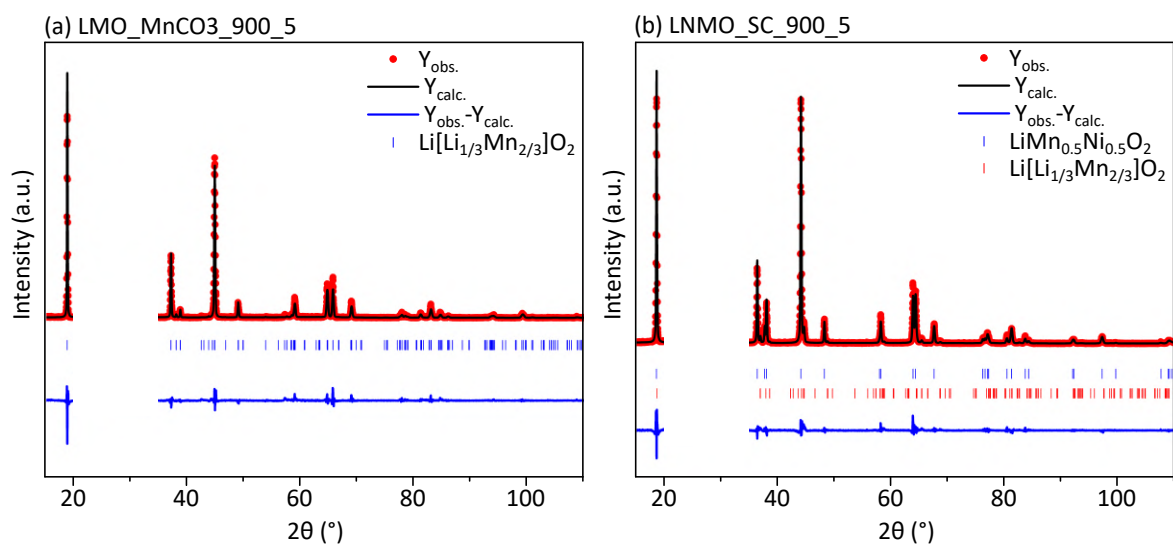


Fig. 6.5 Rietveld refinements of (a) LMO\_MnCO3\_900\_5 and (b) LNMO\_SC\_900\_5 samples.

Table 6.2 Rietveld refined parameters for LNMO\_SC\_900\_5.

Space group	$R\bar{3}m$		
Lattice parameters (Å)	$a, b$	2.89402(7)	
	$c$	14.3123(6)	
	Volume	103.8113	
Atomic positions	x	y	z
3a	0.00000	0.00000	0.00000
3b	0.00000	0.00000	0.50000
6c	0.00000	0.00000	0.2428(5)
Occupancies	3b M/Li	0.884(4)/0.116(1)	
	3a Li/M	0.884(4)/0.116(1)	
Microstructural parameters	Particle size (nm)	73	
	Strains (%%)	13	
Agreement factors	$R_p$	15.3	
	$wR_p$	20.0	
	$R_{exp}$	12.3	
	$\chi^2$	2.653	

Table 6.3 Rietveld refined parameters for LMO\_MnCO3\_900.

Space group	$C2/m$		
Lattice parameters (Å)	$a$	4.9250(6)	
	$b$	8.528(1)	
	$c$	5.0182(4)	
	$\beta$	109.22(1)	
	Volume	199.198	
Atomic positions	x	y	z
$2b$	0.00000	0.00000	0.00000
$4g$	0.00000	0.326(2)	0.00000
$2c$	0.50000	0.00000	0.50000
$4h$	0.00000	0.84000	0.50000
$4i$	0.27(1)	0.00000	0.77(1)
$8j$	0.749(9)	0.844(4)	0.766(6)
Occupancies	4g Mn/Li	0.70(2)/0.30(1)	
	2b Li/Mn	0.70(2)/0.30(1)	
Microstructural parameters	Particle size (nm)	120	
	Strains (%%)	17	
Agreement factors	$R_p$	22.7	
	$wR_p$	28.4	
	$R_{exp}$	16.7	
	$\chi^2$	2.89	

### 6.2.2 Intergrowth models

According to the results shown in the previous section, the scenario of intergrowth of two models would only be in agreement with experimental XRD patterns if both components share the same unit cell dimensions. This possibility is not totally unlikely, as could be the result of local composition differences or strained unit cells similar to those occurring in epitaxial growth of thin films. In this section, XRD patterns corresponding to intergrowth structures of  $\text{Li}[\text{Li}_{1/3}\text{Mn}_{2/3}]\text{O}_2$  and  $\text{LiMn}_{0.5}\text{Ni}_{0.5}\text{O}_2$  are simulated. Two possibilities have been considered: in a first more simplified model the intergrowth of the two phases is considered to occur only along the  $c$  direction, so that layers corresponding to  $\text{Li}[\text{Li}_{1/3}\text{Mn}_{2/3}]\text{O}_2$  and  $\text{LiMn}_{0.5}\text{Ni}_{0.5}\text{O}_2$  alternate in the structure, as proposed by Boulineau *et al.* for  $\text{Li}_{1.2}\text{Mn}_{0.6}\text{Ni}_{0.2}\text{O}_2$  (see Figure 6.1c). [9] In the second model an intergrowth in three dimensions (3D) has been simulated, varying their average size.

### 6.2.2.1 Layered intergrowth of $\text{Li}[\text{Li}_{1/3}\text{Mn}_{2/3}]\text{O}_2$ and $\text{LiMn}_{0.5}\text{Ni}_{0.5}\text{O}_2$

As a first approach, a random stacking of layers is considered. By varying the stacking probabilities we are able to build structures made of blocks of different sizes in  $c$  so that the effect of the blocks' average size in the patterns can be evaluated. The average size of the blocks has been calculated by varying the stacking probabilities (details given in Section A.5.3 in Appendix A).

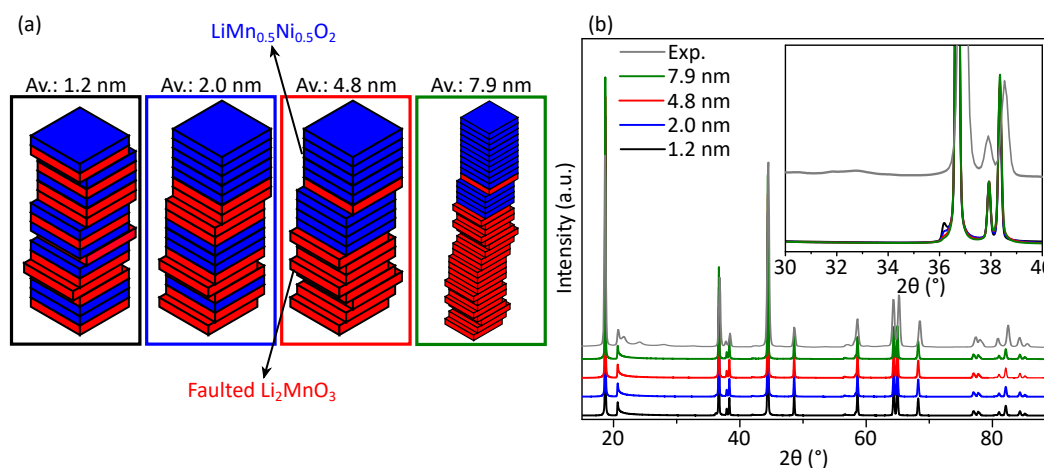


Fig. 6.6 (a) Schematic representation of the structures built where red layers represent  $\text{Li}[\text{Li}_{1/3}\text{Mn}_{2/3}]\text{O}_2$  and blue layers  $\text{LiMn}_{0.5}\text{Ni}_{0.5}\text{O}_2$ . Note that the average block thickness varies from one representation to the other. (b) Simulated XRD patterns corresponding to the four studied samples. The inset shows a zoom to the  $2\theta$  range  $30\text{--}40^\circ$

Figure 6.6a shows a graphic representation of the four simulated structures. Red layers represent  $\text{Li}[\text{Li}_{1/3}\text{Mn}_{2/3}]\text{O}_2$ , while blue layers correspond to  $\text{LiMn}_{0.5}\text{Ni}_{0.5}\text{O}_2$ . Note that in  $\text{Li}[\text{Li}_{1/3}\text{Mn}_{2/3}]\text{O}_2$  stacking faults have been included considering a completely faulted structure for a more realistic study. The structure in the black square has the smallest average block thickness while the blocks in the green square are the largest. Figure 6.6b shows the simulated XRD patterns corresponding to average thicknesses of 1.2, 2.0, 4.0 and 7.9 nm for the black, blue, red and green lines respectively. The main reflections are similar in all cases. Nevertheless, the inset in the figure shows that there is a small peak at  $2\theta = 36^\circ$  which becomes weaker with increasing size of the blocks. At 7.9 nm the peak is still visible.

The TEM images published in Boulineau's work [9] exhibit blocks of about 5-10 layers, which approximately correspond to 3.5 nm. [9] At these size values this peak should be visible in the XRD patterns. In our experimental diffraction pattern, however, this peak is not present. The absence of this peak can therefore be used to discard the intergrowth of pure layers as a valid model for the structure of our  $\text{Li}_{1.2}\text{Mn}_{0.6}\text{Ni}_{0.2}\text{O}_2$  sample.

### 6.2.2.2 3D intergrowth of $\text{Li}[\text{Li}_{1/3}\text{Mn}_{2/3}]\text{O}_2$ and $\text{LiMn}_{0.5}\text{Ni}_{0.5}\text{O}_2$

Wen *et al.* [7] observed a 3D intergrowth of the two phases by TEM. In this section 2D intergrowth structures are simulated using a large cell of  $50 \times 50 \text{ \AA}$  in the  $ab$  plane, i.e. a  $5 \times 5 \times 1$  supercell of the FAULTS unit cell, which has been built using pymatgen module. Three different layer types have been considered to take into account the effect of domain size. The first one, shown in the black square of Figure 6.7a, consists in clusters of  $\text{LiMn}_{0.5}\text{Ni}_{0.5}\text{O}_2$  and  $\text{Li}[\text{Li}_{1/3}\text{Mn}_{2/3}]\text{O}_2$  with a fixed size of  $2.5 \times 2.5 \text{ nm}$ . In the second and third layer types, shown in the red and blue squares, the  $\text{Li}[\text{Li}_{1/3}\text{Mn}_{2/3}]\text{O}_2$  and  $\text{LiMn}_{0.5}\text{Ni}_{0.5}\text{O}_2$  units are stochastically distributed. By varying the stochastic distribution average, larger or smaller domains are obtained (note that the average domains in the red square are larger than in the blue square). For each simulation 10 different layers (same type of layer but different motif) are used to build the 3D model in order to minimize the effect of their ordering along the  $c$  axis.

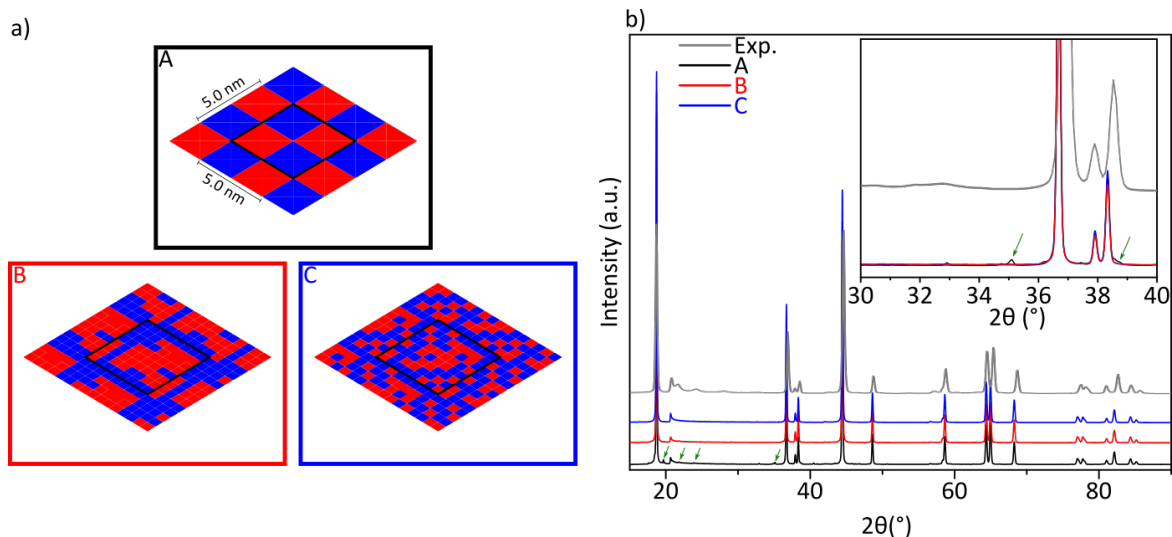


Fig. 6.7 (a) Representation of the layers formed by clusters of  $\text{Li}[\text{Li}_{1/3}\text{Mn}_{2/3}]\text{O}_2$  (in red) and  $\text{LiMn}_{0.5}\text{Ni}_{0.5}\text{O}_2$  (in blue) along the same  $ab$  plane used in the simulation of the XRD patterns. (b) simulated XRD patterns using the layers represented in (a). The inset shows a zoom to the  $2\theta$  range  $30\text{-}40^\circ$ .

Figure 6.7b shows the simulated XRD patterns obtained using these models. Note that the colors of the diffractogram match with the colors of the boxes. In addition, the experimental XRD pattern is included for comparison. The XRD pattern for the structure in the black box shows extra peaks (marked with green arrows) as a consequence of the regular motif in the  $ab$  plane. In contrast, the XRD patterns for the stochastically distributed domains show no additional peaks regardless the average size of the domain and no difference is observed between them. In this case, the XRD patterns reproduce well the experimental patterns.

Again, the intensity differences between the simulated and the experimental patterns are consequence of slightly different atomic positions and occupancies. It can be thus concluded that, as long as the domains are stochastically distributed,  $\text{Li}_{1.2}\text{Mn}_{0.6}\text{Ni}_{0.2}\text{O}_2$  can be formed of nanodomains of  $\text{Li}[\text{Li}_{1/3}\text{Mn}_{2/3}]\text{O}_2$  and  $\text{LiMn}_{0.5}\text{Ni}_{0.5}\text{O}_2$ , regardless their size.

### 6.2.3 $\text{Li}_{1.2}\text{Mn}_{0.6}\text{Ni}_{0.2}\text{O}_2$ solid solution

In this section, the solid solution model is studied. Firstly, the Ewald's sampling method is used to find the most electrostatically stable metal distribution, which is later corroborated with DFT calculations. Secondly, the XRD patterns of the resulting solid solution structure are simulated.

#### 6.2.3.1 Atomic distribution in the transition metal layer

In order to study the atomic distribution in the transition metal layer a supercell is built by applying the transformation Matrix 6.3 to the FAULTS unit cell.

$$\begin{pmatrix} 1 & 1 & 0 \\ 5 & -5 & 0 \\ 0 & 0 & 1 \end{pmatrix} \quad (6.3)$$

Two different approaches have been considered. In the first one the superstructure of  $\text{Li}[\text{Li}_{1/3}\text{Mn}_{2/3}]\text{O}_2$  is partially maintained and nickel replaces some manganese and some lithium atoms. In this case, the transition metal layer is modified from  $[\text{Li}_{1/3}]_{2b}[\text{Mn}_{2/3}]_{4g}$  to  $[\text{Li}_{0.2}\text{Ni}_{0.13}]_{2b}[\text{Mn}_{0.6}\text{Ni}_{0.07}]_{4g}$ . In the second approach the atoms are randomly distributed along the transition metal layer. For the first possibility the amount of possible structures is limited to 140, whose Ewald's energy is shown in Figure 6.8a. The structure shown as an inset is a representation of one of the structure maintaining the superstructure ordering. For the second case, on the contrary, the number of possible different structures is much higher and the Ewald's energy of 10,000 structures have been calculated (Figure 6.8b). The structures in the figure show two selected points, one with low energy and a second one with high energy. Note that the energies of the structures from Figure 6.8a are included in the green square in Figure 6.8b for comparison and are considerably more stable than any configuration with randomly distributed transition metals. The random distribution of the metals can lead to cationic clustering where manganese rich zones and lithium/nickel rich zones are generated. In order to maintain local neutrality, in manganese rich zones manganese will be reduced as  $\text{Mn}^{\text{III}}$  and in Ni/Li-rich zones the nickel will be oxidized



as  $\text{Ni}^{\text{III}}$  or  $\text{Ni}^{\text{IV}}$  (with respect to the most stable configuration:  $\text{Mn}^{\text{IV}}$  and  $\text{Ni}^{\text{II}}$ ). Therefore, manganese and nickel segregation is not favored.

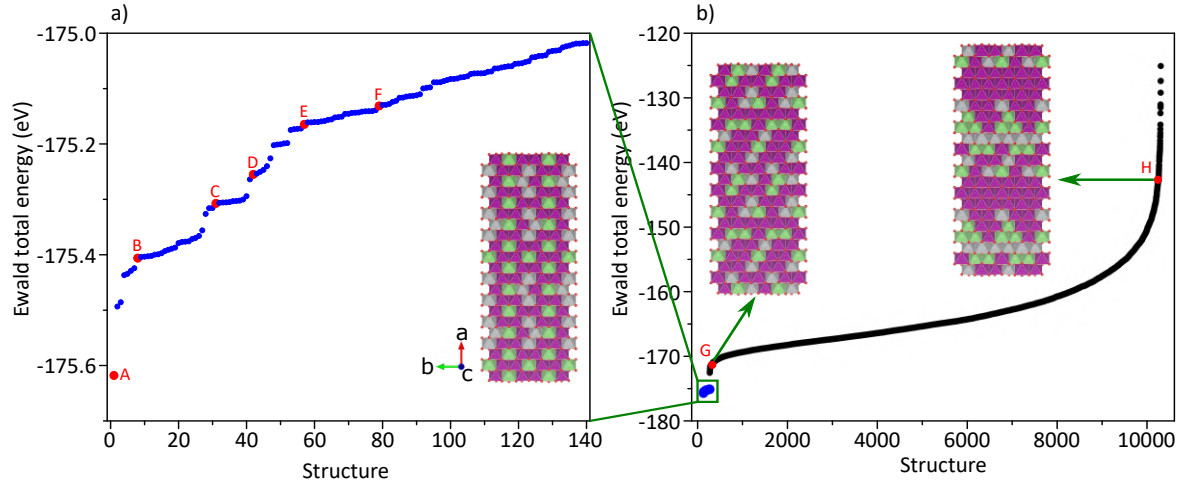


Fig. 6.8 Ewald summation energy of different  $\text{Li}_{1.2}\text{Mn}_{0.6}\text{Ni}_{0.2}\text{O}_2$  configurations (a) maintaining the superstructure ordering and (b) with all the metals randomly distributed in the transition metal layer.

The validity of these results is tested by calculating the DFT energy of some selected structures (A-H points in Figure 6.8). The results in Table 6.4 suggest that while the superstructure is maintained (structures A-F), different energetically degenerated states are achieved and are equally probable at room temperature, but as soon as the order is broken (G, H) the energy of the system considerably increases. Maintaining the initial lithium and manganese positions is thus the most energetically favored metal distribution.

Table 6.4 Calculated DFT energies for structures with different layer transition metal distribution corresponding to the points indicated in Figure 6.8.

Ordered structures	Energy (eV)
A	-36.10
B	-36.10
C	-36.10
D	-36.09
E	-36.09
F	-36.09
Disordered structures	Energy
G	-35.92
H	-35.54

### 6.2.3.2 XRD pattern simulation of solid solution

The FAULTS simulations have been performed using the transition metal distribution with the lowest Ewald's energy. Figure 6.9 shows simulated XRD patterns using a different number of layers: one, three and ten (those with the lowest energy in Figure 6.8a are used). In addition, a small unit cell with partial occupancies corresponding to  $[\text{Li}_{0.2}\text{Ni}_{0.13}]_{2b}$  and  $[\text{Mn}_{0.6}\text{Ni}_{0.07}]_{4g}$  is used as a simulation of infinite different types of layers. If only one type of layer is used in the simulation to describe the whole structure (i.e. the same layer is used to build a stack of layers), extra peaks are present in the diffractogram (some marked with green arrows) as a result of the ordering of the atoms in the  $ab$  plane which is repeated along  $c$ . As the number of different layers is increased, the intensity of these peaks decreases. If an infinite number of different layer types is reproduced (with the use of partial occupancies) the peaks related to this ordering disappear. The XRD pattern generated by the use of partial occupancies reproduces the experimental pattern, which means that this structural model is as well valid for the description of Li-rich compounds.

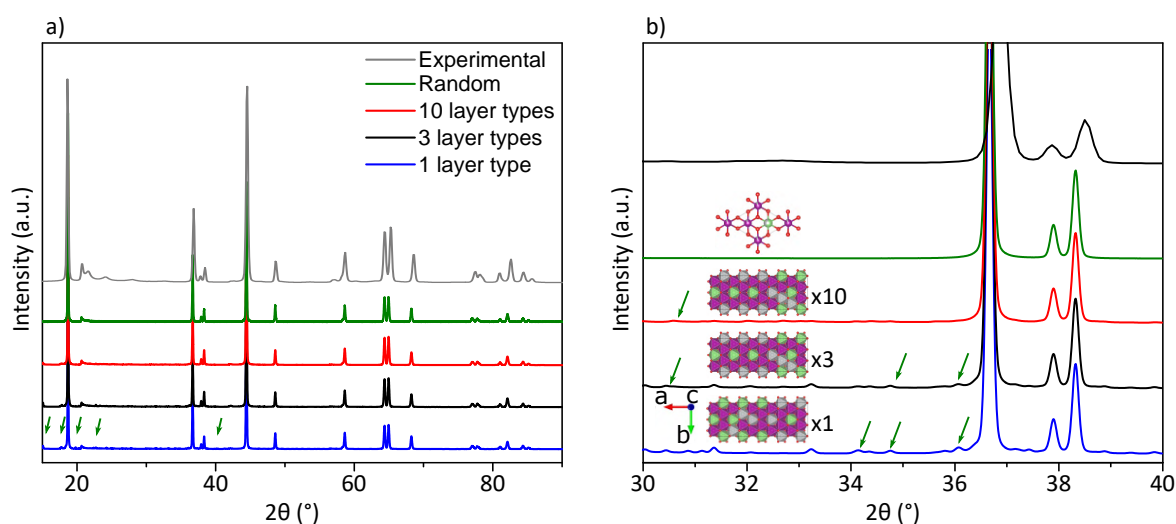


Fig. 6.9 (a) XRD patterns for different solid solution simulations. (b) Zoom of the superstructure zone.

Overall, three different structural models have been studied to describe the structure of  $\text{Li}_{1.2}\text{Mn}_{0.6}\text{Ni}_{0.2}\text{O}_2$ . The two phase model has been rejected as the different unit cell sizes of  $\text{Li}[\text{Mn}_{0.5}\text{Ni}_{0.5}]\text{O}_2$  and  $\text{Li}[\text{Li}_{1/3}\text{Mn}_{2/3}]\text{O}_2$  result in additional peaks in the XRD patterns which are not present in experimental patterns. The layered intergrowth model proposed by Boulineau *et al.* has been discarded as well because it generates a peak at  $36^\circ$  which is not present in experimental patterns. The 3D intergrowth model on the contrary does not present any additional peak so this model could be used to describe the structure. Similarly, the solid

solution structural model has as well shown to be possible. These results confirm that the use of XRD to distinguish between the two models is extremely challenging. However, NPD data could provide interesting information because of the different scattering factor between nickel lithium and manganese, especially in the superstructure zone, where distinguishing between nickel and manganese could be key. In the following section the results obtained in NPD simulations of these two models will be analyzed.

### 6.3 NPD simulations of $\text{Li}_{1.2}\text{Mn}_{0.6}\text{Ni}_{0.2}\text{O}_2$

As explained in Section 2.2, lithium barely diffract X-rays, and nickel and manganese are indistinguishable as a result of its similar scattering factor. In NPD, on the contrary, nickel has a high positive coherent b scattering factor (10.3 fm), while lithium and manganese have a negative coherent b scattering factor (-1.9 and -3.73 fm respectively), meaning that nickel can be easily distinguished from manganese and lithium. Therefore, complementary information about the layer ordering can be extracted from NPD patterns. To illustrate the significant differences between XRD and NPD for this family of compounds, the effect of stacking faults in the superstructure reflection peaks of NPD is firstly studied in  $\text{Li}[\text{Li}_{1/3}\text{Mn}_{2/3}]\text{O}_2$ . Secondly the NPD patterns of the 3D intergrowth model and the solid solution model for  $\text{Li}_{1.2}\text{Mn}_{0.6}\text{Ni}_{0.2}\text{O}_2$  are compared.

#### 6.3.1 Effect of stacking faults in the NPD pattern of $\text{Li}[\text{Li}_{1/3}\text{Mn}_{2/3}]\text{O}_2$

Figure 6.10 shows the comparison between NPD patterns of ideal and defective  $\text{Li}[\text{Li}_{1/3}\text{Mn}_{2/3}]\text{O}_2$ . For an easier comparison with XRD patterns, all the NPD patterns in this chapter have been simulated with the same wavelength as for XRD ( $\lambda_{\text{Cu}} = 1.54056 \text{ \AA}$ ). The negative scattering of both manganese and lithium significantly reduces the peak intensity arising from the Li/Mn honeycomb ordering compared to XRD, as can be seen in the inset of the figure. As a result, the superstructure peaks become invisible. Added to the intense background experimentally obtained, consequence of the inelastic scattering factor of manganese, the superstructure peaks remain invisible even in samples without stacking faults. [311]

#### 6.3.2 NPD simulations for 3D intergrowth versus solid solution models

Once the weak intensity of the superstructure peaks in  $\text{Li}[\text{Li}_{1/3}\text{Mn}_{2/3}]\text{O}_2$  has been shown, the NPD simulations of the 3D intergrowth between  $\text{Li}[\text{Li}_{1/3}\text{Mn}_{2/3}]\text{O}_2$  and  $\text{LiMn}_{0.5}\text{Ni}_{0.5}\text{O}_2$  described in Section 6.2.2.2 and the solid solution structural model described in Section 6.2.3.2

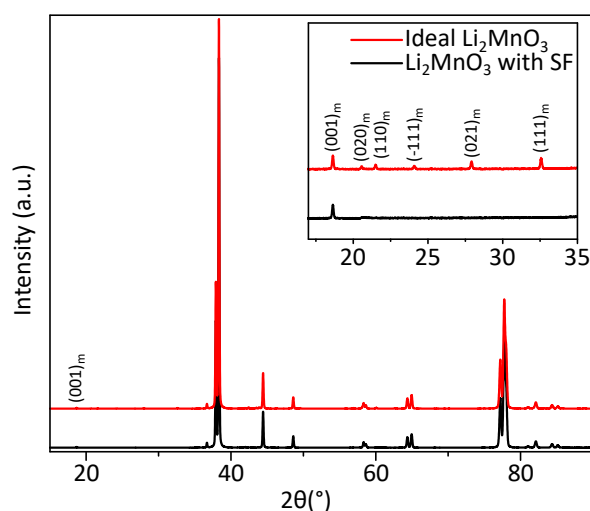


Fig. 6.10 NPD simulations for ideal and defective  $\text{Li}[\text{Li}_{1/3}\text{Mn}_{2/3}]\text{O}_2$  (maximum degree of stacking faults). The inset shows a zoom of the superstructure zone.

are presented in Figure 6.11a. Both patterns show the same diffraction patterns and the same intensities, with the exception of the superstructure region. While in the intergrowth model the  $(020)_m$  reflection is not present, in the solid solution model, a weak signal can be seen. The intensity of the peak is, however very small so it could still be hidden by the background as in  $\text{Li}[\text{Li}_{1/3}\text{Mn}_{2/3}]\text{O}_2$ . [311]

In order to understand the presence of the peak in the solid solution model but not in the intergrowth model we have to take into account that the origin of this peak is the scattering difference between  $2b$  and  $4g$  positions i.e. the honeycomb ordering. In the intergrowth model the structure can be treated as separate domains of  $\text{Li}[\text{Mn}_{0.5}\text{Ni}_{0.5}]\text{O}_2$  and  $\text{Li}[\text{Li}_{1/3}\text{Mn}_{2/3}]\text{O}_2$  (Figure 6.11b). No atomic ordering has been considered for  $\text{Li}[\text{Mn}_{0.5}\text{Ni}_{0.5}]\text{O}_2$ , so no signal is expected in this region. In  $\text{Li}[\text{Li}_{1/3}\text{Mn}_{2/3}]\text{O}_2$  the signal in the superstructure zone comes from the atomic contrast is between Li and Mn. Both atoms have small negative scattering factor so, as we have seen in the previous section, the contrast is small. As a result, the peak remains invisible. In the solid solution model the structure can be described as  $\text{Li}[\text{Li}_{0.2}\text{Ni}_{0.13}]_{2b}[\text{Mn}_{0.6}\text{Ni}_{0.07}]_{4g}\text{O}_2$  (Figure 6.11c). The composition for the  $4g$  position is 90% Mn and 10% Ni. The composition for the  $2b$  position, on the contrary is 60% Li and 40% Ni. The total scattering factor of the  $2b$  position will thus be considerably larger than for  $4g$  position and the contrast will thus be noticeable.

The presence or absence of the superstructure peak in the NPD patterns could be a key element to distinguish between a solid solution and an intergrowth. However, the weak signal, linked to the large background consequence of the inelastic scattering factor of the manganese could hide this peak as for the case of  $\text{Li}[\text{Li}_{1/3}\text{Mn}_{2/3}]\text{O}_2$ . This means that, if in

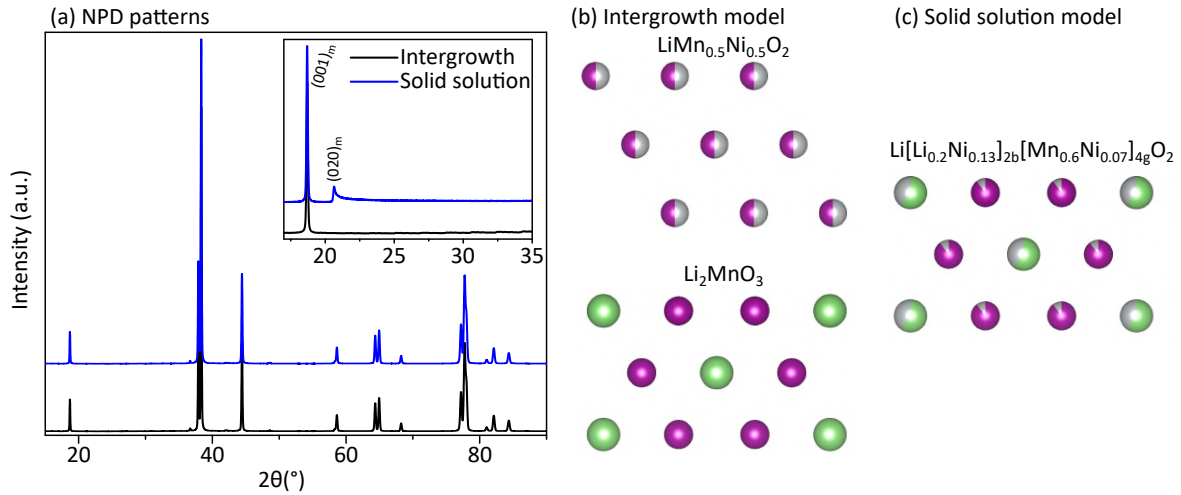


Fig. 6.11 (a) NPD simulations for the intergrowth of two phases and for the solid solution models. The inset of the figure shows a zoom of the superstructure zone. (b,c) Composition of the transition metal layer in the intergrowth of two phases and the solid solution structural models.

experimental patterns the  $(020)_m$  peak is present the structural model for  $\text{Li}_{1.2}\text{Mn}_{0.6}\text{Ni}_{0.2}\text{O}_2$  is unambiguously a solid solution, but if the peak is not present the results will not probably be conclusive. This possibility has been experimentally explored.

### 6.3.3 Analysis of the NPD experimental pattern of $\text{Li}_{1.2}\text{Mn}_{0.6}\text{Ni}_{0.2}\text{O}_2$

Figure 6.12 shows the NPD pattern of  $\text{L}_{1+x}\text{NMO\_SC\_900\_5}$  (see Section 2.1 for synthesis information and Section 2.2.4 for NPD measurement conditions). The zoom of the superstructure region seen in the inset shows no presence of superstructure peaks. Therefore, using XRD and NPD we cannot discriminate between the solid solution or the 3D intergrowth model for this composition. These results illustrate that it is extremely challenging to distinguish between the proposed models for Li-rich compounds as a result of the low signal of the superstructure peak and the large background in the NPD patterns inherent to the manganese atom. This work could however be useful to evaluate other related compositions with enhanced diffraction contrast like manganese free Li-rich compounds which have been used as models to understand the behavior of the materials such as those in References [90, 92, 96, 312–315].

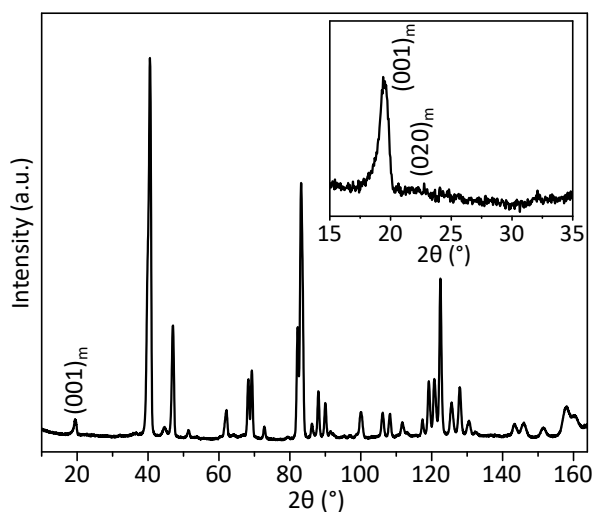


Fig. 6.12 Experimental NPD pattern of  $\text{Li}_{1+x}\text{NMO\_SC\_900\_5}$  with a  $\lambda = 1.623400 \text{ \AA}$ . The inset of the figure shows a zoom of the superstructure zone.

## 6.4 $\text{Li}_{1.2}\text{Mn}_{0.6}\text{Ni}_{0.2}\text{O}_2$ structural and electrochemical characterization

In order to get further insight on the structural transformations occurring in the first cycle of  $\text{Li}_{1.2}\text{Mn}_{0.6}\text{Ni}_{0.2}\text{O}_2$ , a synchrotron X-ray operando experiment was carried out at the APS using the AMPIX cell described in Section 2.6. Since the electrochemical performance of samples synthesized at  $900 \text{ }^\circ\text{C}$  is poor (see Chapter 3), the experiment has been carried out with a sample synthesized at lower temperature (labeled as  $\text{Li}_{1+x}\text{NMO\_SC\_700\_5}$ , synthesized as explained in Section 2.1), because it is expected to fully activate upon the first cycle. Figure 6.13 shows the HR XRD pattern of this sample compared with  $\text{Li}_{1+x}\text{NMO\_SC\_900\_5}$ , both acquired at the 11 ID-B beamline at the APS. For an easier comparison with laboratory XRD patterns, the wavelength was changed to  $2\theta_{\text{Cu}}$  ( $\lambda = 1.54056 \text{ \AA}$ ), while the original  $2\theta$  value is maintained in the top x axis. As expected, the XRD pattern for  $\text{Li}_{1+x}\text{NMO\_SC\_700\_5}$  has considerably wider peaks than that of  $\text{Li}_{1+x}\text{NMO\_SC\_900\_5}$  as a result of its smaller particle size (which in turn is a requirement for electrochemistry). Similarly, the peak shape in the superstructure zone suggests that the degree of stacking faults also is higher for the sample synthesized at lower temperature. The intensity ratio of  $(001)_m$  at  $19^\circ$  and the  $(131)_m$  and  $(\bar{2}02)_m$  pair at  $45^\circ$ , defined as

$$\frac{I_{(131)_m} + I_{(\bar{2}02)_m}}{I_{(001)_m}} \quad (6.4)$$

can be qualitatively used to analyze the amount of nickel in the lithium layer. [316, 317] The large ratio for  $\text{L}_{1+x}\text{NMO\_SC\_700\_5}$  (1.21) with respect to that of  $\text{L}_{1+x}\text{NMO\_SC\_900\_5}$  (1.18) is indicative of a larger amount of nickel in the lithium layer for the former.

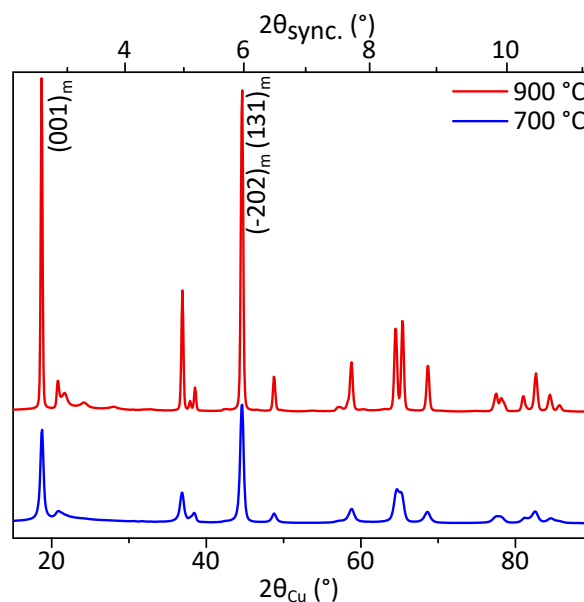


Fig. 6.13 High resolution XRD patterns of  $\text{Li}_{1.2}\text{Mn}_{0.6}\text{Ni}_{0.2}\text{O}_2$  synthesized at 700 and 900°C.

In order to follow the structural evolution of the sample the Rietveld method has been used. Although contrary to FAULTS stacking faults cannot be accounted for, the main structural properties can be followed at a reasonable computational speed. In view that there is no evidence that the intergrowth of two phases model better describes the structure than the solid solution model, the refinement of the patterns is going to be done assuming a solid solution, which is easier to handle with. The refined pattern is shown in Figure 6.14 and the refined values are listed in Table A.9 in Appendix A.

Table 6.5 compares the refined parameters for  $\text{L}_{1+x}\text{NMO\_SC\_700\_5}$  and  $\text{L}_{1+x}\text{NMO\_SC\_900\_5}$ . The unit cell parameters of the samples are slightly different.  $\text{L}_{1+x}\text{NMO\_SC\_700\_5}$  has larger  $a$  and  $b$ , and shorter  $c$ . As expected from the peaks intensity ratio of the XRD patterns, the amount of nickel in the lithium layer is almost three times larger for  $\text{L}_{1+x}\text{NMO\_SC\_700\_5}$  than for  $\text{L}_{1+x}\text{NMO\_SC\_900\_5}$ , which can explain the different unit cell parameters.  $\text{Ni}^{\text{II}}$  and  $\text{Li}^{\text{I}}$  have similar cationic size but different oxidation state, so the larger concentration of nickel in the lithium layer in  $\text{L}_{1+x}\text{NMO\_SC\_700\_5}$  contracts the interlayer distance as a result of the stronger Ni-O bond in comparison with Li-O bond. At the same time, the Ni-Li electrostatic repulsion in the lithium layer is as well more intense than that of Li-Li ions, so a larger size in the  $ab$  plane is expected.

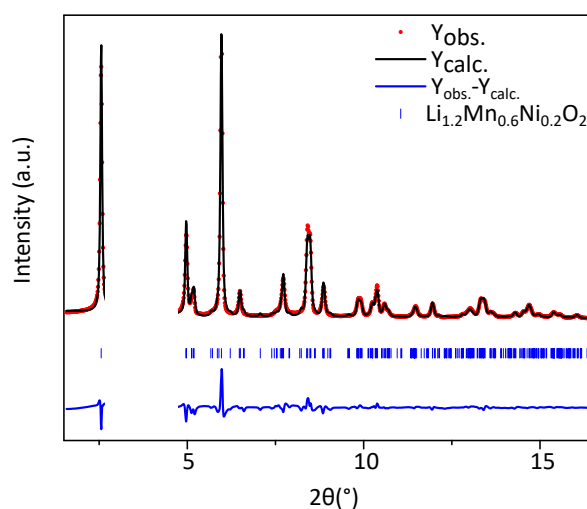


Fig. 6.14 Rietveld refinement pattern of  $\text{L}_{1+x}\text{NMO\_SC\_700\_5}$  sample.

Table 6.5 Main structural parameters obtained from the Rietveld refinement for samples  $\text{L}_{1+x}\text{NMO\_SC\_700\_5}$  and  $\text{L}_{1+x}\text{NMO\_SC\_900\_5}$ . All the refined parameters are shown in Table A.9 in Appendix A.

Sample name	$\text{L}_{1+x}\text{NMO\_SC\_700\_5}$	$\text{L}_{1+x}\text{NMO\_SC\_900\_5}$
$a$	4.960(2)	4.9409(8)
$b$	8.552(3)	8.553(1)
$c$	5.009(1)	5.0256(5)
$\beta$	109.09(5)	109.29(1)
Volume	200.78	200.45
Particle size (nm)	18	92
Occ. $3a$ (Li/Ni)	93.8(8)/6.2(8)	97.6(8)/2.4(8)
Occ. $3b$ (Ni/Li)	93.8(8)/6.2(8)	97.6(8)/2.4(8)

## 6.5 Operando XRD measurement of $\text{Li}_{1.2}\text{Mn}_{0.6}\text{Ni}_{0.2}\text{O}_2$

### 6.5.1 Qualitative HR XRD analysis

The structural evolution of  $\text{Li}_{1.2}\text{Mn}_{0.6}\text{Ni}_{0.2}\text{O}_2$  has been followed with an *operando* XRD measurement for  $\text{L}_{1+x}\text{NMO\_SC\_700\_5}$  sample. Although the nickel in the transition metal layer is known to be detrimental for the electrochemistry, [1, 257, 318] reasonable capacities were found to evaluate the structural changes occurring upon the first charge. The experimental conditions for the XRD and electrochemical measurement are explained in Sections 2.2 and 2.6. Figure 6.15 shows the voltage versus capacity curve of the first two *operando* galvanostatic cycles, whose first charge has been divided into two different regions. The charge region 1, shown as a blue rectangle, and covering from open circuit voltage (OCV) to



4.5 V, is usually related with a classic layered oxide like behavior, while the charge region 2, in the range 4.5-4.8 V, is characteristic from lithium rich layered oxides and it is known to harbor irreversible structural changes.

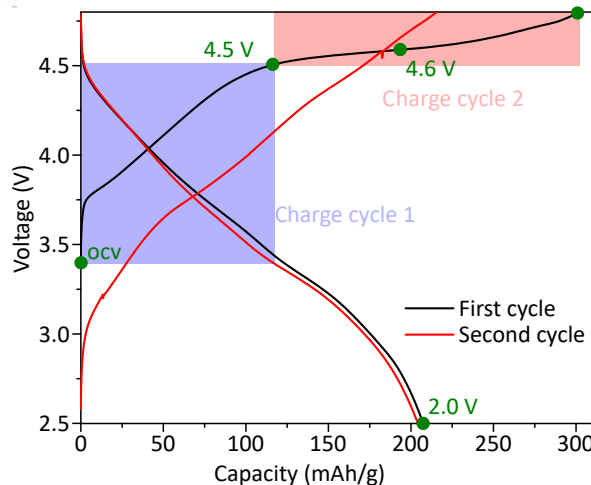


Fig. 6.15 Voltage versus capacity curve of the first two galvanostatic cycles of the *operando* measurement of  $\text{L}_{1+x}\text{NMO\_SC\_700\_5}$ . Points at selected voltages are marked with green circles.

The corresponding evolution of the XRD patterns is plotted in Figure 6.16a. In addition, contour plots of the most relevant peaks are presented in Figure 6.16b, with the corresponding time versus voltage curve. Finally, Figure 6.16c-e show selected points (in green in Figure 6.15) for each of the three regions defined: Figure 6.16c shows the first and last XRD pattern in the charge region 1, Figure 6.16d shows three different XRD patterns within the charge region 2 (at the beginning, at the middle of the process and at the end) and Figure 6.16e shows the initial and final states of the discharge. The pattern of the initial structure at the OCV is modified in the first charge and it is no longer recovered at the end of the charge-discharge cycle. Once this phase transformation occurs, the peak profile of the subsequent cycles are reproducible. From a qualitative point of view, the peaks evolve as follows:

- **Charge region 1:** while the position for the  $(001)_m$  peak does not vary substantially, meaning that the interlayer distance does not vary, at high  $2\theta$  values the peaks are displaced to higher  $2\theta$  values, indicating a unit cell reduction, most likely in the  $ab$  plane. On the other hand, intensity of  $(\bar{2}02)_m$  and  $(131)_m$  peak slightly decreases as a result of the lithium removal from the lithium layer. Finally, intensity of the  $(\bar{1}33)_m$  and  $(202)_m$  peak also exhibit lower intensity, while that related to  $(060)_m$  and  $(\bar{3}31)_m$  remains constant.

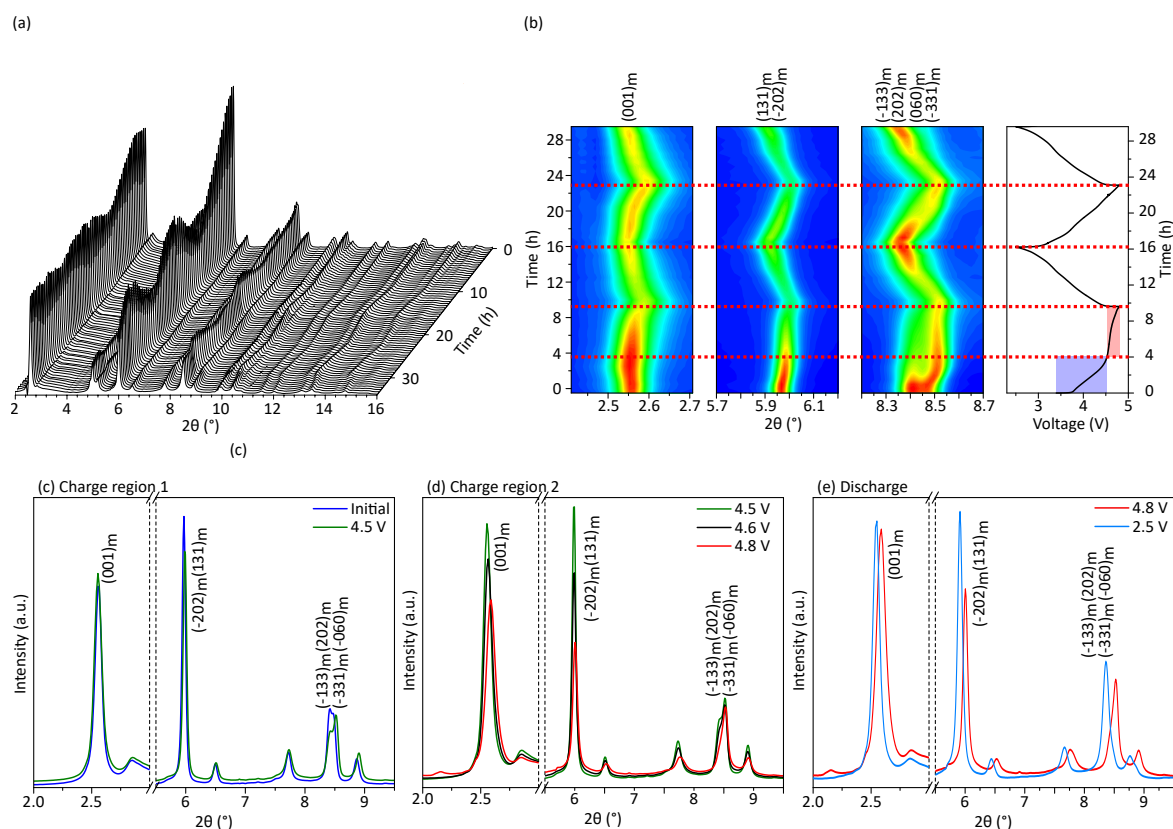


Fig. 6.16 (a) Waterfall plot of XRD patterns resulting from the *operando* measurement of  $\text{Li}_{1+x}\text{NMO\_SC\_700\_5}$ . (b) *operando* XRD peaks evolution upon cycling together with the time versus voltage curve shown as contour plot. (c-e) XRD patterns at selected voltages in (c) the charge region 1, (d) in the charge region 2 and (e) in the discharge.

- Charge region 2:** in this case the  $(001)_m$  peak is displaced to higher  $2\theta$  values, indicating a layer contraction. In addition, the peak becomes smaller and wider. Similarly, the peak at  $6^\circ$  related to  $(\bar{2}02)_m$  and  $(131)_m$  has an important decrease of intensity as a consequence of lithium removal from the lithium layer and possible additional structural modifications. The intensity reduction of the  $(020)_m$  and  $(\bar{1}33)_m$  at  $8.5^\circ$  continues as the voltage increases, while the intensity corresponding to the second peak of the doublet corresponding to  $(060)_m$  and  $(\bar{3}31)_m$  does not vary.
- Discharge:** even if the peaks are displaced to lower  $2\theta$  values in this range, the peak shape does not substantially vary. The main peak intensity increase is registered in the peak at  $6^\circ$  corresponding to  $(\bar{2}02)_m$  and  $(131)_m$  reflections as a consequence of the lithium insertion in the transition metal layers. This means that in this range the structure does not suffer important changes except for the unit cell increase,

consequence of the the lithium insertion in the lithium layer (which is as well perceived in the intensity increase of the peak  $(\bar{2}02)_m$   $(131)_m$ ).

Figure 6.17 shows the XRD patterns corresponding to the fully discharged and fully charged states of the three cycles. Note that in Figure 6.17a, the XRD patterns for the second and third cycles, which are overlapped, are intentionally shifted from the first one for a better appreciation of details. The pattern at the OCV has a different shape from the subsequent ones, which are comparable between them. This is especially noticed in the reduction of the  $(001)_m$  and the  $(\bar{2}02)_m$   $(131)_m$  peaks and in the peak positions at high  $2\theta$  angles. On the other hand, the XRD pattern of the first fully charged state (Figure 6.17b) has the same shape as the second one, which is a clear indicator that after the first structural change the structure does not suffer important changes, in agreement with previous reported works. [98–102]

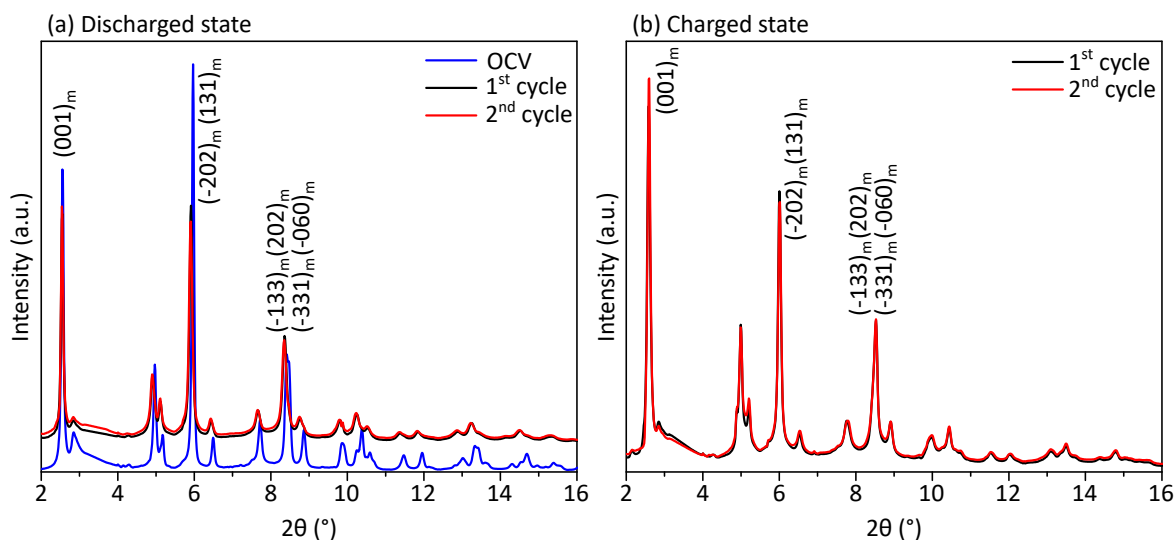


Fig. 6.17 XRD pattern of (a) discharged state of first three cycles and (b) charged states of the first two cycles.

## 6.5.2 Rietveld refinement

For a complete view of the evolution of the peaks as well as to unravel the possible processes occurring upon cycling of the material, the XRD patterns of the first charge-discharge cycle were refined using Rietveld refinement (excluding the superstructure peaks). Regarding that there is no evidence of two phases in the *operando* XRD experiment (e.g. there are no new peaks) a single phase refinement is carried out using the  $C2/m$  space group, which describes best the structure. The *operando* XRD refinements performed by other groups have been done either using the  $R\bar{3}m$  space group [98–102] either with a two phase refinement involving

two different  $R\bar{3}m$  structures or a  $R\bar{3}m$  and a  $C2/m$  structure. [296, 319] The description of the structure using  $R\bar{3}m$  space group is easier to handle, but all the transition metals and all the oxygen atoms treated as equivalent, which it could be an oversimplification and thus result in a loss of important information. Therefore, in this work, the refinement has been carried out using the  $C2/m$  space group. The refined parameters were the scale, the unit cell lattice parameters, and the atomic positions and occupancies, while the zero offset was set to 0. The crystallite average size does not vary, so the size broadening parameter was refined in the first pattern and was maintained constant during all the refinement, as done by Fell *et al.* [222] Similarly, the atomic thermal factors were refined in the first pattern and maintained constant along all the process. Microstrains have been modeled with an anisotropic strain broadening model using a quartic form in reciprocal space. Background was fitted with a linear interpolation of selected points refined for each pattern. Even if the scattering factor of lithium is small, the lithium anode showed diffraction peaks as a consequence of its thickness and the brilliance of the beam, so it was added as a secondary phase and its intensity was refined for each pattern. The lithium in the structure, however, has a really small scattering factor with respect to the rest of the atoms and its contribution to the diffracted intensities is insignificant in comparison with the rest of the atoms. Considering that this compound is known to have nickel in the lithium layer, only nickel atoms were included in the model for the lithium layer. In addition, since nickel and manganese have similar scattering factors only nickel atoms were considered in the model for the transition metal layer. In order to follow the changes in electron density of the layers due to lithium removal and transition metal migration, a relative occupancy parameter has been calculated ( $\text{Occ}_{Relative}$ ), obtained by dividing the occupancy of nickel atoms in the lithium layer with the occupancy of nickel atoms in the transition metal layer, as shown in Equation 6.5.

$$\text{Occ}_{Relative} = \frac{\sum \text{Occupancy}_{Li \text{ layer}}}{\sum \text{Occupancy}_{Transition \text{ metal layer}}} = \frac{\text{Occupancy}_{2c} + \text{Occupancy}_{4h}}{\text{Occupancy}_{2b} + \text{Occupancy}_{4g}} \quad (6.5)$$

A decrease in this ratio indicates that the atomic concentration in the lithium layer is being reduced with respect to the atomic concentration in the transition metal layer, i.e. there is an atomic removal in the lithium layer or an atomic increase in the transition metal layer.

Refined patterns at selected charge states are shown in Figure 6.18. The refined values of  $a$ ,  $b$ ,  $c$  and  $\beta$  can be found in Figure A.4 in Appendix A. However, as the unit cell values for  $R\bar{3}m$  and for  $C2/m$  are different, for an easy comparison with the bibliographic data two parameters are used in this work: the  $ab$  plane area, which is related to  $a$  parameter from the  $R\bar{3}m$  space group, and the  $c'$  interlayer distance value, calculated as  $c \cdot \cos(\beta - 90)$  which

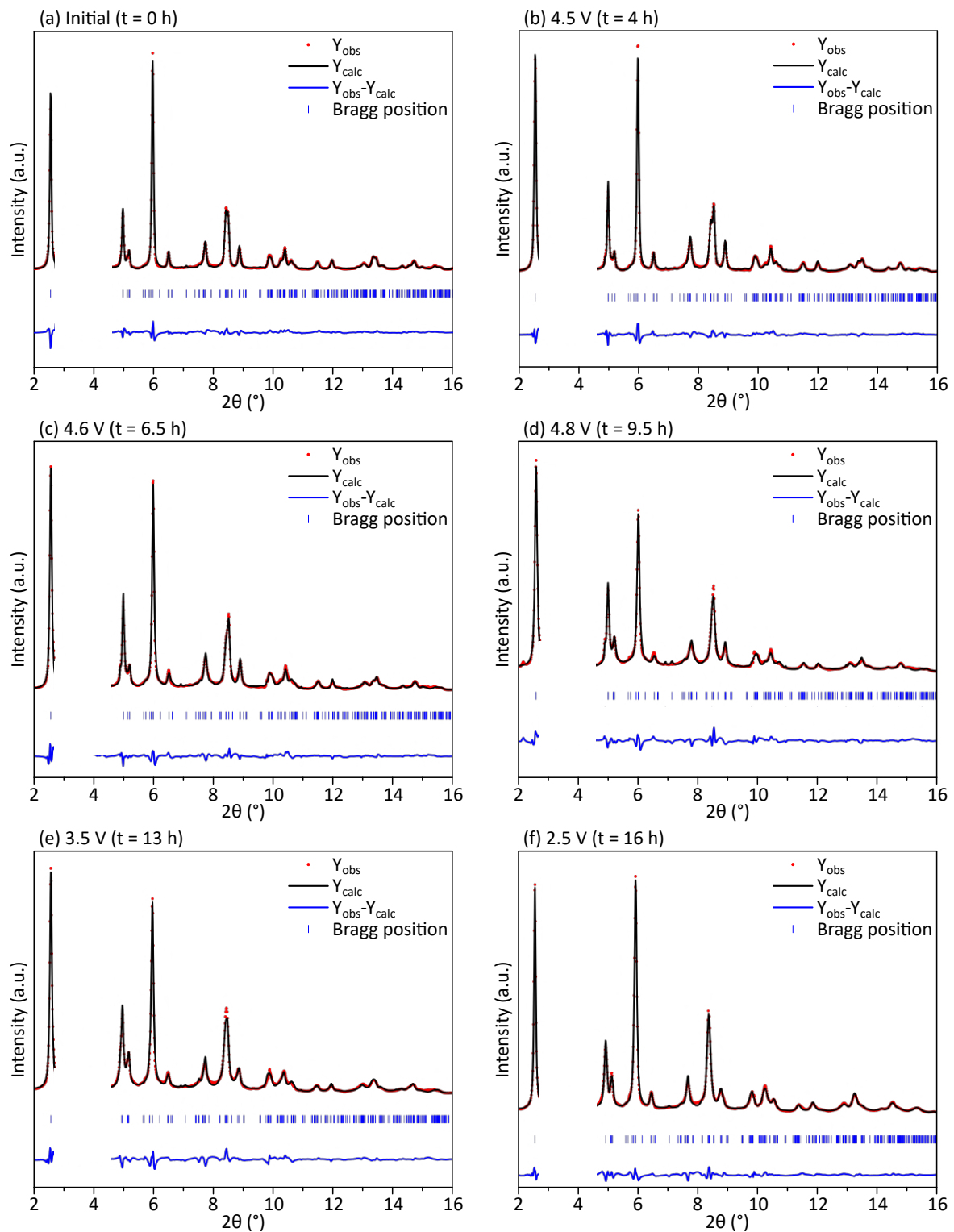


Fig. 6.18 Refined HR XRD patterns of selected voltages of the *operando* experiment of  $\text{Li}_{1.2}\text{Mn}_{0.6}\text{Ni}_{0.2}\text{O}_2$ .

is  $c/3$  in  $R\bar{3}m$  space group. On the other hand, the electronic scattering density difference between the experimental data and the simulated one ( $F_{diff}$ ) has been analyzed to find possible occupied sites (Figure 6.19). The density maps show that when the sample is charged at 4.5 V there is some positive scattering factor in the tetrahedral positions, which indicates that this position is occupied. Therefore, from this point on all the patterns are refined allowing metal migration to tetrahedral positions.

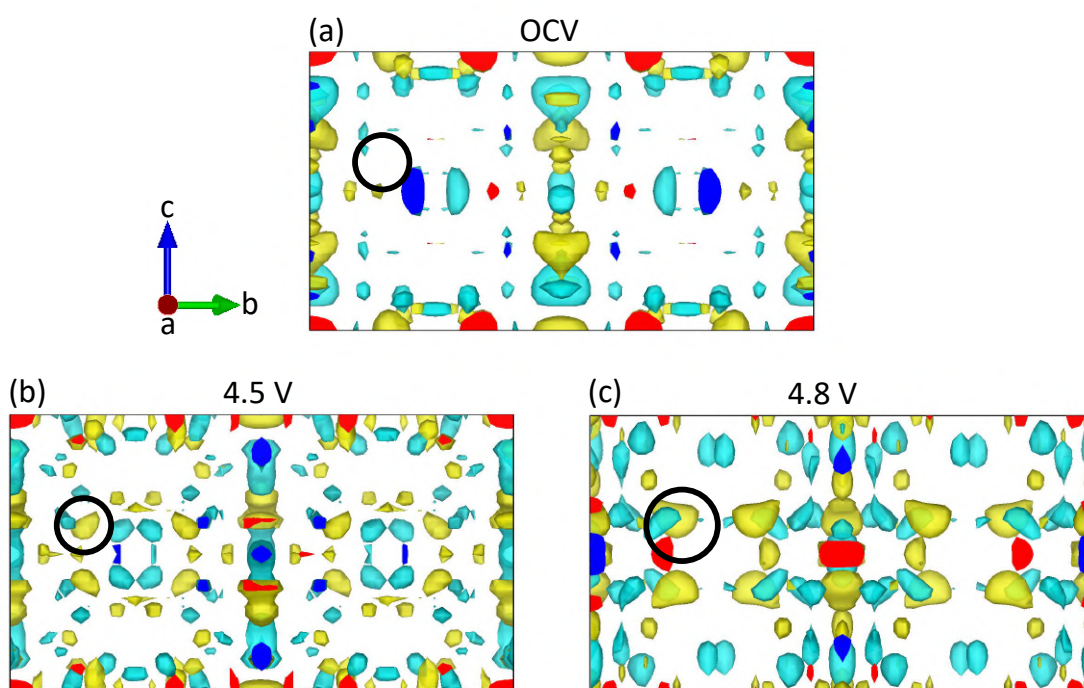


Fig. 6.19 Electronic scattering density difference ( $F_{diff}$ ) between the calculated and the observed experimental pattern at (a) OCV (b) at 4.5 V, (c) 4.8 V. The positive scattering factor is shown in yellow while the negative is shown in blue. The black circles indicate tetrahedral positions.

The main refined parameters for  $\text{L}_{1+x}\text{NMO\_SC\_700\_5}$  are shown in Figure 6.20, which comprise: the  $ab$  plane area, the  $c'$  interlayer distance value,  $\text{Occ}_{Relative}$ , the occupancy in the tetrahedral position, the  $\text{O}4i\text{-O}4i$  distance and the microstrains along the  $ab$  plane and along  $c$ . The following observations have been done:

- In the **charge region 1** the  $ab$  plane area is reduced as a consequence of the oxidation of the nickel from  $\text{Ni}^{\text{II}}$  (atomic radio of 0.83 Å) to  $\text{Ni}^{\text{IV}}$  (atomic radio of 0.62 Å), consistent with previous *operando* experiments in the bibliography. [98–102, 319] At the same time, the  $\text{Occ}_{Relative}$  ratio decreases, meaning that in this range the lithium is

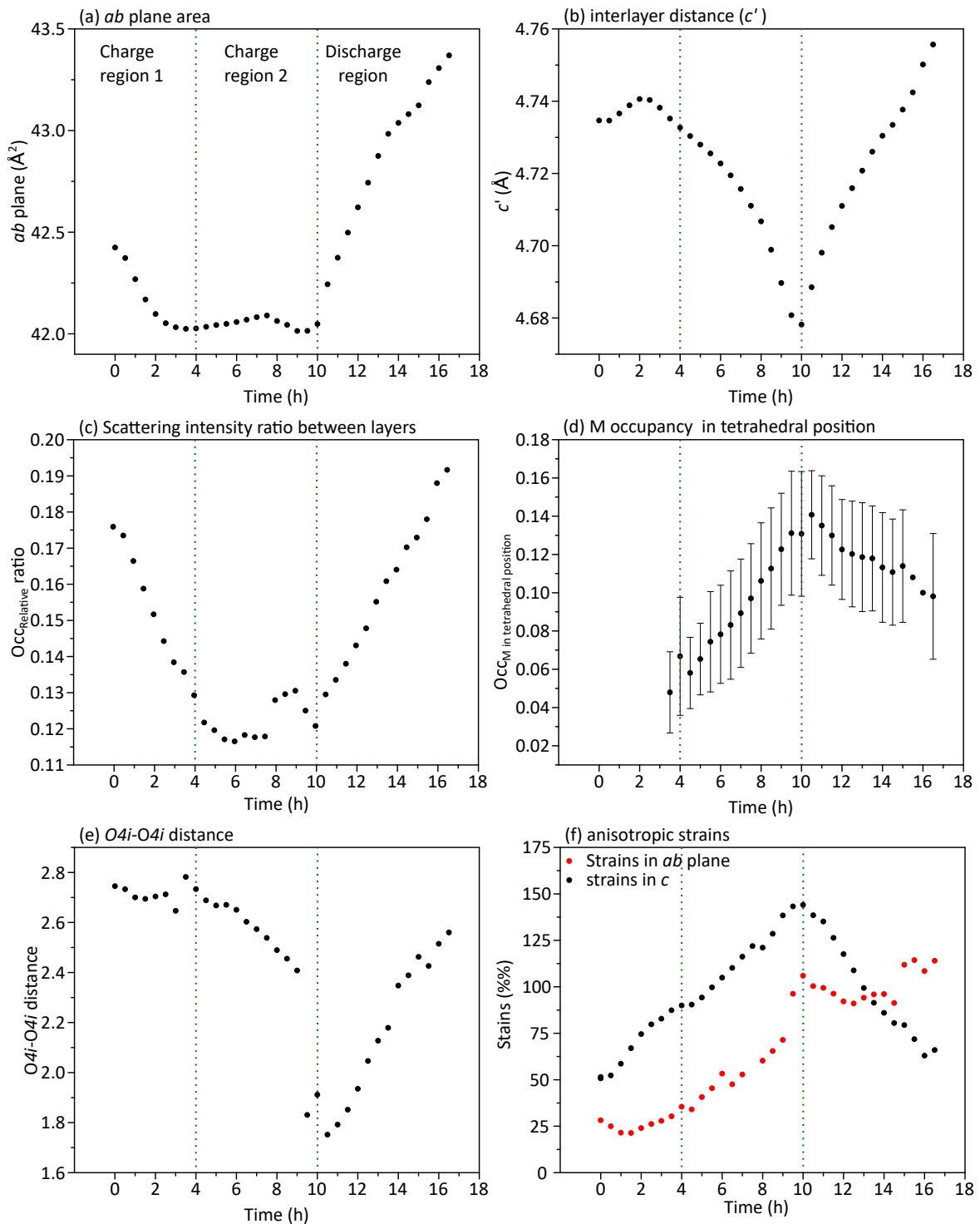


Fig. 6.20 Refined parameters upon charge and discharge. Green dashed lines mark the end of the charge region 1 and charge region 2.

mainly extracted from the transition metal layer. This lithium removal from the lithium layer does not strongly modify the  $c'$  interlayer distance because the nickel atoms in the lithium layer act as pillars. In this range the absence of nickel in the tetrahedral positions have been found.

- In the **charge region 2** the  $ab$  plane area is maintained relatively constant because there is no more transition metal oxidation. The  $c'$  distance, on the contrary, suffers an important contraction, which is linked with transition metal migration to the tetrahedral position. The shorter M-O tetrahedral bonds are believed to contract the interlayer distance. In this range, oxygen is believed to be the main redox active center. As seen in Section 5.3.3, the metal migration to tetrahedral position helps to stabilize the unstable oxidized oxygen atoms. On the other hand,  $\text{Occ}_{\text{Relative}}$  is constant in this range (Figure 6.20c), which suggests that the lithium atom is extracted from both, the lithium layer and the transition metal layer. Interestingly, we have found a  $\text{O4i-O4i}$  distance shortening within the transition metal layer (from 2.75 Å to 1.83 Å, as shown in Figure 6.21), which could demonstrate the peroxide-like bond formation. This distance shrinkage could be the consequence of the absence of  $\text{Li2b}$ . The combination of metal migration to tetrahedral sites with oxygen distance shortening has been recently predicted by Radin *et al.* [264] According to their study, the manganese migrates to the tetrahedral position as  $\text{Mn}^{\text{VII}}$ , which induces a peroxide bond formation or a internally trapped  $\text{O}_2$  molecule which, at the same time, can reduce the  $\text{Mn}^{\text{VII}}$  to  $\text{Mn}^{\text{IV}}$ , pushing it to an octahedral position (either to the lithium layer or to the transition metal layer). In other words, the peroxide formation could be induced by manganese migration to tetrahedral positions.

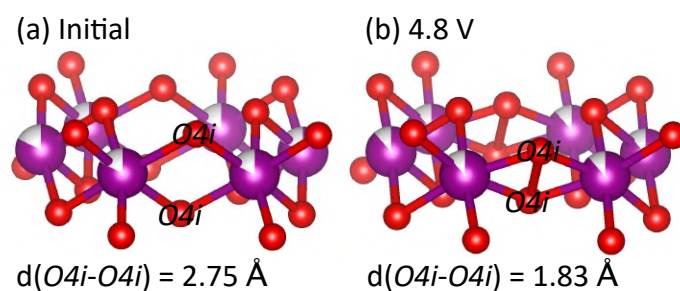


Fig. 6.21  $\text{O4i-O4i}$  distance of the initial structure and the fully charged structure.

- In the **discharge**, both the  $ab$  plane area and the  $c'$  increase their value. While the first one is consequence of the reduction of nickel atoms, the later one is due to the intercalation of lithium atoms in the lithium layer and migration of the metals in the tetrahedral position to the transition metal layer. According to the  $\text{Occ}_{\text{Relative}}$ , there



is more scattering density in the lithium metal layer at the end of the first cycle in comparison with the beginning, which means that some of the metals which were in the tetrahedral position do not migrate back to the transition metal layer but go to the lithium layer. An alternative explanation could be that some  $2b$  positions, which were initially occupied by lithium could remain unoccupied. Finally, the  $O4i-O4i$  distance goes back to its original state, which suggest that the formation of peroxo/trapped  $\text{O}_2$  formation is reversible.

Figure 6.20f shows the evolution of the strains in the  $ab$  plane (calculated averaging the strains in the  $(200)_m$  and  $(040)_m$  planes) and in  $c$ , represented by the strains along the  $(001)_m$  plane. The strains in  $c$  direction are high at OCV and they increase considerably in the charge process, while during discharge the approximate initial value is almost recovered. The initial large  $(001)_m$  strain can be consequence of the complex microstructure of the compound. The slightly different atomic composition of each layer will induce differences in the interlayer distance. In view of our refinement results, three possible explanation are given for the increase of the strains in  $c$  upon delithiation, shown in Figure 6.22a. i) The absence of lithium in some layers increases the interlayer distance consequence of O-O coulombic repulsion, typical of layered oxides. [100, 102] ii) The transition metal migration to the tetrahedral positions induces layer shrinkage as we have previously proposed. iii) Transition metal atoms irregularly spread along the lithium layer and can cause undulations in the structure, as found to happen to other layered compounds. [320, 321] These hypotheses are not excluding and can occur simultaneously, giving rise to varying interlayer distances.

On the other hand, the stains in the  $ab$  are lower at OCV but they increase while charging and the initial value is no longer recovered. In the charge cycle 1 the strains in the  $ab$  plane do not vary substantially. In contrast, in the charge region 2, the strains in the  $ab$  plane considerably increase, which can be linked with the main processes occurring during this region, i.e. the metal migration to tetrahedral positions and the  $O4i-O4i$  distance reduction. In the discharge, not all the metals from the transition metal layer return to octahedral positions, so the microstrain value is maintained constant. Fell *et al.* studied the microstrains isotropically in  $\text{Li}_{1.2}\text{Mn}_{0.6}\text{Ni}_{0.2}\text{O}_2$  and suggested that their increase came from the activity of the manganese, which according to his study became redox active and the presence of  $\text{Mn}^{\text{III}}$  caused Jahn-Teller distortion which increased the strains. [222]

In summary, we have reproduced the unit cell parameters evolution seen in previous works in the  $ab$  plane, while the behavior in the  $c$  plane is different. This difference has been attributed to the initial nickel content in the lithium layer. At high delithiation states, the metal migration to tetrahedral position is reproduced, which has been hypothesized to be consequence of the oxygen oxidation, as explained in Section 5.3.3. The use of the  $C2/m$

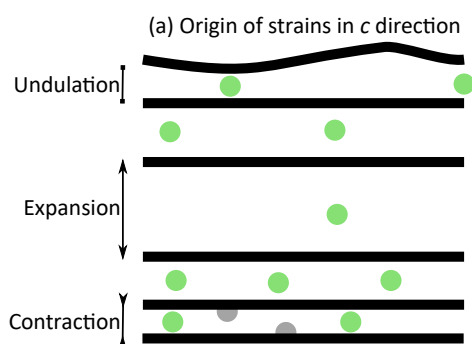


Fig. 6.22 Schematic representation of the origin of strains.

space group has allowed us to find a selective  $O4i$  distance reduction, while the  $O8j$  maintains in its position. Finally, the anisotropic strain model used to determine the strains in the sample has shown that i) the strains in the stacking directions increase during the charge and decrease on the discharge, as a result of the interlayer distance anisotropy and ii) the strains in the  $ab$  plane increase in the first charge and are not recovered, consequence of the transition metal migration to the lithium layer.

## 6.6 Conclusions

XRD and NPD pattern were simulated in order to explore the differences between models (two separated phases, as an intergrowth of two phases -comprising layered intergrowth and 3D intergrowth- or as a solid solution). XRD has allowed us to discard the two phase model and the layered intergrowth model. The patterns for both the 3D intergrowth and the solid solution models match with the experimental XRD patterns, while for NPD patterns small differences in the superstructure peaks are present. Unfortunately, these are weak and are hidden by the experimental background. On the other hand, an *operando* XRD experiment has been performed in  $\text{Li}_{1.2}\text{Mn}_{0.6}\text{Ni}_{0.2}\text{O}_2$  to follow the structural changes upon cycling. It has been found that the  $ab$  plane expands and contracts as previously found in bibliography, but the  $c'$  parameter behavior has found to behave different as a result of the nickel content in the lithium layer. Two different mechanisms have been found to minimize the instability of the oxidized oxygen at high delithiated states: metal migration to tetrahedral position and the  $O4i$ - $O4i$  distance reduction, which could form a peroxo-like bonds or trapped molecular  $\text{O}_2$ . Finally, the structural evolution has shown to generate microstrain along  $c$  and along  $ab$  plane. While in the first one the strains are reversible, consequence of the anisotropic lithium extraction, the strains in the  $ab$  plane irreversibly increase consequence of the metal migration to tetrahedral positions.

# Chapter 7

## General conclusions

*By three methods we may learn wisdom: First, by reflection, which is noblest; Second, by imitation, which is easiest; and third by experience, which is the bitterest.*

**Confucius**

In this thesis a thorough analysis of the microstructural features of  $\text{Li}_2\text{MnO}_3$  and  $\text{Li}_{1.2}\text{Mn}_{0.6}\text{Ni}_{0.2}\text{O}_2$  has been performed, aimed to correlate the microstructure with the electrochemical properties. In the case of  $\text{Li}_2\text{MnO}_3$ , the synthesis conditions have been correlated with amounts of stacking faults, particle size and morphology and the independent impact of these variables in the electrochemical behavior has been decoupled. For  $\text{Li}_{1.2}\text{Mn}_{0.6}\text{Ni}_{0.2}\text{O}_2$  the controversial microstructural arrangement and its evolution upon the first cycle have been studied.

From the structural analysis of  $\text{Li}_2\text{MnO}_3$  we have found that the choice of the precursor and the synthesis temperature has a strong impact in the microstructure of the sample (the crystallite size, the particle shape and the degree of stacking faults).  $\text{MnO}$  and  $\text{Mn}_2\text{O}_3$  precursors result in platelet shaped particles while isotropic particles are obtained when  $\text{MnCO}_3$  is used. On the other hand,  $\text{Mn}_2\text{O}_3$  and  $\text{MnCO}_3$  precursors form structures with high degree of stacking faults, while  $\text{MnO}$  precursor form structures with low degree of stacking faults. In turn, the synthesis temperature mainly affects the crystallite size: the higher the synthesis temperature the larger the crystallite and the particle size. By electron microscopy images we have shown that samples with low degree of stacking faults contain zones without stacking faults, zones with a moderate number of stacking faults and highly defective zones, while samples with a high degree of stacking faults only exhibit highly faulted zones.

The effect of these microstructural variables have shown to affect the electrochemical performance of  $\text{Li}_2\text{MnO}_3$ . Crystallite size has the strongest impact in the capacity and cyclability. While samples with small crystallites have a rapid activation but fast fading, large crystallites have a slow activation. The sample with a crystallite size of  $\sim 200$  nm has been found to have the best activation/fading balance. Alternatively, particles with isotropic size have a superior capacity and lower voltage fading in comparison with the platelet-shaped ones. In turn, stacking faults have a minor impact in the delivered capacity, but samples with low degree of stacking faults have shown to convert to spinel much faster than defective samples.

Stacking faults have been found to modify the  $^6\text{Li}$  ssNMR spectra of  $\text{Li}_2\text{MnO}_3$  as they generate new peaks, as a consequence of the new lithium environments. The comparison of samples with low and high degree of stacking faults enables us to assign the signals of lithium in ideal and defective environments. In fact, DFT calculations have accurately reproduced the new environments generated by stacking faults and they have helped to find and rationalize additional NMR environments in a sample synthesized at high temperature, that were attributed to  $\text{Li}_2\text{O}$  vacancies.

The structural stability of  $\text{Li}_2\text{MnO}_3$  and its behavior upon delithiation has been studied using first principles calculations. Ideal and faulted  $\text{Li}_2\text{MnO}_3$  structures turn out to be

energetically degenerated so they are equally likely to be formed. For  $\text{Li}_x\text{MnO}_3$ , in the  $2 \geq x \geq 1$  range, the delithiation mechanism for ideal and defective structures is the same. In this compositional range lithium has been found to migrate to tetrahedral positions to stabilize the oxidized oxygen atoms. At  $x = 0.5$  the ideal structure tends to transform to  $O1$  like configuration, while stacking faults avoid this transformation. On the other hand, lithium partial replacement with a  $\text{Li}_{1.5}\text{M}_{0.5}\text{MnO}_3$  stoichiometry has been proposed to improve the electrochemical performance. The beryllium-substituted compound is predicted to crystallize in a different unit cell because beryllium is more stable in tetrahedral sites. The large size of potassium lowers the operation voltage and induces important volumetric changes upon delithiation. Sodium and magnesium have been proven to be potential substituents. However,  $\text{Li}_{1.5}\text{Na}_{0.5}\text{MnO}_3$  has been predicted to suffer layer gliding which is detrimental for the electrochemical performance.  $\text{Li}_{1.5}\text{Mg}_{0.5}\text{MnO}_3$ , on the contrary, maintains the  $O3$  configuration upon the whole delithiation process. In addition, the higher oxidation state of magnesium in comparison with lithium involves manganese reduction, and therefore enhances its redox activity and reduces the redox activity of oxygen.

XRD simulations have been used to discriminate between the proposed microstructural models for  $\text{Li}_{1.2}\text{Mn}_{0.6}\text{Ni}_{0.2}\text{O}_2$ : two phase model, layered intergrowth, 3D intergrowth and solid solution. The first one has been discarded as a result of the absence of some peaks that should appear as consequence of their different unit cell sizes. The layered intergrowth of  $\text{Li}_2\text{MnO}_3$  and  $\text{LiMn}_{0.5}\text{Ni}_{0.5}\text{O}_2$  model has as well been discarded, as the simulated patterns show additional peaks not seen experimentally. The 3D intergrowth and the solid solution model have shown to reproduce the experimental XRD patterns. NPD simulations have shown small diffraction differences regarding the different superstructure ordering, but the high background of the experimental NPD pattern inhibits distinguishing clearly between models.

By *operando* synchrotron XRD experiment the structural changes upon cycling have been followed. In the first charge region, the evolution of the  $ab$  plane found previously has been reproduced. The presence of nickel in lithium layer is believed to maintain the interlayer distance value constant. During the second charge region, metal migration to tetrahedral positions has been found, which in addition to the O-O distance shortening is considered to minimize the oxygen oxidation. Finally, microstrains along  $c$  direction have shown to reversibly increase upon charge and decrease upon discharge, consequence of the asymmetric lithium extraction in the compound, while microstrains in the  $ab$  plane irreversibly increase upon the first charge, due to the appearance of lithium in tetrahedral positions.



# References

- [1] Rozier, P.; Tarascon, J. M. Review—Li-Rich Layered Oxide Cathodes for Next-Generation Li-Ion Batteries: Chances and Challenges. *J. Electrochem. Soc.* **2015**, *162*, A2490–A2499.
- [2] Borkiewicz, O. J.; Shyam, B.; Wiaderek, K. M.; Kurtz, C.; Chupas, P. J.; Chapman, K. W. The AMPIX electrochemical cell: a versatile apparatus for *in situ* X-ray scattering and spectroscopic measurements. *J. Appl. Crystallogr.* **2012**, *45*, 1261–1269.
- [3] Lei, C. H.; Wen, J. G.; Sardela, M.; Bareño, J.; Petrov, I.; Kang, S. H.; Abraham, D. P. Structural study of  $Li_2MnO_3$  by electron microscopy. *J. Mater. Sci.* **2009**, *44*, 5579–5587.
- [4] Bareño, J.; Lei, C. H.; Wen, J. G.; Kang, S. H.; Petrov, I.; Abraham, D. P. Local structure of layered oxide electrode materials for lithium-ion batteries. *Adv. Mater.* **2010**, *22*, 1122–1127.
- [5] Xiao, R.; Li, H.; Chen, L. Density functional investigation on  $Li_2MnO_3$ . *Chem. Mater.* **2012**, *24*, 4242–4251.
- [6] Lee, E.; Persson, K. A. Structural and Chemical Evolution of the Layered Li-Excess  $Li_xMnO_3$  as a Function of Li Content from First-Principles Calculations. *Adv. Energy Mater.* **2014**, *4*, 1400498.
- [7] Wen, J. G.; Bareño, J.; Lei, C. H.; Kang, S.-H.; Balasubramanian, M.; Petrov, I.; Abraham, D. P. Analytical electron microscopy of  $Li_{1.2}Co_{0.4}Mn_{0.4}O_2$  for lithium-ion batteries. *Solid State Ion.* **2011**, *182*, 98–107.
- [8] Yu, H.; Ishikawa, R.; So, Y. G.; Shibata, N.; Kudo, T.; Zhou, H.; Ikuhara, Y. Direct atomic-resolution observation of two phases in the  $Li_{1.2}Mn_{0.567}Ni_{0.166}Co_{0.067}O_2$  cathode material for lithium-ion batteries. *Angew. Chem. Int. Ed.* **2013**, *52*, 5969–5973.
- [9] Boulineau, A.; Simonin, L.; Colin, J. F.; Canévet, E.; Daniel, L.; Patoux, S. Evolutions of  $Li_{1.2}Mn_{0.61}Ni_{0.18}Mg_{0.01}O_2$  during the initial charge/discharge cycle studied by advanced electron microscopy. *Chem. Mater.* **2012**, *24*, 3558–3566.
- [10] Meyer, W. B.; Turner, B. L. Human Population Growth and Global Land-Use/Cover Change. *Annu. Rev. Ecol. Syst.* **1992**, *23*, 39–61.
- [11] United Nations, *World Population Prospects The 2017 Revision*; 2017; pp 1–47.
- [12] WHO and UNICEF, *Global Water Supply and Sanitation Assessment Report*; 2000; pp 1–80.

- [13] BP, 2018; Vol. 67; pp 1–54.
- [14] European Environment Agency, Final energy consumption by sector and fuel. 2019; <https://www.eea.europa.eu/data-and-maps/indicators/final-energy-consumption-by-sector-9/assessment-4>.
- [15] Anenberg, S. C.; Miller, J.; Minjares, R.; Du, L.; Henze, D. K.; Lacey, F.; Malley, C. S.; Emberson, L.; Franco, V.; Klimont, Z.; Heyes, C. Impacts and mitigation of excess diesel-related NO<sub>x</sub> emissions in 11 major vehicle markets. *Nat.* **2017**, *545*, 467.
- [16] Blomgren, G. E. The Development and Future of Lithium Ion Batteries. *J. Electrochem. Soc.* **2017**, *164*, A5019–A5025.
- [17] Reinhardt, R.; Amante Garcia, B.; Canals Casals, L.; Gassó Domingo, S. *Project Management and Engineering Research*; Springer International Publishing: Cham, 2019; pp 99–110.
- [18] Raslavičius, L.; Azzopardi, B.; Keršys, A.; Starevičius, M.; Bazaras, Ž.; Makaras, R. Electric vehicles challenges and opportunities: Lithuanian review. *Renew. and Sustain. Energy Rev.* **2015**, *42*, 786–800.
- [19] de Kaa, G.; Scholten, D.; Rezaei, J.; Milchram, C. The Battle between Battery and Fuel Cell Powered Electric Vehicles: A BWM Approach. *Energies* **2017**, *10*.
- [20] Zhang, M.; Song, X.; Ou, X.; Tang, Y. Rechargeable batteries based on anion intercalation graphite cathodes. *Energy Storage Mater.* **2019**, *16*, 65–84.
- [21] Sun, X.; Radovanovic, P. V.; Cui, B. Advances in spinel  $Li_4Ti_5O_{12}$  anode materials for lithium-ion batteries. *New J. Chem.* **2015**, *39*, 38–63.
- [22] Zhang, W. J. A review of the electrochemical performance of alloy anodes for lithium-ion batteries. *J. Power Sources* **2011**, *196*, 13–24.
- [23] Guo, W.; Liu, S.; Guan, X.; Zhang, X.; Liu, X.; Luo, J. Mixed Ion and Electron-Conducting Scaffolds for High-Rate Lithium Metal Anodes. *Adv. Energy Mater.* **2019**, *9*, 1900193.
- [24] Palacín, M. R. Recent advances in rechargeable battery materials: A chemist's perspective. *Chem. Soc. Rev.* **2009**, *38*, 2565–2575.
- [25] Gu, M.; He, Y.; Zheng, J.; Wang, C. Nanoscale silicon as anode for Li-ion batteries: The fundamentals, promises, and challenges. *Nano Energy* **2015**, *17*, 366–383.
- [26] Xia, S.; Wu, X.; Zhang, Z.; Cui, Y.; Liu, W. Practical Challenges and Future Perspectives of All-Solid-State Lithium-Metal Batteries. *Chem.* **2019**, *5*, 753–785.
- [27] Yu, X.; Manthiram, A. Electrode-electrolyte interfaces in lithium-based batteries. *Energy Environ. Sci.* **2018**, *11*, 527–543.
- [28] Zhang, W.; Tu, Z.; Qian, J.; Choudhury, S.; Archer, L. A.; Lu, Y. Design Principles of Functional Polymer Separators for High-Energy, Metal-Based Batteries. *Small* **2018**, *14*, 1–21.



- [29] Mindemark, J.; Lacey, M. J.; Bowden, T.; Brandell, D. Beyond PEO—Alternative host materials for Li<sup>+</sup>-conducting solid polymer electrolytes. *Prog. Polym. Sci.* **2018**, *81*, 114–143.
- [30] Gao, Z.; Sun, H.; Fu, L.; Ye, F.; Zhang, Y.; Luo, W.; Huang, Y. Promises, Challenges, and Recent Progress of Inorganic Solid-State Electrolytes for All-Solid-State Lithium Batteries. *Adv. Mater.* **2018**, *30*, 1–27.
- [31] Amnesty International, This is what we die for: Human rights abuses in the democratic republic of the congo power the global trade in cobalt. *Amnesty International* **2016**, 1–88.
- [32] Dehman, N. A.; Wallis, R.; Boaretto, A. Drilling down into the cobalt supply chain: how investors can promote responsible sourcing practices. *Principles for Responsible Investment* **2018**, 1–14.
- [33] Wood, D. L.; Li, J.; Daniel, C. Prospects for reducing the processing cost of lithium ion batteries. *J. Power Sources* **2015**, *275*, 234–242.
- [34] Padhi, A. K.; Nanjundaswamy, K. S.; Goodenough, J. B. Phospho-olivines as Positive-Electrode Materials for Rechargeable Lithium Batteries. *J. Electrochem. Soc.* **1997**, *144*, 1188–1194.
- [35] Ganose, A. M.; Jain, A. Robocrystallographer: automated crystal structure text descriptions and analysis. *MRS Commun.* **2019**, *9*, 1–8.
- [36] Ravet, N.; Chouinard, Y.; Magnan, J. F.; Besner, S.; Gauthier, M.; Armand, M. Electroactivity of natural and synthetic triphylite. *J. Power Sources* **2001**, *97-98*, 503–507.
- [37] Li, Z.; Zhang, D.; Yang, F. Developments of lithium-ion batteries and challenges of LiFePO<sub>4</sub> as one promising cathode material. *J. Mater. Sci.* **2009**, *44*, 2435–2443.
- [38] Wang, J.; Sun, X. Understanding and recent development of carbon coating on LiFePO<sub>4</sub> cathode materials for lithium-ion batteries. *Energy Environ. Sci.* **2012**, *5*, 5163–5185.
- [39] Thackeray, M. M.; Johnson, P. J.; de Picciotto, L. A.; Bruce, P. G.; Goodenough, J. B. Electrochemical extraction of lithium from LiMn<sub>2</sub>O<sub>4</sub>. *Mater. Res. Bull.* **1984**, *19*, 179–187.
- [40] Tarascon, J. M.; Wang, E.; Shokoh, F. K.; McKinnon, W. R.; Colson, S. The Spinel Phase of LiMn<sub>2</sub>O<sub>4</sub> as a Cathode in Secondary Lithium Cells. *J. Electrochem. Soc.* **1991**, *138*, 2859.
- [41] Thackeray, M. M.; David, W. I. F.; Bruce, P. G.; Goodenough, J. B. Lithium insertion into manganese spinels. *Mater. Res. Bull.* **1983**, *18*, 461–472.
- [42] Gummow, R. J.; de Kock, A.; Thackeray, M. M. Improved capacity retention in rechargeable 4 V lithium/lithium-manganese oxide (spinel) cells. *Solid State Ion.* **1994**, *69*, 59–67.

- [43] Thackeray, M. M.; Kang, S.-H.; Johnson, C. S.; Vaughey, J. T.; Benedek, R.; Hackney, S. A.  $\text{Li}_2\text{MnO}_3$ -stabilized  $\text{LiMO}_2$  (M = Mn, Ni, Co) electrodes for lithium-ion batteries. *J. Mater. Chem.* **2007**, *17*, 3112.
- [44] Manthiram, A.; Chemelewski, K.; Lee, E.-S. A perspective on the high-voltage  $\text{LiMn}_{1.5}\text{Ni}_{0.5}\text{O}_4$  spinel cathode for lithium-ion batteries. *Energy Environ. Sci.* **2014**, *7*, 1339.
- [45] Mizushima, K.; Jones, P.; Wiseman, P.; Goodenough, J.  $\text{Li}_x\text{CoO}_2$  ( $0 < x < 1$ ): A new cathode material for batteries of high energy density. *Mater. Res. Bull.* **1980**, *15*, 783–789.
- [46] Nagaura, T.; Tozawa, K. Lithium ion rechargeable battery. *Prog. Batter. Sol. Cells* **1990**, *9*, 209–217.
- [47] Delmas, C.; Fouassier, C.; Hagenmuller, P. Structural classification and properties of the layered oxides. *Phys. B+C* **1980**, *99*, 81–85.
- [48] Reimers, J. N. Electrochemical and In Situ X-Ray Diffraction Studies of Lithium Intercalation in  $\text{Li}_x\text{CoO}_2$ . *J. Electrochem. Soc.* **1992**, *139*, 2091.
- [49] Van der Ven, A.; Aydinol, M. K.; Ceder, G.; Kresse, G.; Hafner, J. First-principles investigation of phase stability in  $\text{Li}_x\text{CoO}_2$ . *Phys. Rev. B* **1998**, *58*, 2975–2987.
- [50] Lu, X.; Sun, Y.; Jian, Z.; He, X.; Gu, L.; Hu, Y.-S.; Li, H.; Wang, Z.; Chen, W.; Duan, X.; Chen, L.; Maier, J.; Tsukimoto, S.; Ikuhara, Y. New Insight into the Atomic Structure of Electrochemically Delithiated  $\text{O}_3\text{-Li}_{(1-x)}\text{CoO}_2$  ( $0 \leq x \leq 0.5$ ) Nanoparticles. *Nano Letters* **2012**, *12*, 6192–6197.
- [51] Duffiet, M.; Blangero, M.; Cabelguen, P.-E.; Delmas, C.; Carlier, D. Influence of the Initial Li/Co Ratio in  $\text{LiCoO}_2$  on the High-Voltage Phase-Transitions Mechanisms. *J. Phys. Chem. Letters* **2018**, *9*, 5334–5338.
- [52] Croguennec, L.; Palacin, M. R. Recent achievements on inorganic electrode materials for lithium-ion batteries. *J. Am. Chem. Soc.* **2015**, *137*, 3140–3156.
- [53] Croguennec, L.; Deniard, P.; Brec, R.; Lecerf, A. Preparation, physical and structural characterization of  $\text{LiMnO}_2$  samples with variable cationic disorder. *J. Mater. Chem.* **1995**, *5*, 1919–1925.
- [54] Armstrong, A. R.; Bruce, P. G. Synthesis of layered  $\text{LiMnO}_2$  as an electrode for rechargeable lithium batteries. *Nat.* **1996**, *381*, 499–500.
- [55] Hinuma, Y.; Meng, Y. S.; Kang, K.; Ceder, G. Phase Transitions in the  $\text{LiNi}_{0.5}\text{Mn}_{0.5}\text{O}_2$  System with Temperature. *Chem. Mater.* **2007**, *19*, 1790–1800.
- [56] Ammundsen, B.; Paulsen, J. Novel Lithium-Ion Cathode Materials Based on Layered Manganese Oxides. *Adv. Mater.* **2001**, *13*, 943–956.
- [57] Xu, J.; Lin, F.; Doeff, M. M.; Tong, W. A review of Ni-based layered oxides for rechargeable Li-ion batteries. *J. Mater. Chem. A* **2017**, *5*, 874–901.

- [58] Gao, H.; Zeng, X.; Hu, Y.; Tileli, V.; Li, L.; Ren, Y.; Meng, X.; Maglia, F.; Lamp, P.; Kim, S.-J.; Amine, K.; Chen, Z. Modifying the Surface of a High-Voltage Lithium-Ion Cathode. *ACS Appl. Energy Mater.* **2018**, *1*, 2254–2260.
- [59] Sturm, J.; Rheinfeld, A.; Zilberman, I.; Spingler, F.; Kosch, S.; Frie, F.; Jossen, A. Modeling and simulation of inhomogeneities in a 18650 nickel-rich, silicon-graphite lithium-ion cell during fast charging. *J. Power Sources* **2019**, *412*, 204–223.
- [60] Sun, Y.-K.; Myung, S.-T.; Kim, M.-H.; Prakash, J.; Amine, K. Synthesis and Characterization of  $Li[(Ni_{0.8}Co_{0.1}Mn_{0.1})_{0.8}(Ni_{0.5}Mn_{0.5})_{0.2}]O_2$  with the Microscale Core-Shell Structure as the Positive Electrode Material for Lithium Batteries. *J. Am. Chem. Soc.* **2005**, *127*, 13411–13418.
- [61] Sun, Y.-K.; Myung, S.-T.; Shin, H.-S.; Bae, Y. C.; Yoon, C. S. Novel Core-Shell-Structured  $Li[(Ni_{0.8}Co_{0.1}Mn_{0.1})_{0.8}(Ni_{0.5}Mn_{0.5})_{0.2}]O_2$  via Coprecipitation as Positive Electrode Material for Lithium Secondary Batteries. *J. Phys. Chem. B* **2006**, *110*, 6810–6815.
- [62] Berckmans, G.; Messagie, M.; Smekens, J.; Omar, N.; Vanhaverbeke, L.; Mierlo, J. V. Cost projection of state of the art lithium-ion batteries for electric vehicles up to 2030. *Energies* **2017**, *10*.
- [63] Song, J. H.; Kapyrou, A.; Choi, H. S.; Yu, B. Y.; Matulevich, E.; Kang, S. H. Suppression of irreversible capacity loss in Li-rich layered oxide by fluorine doping. *J. Power Sources* **2016**, *313*, 65–72.
- [64] Ong, S. P.; Chevrier, V. L.; Hautier, G.; Jain, A.; Moore, C.; Kim, S.; Ma, X.; Ceder, G. Voltage, stability and diffusion barrier differences between sodium-ion and lithium-ion intercalation materials. *Energy Environ. Sci.* **2011**, *4*, 3680–3688.
- [65] Okubo, M.; Yamada, A. Molecular Orbital Principles of Oxygen-Redox Battery Electrodes. *ACS Appl. Mater. Interfaces* **2017**, *9*, 36463–36472.
- [66] Croy, J. R.; Kang, S. H.; Balasubramanian, M.; Thackeray, M. M.  $Li_2MnO_3$ -based composite cathodes for lithium batteries: A novel synthesis approach and new structures. *Electrochem. commun.* **2011**, *13*, 1063–1066.
- [67] Wu, J. H.; Yang, L.; Liu, H. Synthesis and electrochemical properties of spherical nano-structured and nano-agglomerated  $Li_{1.2}Mn_{0.6}Ni_{0.2}O_2$  cathode materials for lithium-ion batteries. *Integr. Ferroelectr.* **2015**, *164*, 52–59.
- [68] Iddir, H.; Key, B.; Dogan, F.; Russell, J. T.; Long, B. R.; Bareño, J.; Croy, J. R.; Benedek, R. Pristine-state structure of lithium-ion-battery cathode material  $Li_{1.2}Mn_{0.4}Co_{0.4}O_2$  derived from NMR bond pathway analysis. *J. Mater. Chem. A* **2015**, *3*, 11471–11477.
- [69] Cheng, M.; Tang, W.; Sun, Y.; Zhu, K. Electrochemical properties of  $Li_2MnO_3$  nanocrystals synthesized using a hydrothermal method. *RSC Adv.* **2015**, *5*, 71088–71094.

- [70] Bréger, J.; Jiang, M.; Dupré, N.; Meng, Y. S.; Shao-Horn, Y.; Ceder, G.; Grey, C. P. High-resolution X-ray diffraction, DIFFaX, NMR and first principles study of disorder in the  $Li_2MnO_3 - Li[Ni_{1/2}Mn_{1/2}]O_2$  solid solution. *J. Solid State Chem.* **2005**, *178*, 2575–2585.
- [71] Matsunaga, T.; Komatsu, H.; Shimoda, K.; Minato, T.; Yonemura, M.; Kamiyama, T.; Kobayashi, S.; Kato, T.; Hirayama, T.; Ikuhara, Y.; Arai, H.; Ukyo, Y.; Uchimoto, Y.; Ogumi, Z. Dependence of Structural Defects in  $Li_2MnO_3$  on Synthesis Temperature. *Chem. Mater.* **2016**, *28*, 4143–4150.
- [72] Armstrong, A.; Robertson, A.; Bruce, P. Overcharging manganese oxides: Extracting lithium beyond  $Mn^{4+}$ . *J. Power Sources* **2005**, *146*, 275–280.
- [73] Amalraj, S. F.; Markovsky, B.; Sharon, D.; Talianker, M.; Zinigrad, E.; Persky, R.; Haik, O.; Grinblat, J.; Lampert, J.; Schulz-Dobrick, M.; Garsuch, A.; Burlaka, L.; Aurbach, D. Study of the electrochemical behavior of the "inactive"  $Li_2MnO_3$ . *Electrochim. Acta* **2012**, *78*, 32–39.
- [74] Dogan, F.; Croy, J. R.; Balasubramanian, M.; Slater, M. D.; Iddir, H.; Johnson, C. S.; Vaughey, J. T.; Key, B. Solid State NMR Studies of  $Li_2MnO_3$  and Li-Rich Cathode Materials: Proton Insertion, Local Structure, and Voltage Fade. *J. Electrochem. Soc.* **2014**, *162*, A235–A243.
- [75] Wu, Y.; Ming, J.; Zhuo, L.; Yu, Y.; Zhao, F. Simultaneous surface coating and chemical activation of the Li-rich solid solution lithium rechargeable cathode and its improved performance. *Electrochim. Acta* **2013**, *113*, 54–62.
- [76] Jacob, C.; Jian, J.; Su, Q.; Verkhoturov, S.; Guillemette, R.; Wang, H. Electrochemical and structural effects of in situ  $Li_2O$  extraction from  $Li_2MnO_3$  for Li-ion batteries. *ACS Appl. Mater. Interfaces* **2015**, *7*, 2433–2438.
- [77] Armstrong, A. R.; Holzapfel, M.; Novák, P.; Johnson, C. S.; Kang, S.-H.; Thackeray, M. M.; Bruce, P. G. Demonstrating oxygen loss and associated structural reorganization in the lithium battery cathode  $Li[Ni_{0.2}Li_{0.2}Mn_{0.6}]O_2$ . *J. Am. Chem. Soc.* **2006**, *128*, 8694–8698.
- [78] Yu, D. Y. W.; Yanagida, K.; Kato, Y.; Nakamura, H. Electrochemical Activities in  $Li_2MnO_3$ . *J. Electrochem. Soc.* **2009**, *156*, A417.
- [79] Rana, J.; Stan, M.; Kloepsch, R.; Li, J.; Schumacher, G.; Welter, E.; Zizak, I.; Banhart, J.; Winter, M. Structural Changes in  $Li_2MnO_3$  Cathode Material for Li-Ion Batteries. *Adv. Energy Mater.* **2014**, *4*.
- [80] Delmas, C. Battery materials: Operating through oxygen. *Nat. Chem.* **2016**, *8*, 641–643.
- [81] Seo, D. H.; Lee, J.; Urban, A.; Malik, R.; Kang, S.; Ceder, G. The structural and chemical origin of the oxygen redox activity in layered and cation-disordered Li-excess cathode materials. *Nat. Chem.* **2016**, *8*, 692–697.

- [82] Luo, K.; Roberts, M. R.; Hao, R.; Guerrini, N.; Pickup, D. M.; Liu, Y. S.; Edström, K.; Guo, J.; Chadwick, A. V.; Duda, L. C.; Bruce, P. G. Charge-compensation in 3d-transition-metal-oxide intercalation cathodes through the generation of localized electron holes on oxygen. *Nat. Chem.* **2016**, *8*, 684–691.
- [83] Li, X.; Qiao, Y.; Guo, S.; Xu, Z.; Zhu, H.; Zhang, X.; Yuan, Y.; He, P.; Ishida, M.; Zhou, H. Direct Visualization of the Reversible  $O^{2-}/O^-$  Redox Process in Li-Rich Cathode Materials. *Adv. Mater.* **2018**, *30*, 2–7.
- [84] Hong, J. et al. Metal–oxygen decoordination stabilizes anion redox in Li-rich oxides. *Nat. Mater.* **2019**, *18*, 256–265.
- [85] Koyama, Y.; Tanaka, I.; Nagao, M.; Kanno, R. First-principles study on lithium removal from  $Li_2MnO_3$ . *J. Power Sources* **2009**, *189*, 798–801.
- [86] Okamoto, Y. Ambivalent Effect of Oxygen Vacancies on  $Li_2MnO_3$ : A First-Principles Study. *J. Electrochem. Soc.* **2012**, *159*, A152.
- [87] Lim, J. M.; Kim, D.; Lim, Y. G.; Park, M. S.; Kim, Y. J.; Cho, M.; Cho, K. The origins and mechanism of phase transformation in bulk  $Li_2MnO_3$ : First-principles calculations and experimental studies. *J. Mater. Chem. A* **2015**, *3*, 7066–7076.
- [88] Marusczyk, A.; Albina, J. M.; Hammerschmidt, T.; Drautz, R.; Eckl, T.; Henkelman, G. Oxygen activity and peroxide formation as charge compensation mechanisms in  $Li_2MnO_3$ . *J. Mater. Chem. A* **2017**, *5*, 15183–15190.
- [89] Chen, H.; Islam, M. S. Lithium extraction mechanism in Li-rich  $Li_2MnO_3$  involving oxygen hole formation and dimerization. *Chem. Mater.* **2016**, *28*, 6656–6663.
- [90] Xu, J.; Sun, M.; Qiao, R.; Renfrew, S. E.; Ma, L.; Wu, T.; Hwang, S.; Nordlund, D.; Su, D.; Amine, K.; Lu, J.; McCloskey, B. D.; Yang, W.; Tong, W. Elucidating anionic oxygen activity in lithium-rich layered oxides. *Nat. Commun.* **2018**, *9*, 1–10.
- [91] Sathiya, M.; Leriche, J. B.; Salager, E.; Gourier, D.; Tarascon, J. M.; Vezin, H. Electron paramagnetic resonance imaging for real-time monitoring of Li-ion batteries. *Nat. Commun.* **2015**, *6*, 1–7.
- [92] Foix, D.; Sathiya, M.; McCalla, E.; Tarascon, J. M.; Gonbeau, D. X-ray Photoemission Spectroscopy Study of Cationic and Anionic Redox Processes in High-Capacity Li-Ion Battery Layered-Oxide Electrodes. *J. Phys. Chem. C* **2016**, *120*, 862–874.
- [93] McCalla, E.; Abakumov, A. M.; Saubanere, M.; Foix, D.; Berg, E. J.; Rouse, G.; Doublet, M.-L.; Gonbeau, D.; Novak, P.; Van Tendeloo, G.; Dominko, R.; Tarascon, J.-M. Visualization of O-O peroxo-like dimers in high-capacity layered oxides for Li-ion batteries. *Sci.* **2015**, *350*, 1516–1521.
- [94] Saubanère, M.; McCalla, E.; Tarascon, J. M.; Doublet, M. L. The intriguing question of anionic redox in high-energy density cathodes for Li-ion batteries. *Energy Environ. Sci.* **2016**, *9*, 984–991.

- [95] Grimaud, A.; Demortiere, A.; Saubanere, M.; Dachraoui, W.; Duchamp, M.; Doublet, M. L.; Tarascon, J. M. Activation of surface oxygen sites on an iridium-based model catalyst for the oxygen evolution reaction. *Nat. Energy* **2017**, *2*.
- [96] Assat, G.; Iadecola, A.; Delacourt, C.; Dedryvère, R.; Tarascon, J. M. Decoupling Cationic-Anionic Redox Processes in a Model Li-Rich Cathode via Operando X-ray Absorption Spectroscopy. *Chem. Mater.* **2017**, *29*, 9714–9724.
- [97] Assat, G.; Tarascon, J. M. Fundamental understanding and practical challenges of anionic redox activity in Li-ion batteries. *Nat. Energy* **2018**, *3*, 373–386.
- [98] Liu, H.; Chen, Y.; Hy, S.; An, K.; Venkatachalam, S.; Qian, D.; Zhang, M.; Meng, Y. S. Operando Lithium Dynamics in the Li-Rich Layered Oxide Cathode Material via Neutron Diffraction. *Adv. Energy Mater.* **2016**, *6*, 1–7.
- [99] Lu, Z.; Dahn, J. R. Understanding the Anomalous Capacity of  $Li/Li[Ni_xLi_{(1/3-2x/3)}Mn_{(2/3-x/3)}]O_2$  Cells Using In Situ X-Ray Diffraction and Electrochemical Studies. *J. Electrochem. Soc.* **2002**, *149*, A815.
- [100] Ye, D.; Zeng, G.; Nogita, K.; Ozawa, K.; Hankel, M.; Searles, D. J.; Wang, L. Understanding the Origin of  $Li_2MnO_3$  Activation in Li-Rich Cathode Materials for Lithium-Ion Batteries. *Adv. Funct. Mater.* **2015**, *25*, 7488–7496.
- [101] Mohanty, D.; Kalnaus, S.; Meisner, R. A.; Rhodes, K. J.; Li, J.; Payzant, E. A.; Wood, D. L.; Daniel, C. Structural transformation of a lithium-rich  $Li_{1.2}Co_{0.1}Mn_{0.55}Ni_{0.15}O_2$  cathode during high voltage cycling resolved by in situ X-ray diffraction. *J. Power Sources* **2013**, *229*, 239–248.
- [102] Muhammad, S.; Kim, H.; Kim, Y.; Kim, D.; Song, J. H.; Yoon, J.; Park, J. H.; Ahn, S. J.; Kang, S. H.; Thackeray, M. M.; Yoon, W. S. Evidence of reversible oxygen participation in anomalously high capacity Li- and Mn-rich cathodes for Li-ion batteries. *Nano Energy* **2016**, *21*, 172–184.
- [103] Kleiner, K.; Strehle, B.; Baker, A. R.; Day, S. J.; Tang, C. C.; Buchberger, I.; Chesneau, F. F.; Gasteiger, H. A.; Piana, M. Origin of High Capacity and Poor Cycling Stability of Li-Rich Layered Oxides: A Long-Duration in Situ Synchrotron Powder Diffraction Study. *Chem. Mater.* **2018**, *30*, 3656–3667.
- [104] Ates, M. N.; Jia, Q.; Shah, A.; Busnaina, A.; Mukerjee, S.; Abrahamab, K. M. Mitigation of layered to spinel conversion of a li-rich layered metal oxide cathode material for li-ion batteries. *J. Electrochem. Soc.* **2014**, *161*, 290–301.
- [105] Amalraj, S. F.; Sharon, D.; Talianker, M.; Julien, C. M.; Burlaka, L.; Lavi, R.; Zhecheva, E.; Markovsky, B.; Zinigrad, E.; Kovacheva, D.; Stoyanova, R.; Aurbach, D. Study of the nanosized  $Li_2MnO_3$ : Electrochemical behavior, structure, magnetic properties, and vibrational modes. *Electrochim. Acta* **2013**, *97*, 259–270.
- [106] Boulineau, A.; Croguennec, L.; Delmas, C.; Weill, F. Thermal stability of  $Li_2MnO_3$ : From localized defects to the spinel phase. *Dalton Trans.* **2012**, *41*, 1574–1581.

- [107] Croy, J. R.; Iddir, H.; Gallagher, K.; Johnson, C. S.; Benedek, R.; Balasubramanian, M. First-charge instabilities of layered-layered lithium-ion-battery materials. *Phys. Chem. Chem. Phys.* **2015**, *17*, 24382–24391.
- [108] Kim, D.; Lim, J. M.; Lim, Y. G.; Park, M. S.; Kim, Y. J.; Cho, M.; Cho, K. Understanding of Surface Redox Behaviors of  $Li_2MnO_3$  in Li-Ion Batteries: First-Principles Prediction and Experimental Validation. *ChemSusChem*. **2015**, *8*, 3255–3262.
- [109] Koga, H.; Croguennec, L.; Mannessiez, P.; Ménétrier, M.; Weill, F.; Bourgeois, L.; Duttine, M.; Suard, E.; Delmas, C.  $Li_{1.20}Mn_{0.54}Co_{0.13}Ni_{0.13}O_2$  with Different Particle Sizes as Attractive Positive Electrode Materials for Lithium-Ion Batteries: Insights into Their Structure. *J. Phys. Chem. C* **2012**, *116*, 13497–13506.
- [110] Koga, H.; Croguennec, L.; Ménétrier, M.; Mannessiez, P.; Weill, F.; Delmas, C. Different oxygen redox participation for bulk and surface: A possible global explanation for the cycling mechanism of  $Li_{1.20}Mn_{0.54}Co_{0.13}Ni_{0.13}O_2$ . *J. Power Sources* **2013**, *236*, 250–258.
- [111] Meng, J.; Zhang, S.; Wei, X.; Yang, P.; Wang, S.; Wang, J.; Li, H.; Xing, Y.; Liu, G. Synthesis, structure and electrochemical properties of lithium-rich cathode material  $Li_{1.2}Mn_{0.6}Ni_{0.2}O_2$  microspheres. *RSC Adv.* **2015**, *5*, 81565–81572.
- [112] Duraisamy, S.; Penki, T. R.; Nookala, M. Hierarchically porous  $Li_{1.2}Mn_{0.6}Ni_{0.2}O_2$  as a high capacity and high rate capability positive electrode material. *New J. Chem.* **2016**, *40*, 1312–1322.
- [113] Xiao, B.; Wang, B.; Liu, J.; Kaliyappan, K.; Sun, Q.; Liu, Y.; Dadheech, G.; Balogh, M. P.; Yang, L.; Sham, T. K.; Li, R.; Cai, M.; Sun, X. Highly stable  $Li_{1.2}Mn_{0.54}Co_{0.13}Ni_{0.13}O_2$  enabled by novel atomic layer deposited  $AlPO_4$  coating. *Nano Energy* **2017**, *34*, 120–130.
- [114] Qiu, B.; Zhang, M.; Wu, L.; Wang, J.; Xia, Y.; Qian, D.; Liu, H.; Hy, S.; Chen, Y.; An, K.; Zhu, Y.; Liu, Z.; Meng, Y. S. Gas–solid interfacial modification of oxygen activity in layered oxide cathodes for lithium-ion batteries. *Nat. Commun.* **2016**, *7*, 12108.
- [115] Iddir, H.; Bareño, J.; Benedek, R. Stability of Li- and Mn-Rich Layered-Oxide Cathodes within the First-Charge Voltage Plateau. *J. Electrochem. Soc.* **2016**, *163*, A1784–A1789.
- [116] Long, B. R.; Croy, J. R.; Park, J. S.; Wen, J.; Miller, D. J.; Thackeray, M. M. Advances in Stabilizing 'Layered-Layered'  $xLi_2MnO_3 \cdot (1-x)LiMO_2$  (M=Mn, Ni, Co) Electrodes with a Spinel Component. *J. Electrochem. Soc.* **2014**, *161*, A2160–A2167.
- [117] Rinaldo, S. G.; Gallagher, K. G.; Long, B. R.; Croy, J. R.; Bettge, M.; Abraham, D. P.; Bareño, J.; Dees, D. W. Physical Theory of Voltage Fade in Lithium- and Manganese-Rich Transition Metal Oxides. *J. Electrochem. Soc.* **2015**, *162*, A897–A904.
- [118] Malik, R. Li-Rich Layered Cathode Materials: Transition Metals in Transit. *Joule* **2017**, *1*, 647–648.

- [119] Zhang, Q.; Hu, X.; Zhan, D.; Peng, T. Pyrolysis of in situ formed lithium stearate: An effective strategy to activate  $Li_2MnO_3$ . *Electrochim. Acta* **2013**, *113*, 424–432.
- [120] Cheng, F.; Xin, Y.; Chen, J.; Lu, L.; Zhang, X.; Zhou, H. Monodisperse  $Li_{1.2}Mn_{0.6}Ni_{0.2}O_2$  microspheres with enhanced lithium storage capability. *J. Mater. Chem. A* **2013**, *1*, 5301–5308.
- [121] Shen, C. H.; Wang, Q.; Fu, F.; Huang, L.; Lin, Z.; Shen, S. Y.; Su, H.; Zheng, X. M.; Xu, B. B.; Li, J. T.; Sun, S. G. Facile synthesis of the Li-rich layered oxide  $Li_{1.23}Ni_{0.09}Co_{0.12}Mn_{0.56}O_2$  with superior lithium storage performance and new insights into structural transformation of the layered oxide material during charge-discharge cycle: In situ XRD characterization. *ACS Appl. Mater. Interfaces* **2014**, *6*, 5516–5524.
- [122] Li, H.; Fan, L. Z. Effects of fluorine substitution on the electrochemical performance of layered Li-excess nickel manganese oxides cathode materials for lithium-ion batteries. *Electrochim. Acta* **2013**, *113*, 407–411.
- [123] Wang, Z.; Wu, M.; Xu, B.; Ouyang, C. Improving the electrical conductivity and structural stability of the  $Li_2MnO_3$  cathode via P doping. *J. Alloys Compd.* **2016**, *658*, 818–823.
- [124] Gao, Y.; Ma, J.; Wang, X.; Lu, X.; Bai, Y.; Wang, Z.; Chen, L. Improved electron/Li-ion transport and oxygen stability of Mo-doped  $Li_2MnO_3$ . *J. Mater. Chem. A* **2014**, *2*, 4811–4818.
- [125] Gao, Y.; Wang, X.; Ma, J.; Wang, Z.; Chen, L. Selecting substituent elements for Li-rich Mn-based cathode materials by Density Functional Theory (DFT) calculations. *Chem. Mater.* **2015**, *27*, 3456–3461.
- [126] Kong, F.; Longo, R. C.; Yeon, D. H.; Yoon, J.; Park, J. H.; Liang, C.; Kc, S.; Zheng, Y.; Doo, S. G.; Cho, K. Multivalent Li-Site Doping of Mn Oxides for Li-Ion Batteries. *J. Phys. Chem. C* **2015**, *119*, 21904–21912.
- [127] Yi, T. F.; Li, Y. M.; Yang, S. Y.; Zhu, Y. R.; Xie, Y. Improved Cycling Stability and Fast Charge-Discharge Performance of Cobalt-Free Lithium-Rich Oxides by Magnesium-Doping. *ACS Appl. Mater. Interfaces* **2016**, *8*, 32349–32359.
- [128] Yu, R.; Wang, X.; Fu, Y.; Wang, L.; Cai, S.; Liu, M.; Lu, B.; Wang, G.; Wang, D.; Ren, Q.; Yang, X. Effect of magnesium doping on properties of lithium-rich layered oxide cathodes based on a one-step co-precipitation strategy. *J. Mater. Chem. A* **2016**, *4*, 4941–4951.
- [129] Qing, R. P.; Shi, J. L.; Xiao, D. D.; Zhang, X. D.; Yin, Y. X.; Zhai, Y. B.; Gu, L.; Guo, Y. G. Enhancing the Kinetics of Li-Rich Cathode Materials through the Pinning Effects of Gradient Surface  $Na^+$  Doping. *Adv. Energy Mater.* **2016**, *6*, 1–6.
- [130] Zhao, Y.; Liu, J.; Wang, S.; Ji, R.; Xia, Q.; Ding, Z.; Wei, W.; Liu, Y.; Wang, P.; Ivey, D. G. Surface Structural Transition Induced by Gradient Polyanion-Doping in Li-Rich Layered Oxides: Implications for Enhanced Electrochemical Performance. *Adv. Funct. Mater.* **2016**, *26*, 4760–4767.



- [131] Zheng, Z.; Guo, X. D.; Zhong, Y. J.; Hua, W. B.; Shen, C. H.; Chou, S. L.; Yang, X. S. Host Structural Stabilization of  $Li_{1.232}Mn_{0.615}Ni_{0.154}O_2$  through K-Doping Attempt: Toward Superior Electrochemical Performances. *Electrochim. Acta* **2016**, *188*, 336–343.
- [132] Pang, W. K.; Lin, H.-F.; Peterson, V. K.; Lu, C.-Z.; Liu, C.-E.; Liao, S.-C.; Chen, J.-M. Effects of Fluorine and Chromium Doping on the Performance of Lithium-Rich  $Li_{1+x}MO_2$  (M = Ni, Mn, Co) Positive Electrodes. *Chem. Mater.* **2017**, *29*, 10299–10311.
- [133] Xiang, Y.; Wu, X. Enhanced electrochemical performances of  $Li_2MnO_3$  cathode materials by Al doping. *Ionics* **2018**, *24*, 83–89.
- [134] Blazquez-Alcover, I.; Rouse, G.; Alves Dalla Corte, D.; Badot, J. C.; Grimaud, A.; Rozier, P.; Tarascon, J. M. Improving ionic conductivity by Mg-doping of  $A_2SnO_3$  (A =  $Li^+$ ,  $Na^+$ ). *Solid State Ion.* **2017**, *308*, 16–21.
- [135] Yan, P.; Zheng, J.; Zhang, X.; Xu, R.; Amine, K.; Xiao, J.; Zhang, J.-G.; Wang, C.-M. Atomic to Nanoscale Investigation of Functionalities of an  $Al_2O_3$  Coating Layer on a Cathode for Enhanced Battery Performance. *Chem. Mater.* **2016**, *28*, 857–863.
- [136] Nayak, P. K.; Erickson, E. M.; Schipper, F.; Penki, T. R.; Munichandraiah, N.; Adelhelm, P.; Sclar, H.; Amalraj, F.; Markovsky, B.; Aurbach, D. Review on Challenges and Recent Advances in the Electrochemical Performance of High Capacity Li- and Mn-Rich Cathode Materials for Li-Ion Batteries. *Adv. Energy Mater.* **2018**, *8*, 1–16.
- [137] Hu, S.; Pillai, A. S.; Liang, G.; Pang, W. K.; Wang, H.; Li, Q.; Guo, Z. Li-Rich Layered Oxides and Their Practical Challenges: Recent Progress and Perspectives. *Electrochem. Energy Rev.* **2019**, *2*, 277–311.
- [138] Thackeray, M. M.; Johnson, C. S.; Vaughey, J. T.; Li, N.; Hackney, S. A. Advances in manganese-oxide 'composite' electrodes for lithium-ion batteries. *J. Mater. Chem.* **2005**, *15*, 2257–2267.
- [139] Thackeray, M. M.; Kang, S.-H.; Johnson, C. S.; Vaughey, J. T.; Hackney, S. A. Comments on the structural complexity of lithium-rich  $Li_{1+x}M_{1-x}O_2$  electrodes (M = Mn, Ni, Co) for lithium batteries. *Electrochem. commun.* **2006**, *8*, 1531–1538.
- [140] Croy, J. R.; Kim, D.; Balasubramanian, M.; Gallagher, K.; Kang, S.-H.; Thackeray, M. M. Countering the Voltage Decay in High Capacity  $xLi_2MnO_3 \cdot (1-x)LiMO_2$  Electrodes (M = Mn, Ni, Co) for  $Li^+$ -Ion Batteries. *J. Electrochem. Soc.* **2012**, *159*, A781–A790.
- [141] Lu, Z.; Chen, Z.; Dahn, J. R. Lack of Cation Clustering in  $Li[Ni_xLi_{1/3-2x/3}Mn_{2/3-x/3}]O_2$  ( $0 < x < 1/2$ ) and  $Li[Cr_xLi_{(1-x)/3}Mn_{(2-2x)/3}]O_2$  ( $0 < x < 1$ ). *Chem. Mater.* **2003**, *15*, 3214–3220.
- [142] Koyama, Y.; Yabuuchi, N.; Tanaka, I.; Adachi, H.; Ohzuku, T. Solid-State Chemistry and Electrochemistry of  $LiCo_{1/3}Ni_{1/3}Mn_{1/3}O_2$  for Advanced Lithium-Ion Batteries. *J. Electrochem. Soc.* **2004**, *151*, A1545.

- [143] Jarvis, K. A.; Deng, Z.; Manthiram, A.; Ferreira, P. Understanding the Role of Lithium Content on the Structure and Capacity of Lithium-Rich Layered Oxides by Aberration-Corrected STEM, D-STEM, and EDS. *Microsc. Microanal.* **2012**, *18*, 1484–1485.
- [144] Gu, M.; Belharouak, I.; Zheng, J.; Wu, H.; Xiao, J.; Genc, A.; Amine, K.; Thiruvathanan, S.; Baer, D. R.; Zhang, J. G.; Browning, N. D.; Liu, J.; Wang, C. Formation of the spinel phase in the layered composite cathode used in Li-Ion batteries. *ACS Nano* **2013**, *7*, 760–767.
- [145] Shukla, A. K.; Ramasse, Q. M.; Ophus, C.; Duncan, H.; Hage, F.; Chen, G. Unravelling structural ambiguities in lithium- and manganese-rich transition metal oxides. *Nat. Commun.* **2015**, *6*, 8711.
- [146] Umicore, *Information on ITC patent case*; 2017; pp 1 – 2.
- [147] Pechini, M. P. Method of preparing lead and alkaline earth titanates and niobates and coating method using the same to form a capacitor. 1967; US3330697.
- [148] Röntgen, W. Über eine neue Art von Strahlen. *Sitzungsberichte der Physik.-Med. Gesellschaft zu Würzburg* **1895**, *137*, 132–141.
- [149] Friedrich, W.; Knipping, P.; Laue, M. Interferenzerscheinungen bei Röntgenstrahlen. *Annalen der Physik* **1913**, *346*, 971–988.
- [150] Etter, M.; Dinnebier, R. E. A century of powder diffraction: A brief history. *Z. Anorg. Allg. Chem.* **2014**, *640*, 3015–3028.
- [151] Rietveld, H. M. The crystal structure of some alkaline earth metal uranates of the type  $M_3UO_6$ . *Acta Crystallogr.* **1966**, *20*, 508–513.
- [152] Rietveld, H. M. A profile refinement method for nuclear and magnetic structures. *J. Appl. Crystallogr.* **1969**, *2*, 65–71.
- [153] Pawley, G. S. Unit-cell refinement from powder diffraction scans. *J. Appl. Crystallogr.* **1981**, *14*, 357–361.
- [154] Bonn, M. A.; Dai, M. Using Hotel Capacity to Estimate Direct Economic Impact. *J. Convention Event Tourism* **2004**, *6*, 5–20.
- [155] Petráček, V.; Dušek, M.; Palatinus, L. Crystallographic computing system JANA2006: General features. *Z. Kristallogr.* **2014**, *229*, 345–352.
- [156] Bruker, General profile and structure analysis software for powder diffraction data. *Karlsruhe, Germany* **2000**,
- [157] Larson, A. C.; Von Dreele, R. B. GSAS GENERAL STRUCTURE ANALYSIS SYSTEM manual. **2000**, 86–748.
- [158] Rodríguez-Carvajal, J. An introduction to the program FullProf. *Phys. B* **1993**, *192*, 55–69.
- [159] Rodríguez-Carvajal, J. Recent advances in magnetic structure determination by neutron powder diffraction. *Phys. B: Phys. Condens. Matter* **1993**, *192*, 55–69.

- [160] Thompson, P.; Cox, D. E.; Hastings, J. B. Rietveld refinement of Debye–Scherrer synchrotron X-ray data from  $Al_2O_3$ . *J. Appl. Crystallogr.* **1987**, *20*, 79–83.
- [161] Caglioti, G.; Paoletti, A.; Ricci, F. Choice of collimators for a crystal spectrometer for neutron diffraction. *Nucl. Instrum.* **1958**, *3*, 223–228.
- [162] Casas-Cabanas, M.; Reynaud, M.; Rikarte-Ormazabal, J.; Horbach, P.; Rodríguez-Carvajal, J. FAULTS. Available as a Sub-Program of the FullProf Suite. **2015**, FAULTS. Available as a sub-program of the FullProf.
- [163] Casas-Cabanas, M.; Rodríguez-Carvajal, J.; Palacín, M. R. Faults , a New Program for Refinement of Powder Diffraction Patterns From Layered Structures. *Z. Kristallogr., Suppl* **2006**, *23*, 243–248.
- [164] Casas-Cabanas, M.; Reynaud, M.; Rikarte, J.; Horbach, P.; Rodríguez-Carvajal, J. FAULTS: A program for refinement of structures with extended defects. *J. Appl. Crystallogr.* **2016**, *49*, 2259–2269.
- [165] Scherrer, P. Bestimmung der Größe und der inneren Struktur von Kolloidteilchen mittels Röntgenstrahlen. *Nachrichten von der Gesellschaft der Wissenschaften zu Göttingen, Mathematisch-Physikalische Klasse* **1918**, *1918*, 98–100.
- [166] Langford, J. I.; Wilson, A. J. C. Scherrer after sixty years: A survey and some new results in the determination of crystallite size. *J. Appl. Crystallogr.* **1978**, *11*, 102–113.
- [167] Stokes, A. R.; Wilson, A. J. C. The diffraction of X rays by distorted crystal aggregates - I. *Proc. Phys. Soc.* **1944**, *56*, 174–181.
- [168] de Keijser, T. H.; Langford, J. I.; Mittemeijer, E. J.; Vogels, A. B. P. Use of the Voigt function in a single-line method for the analysis of X-ray diffraction line broadening. *J. Appl. Cryst.* **1982**, *15*, 308–314.
- [169] Langford, J. I.; Louer, D. Powder diffraction. *Rep. Prog. Phys.* **1996**, *59*, 131.
- [170] Treacy, M. M.; Newsam, J. M.; Deem, M. W. A general recursion method for calculating diffracted intensities from crystals containing planar faults. *Proc. R. Soc. Lond. A* **1991**, *433*, 499–520.
- [171] Rodríguez-Carvajal, J.; González-Platas, J. Crystallographic Fortran90 Modules Library (CrysFML): a simple toolbox for crystallographic computing programs. *IUCr Comp. Comm. Newsl.* **2003**, *1*, 50–58.
- [172] Robinson, A. L. History of Synchrotron Radiation. *Synchrotron Radiat. News* **2015**, *28*, 4–9.
- [173] Larmor, J. LXIII. On the theory of the magnetic influence on spectra; and on the radiation from moving ions. *Philos. Mag.* **1897**, *44*, 503–512.
- [174] Liénard, A.-M. *L'Éclairage Électrique*; G. Carré et C. Naud, 1898; Vol. 16; pp 53–59.
- [175] Elder, F.; Gurewitsch, A.; Langmuir, R.; Pollock, H. Radiation from electrons in a synchrotron. *Phys. Rev.* **1947**, *71*, 829.

- [176] Tombouliau, D. *Röntgenstrahlen/X-Rays*; Springer, 1957; pp 246–304.
- [177] Gordon, I.; Pichakhchi, L. Radiation from Hydrogen Atoms Excited by the Synchrotron Radiation of Relativistic Electrons. *Sov. Astron.* **1961**, *5*, 63.
- [178] Blake, A. J.; Clegg, W.; Cole, J. M.; Evans, J. S.; Main, P.; Parsons, S.; Watkin, D. J. In *Nat.*; Clegg, W., Ed.; Oxford University Press Inc.: New York, 1953; Vol. 172; p 613.
- [179] Bloch, F. Nuclear induction. *Phys. Rev.* **1946**, *70*, 460.
- [180] Bloch, F.; Hansen, W.; Packard, M. The nuclear induction experiment. *Phys. Rev.* **1946**, *70*, 474–485.
- [181] Purcell, E. M.; Torrey, H. C.; Pound, R. V. Resonance absorption by nuclear magnetic moments in a solid. *Phys. Rev.* **1946**, *69*, 37.
- [182] Blümich, B. *Essential NMR: for scientists and engineers*; Springer Science & Business Media, 2005.
- [183] Carrington, A.; McLachlan, A. D. *Introduction To Magnetic Resonance*; Chapman and Hall, 1967.
- [184] Lowe, I. J. Free Induction Decays of Rotating Solids. *Phys. Rev. Lett.* **1959**, *2*, 285–287.
- [185] Andrew, E. R.; Bradbury, A.; Eades, R. G. Nuclear Magnetic Resonance Spectra from a Crystal rotated at High Speed. *Nat.* **1958**, *182*, 1659.
- [186] Polenova, T.; Gupta, R.; Goldbourt, A. Magic Angle Spinning NMR Spectroscopy: A Versatile Technique for Structural and Dynamic Analysis of Solid-Phase Systems. *Anal. Chem.* **2015**, *87*, 5458–5469.
- [187] Massiot, D.; Fayon, F.; Capron, M.; King, I.; Le Calvé, S.; Alonso, B.; Durand, J. O.; Bujoli, B.; Gan, Z.; Hoatson, G. Modelling one- and two-dimensional solid-state NMR spectra. *Magn. Reson. Chem.* **2002**, *40*, 70–76.
- [188] Meng, Y. S.; Arroyo-De Dompablo, M. E. First principles computational materials design for energy storage materials in lithium ion batteries. *Energy Environ. Sci.* **2009**, *2*, 589–609.
- [189] Foresman, J. B. Computational Chemistry: A Practical Guide for Applying Techniques to Real World Problems. *J. Am. Chem. Soc.* **2001**, *123*, 10142–10143.
- [190] Hohenberg, P.; Kohn, W. Inhomogeneous Electron Gas. *Phys. Rev.* **1964**, *136*, B864–B871.
- [191] Kohn, W.; Sham, L. J. Self-Consistent Equations Including Exchange and Correlation Effects. *Phys. Rev.* **1965**, *140*, A1133–A1138.
- [192] Hafner, J.; Wolverton, C.; Ceder, G. Toward Computational Materials Design: The Impact of Density Functional Theory on Materials Research. *MRS Bull.* **2006**, *31*, 659–668.

- [193] Joubert, D. From ultrasoft pseudopotentials to the projector augmented-wave method. *Phys. Rev. B Condens. Matter Mater. Phys.* **1999**, *59*, 1758–1775.
- [194] Kresse, G.; Marsman, M.; Furthmüller, J. VASP 5.2.2 Manual. **2014**, 237.
- [195] Blöchl, P. E. First-principles calculations of defects in oxygen-deficient silica exposed to hydrogen. *Phys. Rev. B Condens. Matter Mater. Phys.* **2000**, *62*, 6158–6179.
- [196] Kresse, G.; Furthmüller, J. Efficiency of ab-initio total energy calculations for metals and semiconductors using a plane-wave basis set. *Compu. Mater. Sci.* **1996**, *6*, 15–50.
- [197] Perdew, J. P.; Burke, K.; Ernzerhof, M. Generalized gradient approximation made simple. *Phys. Rev. Lett.* **1996**, *77*, 3865–3868.
- [198] Dudarev, S. L.; Botton, G. A.; Savrasov, S. Y.; Szotek, Z.; Temmerman, W. M.; Sutton, A. P. Electronic structure and elastic properties of strongly correlated metal oxides from first principles: LSD A + U, SIC-LSDA and EELS study of  $UO_2$  and  $NiO$ . *Phys. Status Solidi A* **1998**, *166*, 429–443.
- [199] Jain, A.; Hautier, G.; Ong, S. P.; Moore, C. J.; Fischer, C. C.; Persson, K. A.; Ceder, G. Formation enthalpies by mixing GGA and GGA + U calculations. *Phys. Rev. B Condens. Matter Mater. Phys.* **2011**, *84*, 1–10.
- [200] Ewald, P. P. Die Berechnung optischer und elektrostatischer Gitterpotentiale. *Annalen der Physik* **1921**, *369*, 253–287.
- [201] Iturrondobeitia, A.; Kvasha, A.; Lopez del Amo, J.-M.; Colin, J.; Sotta, D.; Urdampilleta, I.; Casas-Cabanas, M. A comparative study of aqueous and organic processed  $Li_{1.2}Ni_{0.2}Mn_{0.6}O_2$  Li-rich cathode materials for advanced lithium-ion batteries. *Electrochim. Acta* **2017**, *247*, 420–425.
- [202] Humphreys, C. J. In *Introduction to Analytical Electron Microscopy*; Hren, J. J., Goldstein, J. I., Joy, D. C., Eds.; Springer US: Boston, MA, 1979; pp 305–332.
- [203] Lei, C. H.; Bareño, J.; Wen, J. G.; Petrov, I.; Kang, S. H.; Abraham, D. P. Local structure and composition studies of  $Li_{1.2}Ni_{0.2}Mn_{0.6}O_2$  by analytical electron microscopy. *J. Power Sources* **2008**, *178*, 422–433.
- [204] Boulineau, A.; Croguennec, L.; Delmas, C.; Weill, F. Reinvestigation of  $Li_2MnO_3$  structure: Electron diffraction and high resolution TEM. *Chem. Mater.* **2009**, *21*, 4216–4222.
- [205] Casas-Cabanas, M.; Rodríguez-Carvajal, J.; Canales-Vázquez, J.; Lalignant, Y.; Laccorre, P.; Palacín, M. R. Microstructural characterisation of battery materials using powder diffraction data: DIFFaX, FAULTS and SH-FullProf approaches. *J. Power Sources* **2007**, *174*, 414–420.
- [206] Boulineau, A.; Croguennec, L.; Delmas, C.; Weill, F. Structure of  $Li_2MnO_3$  with different degrees of defects. *Solid State Ion.* **2010**, *180*, 1652–1659.
- [207] Shunmugasundaram, R.; Arumugam, R. S.; Dahn, J. R. A Study of Stacking Faults and Superlattice Ordering in Some Li-Rich Layered Transition Metal Oxide Positive Electrode Materials. *J. Electrochem. Soc.* **2016**, *163*, A1394–A1400.

- [208] Matsunaga, T.; Komatsu, H.; Shimoda, K.; Minato, T.; Yonemura, M.; Kamiyama, T.; Kobayashi, S.; Kato, T.; Hirayama, T.; Ikuhara, Y.; Arai, H.; Ukyo, Y.; Uchimoto, Y.; Ogumi, Z. Structural Understanding of Superior Battery Properties of Partially Ni-Doped  $Li_2MnO_3$  as Cathode Material. *The J. Phys. Chem. Letters* **2016**, *7*, 2063–2067.
- [209] Lide, D. R. CRC Handbook of Chemistry and Physics. *J. Mol. Struct.* **1992**, *268*, 320.
- [210] Sabry, A. I.; Mahdy, A. M.; Abadir, M. F. Thermal decomposition of  $MnCO_3$  (in air). *Thermochim. Acta* **1986**, *98*, 269–276.
- [211] West, A. R. Solid State Chemistry and its Applications. *Wiley* **2014**, *2*, 582.
- [212] Englert, U. Symmetry Relationships between Crystal Structures. Applications of Crystallographic Group Theory in Crystal Chemistry. By Ulrich Müller. *Angew. Chem. Int. Ed.* **2013**, *52*, 11973–11973.
- [213] Weill, F.; Tran, N.; Croguennec, L.; Delmas, C. Cation ordering in the layered  $Li_{1+x}(Ni_{0.425}Mn_{0.425}Co_{0.15})_{1-x}O_2$  materials ( $x = 0$  and  $0.12$ ). *J. Power Sources* **2007**, *172*, 893–900.
- [214] Pennycook, S. J. Z-contrast stem for materials science. *Ultramicroscopy* **1989**, *30*, 58–69.
- [215] Yan, P.; Xiao, L.; Zheng, J.; Zhou, Y.; He, Y.; Zu, X.; Mao, S. X.; Xiao, J.; Gao, F.; Zhang, J. G.; Wang, C. M. Probing the degradation mechanism of  $Li_2MnO_3$  cathode for Li-ion batteries. *Chem. Mater.* **2015**, *27*, 975–982.
- [216] Phillips, P. J.; Bareño, J.; Li, Y.; Abraham, D. P.; Klie, R. F. On the Localized Nature of the Structural Transformations of  $Li_2MnO_3$  Following Electrochemical Cycling. *Adv. Energy Mater.* **2015**, *5*, 1501252.
- [217] Liu, J.; Yin, L.; Wu, L.; Bai, J.; Bak, S. M.; Yu, X.; Zhu, Y.; Yang, X. Q.; Khalifah, P. G. Quantification of Honeycomb Number-Type Stacking Faults: Application to  $Na_3Ni_2BiO_6$  Cathodes for Na-Ion Batteries. *Inorg. Chem.* **2016**, *55*, 8478–8492.
- [218] Tan, X.; Liu, R.; Xie, C.; Shen, Q. Modified structural characteristics and enhanced electrochemical properties of oxygen-deficient  $Li_2MnO_{3-\Delta}$  obtained from pristine  $Li_2MnO_3$ . *J. Power Sources* **2018**, *374*, 134–141.
- [219] Croy, J. R.; Gallagher, K. G.; Balasubramanian, M.; Chen, Z.; Ren, Y.; Kim, D.; Kang, S. H.; Dees, D. W.; Thackeray, M. M. Examining hysteresis in composite  $x Li_2MnO_3 \cdot (1-x) LiMO_2$  cathode structures. *J. Phys. Chem. C* **2013**, *117*, 6525–6536.
- [220] Assat, G.; Foix, D.; Delacourt, C.; Iadecola, A.; Dedryvère, R.; Tarascon, J. M. Fundamental interplay between anionic/cationic redox governing the kinetics and thermodynamics of lithium-rich cathodes. *Nat. Commun.* **2017**, *8*, 2219.
- [221] Assat, G.; Delacourt, C.; Corte, D. A. D.; Tarascon, J.-M. Practical Assessment of Anionic Redox in Li-Rich Layered Oxide Cathodes: A Mixed Blessing for High Energy Li-Ion Batteries. *J. Electrochem. Soc.* **2016**, *163*, A2965–A2976.

- [222] Fell, C. R.; Qian, D.; Carroll, K. J.; Chi, M.; Jones, J. L.; Meng, Y. S. Correlation between oxygen vacancy, microstrain, and cation distribution in lithium-excess layered oxides during the first electrochemical cycle. *Chem. Mater.* **2013**, *25*, 1621–1629.
- [223] Dogan, F.; Long, B. R.; Croy, J. R.; Gallagher, K. G.; Iddir, H.; Russell, J. T.; Balasubramanian, M.; Key, B. Re-entrant lithium local environments and defect driven electrochemistry of Li- and Mn-Rich Li-Ion battery cathodes. *J. Am. Chem. Soc.* **2015**, *137*, 2328–2335.
- [224] Reimers, J. N. Synthesis and Electrochemical Studies of  $\text{LiMnO}_2$  Prepared at Low Temperatures. *J. Electrochem. Soc.* **1993**, *140*, 3396.
- [225] Sun, Y.; Cong, H.; Zan, L.; Zhang, Y. Oxygen Vacancies and Stacking Faults Introduced by Low-Temperature Reduction Improve the Electrochemical Properties of  $\text{Li}_2\text{MnO}_3$  Nanobelts as Lithium-Ion Battery Cathodes. *ACS Appl. Mater. Interfaces* **2017**, *9*, 38545–38555.
- [226] Pecher, O.; Mausolf, B.; Lamberts, K.; Oligschläger, D.; Niewieszol (née Merkens), C.; Englert, U.; Haarmann, F. The Solid Solution  $\text{Sr}_{1-x}\text{Ba}_x\text{Ga}_2$ : Substitutional Disorder and Chemical Bonding Visited by NMR Spectroscopy and Quantum Mechanical Calculations. *Chem.: Eur. J* **2015**, *21*, 13971–13982.
- [227] Haouas, M.; Taulelle, F.; Martineau, C. Recent advances in application of  $^{27}\text{Al}$  NMR spectroscopy to materials science. *Prog. Nucl. Mag. Res. Sp.* **2016**, *94-95*, 11–36.
- [228] Youngman, R. NMR spectroscopy in glass science: A review of the elements. *Mater.* **2018**, *11*.
- [229] Pecher, O.; Carretero-Gonzalez, J.; Griffith, K. J.; Grey, C. P. Materials' methods: NMR in battery research. *Chem. Mater.* **2017**, *29*, 213–242.
- [230] Magusin, P. C. M. M.; Seymour, I. D.; Pecher, O.; Grey, C. P. *Modern Methods in Solid-state NMR: A Practitioner's Guide*; RSC, 2018; pp 322–355.
- [231] Grey, C. P.; Dupre, N. NMR Studies of Cathode Materials for Lithium-Ion Rechargeable Batteries. *Chem. Rev. (Washington, DC, United States)* **2004**, *104*, 4493–4512.
- [232] Pell, A. J.; Pintacuda, G.; Grey, C. P. *Prog. Nucl. Mag. Res. Sp.*; Chapman and Hall, 2018.
- [233] Hodgkinson, P. *Modern Methods in Solid-state NMR: A Practitioner's Guide*; R. Soc. Chem., 2018; Vol. 15.
- [234] Delmas, C.; Carlier, D.; Ceder, G.; Ménétrier, M.; Grey, C. P. Understanding the NMR shifts in paramagnetic transition metal oxides using density functional theory calculations. *Phys. Rev. B Condens. Matter Mater. Phys.* **2003**, *67*, 174103.
- [235] Middlemiss, D. S.; Illott, A. J.; Clément, R. J.; Strobridge, F. C.; Grey, C. P. Density functional theory-based bond pathway decompositions of hyperfine shifts: Equipping solid-state NMR to characterize atomic environments in paramagnetic materials. *Chem. Mater.* **2013**, *25*, 1723–1734.

- [236] Seymour, I. D.; Middlemiss, D. S.; Halat, D. M.; Trease, N. M.; Pell, A. J.; Grey, C. P. Characterizing Oxygen Local Environments in Paramagnetic Battery Materials via  $^{17}\text{O}$  NMR and DFT Calculations. *J. Am. Chem. Soc.* **2016**, *138*, 9405–9408.
- [237] Bamine, T.; Boivin, E.; Boucher, F.; Messinger, R. J.; Salager, E.; Deschamps, M.; Masquelier, C.; Croguennec, L.; Ménétrier, M.; Carlier, D. Understanding Local Defects in Li-Ion Battery Electrodes through Combined DFT/NMR Studies: Application to  $\text{LiVPO}_4\text{F}$ . *J. Phys. Chem. C* **2017**, *121*, 3219–3227.
- [238] Grey, C. P.; Lee, Y. J. Lithium MAS NMR studies of cathode materials for lithium-ion batteries. *Solid State Sci.* **2003**, *5*, 883–894.
- [239] Zhang, Y.; Castets, A.; Carlier, D.; Ménétrier, M.; Boucher, F. Simulation of NMR Fermi contact shifts for lithium battery materials: The need for an efficient hybrid functional approach. *J. Phys. Chem. C* **2012**, *116*, 17393–17402.
- [240] Castets, A.; Carlier, D.; Zhang, Y.; Boucher, F.; Ménétrier, M. A DFT-based analysis of the NMR fermi contact shifts in tavorite-like  $\text{LiMPO}_4\cdot\text{OH}$  and  $\text{MPO}_4\cdot\text{H}_2\text{O}$  (M = Fe, Mn, V). *J. Phys. Chem. C* **2012**, *116*, 18002–18014.
- [241] Morgan, K. R.; Collier, S.; Burns, G.; Ooi, K. A  $^6\text{Li}$  and  $^7\text{Li}$  MAS NMR study of the spinel-type manganese oxide  $\text{LiMn}_2\text{O}_4$  and the rock salt-type manganese oxide  $\text{Li}_2\text{MnO}_3$ . *J. Chem. Soc. Chem. Commun.* **1994**, *2*, 1719–1720.
- [242] Mustarelli, P.; Massarotti, V.; Bini, M.; Capsoni, D. Transferred hyperfine interaction and structure in  $\text{LiMn}_2\text{O}_4$  and  $\text{Li}_2\text{MnO}_3$  coexisting phases: A XRD and  $^7\text{Li}$  NMR-MAS study. *Phys. Rev. B Condens. Matter Mater. Phys.* **1997**, *55*, 12018–12024.
- [243] Lee, Y. J.; Wang, F.; Grey, C. P.  $^6\text{Li}$  and  $^7\text{Li}$  MAS NMR studies of lithium manganate cathode materials. *J. Am. Chem. Soc.* **1998**, *120*, 12601–12613.
- [244] Lee, Y. J.; Grey, C. P. Determining the lithium local environments in the lithium manganates  $\text{LiZn}_{0.5}\text{Mn}_{1.5}\text{O}_4$  and  $\text{Li}_2\text{MnO}_3$  by analysis of the  $^6\text{Li}$  MAS NMR spinning sideband manifolds. *J. Phys. Chem. B* **2002**, *106*, 3576–3582.
- [245] Pecher, O.; Halat, D. M.; Lee, J.; Liu, Z.; Griffith, K. J.; Braun, M.; Grey, C. P. Enhanced efficiency of solid-state NMR investigations of energy materials using an external automatic tuning/matching (eATM) robot. *J. Magn. Reson.* **2017**, *275*, 127–136.
- [246] Bertini, I.; Luchinat, C.; Parigi, G. Magnetic susceptibility in paramagnetic NMR. *Prog. Nucl. Mag. Res. Sp.* **2002**, *40*, 249–273.
- [247] Zhou, F.; Cococcioni, M.; Kang, K.; Ceder, G. The Li intercalation potential of  $\text{LiMPO}_4$  and  $\text{LiMSiO}_4$  olivines with M = Fe, Mn, Co, Ni. *Electrochem. commun.* **2004**, *6*, 1144–1148.
- [248] Zhou, F.; Cococcioni, M.; Marianetti, C. A.; Morgan, D.; Ceder, G. First-principles prediction of redox potentials in transition-metal compounds with LDA + U. *Phys. Rev. B Condens. Matter Mater. Phys.* **2004**, *70*, 1–8.



- [249] Shin, Y.; Ding, H.; Persson, K. A. Revealing the Intrinsic Li Mobility in the  $Li_2MnO_3$  Lithium-Excess Material. *Chem. Mater.* **2016**, *28*, 2081–2088.
- [250] Ong, S. P.; Richards, W. D.; Jain, A.; Hautier, G.; Kocher, M.; Cholia, S.; Gunter, D.; Chevrier, V. L.; Persson, K. A.; Ceder, G. Python Materials Genomics (pymatgen): A robust, open-source python library for materials analysis. *Comput. Mater. Chem.* **2013**, *68*, 314–319.
- [251] Tang, W.; Kanoh, H.; Yang, X.; Ooi, K. Preparation of plate-form manganese oxide by selective lithium extraction from monoclinic  $Li_2MnO_3$  under hydrothermal conditions. *Chem. Mater.* **2000**, *12*, 3271–3279.
- [252] Robertson, A. D.; Bruce, P. G. Mechanism of electrochemical activity in  $Li_2MnO_3$ . *Chem. Mater.* **2003**, *15*, 1984–1992.
- [253] Benedek, R.; Thackeray, M. M.; van de Walle, A. Free Energy for Protonation Reaction in Lithium-Ion Battery Cathode Materials. *Chem. Mater.* **2008**, *20*, 5485–5490.
- [254] Kubota, K.; Kaneko, T.; Hirayama, M.; Yonemura, M.; Imanari, Y.; Nakane, K.; Kanno, R. Direct synthesis of oxygen-deficient  $Li_2MnO_{3-x}$  for high capacity lithium battery electrodes. *J. Power Sources* **2012**, *216*, 249–255.
- [255] James, C.; Wu, Y.; Sheldon, B. W.; Qi, Y. The impact of oxygen vacancies on lithium vacancy formation and diffusion in  $Li_{2-x}MnO_{3-\delta}$ . *Solid State Ion.* **2016**, *289*, 87–94.
- [256] Johnson, C. S.; Kim, J. S.; Lefief, C.; Li, N.; Vaughey, J. T.; Thackeray, M. M. The significance of the  $Li_2MnO_3$  component in 'composite'  $xLi_2MnO_3 \cdot (1-x)LiMn_{0.5}Ni_{0.5}O_2$  electrodes. *Electrochem. commun.* **2004**, *6*, 1085–1091.
- [257] Neudecker, B.; Zuhr, R.; Kwak, B.; Bates, J. Lithium Manganese Nickel Oxides  $Li_x(Mn_yNi_{1-y})_{2-x}O_2$ . *J. Electrochem. Soc.* **1998**, *145*, 4148–4159.
- [258] Rossouw, M.; Thackeray, M. M. Lithium manganese oxides from  $Li_2MnO_3$  for rechargeable lithium battery applications. *Mater. Res. Bull.* **1991**, *26*, 463–473.
- [259] Kang, S.-H.; Johnson, C. S.; Vaughey, J. T.; Amine, K.; Thackeray, M. M. The Effects of Acid Treatment on the Electrochemical Properties of  $0.5Li_2MnO_3 \cdot 0.5LiNi_{0.44}Co_{0.25}Mn_{0.31}O_2$  Electrodes in Lithium Cells. *J. Electrochem. Soc.* **2006**, *153*, A1186.
- [260] Hoang, K. Defect physics, delithiation mechanism, and electronic and ionic conduction in layered lithium manganese oxide cathode materials. *Phys. Rev. Appl.* **2015**, *3*, 1–17.
- [261] Longo, R. C.; Kong, F. T.; Santosh, K. C.; Park, M. S.; Yoon, J.; Yeon, D. H.; Park, J. H.; Doo, S. G.; Cho, K. Phase stability of Li-Mn-O oxides as cathode materials for Li-ion batteries: Insights from ab initio calculations. *Phys. Chem. Chem. Phys.* **2014**, *16*, 11233–11242.
- [262] Ruther, R. E.; Dixit, H.; Pezeshki, A. M.; Sacci, R. L.; Cooper, V. R.; Nanda, J.; Veith, G. M. Correlating Local Structure with Electrochemical Activity in  $Li_2MnO_3$ . *J. Phys. Chem. C* **2015**, *119*, 18022–18029.

- [263] House, R. A. et al. What Triggers Oxygen Loss in Oxygen Redox Cathode Materials? *Chem. Mater.* **2019**, *31*, 3293–3300.
- [264] Radin, M. D.; Vinckeviciute, J.; Seshadri, R.; Van der Ven, A. Manganese oxidation as the origin of the anomalous capacity of Mn-containing Li-excess cathode materials. *Nat. Energy* **2019**,
- [265] Hoang, K. Doping Li-rich cathode material  $Li_2MnO_3$ : Interplay between lattice site preference, electronic structure, and delithiation mechanism. *Phys. Rev. Mater.* **2017**, *075404*, 1–10.
- [266] Xiao, P.; Deng, Z. Q.; Manthiram, A.; Henkelman, G. Calculations of Oxygen Stability in Lithium-Rich Layered Cathodes. *J. Phys. Chem. C* **2012**, *116*, 23201–23204.
- [267] An, J.; Shi, L.; Chen, G.; Li, M.; Liu, H.; Yuan, S.; Chen, S.; Zhang, D. Insights into the stable layered structure of a Li-rich cathode material for lithium-ion batteries. *J. Mater. Chem. A* **2017**, *5*, 19738–19744.
- [268] Kong, F.; Longo, R. C.; Park, M. S.; Yoon, J.; Yeon, D. H.; Park, J. H.; Wang, W. H.; Kc, S.; Doo, S. G.; Cho, K. Ab initio study of doping effects on  $LiMnO_2$  and  $Li_2MnO_3$  cathode materials for Li-ion batteries. *J. Mater. Chem. A* **2015**, *3*, 8489–8500.
- [269] Delmas, C.; Ménétrier, M.; Croguennec, L.; Saadoune, I.; Rougier, A.; Pouillier, C.; Prado, G.; Grüne, M.; Fournès, L. An overview of the  $Li(Ni,M)O_2$  systems: syntheses, structures and properties. *Electrochim. Acta* **1999**, *45*, 243–253.
- [270] Sun, Y. K.; Kim, M. G.; Kang, S. H.; Amine, K. Electrochemical performance of layered  $Li[Li_{0.15}Ni_{0.275-x}Mg_xMn_{0.575}]O_2$  cathode materials for lithium secondary batteries. *J. Mater. Chem.* **2003**, *13*, 319–322.
- [271] Liu, W.; Oh, P.; Liu, X.; Lee, M.-J.; Cho, W.; Chae, S.; Kim, Y.; Cho, J. Nickel-Rich Layered Lithium Transition-Metal Oxide for High-Energy Lithium-Ion Batteries. *Angew. Chem. Int. Ed.* **2015**, *54*, 4440–4457.
- [272] Wang, Y. X.; Shang, K. H.; He, W.; Ai, X. P.; Cao, Y. L.; Yang, H. X. Magnesium-Doped  $Li_{1.2}[Co_{0.13}Ni_{0.13}Mn_{0.54}]O_2$  for Lithium-Ion Battery Cathode with Enhanced Cycling Stability and Rate Capability. *ACS Appl. Mater. Interfaces* **2015**, *7*, 13014–13021.
- [273] Nayak, P. K.; Grinblat, J.; Levi, E.; Levi, M.; Markovsky, B.; Aurbach, D. Understanding the influence of Mg doping for the stabilization of capacity and higher discharge voltage of Li- and Mn-rich cathodes for Li-ion batteries. *Phys. Chem. Chem. Phys.* **2017**, *19*, 6142–6152.
- [274] Torres-Castro, L.; Abreu-Sepulveda, M. A.; Katiyar, R. S.; Manivannan, A. Electrochemical Investigations on the Effect of Mg-Substitution in  $Li_2MnO_3$  Cathode. *J. Electrochem. Soc.* **2017**, *164*, A1464–A1473.
- [275] Zhang, S.; Tang, T.; Ma, Z.; Gu, H.; Du, W.; Gao, M.; Liu, Y.; Jian, D.; Pan, H. Tuning  $Li_2MO_3$  phase abundance and suppressing migration of transition metal ions to improve the overall performance of Li- and Mn-rich layered oxide cathode. *J. Power Sources* **2018**, *380*, 1–11.

- [276] Chen, S.; Chen, Z.; Xia, M.; Cao, C.; Luo, Y. Toward Alleviating Voltage Decay by Sodium Substitution in Lithium-Rich Manganese-Based Oxide Cathodes. *ACS Appl. Energy Mater.* **2018**, *1*, 4065–4074.
- [277] Li, Q.; Li, G.; Fu, C.; Luo, D.; Fan, J.; Li, L.  $K^+$ -doped  $Li_{1.2}Mn_{0.54}Co_{0.13}Ni_{0.13}O_2$ : A novel cathode material with an enhanced cycling stability for lithium-ion batteries. *ACS Appl. Mater. Interfaces* **2014**, *6*, 10330–10341.
- [278] Tang, W.; Sanville, E.; Henkelman, G. A grid-based Bader analysis algorithm without lattice bias. *J. Phys. Condens. Matter.* **2009**, *21*, 84204.
- [279] Henkelman, G.; Arnaldsson, A.; Jónsson, H. A fast and robust algorithm for Bader decomposition of charge density. *Comput. Mater. Chem.* **2006**, *36*, 354–360.
- [280] Sanville, E.; Kenny, S. D.; Smith, R.; Henkelman, G. Improved grid-based algorithm for Bader charge allocation. *J. Comput. Chem.* **2007**, *28*, 899–908.
- [281] Mortemard de Boisse, B.; Reynaud, M.; Ma, J.; Kikkawa, J.; Nishimura, S.-i.; Casas-Cabanas, M.; Delmas, C.; Okubo, M.; Yamada, A. Coulombic self-ordering upon charging a large-capacity layered cathode material for rechargeable batteries. *Nat. Commun.* **2019**, *10*, 2185.
- [282] Zheng, L.; Wang, H.; Luo, M.; Wang, G.; Wang, Z.; Ouyang, C.  $Na_2MnO_3$  as cathode materials for Na ion batteries: From first-principles investigations. *Solid State Ion.* **2018**, *320*, 210–214.
- [283] Kim, H.; Hong, J.; Park, K.-Y.; Kim, H.; Kim, S.-W.; Kang, K. Aqueous Rechargeable Li and Na Ion Batteries. *Chem. Rev.* **2014**, *114*, 11788–11827.
- [284] Palacín, M. R.; Simon, P.; Tarascon, J. M. Nanomaterials for Electrochemical Energy Storage: the Good and the Bad. *Acta Chim. Slov.* **2016**, *63*, 417–423.
- [285] Malik, R.; Zhou, F.; Ceder, G. Kinetics of non-equilibrium lithium incorporation in  $LiFePO_4$ . *Nat. Mater.* **2011**, *10*, 587–590.
- [286] Vinckevičiūtė, J.; Radin, M. D.; der Ven, A. Stacking-Sequence Changes and Na Ordering in Layered Intercalation Materials. *Chem. Mater.* **2016**, *28*, 8640–8650.
- [287] Kaufman, J. L.; der Ven, A.  $Na_xCoO_2$  phase stability and hierarchical orderings in the  $O3/P3$  structure family. *Phys. Rev. Mater.* **2019**, *3*, 15402.
- [288] Radin, M. D.; Alvarado, J.; Meng, Y. S.; Van Der Ven, A. Role of Crystal Symmetry in the Reversibility of Stacking-Sequence Changes in Layered Intercalation Electrodes. *Nano Lett.* **2017**, *17*, 7789–7795.
- [289] Gallagher, K. G.; Croy, J. R.; Balasubramanian, M.; Bettge, M.; Abraham, D. P.; Burrell, A. K.; Thackeray, M. M. Correlating hysteresis and voltage fade in lithium- and manganese-rich layered transition-metal oxide electrodes. *Electrochem. commun.* **2013**, *33*, 96–98.
- [290] Croy, J. R.; Balasubramanian, M.; Gallagher, K. G.; Burrell, A. K. Review of the U.S. Department of Energy's "deep Dive" Effort to Understand Voltage Fade in Li- and Mn-Rich Cathodes. *Acc. Chem. Res.* **2015**, *48*, 2813–2821.

- [291] Arcelus, O.; Carrasco, J. Atomistic Insight into Glide-Driven Phase Transformations in Layered Oxides for Sodium-Ion Batteries: A Case Study on  $Na_xVO_2$ . *ACS Appl. Mater. Interfaces* **2019**, *11*, 12562–12569.
- [292] Mishra, S. K.; Ceder, G. Structural stability of lithium manganese oxides. *Phys. Rev. B Condens. Matter Mater. Phys.* **1999**, *59*, 6120–6130.
- [293] Bareño, J.; Balasubramanian, M.; Kang, S. H.; Wen, J. G.; Lei, C. H.; Pol, S. V.; Petrov, I.; Abraham, D. P. Long-range and local structure in the layered oxide  $Li_{1.2}Co_{0.4}Mn_{0.4}O_2$ . *Chem. Mater.* **2011**, *23*, 2039–2050.
- [294] Genevois, C.; Koga, H.; Croguennec, L.; Ménétrier, M.; Delmas, C.; Weill, F. Insight into the atomic structure of cycled lithium-rich layered oxide  $Li_{1.20}Mn_{0.54}Co_{0.13}Ni_{0.13}O_2$  using HAADF STEM and electron nanodiffraction. *J. Phys. Chem. C* **2015**, *119*, 75–83.
- [295] Jarvis, K. A.; Deng, Z.; Allard, L. F.; Manthiram, A.; Ferreira, P. J. Atomic structure of a lithium-rich layered oxide material for lithium-ion batteries: Evidence of a solid solution. *Chem. Mater.* **2011**, *23*, 3614–3621.
- [296] Mohanty, D.; Huq, A.; Payzant, E. A.; Sefat, A. S.; Li, J.; Abraham, D. P.; Wood, D. L.; Daniel, C. Neutron diffraction and magnetic susceptibility studies on a high-voltage  $Li_{1.2}Mn_{0.55}Ni_{0.15}Co_{0.10}O_2$  lithium ion battery cathode: Insight into the crystal structure. *Chem. Mater.* **2013**, *25*, 4064–4070.
- [297] Riekehr, L.; Liu, J.; Schwarz, B.; Sigel, F.; Kerkamm, I.; Xia, Y.; Ehrenberg, H. Fatigue in  $0.5Li_2MnO_3 \cdot 0.5Li(Ni_{1/3}Co_{1/3}Mn_{1/3})O_2$  positive electrodes for lithium ion batteries. *J. Power Sources* **2016**, *325*, 391–403.
- [298] Riekehr, L.; Liu, J.; Schwarz, B.; Sigel, F.; Kerkamm, I.; Xia, Y.; Ehrenberg, H. Effect of pristine nanostructure on first cycle electrochemical characteristics of lithium-rich lithium-nickel-cobalt-manganese-oxide cathode ceramics for lithium ion batteries. *J. Power Sources* **2016**, *306*, 135–147.
- [299] de Biasi, L.; Schwarz, B.; Brezesinski, T.; Hartmann, P.; Janek, J.; Ehrenberg, H. Chemical, Structural, and Electronic Aspects of Formation and Degradation Behavior on Different Length Scales of Ni-Rich NCM and Li-Rich HE-NCM Cathode Materials in Li-Ion Batteries. *Adv. Mater.* **2019**, *31*.
- [300] Yabuuchi, N.; Yoshii, K.; Myung, S. T.; Nakai, I.; Komaba, S. Detailed studies of a high-capacity electrode material for rechargeable batteries,  $Li_2MnO_3 - LiCo_{1/3}Ni_{1/3}Mn_{1/3}O_2$ . *J. Am. Chem. Soc.* **2011**, *133*, 4404–4419.
- [301] Gent, W. E. et al. Coupling between oxygen redox and cation migration explains unusual electrochemistry in lithium-rich layered oxides. *Nat. Commun.* **2017**, *8*.
- [302] Perez, A. J.; Jacquet, Q.; Batuk, D.; Iadecola, A.; Saubanère, M.; Rouse, G.; Larcher, D.; Vezin, H.; Doublet, M. L.; Tarascon, J. M. Approaching the limits of cationic and anionic electrochemical activity with the Li-rich layered rocksalt  $Li_3IrO_4$ . *Nat. Energy* **2017**, *2*, 954–962.

- [303] Grimaud, A.; Hong, W. T.; Shao-Horn, Y.; Tarascon, J.-M. Anionic redox processes for electrochemical devices. *Nat. Mater.* **2016**, *15*, 121–126.
- [304] Manthiram, A.; Knight, J. C.; Myung, S. T.; Oh, S. M.; Sun, Y. K. Nickel-Rich and Lithium-Rich Layered Oxide Cathodes: Progress and Perspectives. *Adv. Energy Mater.* **2016**, *6*.
- [305] Wang, E.; Shao, C.; Qiu, S.; Chu, H.; Zou, Y.; Xiang, C.; Xu, F.; Sun, L. Organic carbon gel assisted-synthesis of  $Li_{1.2}Mn_{0.6}Ni_{0.2}O_2$  for a high-performance cathode material for Li-ion batteries. *RSC Adv.* **2017**, *7*, 1561–1566.
- [306] Li, J.; Zhan, C.; Lu, J.; Yuan, Y.; Shahbazian-Yassar, R.; Qiu, X.; Amine, K. Improve First-Cycle Efficiency and Rate Performance of Layered-Layered  $Li_{1.2}Mn_{0.6}Ni_{0.2}O_2$  Using Oxygen Stabilizing Dopant. *ACS Appl. Mater. Interfaces* **2015**, *7*, 16040–16045.
- [307] He, X.; Wang, J.; Wang, L.; Li, J. Nano-crystalline  $Li_{1.2}Mn_{0.6}Ni_{0.2}O_2$  prepared via amorphous complex precursor and its electrochemical performances as cathode material for lithium-ion batteries. *Mater.* **2016**, *9*, 16–20.
- [308] Huang, J. X.; Li, B.; Liu, B.; Liu, B. J.; Zhao, J. B.; Ren, B. Structural evolution of NM (Ni and Mn) lithium-rich layered material revealed by in-situ electrochemical Raman spectroscopic study. *J. Power Sources* **2016**, *310*, 85–90.
- [309] Setyawan, W.; Curtarolo, S. High-throughput electronic band structure calculations: Challenges and tools. *Comput. Mater. Sci.* **2010**, *49*, 299–312.
- [310] Bréger, J.; Dupré, N.; Chupas, P. J.; Lee, P. L.; Proffen, T.; Parise, J. B.; Grey, C. P. Short- and long-range order in the positive electrode material,  $Li(NiMn)_{0.5}O_2$ : A joint X-ray and neutron diffraction, pair distribution function analysis and NMR study. *J. Am. Chem. Soc.* **2005**, *127*, 7529–7537.
- [311] Lee, S.; Choi, S.; Kim, J.; Sim, H.; Won, C.; Lee, S.; Kim, S. A.; Hur, N.; Park, J. G. Antiferromagnetic ordering in  $Li_2MnO_3$  single crystals with a two-dimensional honeycomb lattice. *J. Phys. Condens. Matter* **2012**, *24*.
- [312] Sathiya, M.; Rousse, G.; Ramesha, K.; Laisa, C. P.; Vezin, H.; Sougrati, M. T.; Doublet, M. L.; Foix, D.; Gonbeau, D.; Walker, W.; Prakash, A. S.; Ben Hassine, M.; Dupont, L.; Tarascon, J. M. Reversible anionic redox chemistry in high-capacity layered-oxide electrodes. *Nat. Mater.* **2013**, *12*, 827–835.
- [313] McCalla, E.; Sougrati, M. T.; Rousse, G.; Berg, E. J.; Abakumov, A.; Recham, N.; Ramesha, K.; Sathiya, M.; Dominko, R.; Van Tendeloo, G.; Novák, P.; Tarascon, J. M. Understanding the Roles of Anionic Redox and Oxygen Release during Electrochemical Cycling of Lithium-Rich Layered  $Li_4FeSbO_6$ . *J. Am. Chem. Soc.* **2015**, *137*, 4804–4814.
- [314] Li, B.; Shao, R.; Yan, H.; An, L.; Zhang, B.; Wei, H.; Ma, J.; Xia, D.; Han, X. Understanding the Stability for Li-Rich Layered Oxide  $Li_2RuO_3$  Cathode. *Adv. Funct. Mater.* **2016**, *26*, 1330–1337.
- [315] Li, W.; Song, B.; Manthiram, A. High-voltage positive electrode materials for lithium-ion batteries. *Chem. Soc. Rev.* **2017**, *46*, 3006–3059.

- [316] Kosova, N. V.; Devyatkina, E. T.; Kaichev, V. V. Optimization of  $Ni^{2+}/Ni^{3+}$  ratio in layered  $Li(Ni,Mn,Co)O_2$  cathodes for better electrochemistry. *J. Power Sources* **2007**, *174*, 965–969.
- [317] Zhang, X.; Jiang, W. J.; Mauger, A.; Qilu,; Gendron, F.; Julien, C. M. Minimization of the cation mixing in  $Li_{1+x}(NMC)_{1-x}O_2$  as cathode material. *J. Power Sources* **2010**, *195*, 1292–1301.
- [318] Amatucci, G. G.; Tarascon, J.-M.; Klein, L. C.  $CoO_2$ , The End Member of the  $LiCoO_2$  Solid Solution. *Electrochem. Soc.* **1996**, *143*, 1114–1123.
- [319] Gummow, R. J.; Sharma, N.; Feng, R.; Han, G.; He, Y. High Performance Composite Lithium-Rich Nickel Manganese Oxide Cathodes for Lithium-Ion Batteries. *J. Electrochem. Soc.* **2013**, *160*, A1856–A1862.
- [320] Toriyama, M. Y.; Kaufman, J. L.; Van Der Ven, A. Potassium Ordering and Structural Phase Stability in Layered  $K_xCoO_2$ . *ACS Appl. Energy Mater.* **2019**, *2*, 2629–2636.
- [321] Li, H.; Zhou, P.; Liu, F.; Li, H.; Cheng, F.; Chen, J. Stabilizing nickel-rich layered oxide cathodes by magnesium doping for rechargeable lithium-ion batteries. *Chem. Sci.* **2019**, *10*, 1374–1379.

# Appendix A

## A.1 Chapter 2

Figure A.1 shows the difference between a Lorentzian and Gaussian distribution. The former one is thinner on the top and wider on the lower part, showing a longer tail. Generally speaking for XRD, Lorentzian broadening is related with crystallite size (the lower the crystallite size the higher the Lorentzian contribution will be to the peak shape) and Gaussian distribution is typically related with crystallite microstrains.

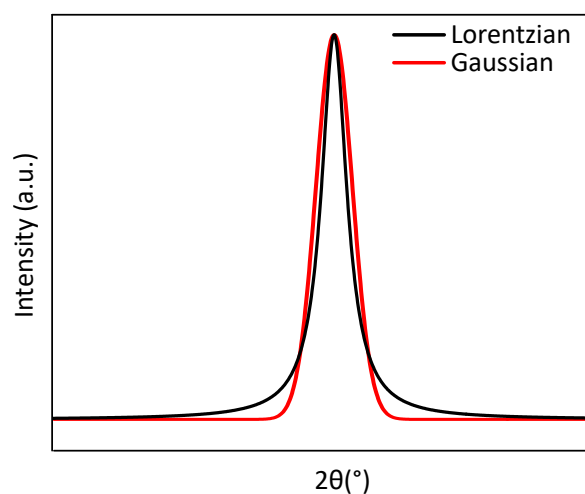


Fig. A.1 Visualization of Gaussian and Lorentzian profile functions.

## A.2 Chapter 3

Table A.1 FAULTS unit cell values for the refined samples.

	T (°C)	a,b (Å)	c (Å)	( $\gamma$ )
LMO_MnO_	900	4.92146(1)	4.73833(4)	60.012(1)
	800	4.92197(1)	4.73754(5)	60.029(2)
	700	4.92365(1)	4.73819(5)	60.02(2)
LMO_Mn2O3_	900	4.92027(2)	4.74157(4)	60.0186(7)
	800	4.92300(2)	4.73879(4)	60.0317(3)
	700	4.92192(1)	4.73900(4)	60.031(1)
LMO_MnCO3_	900	4.92378(1)	4.73783(3)	60.029(1)
	800	4.92485(7)	4.73878(3)	60.011(2)
	700	4.92394(3)	4.73631(6)	60.0303(6)



Table A.2 Refined atomic positions in the TM layers (L2=L3=L4) obtained from the FAULTS refinements of the XRD patterns of the 9 samples.

LMO_MnCO3_												
700												
Atom	x	y	z	x	y	z	x	y	z	x	y	z
Li <sup>I</sup>	0	0	0	0	0	0	0	0	0	0	0	0
Mn <sup>IV</sup>	0.3353(2)	0.3353(2)	0	0.3363(3)	0.3363(3)	0	0.3336(3)	0.3336(3)	0	0.3336(3)	0.3336(3)	0
Mn <sup>IV</sup>	0.6647(2)	0.6647(2)	0	0.6637(3)	0.6637(3)	0	0.6664(3)	0.6664(3)	0	0.6664(3)	0.6664(3)	0
O <sup>II-</sup>	0.3579(9)	-0.0057(8)	0.2287(2)	0.37(7)	0.64(7)	-0.22(4)	0.352(3)	0.633(2)	-0.218(1)	0.352(3)	0.633(2)	-0.218(1)
O <sup>II-</sup>	0.64166(4)	0.0064(2)	-0.22842(2)	0.63(8)	0.36(7)	0.22(4)	0.6328(3)	0.3537(2)	0.21792(3)	0.6328(3)	0.3537(2)	0.21792(3)
O <sup>II-</sup>	-0.0089(3)	0.3727(1)	-0.20930(1)	0.37(4)	0.01(3)	0.20(3)	0.3593(7)	0.0085(8)	0.2200(4)	0.3593(7)	0.0085(8)	0.2200(4)
O <sup>II-</sup>	0.3581(7)	0.6413(2)	-0.2270(2)	0.63(4)	-0.01(4)	-0.21(3)	0.6290(2)	0.0229(5)	-0.22035(5)	0.6290(2)	0.0229(5)	-0.22035(5)
O <sup>II-</sup>	0.6435(2)	0.36008(5)	0.22715(1)	-0.02(6)	0.36(7)	-0.23(4)	0.00820(8)	0.36123(4)	-0.22024(2)	0.00820(8)	0.36123(4)	-0.22024(2)
O <sup>II-</sup>	0.0083(1)	0.62724(2)	0.2096(8)	0.02(6)	0.64(7)	0.23(4)	0.0289(1)	0.62333(6)	0.21720(6)	0.0289(1)	0.62333(6)	0.21720(6)
LMO_Mn2O3_												
700												
Atom	x	y	z	x	y	z	x	y	z	x	y	z
Li <sup>I</sup>	0	0	0	0	0	0	0	0	0	0	0	0
Mn <sup>IV</sup>	0.33242(5)	0.33242(5)	0	0.33182(5)	0.33182(5)	0	0.3358(2)	0.3358(2)	0	0.3358(2)	0.3358(2)	0
Mn <sup>IV</sup>	0.66758(5)	0.66758(5)	0	0.66818(5)	0.66818(5)	0	0.6642(2)	0.6642(2)	0	0.6642(2)	0.6642(2)	0
O <sup>II-</sup>	0.3581(8)	0.6377(3)	-0.2185(2)	0.356(1)	0.6335(7)	-0.2079(3)	0.370(1)	0.6298(1)	-0.2225(2)	0.370(1)	0.6298(1)	-0.2225(2)
O <sup>II-</sup>	0.6408(1)	0.36016(8)	0.21849(1)	0.62996(6)	0.3551(2)	0.20786(2)	0.62980(6)	0.36949(6)	0.22239(2)	0.62980(6)	0.36949(6)	0.22239(2)
O <sup>II-</sup>	0.36797(5)	-0.0084(1)	0.23319(4)	0.36477(5)	0.0027(4)	0.22910(3)	0.37539(3)	-0.0018(4)	0.22049(2)	0.37539(3)	-0.0018(4)	0.22049(2)
O <sup>II-</sup>	0.62891(3)	0.0096(1)	-0.23294(1)	0.62384(3)	0.032(2)	-0.2300(9)	-0.221(1)	0.003(3)	0.623(1)	-0.221(1)	0.003(3)	0.623(1)
O <sup>II-</sup>	0.000(1)	0.3640(8)	-0.2271(8)	0.011(1)	0.3579(8)	-0.2280(1)	-0.0033(5)	0.37544(7)	-0.22056(4)	-0.0033(5)	0.37544(7)	-0.22056(4)
O <sup>II-</sup>	0.010(1)	0.6333(1)	0.22716(6)	0.0284(2)	0.6275(1)	0.23028(4)	0.0028(3)	0.62368(3)	0.22062(2)	0.0028(3)	0.62368(3)	0.22062(2)
700												
Atom	x	y	z	x	y	z	x	y	z	x	y	z
Li <sup>I</sup>	0	0	0	0	0	0	0	0	0	0	0	0
Mn <sup>IV</sup>	0.33242(5)	0.33242(5)	0	0.33182(5)	0.33182(5)	0	0.3358(2)	0.3358(2)	0	0.3358(2)	0.3358(2)	0
Mn <sup>IV</sup>	0.66758(5)	0.66758(5)	0	0.66818(5)	0.66818(5)	0	0.6642(2)	0.6642(2)	0	0.6642(2)	0.6642(2)	0
O <sup>II-</sup>	0.3581(8)	0.6377(3)	-0.2185(2)	0.356(1)	0.6335(7)	-0.2079(3)	0.370(1)	0.6298(1)	-0.2225(2)	0.370(1)	0.6298(1)	-0.2225(2)
O <sup>II-</sup>	0.6408(1)	0.36016(8)	0.21849(1)	0.62996(6)	0.3551(2)	0.20786(2)	0.62980(6)	0.36949(6)	0.22239(2)	0.62980(6)	0.36949(6)	0.22239(2)
O <sup>II-</sup>	0.36797(5)	-0.0084(1)	0.23319(4)	0.36477(5)	0.0027(4)	0.22910(3)	0.37539(3)	-0.0018(4)	0.22049(2)	0.37539(3)	-0.0018(4)	0.22049(2)
O <sup>II-</sup>	0.62891(3)	0.0096(1)	-0.23294(1)	0.62384(3)	0.032(2)	-0.2300(9)	-0.221(1)	0.003(3)	0.623(1)	-0.221(1)	0.003(3)	0.623(1)
O <sup>II-</sup>	0.000(1)	0.3640(8)	-0.2271(8)	0.011(1)	0.3579(8)	-0.2280(1)	-0.0033(5)	0.37544(7)	-0.22056(4)	-0.0033(5)	0.37544(7)	-0.22056(4)
O <sup>II-</sup>	0.010(1)	0.6333(1)	0.22716(6)	0.0284(2)	0.6275(1)	0.23028(4)	0.0028(3)	0.62368(3)	0.22062(2)	0.0028(3)	0.62368(3)	0.22062(2)

LMO_MnO_												
700				800				900				
Atom	x	y	z	x	y	z	x	y	z	x	y	z
Li <sup>I</sup>	0	0	0	0	0	0	0	0	0	0	0	0
Mn <sup>IV</sup>	0.3355(4)	0.3355(4)	0	0.3314(2)	0.3314(2)	0	0.3314(2)	0.3314(2)	0	0.336(2)	0.336(2)	0
Mn <sup>IV</sup>	0.6645(4)	0.6645(4)	0	0.6686(2)	0.6686(2)	0	0.6686(2)	0.6686(2)	0	0.664(2)	0.664(2)	0
O <sup>II-</sup>	0.351(2)	0.6472(4)	-0.2026(6)	0.365(3)	0.637(1)	-0.228(1)	0.365(3)	0.637(1)	-0.228(1)	0.374(3)	0.631(1)	-0.222(1)
O <sup>II-</sup>	0.6469(1)	0.35166(6)	0.20238(2)	0.6387(3)	0.3631(2)	0.22731(2)	0.6387(3)	0.3631(2)	0.22731(2)	0.6262(2)	0.3699(2)	0.22176(3)
O <sup>II-</sup>	0.37406(5)	-0.0186(9)	0.23727(2)	0.3843(5)	-0.025(1)	0.2297(2)	0.3843(5)	-0.025(1)	0.2297(2)	0.379(1)	-0.0054(6)	0.2241(4)
O <sup>II-</sup>	0.62625(3)	0.0189(3)	-0.23757(2)	0.62418(6)	0.0145(3)	-0.2285(4)	0.62418(6)	0.0145(3)	-0.2285(4)	0.62656(9)	0.0037(5)	-0.22120(5)
O <sup>II-</sup>	-0.01842(9)	0.37394(3)	-0.23771(2)	-0.0250(1)	0.38341(3)	-0.23027(2)	-0.0250(1)	0.38341(3)	-0.23027(2)	-0.0063(2)	0.38110(5)	-0.22384(3)
O <sup>II-</sup>	0.0189(1)	0.626(2)	0.237(2)	0.0168(2)	0.62373(4)	0.22787(2)	0.0168(2)	0.62373(4)	0.22787(2)	0.0035(3)	0.62753(4)	0.22109(3)

## A.3 Chapter 4

### A.3.1 Magnetic measurement

The calculation of the  $C$  and  $\theta$  experimental parameters are calculated plotting the inverse of the molar susceptibility versus the temperature, as seen in Figure A.2. The obtained values for  $C$  and  $\theta$  are  $1.75 \text{ emu} \cdot \text{K} \cdot \text{mol}^{-1}$   $-21.5 \text{ K}$  respectively.

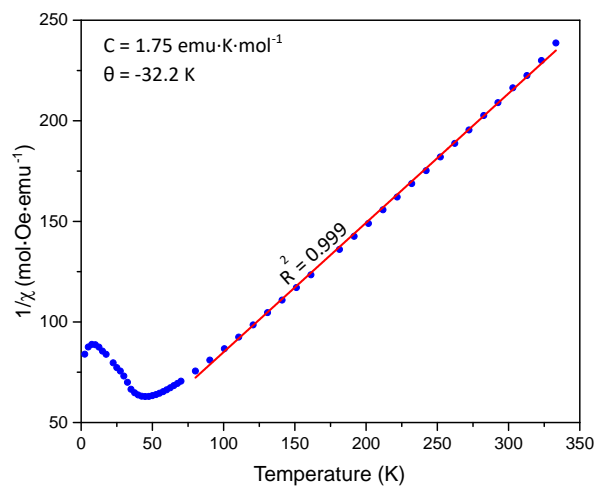


Fig. A.2 The inverse of the molar susceptibility in function of the temperature of LMO\_MnCO3\_900\_5.

## A.4 Chapter 5

### A.4.1 Linear regression of the oxidation state of the oxygen atoms in $\text{Li}_2\text{MnO}_3$

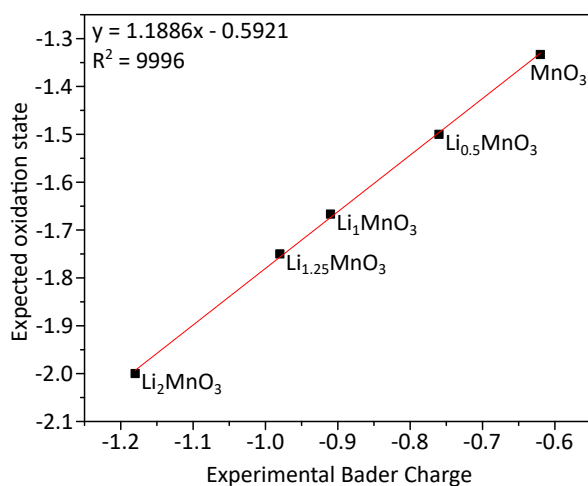


Fig. A.3 Relationship between the calculated Bader charge and the expected oxidation state.

### A.4.2 Bader charges of $\text{Li}_x\text{MnO}_3$

In this section the Bader charges of two different ideal and defective structures for  $\text{Li}_{1.25}\text{MnO}_3$  and  $\text{LiMnO}_3$  are shown with their standard deviation and the number of atoms which are with that configuration in that structure.

Table A.3 Bader charges of  $\text{Li}_{1.25}\text{MnO}_3$  ideal structures.

Structure 1		
Coord. N	N Li tetra	Aver.
3	1	-0.84
	0	-0.81(1)
4	2	-1.00(1)
	1	-1.00(1)
5	0	-0.92(5)
	0	-1.04(4)
6	0	-1.11(3)
Structure 2		
Coord. N	N Li tetra	Aver.
3	1	-0.82(1)
	0	-0.80(1)
4	1	-1.00(1)
	0	-0.91(4)
5	0	-1.05(3)
6	0	-1.12(2)

Table A.4 Bader charges of  $\text{Li}_{1.25}\text{MnO}_3$  defective structures.

Structure 1		
Coord. N	N Li tetra	Aver.
3	0	-0.80(1)
4	1	-0.99(1)
	0	-0.91(5)
5	0	-1.03(4)
6	0	-1.12(3)
Structure 2		
Coord. N	N Li tetra	Aver.
3	1	-0.83
	0	-0.80(1)
4	1	-0.99(1)
	0	-0.92(4)
5	0	-1.03(3)
6	0	-1.12(3)

Table A.5 Bader charges of LiMnO<sub>3</sub> ideal structures.

Structure 1		
Coord. N	N Li tetra	Aver.
2	0	-0.70
3	1	-0.84(2)
	0	-0.81(1)
4	1	-0.99(1)
	0	-0.91 (5)
5	0	-1.02(4)
Structure 2		
Coord. N	N Li tetra	Aver.
2	0	-0.66
3	1	-0.82(1)
	0	-0.81(2)
4	1	-0.98(2)
	0	-0.92(5)
5	0	-1.02(4)
6	0	-1.11(1)

Table A.6 Bader charges of LiMnO<sub>3</sub> defective structures.

Structure 1		
Coord. N	N Li tetra	Aver.
3	1	-0.84
	0	-0.81(1)
4	2	-1.00(1)
	1	-1.00(1)
5	0	-0.92(5)
	0	-1.04(4)
6	0	-1.11(3)
Structure 1		
Coord. N	N Li tetra	Aver.
2	0	-0.66
3	1	-0.82(1)
	0	-0.81(2)
4	1	-0.98(2)
	0	-0.92(5)
5	0	-1.02(4)
6	0	-1.11

## A.5 Chapter 6

### A.5.1 Atomic positions for the unified FAULTS cell

Table A.7 Atomic positions for the averaged  $\text{Li}_{1.2}\text{Mn}_{0.6}\text{Ni}_{0.2}\text{O}_2$  structure in the FAULTS unit cell.

Atom	$x$	$y$	$z$
Li	0.00000	0.00000	0.00000
Li	0.32617	0.34767	0.00000
Li	0.67383	0.65233	0.00000
Li/Mn/Ni	0.33333	0.00000	0.50000
Li/Mn/Ni	0.00102	0.66463	0.50000
Li/Mn/Ni	0.66565	0.33537	0.50000
O	-0.01042	0.34367	0.27272
O	-0.00883	0.00000	0.72602
O	0.33325	0.65633	0.27272
O	0.33342	0.34367	0.72728
O	0.67550	0.00000	0.27397
O	0.67708	0.65633	0.72728

### A.5.2 Rietveld refinement of $\text{Li}_{1.2}\text{Mn}_{0.6}\text{Ni}_{0.2}\text{O}_2$

### A.5.3 Stacking probability of $\text{LiMn}_{0.5}\text{Ni}_{0.5}\text{O}_2$ and $\text{Li}[\text{Li}_{1/3}\text{Mn}_{2/3}]\text{O}_2$

The use of different stacking probabilities generate blocks of layers whose average block size (and therefore the average layer size) varies. Table A.8 shows the transition probabilities required to form blocks of a given size, whose final composition must be 0.4:0.6 for  $\text{LiMn}_{0.5}\text{Ni}_{0.5}\text{O}_2$  and  $\text{Li}[\text{Li}_{1/3}\text{Mn}_{2/3}]\text{O}_2$ .

Table A.8 Transition percentages used in FAULTS program to form blocks with desired the average number of layers and size.

L1 $\rightarrow$ L1	L1 $\rightarrow$ L2	L2 $\rightarrow$ L1	L2 $\rightarrow$ L2	Av. number layers	Av. layer size (nm)
40%	60%	60%	40%	2.5	1.2
20%	80%	30%	70%	4	2.0
10%	90%	15%	85%	10	4.8
5%	95%	7.5%	92.5%	16.7	7.9

\* L1 refers to  $\text{LiMn}_{0.5}\text{Ni}_{0.5}\text{O}_2$  layers and L2 to  $\text{Li}[\text{Li}_{1/3}\text{Mn}_{2/3}]\text{O}_2$  layers.

\*\* Av. stands form average.

Table A.9 Comparison of the Rietveld refined parameters of synchrotron data for  $L_{1+x}NMO\_SC\_900$  and  $L_{1+x}NMO\_SC\_700$ . The refinement has been done using  $C2/m$  space group.

Sample name	$L_{1+x}NMO\_SC\_900$	$L_{1+x}NMO\_SC\_700$				
Space group	$C2/m$					
	<i>a</i>	4.9409(8)				
	<i>b</i>	8.552(3)				
	<i>c</i>	5.0256(5)				
	$\beta$	109.29(1)				
	Volume	200.4543				
Atomic positions	x	y	z	x	y	z
<i>2b</i>	0.00000	0.00000	0.00000	0.00000	0.00000	0.00000
<i>4g</i>	0.00000	0.334(1)	0.00000	0.00000	0.334(3)	0.00000
<i>2c</i>	0.50000	0.00000	0.50000	0.50000	0.00000	0.50000
<i>4h</i>	0.00000	0.84000	0.50000	0.00000	0.84000	0.50000
<i>4i</i>	0.27(1)	0.00000	0.771(7)	0.27(2)	0.00000	0.770(1)
<i>8j</i>	0.754(8)	0.830(4)	0.776(4)	0.75(1)	0.826(6)	0.778(7)
Ni/Li intermixing	Ni in 4h	2.4%		6.2%		
Microstructural parameters	Particle size (nm)	92.5(2)		18.4(1)		
	Strains (%)	17.33		26.64		
Agreement factors	$R_p$	10.3		12		
	$wR_p$	12.6		13.8		
	$R_{exp}$	0.607		0.816		
	$\chi^2$	431.6		285.8		



### A.5.4 Operando XRD patterns refinement results

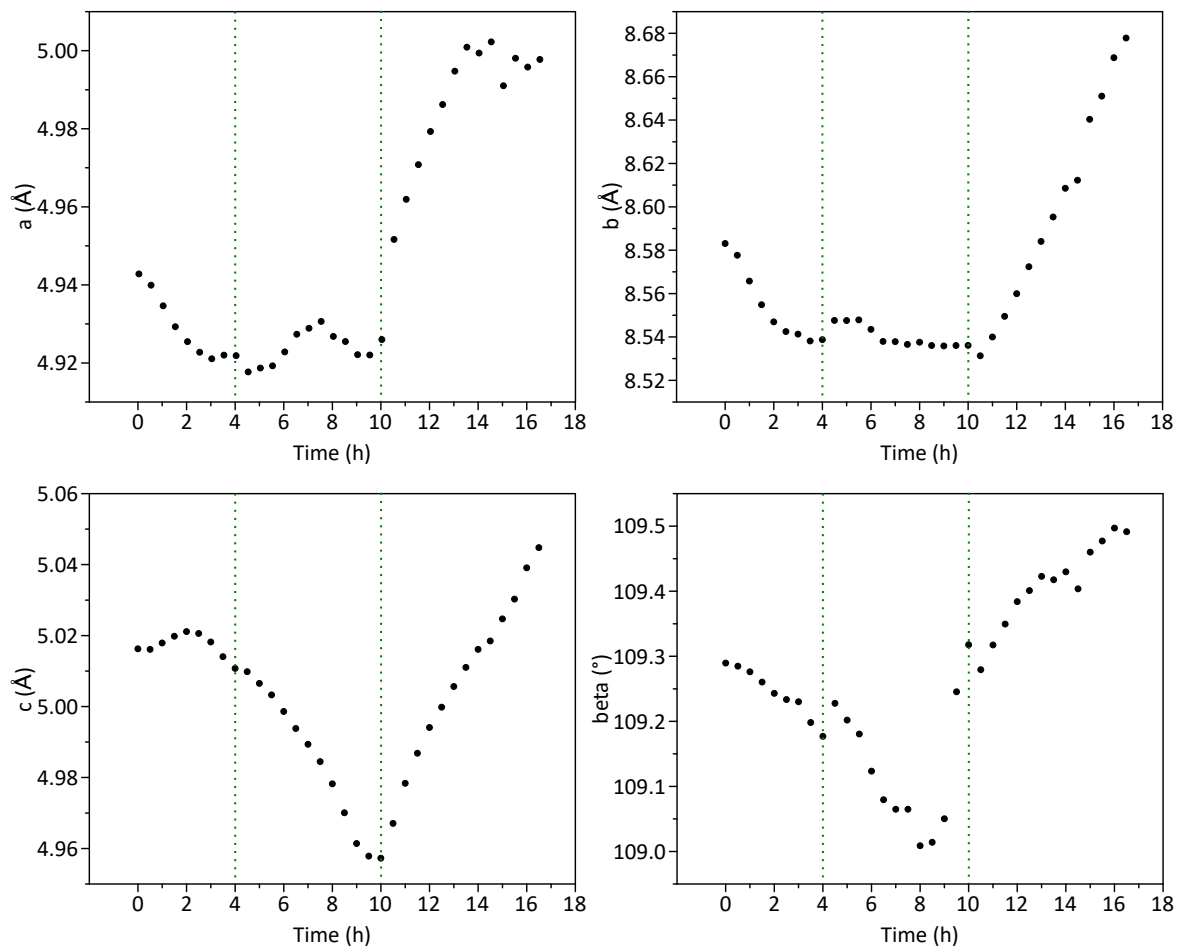


Fig. A.4 Refined unit cell parameters ( $a$ ,  $b$ ,  $c$  and  $\beta$ ) upon charge and discharge. Green dashed lines mark the end of the charge region 1 and the end of charge region 2.

